Measurement of the Muon Beam Properties and Muon Neutrino Inclusive Charged-Current Cross Section in an Accelerator-produced Neutrino Experiment

Kento Suzuki

May, 2015

Department of Physics, Graduate School of Science
Kyoto University

Measurement of the Muon Beam Properties and Muon Neutrino Inclusive Charged-Current Cross Section in an Accelerator-produced Neutrino Experiment

A dissertation
submitted in partial fulfillment of the requirements
for the Degree of Doctor of Science
in the Graduate School of Science, Kyoto Univeristy

Kento Suzuki

Department of Physics, Graduate School of Science
Kyoto University

May, 2015

Abstract

In this thesis, we report two measurements: a measurement of the beam properties and a measurement of the ν_μ-Fe CC inclusive cross section in the T2K neutrino oscillation experiment. In order to accomplish a precise measurement of the neutrino oscillation parameters and a search for the unknown parameter δ_{CP}, a good control of the neutrino beam and understanding the neutrino-nucleus interaction mechanism are essential in T2K.

We first describe the measurements of the direction and intensity of the muon beam, and the absolute muon flux to monitor the neutrino beam. The T2K muon monitor was installed to measure the direction and stability of the muon beam which is produced together with the muon neutrino beam. The result of the measurement of the muon beam profile center for the entire run period is (X,Y) = $(0.0 \pm 2.3, -1.0 \pm 2.3)$ cm, and its root mean square (RMS) of the beam-by-beam fluctuation is (X,Y) = $(1.0, 1.6)$ cm. The result of measurement of the total collected charge for 250 (205) kA horn operation is 32.5 (21.7) nC/10^{12} p.o.t., and its RMS of the beam-by-beam fluctuation is 1.2% (0.7%). Accordingly, the muon beam direction is kept within 0.3 mrad with respect to the designed beam-axis for most of the span of beam operation, and the total collected charge is also kept stable with the RMS of 1%. In order to confirm our understanding of muon beam and neutrino beam, the absolute muon flux is measured with the emulsion detector with a precision of 3%, which is in good agreement with the prediction of our beam simultion. From these results, we ensure that the detector response of the muon monitor is well understood and the validity of the beam control by the muon monitor is confirmed. All the beam measurements have guaranteed good quality beam data for the neutrino oscillation measurements and our cross section measurement.

Second, we report the measurement of the ν_μ-Fe CC inclusive cross section in neutrino energy range of 1-3 GeV. In this measurement, we develop a new method to utilize a dependence of the neutrino energy on the off-axis angle in addition to the event topologies. The obtained cross sections are $\sigma^{cc}(1.1\text{ GeV}) = 1.10 \pm 0.15$ (10^{-38}cm^2/nucleon), $\sigma^{cc}(2.0\text{ GeV}) = 2.07 \pm 0.27$ (10^{-38}cm^2/nucleon), and $\sigma^{cc}(3.3\text{ GeV}) = 2.29 \pm 0.45$ (10^{-38}cm^2/nucleon), at mean energies of 1.1, 2.0, and 3.3 GeV. Our results are consistent with the past measurements and predictions by the neutrino event generators of NEUT and GENIE. The measurement of the energy dependent cross section using neutrino beams with different off-axis angles is the first attempt in the world. Our analysis also demonstrates the feasibility of the precise CC inclusive cross section measurement which could be useful for the neutrino oscillation experiment.

Acknowledgements

First of all, I would like to denote that this thesis is the product of years with the tremendous supports.

I would like to express my most sincere gratitude to Prof. Nakaya Tsuyoshi for his instructions and encouragements throughout my research life. His great insight about physics was very educational and impressive to me. I would like to thank Prof. Atsuko K. Ichikawa from the bottom of my heart. She always pushed me into the correct way when I was lost in my study. I never forget her strong encourages and supports given for the 6 years of my research life. I also would like to thank Dr. Akihiro Minamino. Discussions with him were always productive and helpful in my study.

Most of my research life in this laboratory was always with the muon monitor and MUMONers. I would like to express a special thank to Prof. Masashi Yokoyama. Although the time I spent with him at Kyoto University was only 1 year, the work with him at the Uji beam test in 2009 was very impressive to me. I want to give a grateful thank to Dr. Kodai Matsuoka for his educational instructions given when I was a master's student. I always admire his stoical attitude, which is a model for my research life. I want to appreciate Hajime Kubo who gave me a lot of advice on analyses with the beam data and the beam simulation. I also want to appreciate Dr. Akira Murakami and Takahiro Hiraki who always worked with me for management of the muon monitor. I would like to thank members of the emulsion group: Dr. Akitaka Ariga and Prof. Shigeki Aoki. The work for installation of the emulsion detector with them was a precious experience. The works with the muon monitor were always supported by people of the KEK neutrino group. After the Grate East Japan Earthquake in 2011, the strong leadership by Prof. Takashi Kobayashi returned the T2K experiment into physics operation. Prof. Takeshi Nakadaira and Dr. Ken Sakashita gave me a lot of advice on analyses with the beam data. Discussions with them at NU1 and CCR were irreplaceable experiences to me. Prof. Takasumi Maruyama, Dr. Taku Ishida, and Dr. Takanobu Ishii always supported the works at on-site. I also wish to extend my thanks to Prof. Yoshiaki Fujii, Prof. Yoshikazu Yamada, Prof. Toshifumi Tsukamoto, Prof. Masaru Tada, Dr. Kazuo Nakayoshi, Dr. Tetsuro Sekiguch, Dr. Soh Y. Suzuki, and Dr. Friend Megan. My sincere thanks also go to the experts on the primary beam monitors: Dr. Mark Hartz, Prof. Hidekazu Kakuno, and Dr. Masahiro Shibata. Discussions with them were very instructive to me.

Regarding the neutrino cross section measurement, I would like to express my gratitude to Prof. Yoshinari Hayato, who is one of the developer of NEUT. He brought me into the world of the neutrino interaction physics. I would like to thank Dr. Mark Scott, Dr. Mark Rayner, Dr. Michael Wilking, Dr. Ryan Terri, and Prof. Yusuke Koshio. They gave me a lot of comment and advice in the course of the review of my cross section analysis. Without their helps, I would not be able to accomplish this measurement. I also would like to show my appreciation for continuous encouragements and supports

from the T2K cross section convenors: Prof. Alysia Diane Marino, Prof. Alfons Weber, Dr. Bruce Barger, Prof. Francesca Di Lodovico, and Prof. Kendall Mahn. I wish to extend my gratitude to all the T2K members and people working in the J-PARC accelerator.

I am very happy that most of my research life was shared with Dr. Tatsuya Kikawa, Shota Takahashi, and Huang Kunxian. I really enjoyed living at Ohta-danch and working with them at J-PARC. I hope that our friendship continues eternally. It was pleasure to stay with Dr. Kei Ieki in the same room of Ohta-danchi. He always pointed out mistakes in my Japanese with a smug face. I also thank Dr. Takatomi Yano, Dr. Motoyasu Ikeda, Dr. Ryosuke Ohta, Dr. Christophe Bronner, and Dr. Philip Litchfield. Living with them at Tokai was also wonderful and memorable.

Special thanks go to all the members in Room 304: Dr. Nikhul Patel, Dr. Tatsuya Kikawa, Yousuke Maeda, Mika Yamamoto, and Satoshi Shinohara. Chatting with them was a pleasant time. In particular, I have to say a big thank to Nikhul Patel who gave me a lot of advice on English grammar.

I would like to give many thanks to the members in our laboratory: Prof. Masaya Ishino, Dr. Hajime Nanjo, Dr. Toshi Sumida, Dr. Kiseki Nakamura, Dr. Son van Cao, Eriko Hayashi, Saki Yamashita, Naoki Kawasaki, Daichi Naito, Seiko Hirota, Shigeto Seki, Takuya Tashiro, Ichinori Kamiji, Kunigo Takuto, Kouta Nakagiri, Keigo Nakamura, Kento Yoshida, Tatuya Hayashino, Yuuki Ishiyama, Jiang Miao, Keisuke Kondo, Kento Haneda, Ban Sei, Ryutaro Monden, and Saori Yanagita.

I would like to acknowledge supports from the Japan Society for Promotion of Science (JSPS) and the global COE program.

Finally, I want to express my deepest appreciation to my family: Tetsuo Suzuki, Youko Suzuki, and Eri Ishibashi.

Kento Suzuki
Kyoto, Japan
May, 2015

Contents

Part I.

Neutrino experiment with an accelerator-produced neutrino beam

Chapter 1

Introduction

The Standard Model (SM) was established in 1970s, and almost all the experimental results in the particle physics are successfully explained by this model. A Higgs boson, which is the last particle predicted by the SM was finally discovered by the ATLAS and CMS collaborations in 2012. The result ensures that the SM is the best model to explain all of the phenomena in the particle physics. However, even though the SM is considered to be the most reliable model, there are still subjects not to be fully understood. Matter-antimatter asymmetry in the universe is one of those subjects that the SM cannot explain.

Andrei Sakharov showed a list of three necessary conditions to produce the matter-antimatter asymmetry, which is named the "Sakharov condition" [1]. One of the conditions requires the violation of CP symmetry in the very early universe.

The CP transformation is a combination of charge conjugation C and parity P. The CP symmetry indicates the laws of Natures are same for matter and antimatter. The CP symmetry was, however, found to be violated in the neutral K meson decay via the weak interaction in 1964 [2]. Recent measurements in the B meson decays have also showed that CP is violated in the weak interaction. The CP violation has been observed, measured in the quark sector and understood in the context of the SM whereas it is not yet observed in the lepton sector.

Neutrino is one of the elementary particles and has three known types (flavors). The flavor is conserved in the interaction, however it was found that neutrino changes its flavor while propagating a long distance. This phenomenon is called as "neutrino oscillation". Super-Kamiokande (Super-K) [3] reported the evidence of neutrino oscillation in 1998 [4], and much progress has been made in the understandings of the phenomenon. Present and future neutrino oscillation experiments focus on the measurement of the CP violating phase (δ_{CP}) in the lepton sector, which could be a key to solve the matter-antimatter asymmetry in the universe.

1.1. Neutrino and weak interaction

A neutrino was first proposed by Wolfgang Pauli in 1930 and discovered by Cowan and Reines in 1956 [5] using a reaction:

$$\bar{\nu}_e + p \rightarrow e^+ + n \tag{1.1}$$

of neutrinos from a reactor. The interaction of neutrino occurs mediated by weak bosons $W^{\pm}$ and Z^0 and is known as "weak interaction". The diagram of the reaction in Eq. (1.1) is shown in Fig. 1.1.

Historically, study of the weak interaction began with the nuclear β-decay: $n \rightarrow p + e^- + \bar{\nu}_e$. In 1934, Enrico Fermi developed his model for the β-decay in analogy with electromagnetism assuming the interaction is pointlike:

$$\mathcal{M} = \frac{G_F}{\sqrt{2}}(\bar{u}_p \gamma^\mu u_n)(\bar{u}_e \gamma_\mu u_\nu) \ , \tag{1.2}$$

where u's are particle spinors and G_F is the coupling constant known as the Fermi constant. In 1957, the parity violation in the weak interaction was discovered by Chien-Shiung Wu and her collaboration [6]. This result required modifications in Eq. (1.2):

$$\mathcal{M} = \frac{G_F}{\sqrt{2}} \left\{ \bar{u}_p \gamma^\mu \frac{1}{2}(1-\gamma^5) u_n \right\} \left\{ \bar{u}_e \gamma_\mu \frac{1}{2}(1-\gamma^5) u_\nu \right\} \ . \tag{1.3}$$

This structure is called as vector-axial (V-A) theory where only the left-handed particles (right-handed antiparticle) are involved in the weak interaction. In the late 1960s, a unified theory of the weak and electromagnetic interactions was developed by Glashow, Weiberg and Salam, which is known as the "electroweak theory". In the theory, the W and Z bosons are predicted as the vector bosons which mediate the charged- and neutral-current weak interactions. The β decay can be interpreted as the weak charged-current (CC) process which occurs mediated by W boson. Associated with the existence of Z boson, the weak neutral current (NC) should exist in nature. It was indeed discovered in a bubble chamber experiment at CERN in 1973 [7]. This result supported the existence of the Z boson and hence the electroweak theory. In the 1970s, the electroweak theory was incorporated into the SM together with the quantum chromodynamics. In 1983, both of the vector bosons, W and Z, were discovered by two experiments, UA1 and UA2, at the CERN SPS collider [8, 9]. Based on this discovery, the weak interaction was experimentally established.

In the SM, neutrinos are depicted as:

- massless and spin 1/2 particle,
- with three generations (ν_e, ν_μ, and ν_τ),
- having left handed chirality, and

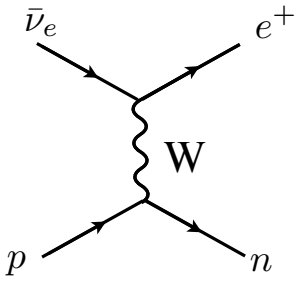

Figure 1.1.: Diagram for the reaction of the β-decay ($\bar{\nu}_e + p \rightarrow e^+ + n$).

- electrically neutral and weakly interacting elementary particle.

Now neutrino has been used for studies in many fields: solar-physics, astrophysics and geophysics. Although the neutrino mass is set to zero in the SM, it indeed has a mass as described in Sec. 1.2. Neutrino could give a hint of the physics beyond the SM. It is now being explored via the phenomenon of neutrino oscillation.

1.2. Neutrino oscillation

Neutrino oscillation is a phenomenon in which neutrino changes their flavors as a consequence of a mismatch between the flavor and mass eigenstates. The flavor eigenstate of a neutrino is expressed as a combination of the mass eigenstates. Each of the mass eigenstates propagates with different velocity due to the different masses, resulting in changing the flavors as time evolves. An idea of the neutrino oscillation was first born by Pontecorvo in 1957. He postulated an neutrino-antineutrino transition in analogy with the neutral K decay. In 1962, oscillation among two different neutrinos (ν_e and ν_μ) was modeled by Maki, Nakagawa, and Sakata [10].

Although neutrinos are treated as massless particles in the SM, the oscillation indicates that neutrinos have finite masses. Therefore, this phenomenon cannot be explained in the SM.

1.2.1. Evidence for neutrino oscillation

Experimentally neutrino oscillation was confirmed by the Super-K collaborator in 1998 [4] using a gigantic water Cherenkov detector, details of which is given in Sec. 2.1. They used atmospheric neutrino samples, which are decay products of the hadrons produced in the the collision of cosmic rays in the upper atmosphere. Production of electron and muon neutrinos is dominated by the process $\pi^+ \rightarrow \mu^+ + \nu_\mu$ followed by $\mu^+ \rightarrow e^+ + \bar{\nu}_\mu + \nu_e$ (and their charge conjugates). After entering the water tank, the neutrino interacts with a hydrogen or oxygen nucleus, and produces muon (or electron) via the weak interaction, which undergoes the Cherenkov radiation. In the analysis, single ring fully-contained (FC)

events and partially-contained (PC) events were selected. Here, FC events deposit all the Cherenkov light in the inner detector volume and PC events deposit some Cherenkov light in the outer detector. The selected events were categoized according to the charged lepton momentum, flavor (e-like or μ-like), and zenith angle ($\cos\Theta$). For each event sample, the up-down asymmetry was calculated, which is defined as follows:

$$A = \frac{U - D}{U + D} \ , \tag{1.4}$$

where U is the number of upward-going events ($-1 < \cos\Theta < -0.2$) and D is the number of downward-going events ($0.2 < \cos\Theta < 1$). The obtained asymmetry is shown in Fig. 1.2. The expectation with no neutrino oscillation hypothesis is overlaid as a hatched region in the figure. As seen in the figure, the asymmetry was significantly deviated from the expectation for μ-like events, resulting from the deficit of the upward-going μ-like events. The result is interpreted as follows. The neutrinos produced at a zenith angle of $\cos\Theta = -1$ have to travel more than 12000 km before interacting and hence oscillation probability is large. The two-flavor oscillation hypothesis, $\nu_\mu \leftrightarrow \nu_\tau$ was examined using a χ^2 comparison and was consistent with the data. This result showed the first evidence of the neutrino oscillation.

1.2.2. Theory of neutrino oscillation in vacuum

A flavor eigenstate of neutrino, $|\nu_\alpha\rangle$ ($\alpha = e, \mu, \tau$) is not identical to a mass eigenstate, $|\nu_i\rangle$ ($i = 1, 2, 3$). The flavor eigenstate can be expressed as superposition of the mass eigenstate:

$$|\nu_\alpha\rangle = \sum_i U_{\alpha i} |\nu_i\rangle \ , \tag{1.5}$$

where $U_{\alpha,i}$ is an unitary matrix and is known as the Pontecorov-Maki-Nakagawa-Sakata (PMNS) matrix. The PMNS matrix is expressed as follows:

$$\begin{aligned} U &= \begin{pmatrix} 1 & 0 & 0 \\ 0 & c_{23} & s_{23} \\ 0 & -s_{23} & c_{23} \end{pmatrix} \begin{pmatrix} c_{13} & 0 & s_{13}e^{-i\delta_{CP}} \\ 0 & 1 & 0 \\ -s_{13}e^{i\delta_{CP}} & 0 & c_{13} \end{pmatrix} \begin{pmatrix} c_{12} & s_{12} & 0 \\ -s_{12} & c_{12} & 0 \\ 0 & 0 & 1 \end{pmatrix} \\ &= \begin{pmatrix} c_{12}c_{13} & s_{12}c_{13} & s_{13}e^{-i\delta_{CP}} \\ -s_{12}c_{23} - c_{12}s_{13}s_{23}e^{i\delta_{CP}} & c_{12}c_{23} - s_{12}s_{23}s_{13}e^{i\delta_{CP}} & c_{13}s_{23} \\ s_{12}s_{23} - c_{12}s_{13}c_{23}e^{i\delta_{CP}} & -c_{12}s_{23} - s_{12}s_{13}c_{23}e^{i\delta_{CP}} & c_{13}c_{23} \end{pmatrix} \ , \end{aligned} \tag{1.6}$$

where s_{ij} and c_{ij} represent $\sin\theta_{ij}$ and $\cos\theta_{ij}$, respectively. δ_{CP} is called "CP violating phase"; existence of this phase makes the probability of $\nu_\alpha \leftrightarrow \nu_\beta$ different from that of $\bar{\nu}_\alpha \leftrightarrow \bar{\nu}_\beta$ in the case of $\alpha \neq \beta$.

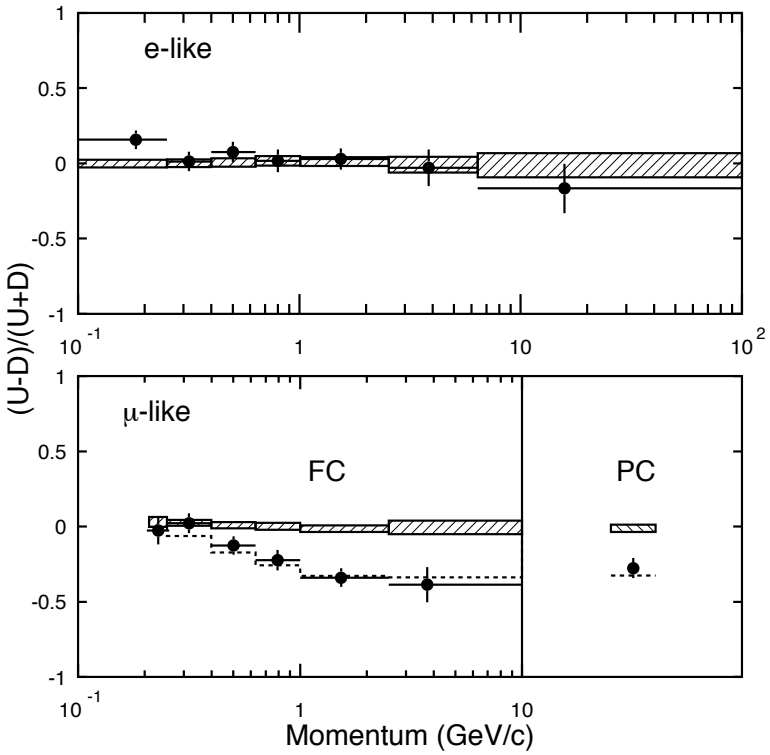

Figure 1.2.: The $(U-D)/(U+D)$ asymmetry for FC e-like and μ-like events and PC events. The hatched region represents the MC prediction with no-oscillation hypothesis. A deficit is seen in the upward-going μ-like events. The two-flavor oscillation hypothesis, $\nu_\mu \leftrightarrow \nu_\tau$, is examined using a χ^2 comparison and the fitted result is shown as a dashed line. The figure is taken from [4].

Time evolution of the mass eigenstate after a time interval of t is expressed as

$$|\nu_i(t)\rangle = e^{-i(E_i t - p_i L)}|\nu_i\rangle \ , \tag{1.7}$$

where E_i and p_i are the neutrino energy and momentum in the laboratory frame, respectively; L is the traveling distance. Since the neutrino is extremely relativistic because of its tiny mass, the energy can be approximately written as

$$E_i \simeq p_i + \frac{m_i^2}{2p_i} \ . \tag{1.8}$$

With Eq. (1.8), Equation (1.7) is re-written as

$$|\nu_i(L)\rangle \simeq e^{-i\frac{m_i^2}{2E_i}L}|\nu_i\rangle \ . \tag{1.9}$$

Here we use an approximation of $t \simeq L$ as the neutrino velocity is almost equal to c. With Eq. (1.5) and (1.9), the state can be expressed as function of energy and travel

distance as:

$$|\nu_\alpha(L)\rangle = \sum_i U_{\alpha i}|\nu_i(L)\rangle = \sum_i U_{\alpha i} e^{-i\frac{m_i^2}{2E_i}L}|\nu_i\rangle \ . \tag{1.10}$$

The oscillation probability that neutrino produced with a flavor α transforms into a flavor β after traveling L is

$$\begin{aligned} P(\nu_\alpha \to \nu_\beta) &= |\langle \nu_\beta|\nu_\alpha(L)\rangle|^2 \\ &= |\sum_i U_{\alpha i} e^{-i\frac{m_i^2}{2E_i}L} U^*_{\beta i}|^2 \\ &= \delta_{\alpha\beta} - 4\sum_{i>j=1}^{3} \mathrm{Re}(U_{\alpha i}U^*_{\beta i}U^*_{\alpha j}U_{\beta j}) \sin^2\left(\frac{\Delta m^2_{ij}L}{4E}\right) \\ &\quad + 4\sum_{i>j=1}^{3} \mathrm{Im}(U_{\alpha i}U^*_{\beta i}U^*_{\alpha j}U_{\beta j}) \sin\left(\frac{\Delta m^2_{ij}L}{4E}\right)\cos\left(\frac{\Delta m^2_{ij}L}{4E}\right) \ , \end{aligned} \tag{1.11}$$

where Δm^2_{ij} is a mass squared difference between ν_i and ν_j ($m_i^2 - m_j^2$). Since a sum of Δm^2_{ij} is zero, the number of independent parameters for the mass squared difference is two. Therefore, the neutrino oscillation is described by six independent parameters: three mixing angles, two mass squared difference, and one CP violating phase.

1.2.3. Oscillation in matter

Neutrino, which passes through matter, can undergo a scattering via the NC current. In this case, all three neutrinos (ν_e, ν_μ, and ν_τ) interacts in the same way. In addition to the NC interaction, ν_e can have CC interactions because of the existence of electrons in matter. Threfore, ν_e feels different potential from ν_μ and ν_τ. This effect is called "matter effect" [11]. The effective potentials are written as

$$\begin{aligned} V_e &= V_{CC} + V_{NC} \ , \\ V_{\mu,\tau} &= V_{NC} \ , \end{aligned}$$

where V_{CC} and V_{NC} are the charged and neutral current potentials, respectively and expressed as

$$\begin{aligned} V_{CC} &= \pm\sqrt{2}G_F n_e \ , \\ V_{NC} &= \pm\sqrt{2}G_F n_e(-1/2 + 2\sin^2\theta_W) \ , \end{aligned}$$

where n_e is the number density of electrons and θ_W is the Weinberg angle. The sign is flipped for anti-neutrinos. In the case of vacuum, the time evolution of the neutrino

flavor eigenstate is expressed as:

$$i\frac{d}{dt}\begin{pmatrix}\nu_e\\ \nu_\mu\\ \nu_\tau\end{pmatrix} = iU\frac{d}{dt}\begin{pmatrix}\nu_1\\ \nu_2\\ \nu_3\end{pmatrix} \tag{1.12}$$

$$= iU\begin{pmatrix}m_1^2/2E & 0 & 0\\ 0 & m_2^2/2E & 0\\ 0 & 0 & m_3^2/2E\end{pmatrix}\begin{pmatrix}\nu_1\\ \nu_2\\ \nu_3\end{pmatrix} \tag{1.13}$$

$$= iU\begin{pmatrix}m_1^2/2E & 0 & 0\\ 0 & m_2^2/2E & 0\\ 0 & 0 & m_3^2/2E\end{pmatrix}U^\dagger\begin{pmatrix}\nu_e\\ \nu_\mu\\ \nu_\tau\end{pmatrix} \tag{1.14}$$

$$\equiv H_{vac}\begin{pmatrix}\nu_e\\ \nu_\mu\\ \nu_\tau\end{pmatrix} \tag{1.15}$$

In matter, the extra potential of V needs to be taken into account in Eq. (1.15). Since V_{NC} is a common term for all the neutrino flavors and causes the same degree of the phase shift, we can consider only the effect from V_{CC}, which contributes only to ν_e:

$$i\frac{d}{dt}\begin{pmatrix}\nu_e\\ \nu_\mu\\ \nu_\tau\end{pmatrix} = (H_{vac}+V_{CC})\begin{pmatrix}\nu_e\\ \nu_\mu\\ \nu_\tau\end{pmatrix}$$

$$= \left[iU\begin{pmatrix}m_1^2/2E & 0 & 0\\ 0 & m_2^2/2E & 0\\ 0 & 0 & m_3^2/2E\end{pmatrix}U^\dagger \pm \begin{pmatrix}\sqrt{2}G_F n_e & 0 & 0\\ 0 & 0 & 0\\ 0 & 0 & 0\end{pmatrix}\right]\begin{pmatrix}\nu_e\\ \nu_\mu\\ \nu_\tau\end{pmatrix}. \tag{1.16}$$

Again the sign is flipped for anti-neutrinos for V_{cc}.

Long baseline neutrino experiments use a muon neutrino beam and measure oscillation parameters via the ν_e/ν_τ appearance or ν_μ disappearance channels. As for the ν_e appearance mode, the oscillation probability including the first order of the matter effect

is derived from Eq. (1.16) as

$$\begin{aligned} P(\nu_\mu \to \nu_e) = & 4c_{13}^2 s_{13}^2 s_{23}^2 \cdot \sin^2 \Phi_{31} \\ & + 8c_{13}^2 s_{12} s_{13} s_{23} (c_{12} c_{23} \cos\delta_{CP} - s_{12} s_{13} s_{23}) \cdot \cos\Phi_{32} \sin\Phi_{31} \sin\Phi_{21} \\ & - 8c_{13}^2 s_{12} c_{13} s_{12} s_{13} s_{23} \sin\delta_{CP} \cdot \sin\Phi_{32} \sin\Phi_{31} \sin\Phi_{21} \\ & + 4s_{12}^2 c_{13}^2 (c_{12}^2 c_{23}^2 + s_{12}^2 s_{23}^2 s_{13}^2 - 2c_{12} c_{23} s_{12} s_{13} \cos\delta_{CP}) \cdot \sin^2 \Phi_{21} \\ & - 8c_{13}^2 c_{13}^2 s_{23}^2 \cdot \frac{aL}{4E} (1 - 2s_{13}^2) \cdot \cos\Phi_{32} \sin\Phi_{31} \\ & + 8c_{13}^2 s_{13}^2 s_{23}^2 \cdot \frac{a}{\Delta m_{31}^2} (1 - 2s_{13}^2) \cdot \sin^2 \Phi_{31} \ , \end{aligned} \tag{1.17}$$

where

$$s_{ij} \equiv \sin\theta_{ij} \tag{1.18}$$

$$c_{ij} \equiv \sin\theta_{ij} \tag{1.19}$$

$$\Phi_{ij} \equiv \frac{\Delta m_{ij}^2 L}{4E} \tag{1.20}$$

$$a \equiv 2\sqrt{2} G_F n_e E \ , \tag{1.21}$$

In case of antineutrino ($\bar{\nu}_\mu \to \bar{\nu}_e$), the probability is given by flipping the sign of δ_{CP}. This matter effect is not large ($\sim$10%) in the T2K experiment [12] , where the baseline is 295 km, but becomes significant for the NOνA experiment ($L = 810$ km) [13].

1.2.4. Current knowledge of the oscillation parameters

The neutrino oscillation parameters have been measured with various neutrino sources.

Δm_{21}^2 and θ_{12} are measured with solar ν_e disappearance. The KamLAND experiment also measures these parameters using $\bar{\nu}_e$ emitted from nuclear power reactors [14, 15]. A combined oscillation analysis of solar and KamLAND data gives $\Delta m_{21}^2 = (7.53 \pm 0.18) \times 10^{-5}$ eV^2 and $\tan^2\theta_{12} = 0.436^{+0.029}_{-0.025}$ [16].

The best measurements of θ_{23} and Δm_{32}^2 are provided by the accelerator-produced neutrino experiments which measure ν_μ disappearance. The mixing angle θ_{23} is precisely measured by the T2K experiment [12]: $\sin^2\theta_{23} = 0.514^{+0.055}_{-0.056}$ [17]. The MINOS experiment [18] provides the best measurement of Δm_{32}^2, which is measured to be $|2.28\text{-}2.46| \times 10^{-3}$ eV^2 (68% C.L.) [19]. Both of the two experiments analyzed their data using hypothesis with three-neutrino oscillation formalism.

Only upper limit was known for θ_{13} until T2K reported indication for $\nu_\mu \to \nu_e$ oscillations [20]. The oscillation probability includes δ_{CP} in addition to θ_{13} as in Eq. (1.17). The reactor neutrino experiments measure θ_{13} using the reactor neutrino source($\bar{\nu}_e$) via

the disappearance channel. The oscillation probability is written as:

$$1 - P(\bar{\nu}_e \to \bar{\nu}_e) \simeq \sin^2 2\theta_{13} \sin\left(\frac{2\Delta m^2_{31} L}{4E}\right) . \tag{1.22}$$

As shown in the equation above, the probability does not include δ_{CP} and θ_{13} can be obtained directly. The θ_{13} is now measured precisely by the reactor experiments. The Daya Bay experiment [21] gives the best measurement of θ_{13} as $\sin^2(2\theta_{13}) = 0.089 \pm 0.008$ [22].

Table 1.1.: Current values of the oscillation parameters

Parameter	Best fit value
$\tan^2\theta_{12}$	$0.436^{+0.029}_{-0.025}$ [16]
$\sin^2\theta_{23}$	$0.514^{+0.055}_{-0.056}$ [17]
$\sin^2 2\theta_{13}$	0.089 ± 0.008 [22]
Δm^2_{21}	$(7.53 \pm 0.18) \times 10^{-5}$ eV^2 [16]
Δm^2_{32}	$\lvert 2.28\text{-}2.46 \rvert \times 10^{-3}$ eV^2 [19]

1.2.5. Remaining questions

There are some questions left in the lepton mixing. The distinct feature is that a pattern of the PMSN matrix ($= U^{PMNS}$) is very different from that of the CKM matrix ($= V^{CKM}$). According to Refs. [23] and [24], U^{PMNS} and V^{CKM} are measured to be

$$|U^{PMNS}| = \begin{pmatrix} 0.801 \sim 0.845 & 0.514 \sim 0.580 & 0.137 \sim 0.158 \\ 0.225 \sim 0.517 & 0.441 \sim 0.699 & 0.614 \sim 0.793 \\ 0.246 \sim 0.529 & 0.464 \sim 0.713 & 0.590 \sim 0.776 \end{pmatrix} \quad \text{and}$$

$$V^{CKM} = \begin{pmatrix} 0.97427 \pm 0.00014 & 0.22536 \pm 0.00061 & 0.00355 \pm 0.00015 \\ 0.22522 \pm 0.00061 & 0.97343 \pm 0.00015 & 0.0414 \pm 0.0012 \\ 0.00886^{+0.00033}_{-0.00032} & 0.0405^{+0.0011}_{-0.0012} & 0.99914 \pm 0.000005 \end{pmatrix} ,$$

respectively. Here 3σ range on the magnitude of all elements is shown in U^{PMNS} while 1σ error is shown in V^{CKM}. From the comparison of two mixing matrices, we can see flavor and mass are largely mixed in the lepton sector compared to the quark sector. Some of the theoretical models predict this feature. One of the famous model was "Tri-bimaximal"

(TB) scenario [25], in which the PMNS matrix is written as

$$U = \begin{pmatrix} \sqrt{2/3} & \sqrt{1/3} & 0 \\ -\sqrt{1/6} & \sqrt{1/3} & \sqrt{1/2} \\ \sqrt{1/6} & -\sqrt{1/3} & \sqrt{1/2} \end{pmatrix} . \tag{1.23}$$

This mixing pattern is derived on the assumption of the lepton flavor symmetry. However, this scenario was became less likely since θ_{13} proved to be non-zero[1]. The other famous model is "Anarchy model" [27]. The model explains that values of the mixing angle θ_{12}, θ_{13} and θ_{23} are randomly selected, resulting large mixing angles in U^{PMNS}. There is a model to relate U^{PMNS} to V^{CKM}, which is "quark-lepton complementarity" (QLC) [28]. This model explains the whole lepton mixing is generated as a combination of no mixing, a maximal, and the CKM mixings: the lepton and quark mixings are complementary. Determination of the correct model depends on precise measurement of the neutrino oscillation parameters and determination of δ_{CP}.

Ordering of the neutrino masses has not been determined yet. There are two possibilities: $m_3 \gg m_2 > m_1$ (normal mass hierarchy: NH) and $m_3 \ll m_1 < m_2$ (inverted mass hierarchy: IH). It is known that the matter effect in the neutrino oscillation may play a role in resolving the mass hierarchy. As described in Sec. 1.2.3, the electron neutrino feels the additional potential than the muon and tau neutrinos and the oscillation probability of $\nu_\mu \to \nu_e$ is expressed as in Eq. (1.17). Due to existence of the last two terms in the equation, the probability is different for the different signs of the mass squared difference (Δm^2_{31}). Therefore, the probability for NH is different from that for IH. This effect becomes significant for the neutrino experiments with baselines of order 1000 km. The long baseline oscillation experiment such as NOνA ($L = 810$ km) and other future experiments (e.g. [29]) aim to resolve the mass hierarchy by using this matter effect.

We also do not know about the value of δ_{CP}. The parameter, however, could be measured by comparing probability of $\nu_\alpha \to \nu_\beta$ with that of $\bar{\nu}_\alpha \to \bar{\nu}_\beta$:

$$\begin{aligned} P(\nu_\alpha \to \nu_\beta) - P(\bar{\nu}_\alpha \to \bar{\nu}_\beta) = {} & 16 \sin\theta_{12} \cos\theta_{12} \sin\theta_{23} \cos\theta_{23} \sin\theta_{13} \cos^2\theta_{13} \sin\delta_{CP} \\ & \times \sum_\gamma \epsilon_{\alpha\beta\gamma} \sin\frac{\Delta m^2_{21} L}{4E} \sin\frac{\Delta m^2_{31} L}{4E} \sin\frac{\Delta m^2_{32} L}{4E} , \end{aligned} \tag{1.24}$$

where $\epsilon_{\alpha\beta\gamma}$ is a Levi-Civita symbol. The value of Eq. (1.24) always become zero if $\alpha = \beta$, i.e. the disappearance mode. Namely, δ_{CP} is proved only via the appearance mode ($\alpha \neq \beta$). T2K, NOνA and future projects, such as T2HK [30] and LBNE [29], aim to measure the value of δ_{CP} using $\nu_\mu \to \nu_e$ and $\bar{\nu}_\mu \to \bar{\nu}_e$.

Another question is whether θ_{23} is maximal ($= 45°$) or non-maximal ($\neq 45°$). The θ_{23} is now the least precisely known mixing angle. This is because it is close to maximal mixing and it makes difficult to determine the angle from the measurement of $\sin^2(2\theta_{23})$. The reason is as follows. Now we consider the case when θ_{23} is shifted by a small amount

[1] There is a model to explain the mixing pattern in the PMNS matrix by modifying the TB mixing [26]

of $\Delta\theta_{23}$:

$$\begin{aligned}\sin^2\{2(\theta_{23}+\Delta\theta_{23})\} &\simeq \sin^2(2\theta_{23}) + 2\Delta\theta_{23}\cdot\frac{\partial}{\partial\theta}\sin^2 2\theta\,|_{\theta=\theta_{23}} \\ &= \sin^2(2\theta_{23}) + 8\Delta\theta_{23}\cdot\{\sin(2\theta_{23})\cos(2\theta_{23})\}\ . \end{aligned} \tag{1.25}$$

Here we use a Taylor series. In case that θ_{23} is close to 45°, the second term in Eq. (1.25) is also close to zero as $\cos(2\times 45)^\circ = 0$. Namely, it will be difficult to distinguish these two values: $\sin^2\{2(\theta_{23}+\Delta\theta_{23})\}$ and $\sin^2(2\theta_{23})$. The uncertainty of θ_{23}, especially its octant, could affect in the measurement of δ_{CP} as in Eq. (1.24). Therefore, resolution of the octant of θ_{23} is also important for the measurement of δ_{CP} and would also be useful for modelling the framework of the lepton mixing as described above.

1.3. Accelerator neutrino experiment

The world-first accelerator neutrino experiment was carried out by Lederman *et al.* In 1962, they reported an observation of two neutrino flavours [31]. In this experiment, they injected a proton beam onto a nuclear target in order to produce secondary particles. Neutrino was then produced as a decay product of the secondaries. After that, a magnetic horn was developed by Simon van der Meer. This device enables to collect the secondaries and hence create an intense neutrino beam. The horn is now one of the irreplaceable components in the "conventional" accelerator neutrino experiment. There are also new concepts such as the "beta beam" [32] and the "neutrino factory" [33]. In this section, however, we focus on the "conventional" accelerator neutrino experiment because the T2K experiment, in which the author has engaged, is based on this conventional method.

1.3.1. Production of hadrons

In the accelerator neutrino experiment, a proton beam is injected onto a nuclear target, where mainly pions and kaons are produced. They undergo following decays:

$$\begin{aligned} \pi^\pm &\to \mu\nu_\mu \qquad (\mathrm{BR}\sim 100\%)\ , \\ K^\pm &\to \mu\nu_\mu \qquad (\mathrm{BR}\sim 63.4\%)\ , \\ K_L &\to \pi\mu\nu_\mu \qquad (\mathrm{BR}\sim 27.2\%)\ . \end{aligned}$$

Namely, a muon neutrino beam is created. There are small contamination of ν_e due to K_{e3} decay ($K^\pm \to \pi^0 e\nu_e$), π decay ($\pi^\pm \to e\nu_e$) and μ decay ($\mu \to e\nu_e\nu_\mu$). In the accelerator neutrino experiment where the detectors are placed away from the target and at a certain position, it is important to know productions of the secondaries since the production yields determine the absolute neutrino flux. Indeed, uncertainty in the production of secondaries are one of the major systematics in the neutrino flux prediction. In the T2K experiment, the information of the secondary production are provided by

external experiments. Details of the application of the information are described in Sec. 6.4.2.

1.3.2. Wide band beam with a focusing device

The first accelerator neutrino experiment [31] utilzed a "bare target beam", After that, an idea of meson focusing was born by Simon van der Meer [34]. He first developed a "magnetic horn", which is a focusing device to collect the secondaries and therefore enhance the neutrino flux. The horn structure was a conical surface as illustrated in Fig. 1.3 in order to collect as many secondaries as possible (see Appendix A). The toroidal magnetic field is applied in the region between inner and outer conductors. Then, the Lorentz force focuses particles of one sign (π^+), and defocuses particles of the other sign (π^-), resulting in increasing a ν_μ beam while reducing $\bar{\nu}_\mu$ background. After that, a magnetic horn with the parabolic-shaped inner conductor was proposed by Budker; secondaries in wide angular region can be focused using the parabolic lens. This horn system was first attempted in the e^+e^- collider and then implemented in a neutrino beam at the IHEP accelerator [35, 36].

The present common style of focusing secondaries is to use multiple horn systems which was first noted by Palmer and adopted at the CERN PS neutrino beam [37]. Figure 1.4 shows an example of the multi-horn system. As shown in this figure, two horns are used to improve the collection efficiency for the secondaries: under- and over-focused particles are collected by the second horn. In addition, the second horn also allows the correction for particles which do not enter the first horn. In the case of adopting the multi-horn system, however, the second horn must be placed further away from the target in order to realize the "point source approximation" as described in Appendix A. This system is currently adopted in the Fermilab NuMI beamline [38] where two horns are used as shown in Fig. 1.4.

In the T2K experiment, three horns are used as shown in Fig. 1.5. The target is set inside the first horn in order to focus pions with a large emission angle. This restriction makes the outer radius of the inner conductor large (> 26 mm) and requires large filed integral, length and current. In order to achieve required focusing efficiency under this restriction, we adopted three horns; the first and second horn are close together so that they act as a single focusing device as a collector and the third horn acts a second focusing device [39].

1.3.3. Neutrino generation from meson decay

A neutrino beam is finally generated in the decay volume where focused pions or kaons decay into neutrinos. A beam absorber is placed just downstream of the decay volume in order to absorb the hadron flux which do not decays into neutrinos. Probability that a neutrino is produced in the direction of the detector in a two body decay such as

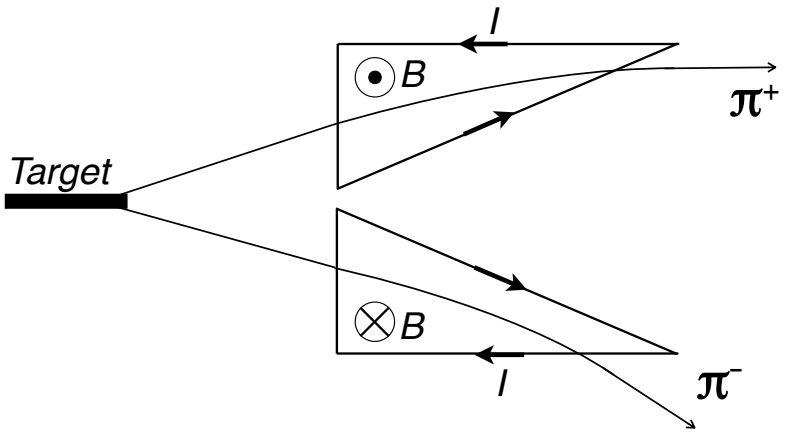

Figure 1.3.: The conical horn which Van der Meer developed as the first magnetic horn.

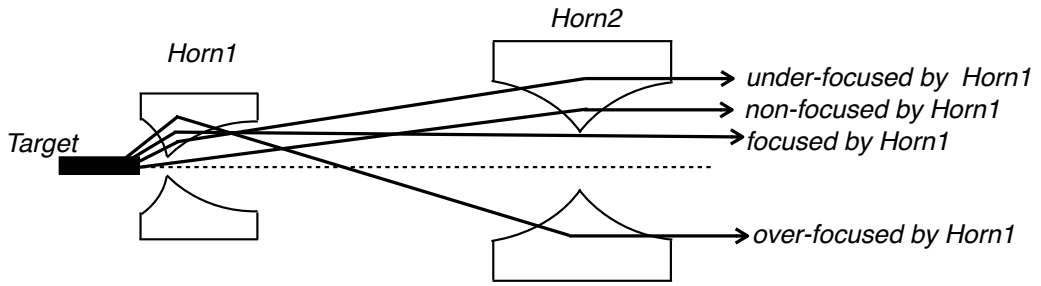

Figure 1.4.: Example of the multi-horn system: two-lens focusing system. The collection efficiency for secondaries is improved by using the second horn.

$\pi \to \nu_\mu \mu$ is formulated as:

$$P = \frac{A}{4\pi L^2} \cdot \frac{1-\beta_\pi^2}{(1-\beta_\pi \cos\theta)^2} \ , \tag{1.26}$$

where A is a transverse area of the detector; L is a distance between the production point and the detector; β_π is a velocity of the parent pion; θ is an angle of a produced neutrino beam with respect to the direction of the parent pion. Details of the derivation of Eq. (1.26) is given in Appendix B.

As in Eq. (1.26), the neutrino flux is dependent on the angle θ. Namely, the uncertainty in the flux is also caused by the uncertainty in the neutrino beam direction as well as the hadron production. Therefore, control of the neutrino beam direction is important in the long baseline neutrino oscillation experiment. In the T2K experiment, the off-axis

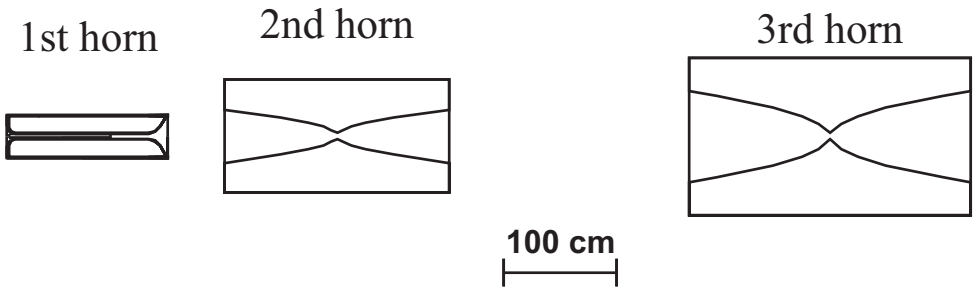

Figure 1.5.: Schematic view of the multi-horn system in the T2K. The target is set inside the first horn to focus pions with a large emission angle. This figure is taken from [39].

beam is adopted, where the control of the neutrino beam direction is more important as discussed in Sec. 2.2.

1.3.4. Detection of neutrino

Neutrino detectors are placed downstream of the absorber. In neutrino oscillation experiments, typically two detectors, near and far detectors, are used: neutrino oscillation parameters are determined by comparing the neutrino beam before oscillation with the near detector and near the oscillation maximum with the far detector. The uncertainty in the absolute neutrino flux can be cancelled out by comparing observations (e.g. the number of neutrino events) measured by the near and far detector. One can also reduce uncertainties in the neutrino interaction. The systematic error from the neutrino interaction is currently major one in the T2K experiment where different targets are used for the near and far detectors, and the cancellation is not perfect.

Understanding of the neutrino interaction mechanism is a key issue in the neutrino oscillation experiment. In accelerator neutrino experiments, the energy of muon neutrinos is typically centered around 1 GeV region. Figure 1.6 shows ν_μ cross sections on carbon divided by neutrino energy, which is calculated based on one of the models. As seen in the figure, several interaction modes are involved in the energy range of 0-5 GeV. The charged current quasi-elastic (CCQE) scattering is a dominant interaction mode for the neutrino energy less than 1 GeV. This interaction is very important in the T2K experiment because T2K uses this as a signal mode. The charged current single pion production (CC1π) becomes comparable with CCQE around 1.5 GeV and a leading mode from 2-4 GeV. The deep inelastic scattering (DIS) becomes important for more higher neutrino energy. More detailes of the neutrino interaction are described in Chapter 7.

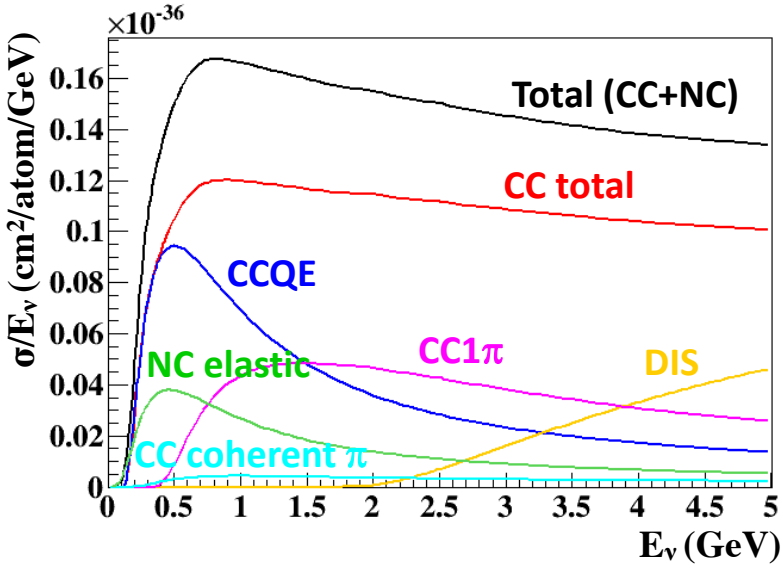

Figure 1.6.: ν_μ cross section divided by neutrino energy calculated by NEUT [40]. The cross sections on carbon for each interaction mode are shown in this figure.

1.4. Overview of this thesis

This thesis is composed of two themes:

- a measurement of the muon beam properties and
- a measurement of the muon neutrino charged-current cross section in the energy range of 1-3 GeV

in the T2K experiment.

First we show an overview of the T2K experiment in Chapter 2, in which we describe the history of the experiment so far, experimental setup and various physics programs. Since the T2K experiment uses the so-called off-axis beam, it is very essential to monitor and control the neutrino beam using beam monitors. T2K uses two kinds of detectors; the muon monitor for the measurement of the muon beam; and INGRID for the measurement of the neutrino beam. An overview and components of these beam monitors are described in Chapter 3.

From Chapter 4, we describe the measurement of the muon beam in the T2K beam operation. First an overview of this measurement is given in Chapter 4. Chapters 5 describes the method of the beam measurement using the muon monitor. We then describe the muon beam properties measured in the T2K beam operation in Chapter 6. In this chapter we discuss the results obtained at the commissioning stage in beam operation. Subsequently, the systematic error on the muon beam direction measurement with the muon monitor is given. The stability of the beam direction and intensity during

beam operation are then described. A measurements of the muon flux, which is produced with the neutrino flux, was conducted with the emulsion detector and the result was compared with the prediction. The details of the measurement and comparison with the prediction is also given in Chapter 6. Quality of the neutrino beam obtained here is used as an input to the measurements of the neutrino oscillation parameters and the neutrino cross sections.

From Chapter 7, we focus on the measurement of the neutrino cross section. Theoretical models of the charged-current neutrino-nucleus interaction is introduced in Chapter 7. We describe the principle of the reconstruction of the neutrino event with INGRID in Chapter 8. In Chapter 9, we finally report the measurement of the muon neutrino CC inclusive cross section on the iron target using INGRID. In this analysis, we developed a new method to utilize a dependence of the neutrino energy on the off-axis angle in addition to the event topologies. With this techniques and with a well-controlled neutrino beam and well-predicted neutrino fluxes, we measure the energy dependence cross section on the iron target. The obtained result and prospect are presented. Finally a conclusion of this thesis is presented in Chapter 10.

Part II.

T2K experiment

Chapter 2

T2K experiment

The Tokai-to-Kamioka (T2K) experiment is a long baseline neutrino oscillation experiment in Japan. The neutrino oscillation parameters are determined by measuring an accelerator-produced neutrino beam before oscillation with the near detector, ND280 and near the oscillation maximum with the far detector, Super-K. An overview of the T2K experiment is shown in Fig. 2.1.

2.1. Experimental setup

T2K uses a 30 GeV proton beam accelerated by Japan Proton Accelerator Research Complex (J-PARC) for a creation of the neutrino beam. The experiment has three main components: a neutrino beamline situated at the J-PARC, a near detector complex, ND280 positioned 280 m away from a neutrino production target and a far detector, Super-K located 295 km away from the J-PARC site. This section briefly describes each component. More details of the experimental setup is described in [12].

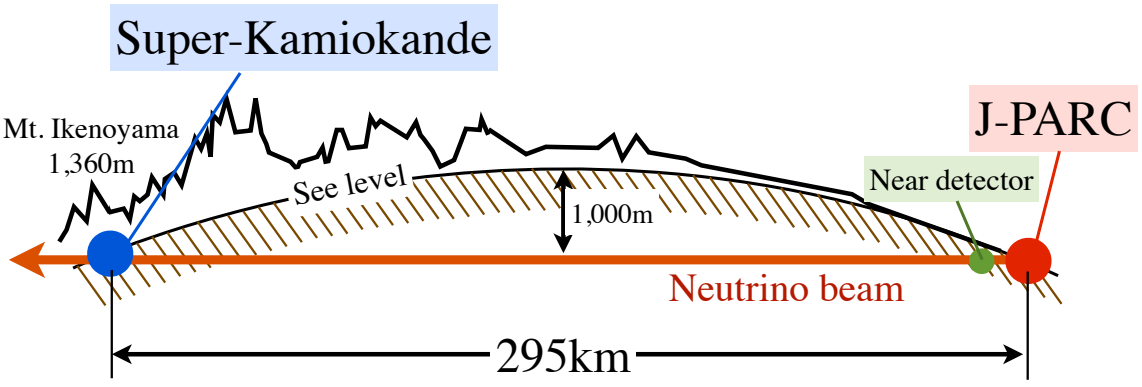

Figure 2.1.: Overview of the T2K experiment.

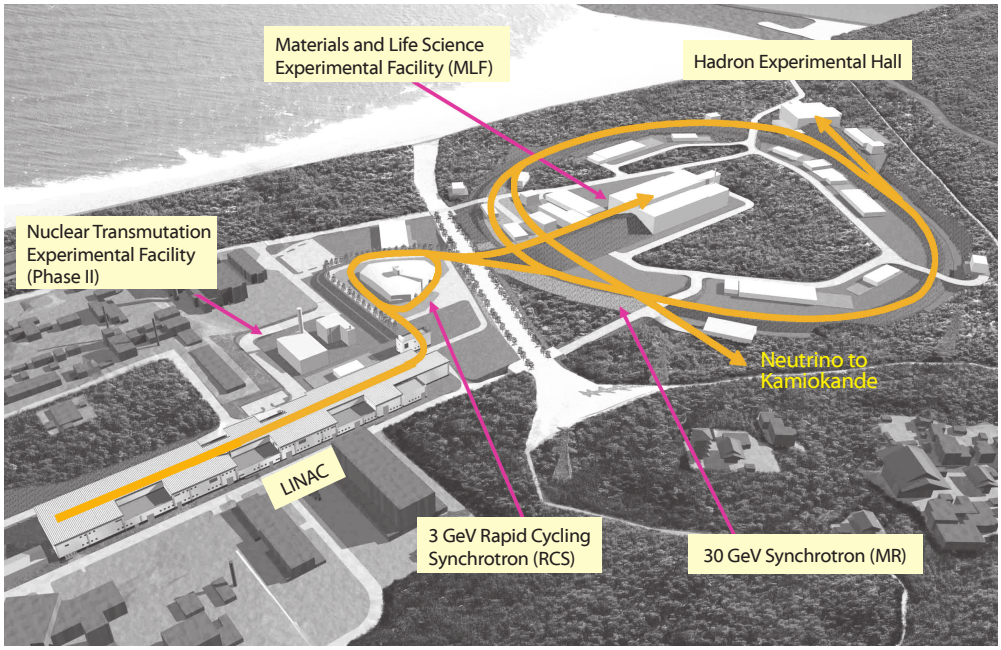

Figure 2.2.: Bird eye's view of J-PARC.

2.1.1. J-PARC main ring synchrotron

Bird eye's view of the J-PARC is shown in Fig. 2.2. J-PARC is situated in Tokai, Japan, and consists of three accelerators:

- a linear accelerator (LINAC), accelerating a negative ion (H^-) beam upto 400 MeV[1],
- a Rapid-Cycling Synchrotron (RCS) accelerating a proton beam upto 3 GeV and
- a 30 GeV synchrotron (Main Ring: MR).

The 30 GeV proton beam is then extracted to the neutrino beamline. Present parameters of the proton beam recorded in October 2014 are listed in Table 2.1.

2.1.2. Neutrino beamline

The neutrino beamline consists of two sections as shown in Fig. 2.3: a primary and secondary beamline.

[1] 181 MeV until Dec. 2013

Table 2.1.: Present parameters (RUN6) of the proton beam from the MR.

Kinetic energy	30 GeV
Beam power	260 kW
Spill cycle	2.48 sec
Number of bunches	8/spill
Bunch interval	581 nsec
Bunch width	58 nsec

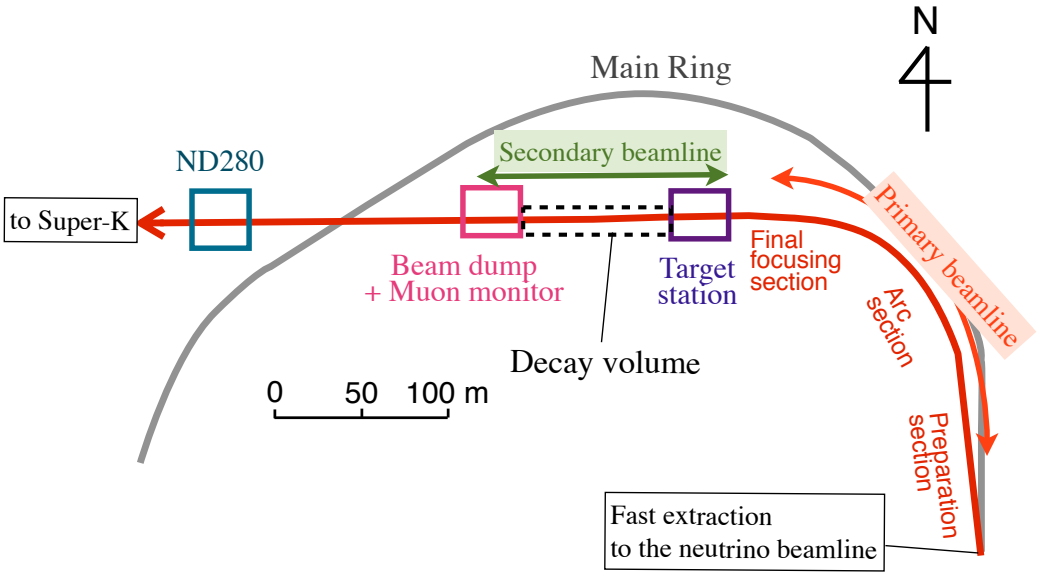

Figure 2.3.: Overview of the T2K beamline.

Primary beamline

The primary beamline consists of the preparation section (54 m long), arc section (147 m long), and final focusing section (37 m long). The proton beam accelerated in the MR first enters into the preparation section where 11 normal conducting magnets is used to tune the orbit of the beam. The arc section is positioned just downstream of the preparation section. In this section, 14 doublets super conducting magnets are used to bend the beamline by 80.7° so that the orbit of the proton beam is directed toward the direction of Super-K. The final focusing section is positioned at the end of the primary beamline and is composed of 10 normal conducting magnets. In this section, the proton beam is directed downward by 3.637° and is focused onto the target.

The proton beam is transported every 2 to 3 seconds. The beam has a time structure of eight narrow bunches, 58 ns long with 581 ns intervals, in a single spill as listed in Table 2.1. The beam forms a two dimensional Gaussian distribution of ∼4 mm 1σ width

corresponding to ∼7 mm radius at the target. In the primary beamline, the proton beam is precisely monitored and controlled by 5 current transformers (CTs); 21 electrostatic monitors (ESMs); 19 segmented secondary emission monitors (SSEMs); and 50 beam loss monitors (BLMs). Photographs of these monitors are shown in Fig. 2.4.

CT

CT is made of a 50-turn toroidal coil around a cylindrical ferromagnetic core. It outputs voltage proportional to the intensity of the proton beam. The uncertainty in the intensity measurement is 2.6%.

ESM

ESM has four segmented cylindrical electrodes. It provides the center position of the proton beam by measuring the top-bottom and left-right asymmetry of the beam induced current on the electrodes. The measurement precision of the projected beam position is better than 450 μm.

SSEM

SSEM has two thin (5 μm) titanium foils stripped horizontally and vertically, and an anode HV foil between them. Secondary electrons are emitted by hits of the proton beam with the strips. SSEM measures currents induced on the strip by electrons' drifting along the electing field. In this way, it reconstructs the profile of the proton beam. The monitor provides both the position and width of the proton beam.

BLM

BLM was installed to monitor the beam loss during operation. BLM (Toshiba Electron Tubes & Devices E6876-400) is a wire proportional counter filled with an $ArCO_2$ mixture [41]. When the beam loss exceeds a threshold, a beam is aborted.

The location of these beam monitors are shown in Fig 2.5 for the final focusing section. Position and angle of the proton beam at the target are determined by extrapolating the measurements of SSEM18, 19 and OTR for each spill. The OTR is a beam monitor positioned just upstream of the target and is described later[2]. The width of the proton beam at the target is estimated as follows. The beam profiles in the final focusing section are measured at several positions by SSEMs. These measurements are then fitted with the expectation which is calculated from combination of the transfer matrices ($\mathcal{M}$), Twiss parameters (α, β, and γ) and emittance (ϵ):

$$\sigma_{exp}^2 = \epsilon(\mathcal{M}_{11}^2\beta - 2\mathcal{M}_{11}\mathcal{M}_{12}\alpha + \mathcal{M}_{12}^2\gamma) \ , \tag{2.1}$$

Therefore, the Twiss parameters and emittance of the beam are derived and the beam width at the target can be reconstructed.

[2]SSEM17 is also used for the measurement in horizontal. Because it is positioned upstream of the vertical dipole magnet (FVD2 in Fig. 2.5), the measurement cannot be used for the extrapolation in the vertical direction.

Figure 2.4.: Photograph of the proton-beam monitors. Upper-left: CT (side view). Upper right: ESM (inside view). Lower left: SSEM (being installed in the beam-line). Lower right: BLM (installed beside a normal conducting magnet). These photographs are taken from [12]

Secondary beamline

The target and other equipment used to produce the neutrino beam are situated in the secondary beam line. Figure 2.6 provides an overview of the secondary beamline. All of the components in the secondary beamline are contained in a single volume of ~ 1500 m^3 filled with helium gas, which is enclosed in a iron vessel. The proton beam, transported to the target via the primary beamline, first enters a baffle which works as a collimator and then is measured by an optical transition radiation (OTR) monitor before hitting the target.

Baffle

The baffle is placed downstream of SSEM19 (see Fig. 2.5), which is the most downstream SSEM and this plays the role of a collimator. It consists of a 1.7 m long graphite block with a 30 mm diameter hole at the beam-axis.

OTR

OTR [43] is placed just upstream of the target and measures the two dimensional profiles of the beam by imaging transition radiation produced when the proton beam

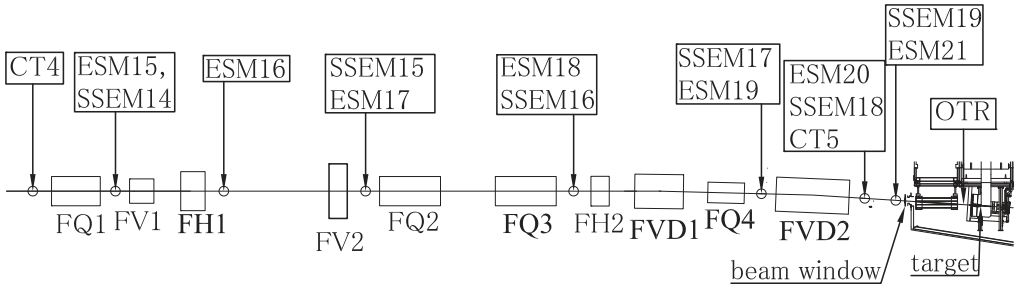

Figure 2.5.: Location of the primary beamline monitors in the final focusing section. The magnets are given names as H(V), Q and VD which are steering in horizontal (vertical), quadrupole, and vertical dipole magnets, respectively. OTR and the target is also shown in this figure, which are described in Sec. 2.1.2. The figure is taken from [42].

passes a foil. A material used for the foil is chosen according to the proton beam intensity: ceramic Al_2O_3, aluminum, and titanium alloy. These foils are mounted on a disk carousel which has eight hole positions of 50 mm as shown in Fig. 2.7. The carousel is occupied by seven foils and has one empty hole. A calibration foil is also mounted on the carousel, which is made of titanium alloy with calibration holes. The image of the foil is periodically taken using a laser and is used for checking the alignment of the foils. The foils used in the OTR system are summarized in Table 2.2.

Graphite target

After passing through the baffle and OTR, the proton beam hits the graphite target and produces secondary particles, mostly pions. Figure 2.8 shows the photograph and schematic view of the target. The target core is a rod of 91.4 cm long along the beam-axis (1.9 interaction length) and 2.6 cm diameter. It is surrounded by a 2 mm thick graphite tube. The core and tube are sealed inside a titanium case which has 0.3 mm thick. The target is cooled by helium gas flowing through a gap between the core and tube.

Magnetic horn

Three magnetic horns [39] are used to focus (defocus) positively (negatively) charged pions along the designed beam-axis. Each of the horns is made of aluminum conductor and produces a maximum toroidal magnetic field of 1.7 T inside the conductor when the horns operate at 250 kA. When polarity of the horn currents are set to be opposite, negatively charged pions are focused.

Decay volume

Figure 2.9 shows an view of the decay volume from the upstream. An intense muon neutrino beam is generated as decay products of pions in this tunnel. The volume is a 96 m long steel tunnel. At the upstream end, the cross section of the volume

Table 2.2.: Foils used in the OTR system.

Material (number of foils)	Thickness (μm)	Operation
Ceramic Al_2O_3 (1)	100	$<$ 1 kW beam power
Al (1)	50	1-40 kW beam power
Ti (4)	50	$>$ 8 kW beam power
Calibration Ti (1)	50	calibration with no beam

is 1.4 m wide and 1.7 m high. It is 3.0 m wide and 5.0 m high at the downstream end. Fourty plate coils are welded on the steel wall along the beam-axis in order to cool down the temperature of the steel wall below 100 °C. All cooling plates are connected by U-shape pipes. The entire volume is surrounded by 6.0 m thick concrete shielding.

Beam dump

The beam dump sits at the end of the decay volume to absorb the hadron flux from the beam (see Fig. 2.6). It consists of a core composed of 75 tons of graphite (1.7 g/cm^3), the thickness of which is 3.174 m. Fifteen (two) iron plates are placed outside (inside) the helium vessel at the downstream end of the core and the total thickness is 2.40 m. The beam dump allows only muons above 5 GeV/c to go through and reach the downstream muon monitor.

Muon monitor

The muon monitor was placed behind the beam dump and 118 m downstream of the graphite target. The monitor was installed to measure the direction and intensity of the muon beam which is produced with the neutrino beam. Details of the instrumentation are described in Sec. 3.1.

2.1.3. Near detector complex:ND280

The neutrino energy spectrum, flavor and interaction rates are measured by a group of detectors called "ND280" which are located 280 m from the graphite target. The overview of the detector complex is shown in Fig. 2.10.

ND280 on-axis detector: INGRID and the Proton Module

T2K has two types of the on-axis near detectors at the near site: INGRID and the Proton Module. INGRID has 14 independent modules. The modules are installed at positions in cross shape (7 in horizontal and 7 in vertical) whose center is on beam-axis and covers a transverse section of 10 m $\times$10 m. INGRID was installed to measure the direction and intensity of the neutrino beam. The detector is also used to measure the neutrino cross

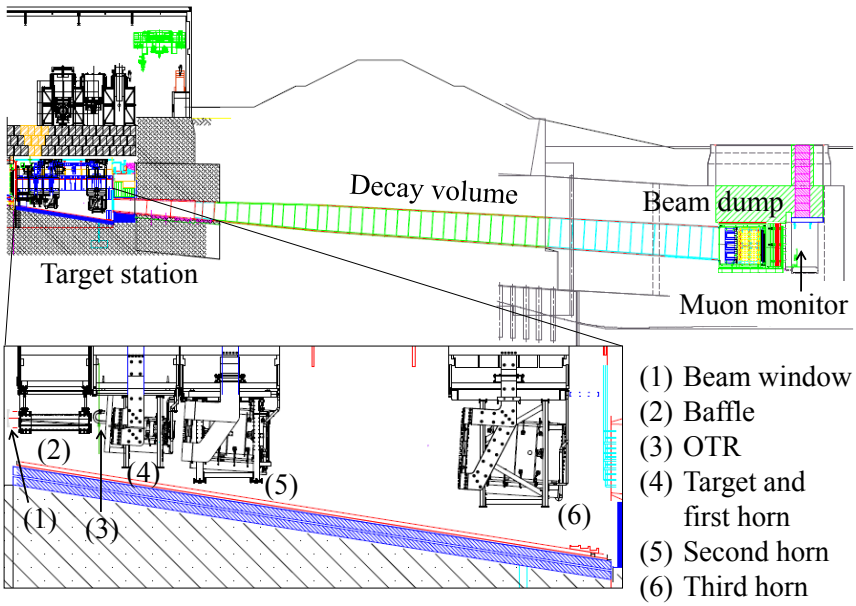

Figure 2.6.: Overview of the secondary beamline. All of the components in the beamline, the target, horns, decay volume and beam dump, are contained in a single volume of 1500 m^3 filled with helium gas. The figure is taken from [42].

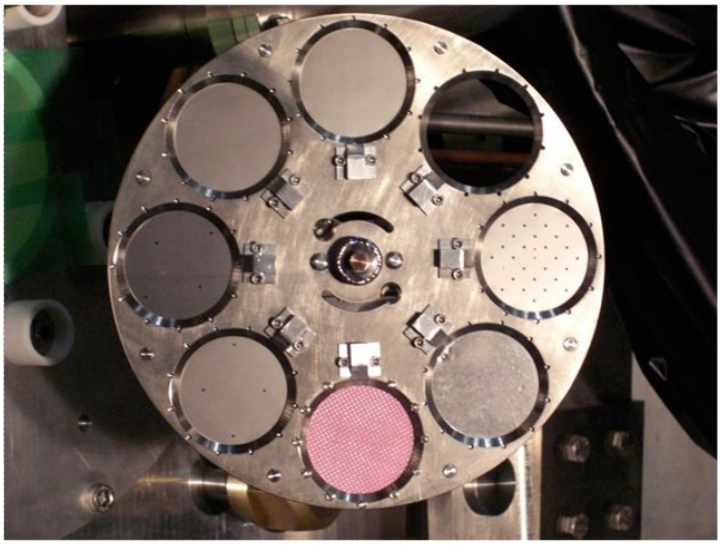

Figure 2.7.: Photograph of the OTR carousel.

section, which is one of the main subjects in this thesis. Details of the detector setup are described in Sec. 3.2. There are two extra INGRID modules called the "shoulder module". These modules are installed to measure axial asymmetry of the neutrino beam and are not used for the measurement of the beam direction.

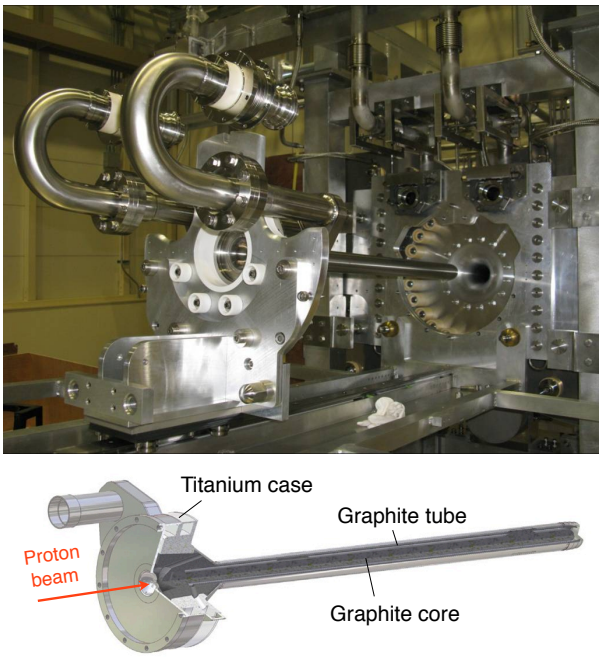

Figure 2.8.: Photograph (Top) and schematic view (bottom) of the graphite target. The proton beam enters from the left side.

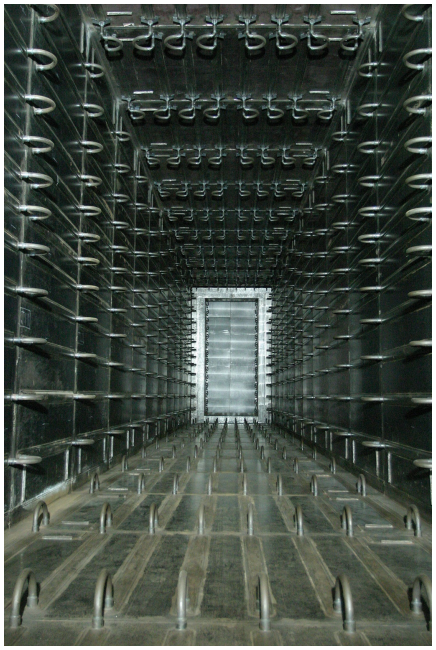

Figure 2.9.: View of the decay volume from upstream. Forty plate coils are welded on the steel wall along the beam-axis.

The Proton Module is an extra module located at the beam center between the horizontal and vertical INGRID modules. It consists of 36 tracking layers surrounded by veto planes. Figure 2.11 shows an exploded view of the Proton Module. Each of the tracking layers contains an array of two types of scintillator bars, making a plane of 120×120 cm^2 in the horizontal and vertical directions. Since the detector is a fully-active tracking detector, it has a capability to reconstruct short tracks of protons or pions which are generated by the neutrino interaction. By applying kinematic cuts and particle identification based on dE/dx information, the neutrino interaction modes can be identified. The module is used to study the neutrino interaction.

ND280 off-axis near detector

The ND280 off-axis detector is a detector complex, composed of various detectors as shown in Fig. 2.12. The detector is located 280 m downstream of the target and along the line between the average pion decay point in the decay tunnel ($\sim$50 m from the target) and Super-K. With this configuration, an angle of neutrino from the average pion decay point with respect to the beam-axis matches 2.5° (see Fig. 2.13). Purpose of the off-axis detector is to measure the neutrino flux. The detector is also used to study the neutrino interaction mechanism. All the detector elements except for muon range detectors are placed in the dipole magnet donated from UA1 experiment at CERN, which supplies a magnetic field of 0.2 T. The off-axis detector has three active target regions: two fine

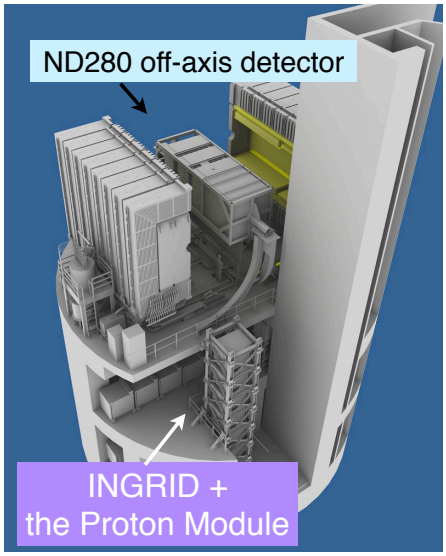

Figure 2.10.: Overview of the ND280 complex. The magnet and off-axis detector are located on the upper level; horizontal INGRID modules and the Proton Module are located on the level below; and the vertical INGRID modules span the bottom two levels.

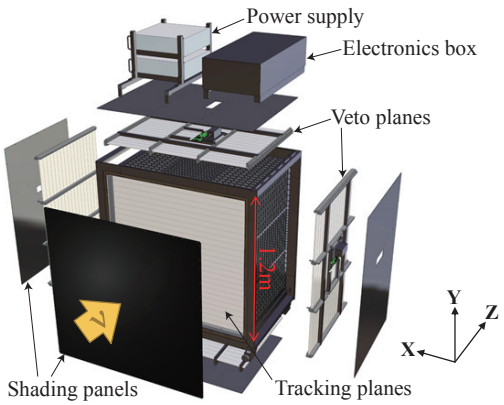

Figure 2.11.: Exploded view of the Proton Module [48].

grained detectors (FGDs) and a Pi-zero detector (P0D), which are followed by time projection chambers (TPC) and surrounded by electromagnetic calorimeters (ECAL) and muon range detectors (SMRD). The most upstream FGD [44] (FGD1) consists of layers of plastic scintillator bars. FGD1 provides the target mass and reconstruction of the short-ranged tracks near the vertexes. TPCs provide PID based on dE/dx information and momentum from the track curvature in the magnetic field. The FGD's and TPC's are called the tracker section. P0D [45] consists of plastic scintillators, brass sheets and water bags. The detector is installed to measure the neutrino interaction accompanied with π^0 production by using the water target. ECAL [46] is composed of the plastic scintillator layers interleaved with Pb foils. It detects γ-rays that do not convert in the inner detector. SMRD [47] consists of the scintillator pads and is inserted into the magnet yoke. The detector was installed to measure the ranges of the muons that exit the sides of the inner detector. It also provides the cosmic-ray triggers for calibration of the detectors.

The measurements of the ND280 off-axis detectors are used to constrain uncertainties in the fluxes and energy spectrum of the neutrino beam, and the neutrino cross section models. In this way, we largely reduce the uncertainties on the expected number of the neutrino events at Super-K and measure the oscillation parameters precisely.

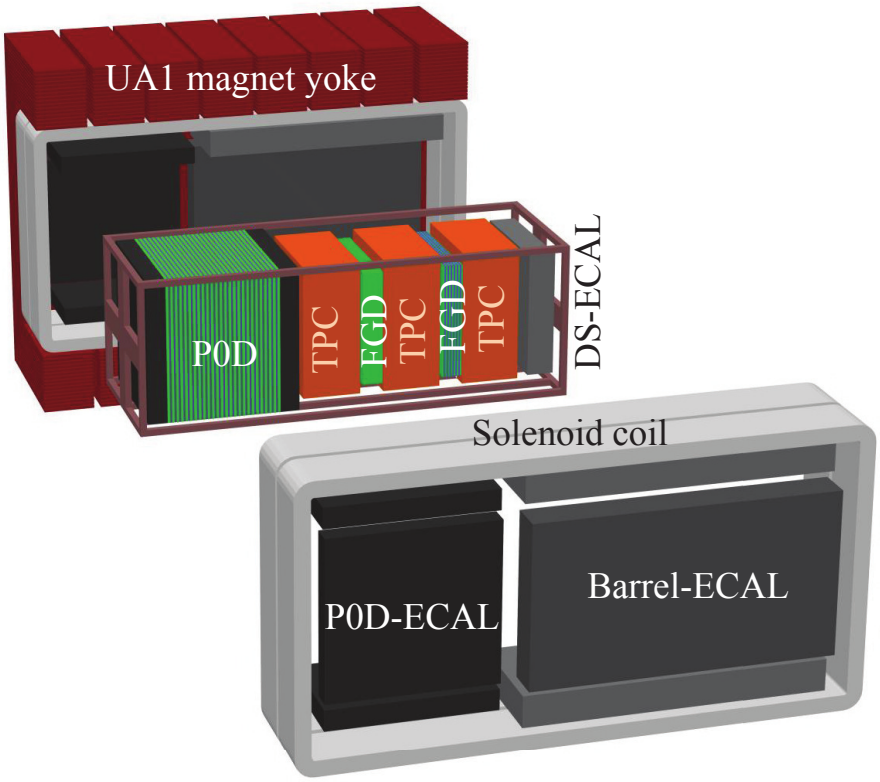

Figure 2.12.: Exploded view of the ND280 off-axis detectors. Neutrino beam enters from the left side of the figure.

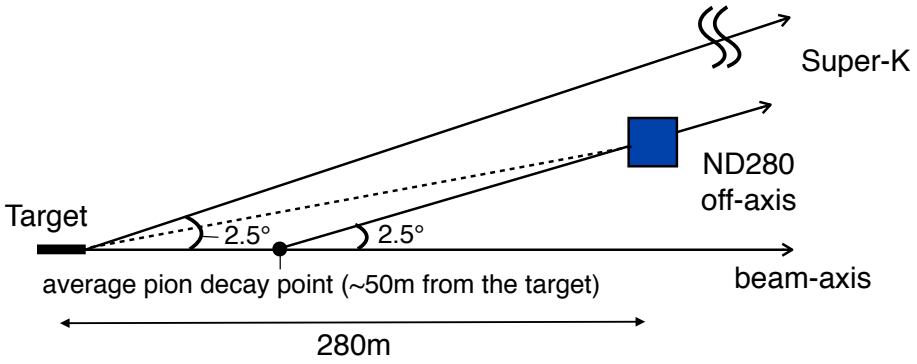

Figure 2.13.: Location of the ND280 off-axis detector. The detector is positioned along the line between the pion decay point and Super-K.

2.1.4. Far detector: Super-K

Super-K [3], the gigantic water Cherenkov detector, serves as the far detector in the T2K experiment. The detector is located 295 km away from the target, Gifu in Japan, and 2.5° from the beam-axis as well as ND280. It lies under the peak of Mt. Ikenoyama, with 1000 m of rock above (see Fig. 2.1). The Super-K detector is a cylindrical cavern filled with 50 kton of pure water and consists of two volumes, an inner and outer detector separated by a cylindrical stainless steel structure. The 111,129 inward-looking 20-inch photo-multipliers (PMTs) are attached with the inner surface of the inner detector (ID) and covers 40% of the surface. The outer detector (OD) contains 1,885 outward-facing 8-inch PMTs. Super-K measures the neutrino interaction via the Cherenkov light emitted by charged particles. Charged particles produced at the surrounding wall and cosmic rays are identified using the OD PMTs. If there are signals only from the ID PMTs, the event is regarded as "Fully contained" (FC) and additional selections are applied to select neutrino events. An incoming neutrino type are identified by the Cherenkov light pattern at ID walls; a ring produced by muon has a sharp image (μ-like) while electron makes a fuzzy ring due to the electromagnetic shower (e-like). Accelerator neutrinos are distinguished from atmospheric neutrinos based on their arrival time defined by the proton beam with the expected neutrino time-of-flight (TOF). The detection time at Super-K is synchronized to the proton beam timing using Global Positioning System (GPS) timing information.

In the T2K experiment, a charged current quasi-elastic (CCQE) scattering is used as the signal mode at Super-K for both ν_e appearance and ν_μ disappearance analyses. The number of ν_e or ν_μ events is measured by counting single e- or μ-like Cherenkov rings, which provide the CCQE enriched samples. The incoming neutrino energy is reconstructed by assuming the CCQE interaction:

$$E_\nu^{rec} = \frac{m_p^2 - (m_n - E_b)^2 - m_l^2 + 2(m_n - E_b)E_l}{2(m_n - E_b - E_l + p_l \cos\theta_l)} , \tag{2.2}$$

where $m_n(m_p)$ is the neutrino (proton) mass; E_b is the neutron binding energy in oxygen (27 MeV); m_l and E_l are the mass and energy of the outgoing lepton, respectively; θ_l is the angle of the outgoing lepton with respect to the incoming neutrino beam direction.

2.2. Off-axis beam method

In the pion two-body decay ($\pi \to \mu\nu_\mu$), the neutrino energy (E_ν) in the laboratory frame is calculated as (see Appendix B):

$$E_\nu = \frac{m_\pi^2 - m_\mu^2}{2(E_\pi - |P_\pi|\cos\theta_\nu)} = \frac{m_\pi^2 - m_\mu^2}{2(1/\beta_\pi - \cos\theta_\nu)|P_\pi|} , \tag{2.3}$$

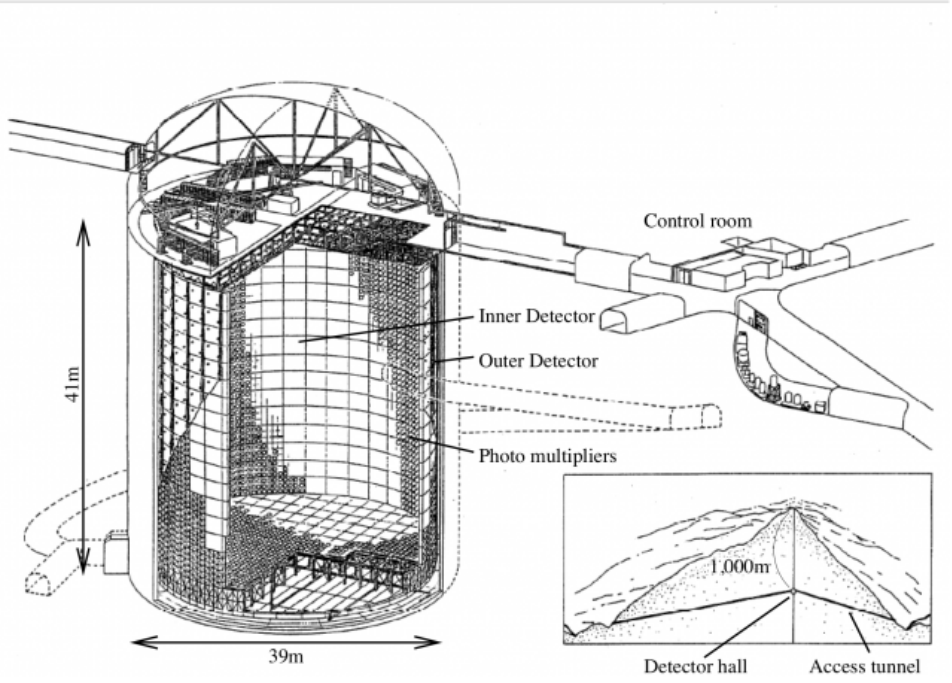

Figure 2.14.: Super-K

where m_π and m_μ are the mass of pion and muon, respectively; E_π and P_π are the energy and momentum of the pion, respectively; θ_ν is the angle between the pion and neutrino directions. The relation in Eq. (2.3) is shown in Fig 2.15. The maximum neutrino energy for given θ_ν is calculated to be:

$$E_\nu^{max} = \frac{m_\pi^2 - m_\mu^2}{2m_\pi \sin\theta_\nu} \ . \tag{2.4}$$

In case of $\theta_\nu = 2.5°$, E_ν^{max} is approximately 680 MeV.

T2K is the first neutrino oscillation experiment which adopts the "off-axis beam method". In this method, detectors are intentionally placed off the beam center axis. The angle with respect to the beam-axis is called off-axis angle: $\theta_{\rm OA}$. Since the direction of the parent particles of the neutrinos are approximately on beam-axis, $\theta_{\rm OA}$ is close to θ_ν in Eq. (2.4). Therefore, a energy spectrum of the neutrino beam is lower and narrower at $\theta_{\rm OA} \neq 0$ compared to that at $\theta_{\rm OA} = 0$. In the T2K experiment, $\theta_{\rm OA} = 2.5°$ is chosen so that the neutrino flux has a narrow band with a peak around 0.7 GeV ($\simeq E_\nu^{max}$) at which the survival probability of the muon neutrino becomes maximum after its traveling 295 km (see Fig. 2.16). In addition, the off-axis beam method can effectively reduce neutrino fluxes in higher energy region, where significant backgrounds for the measurement of oscillation parameters are produced. In order to measure $|\Delta m^2_{32}|$ with our target precision ($\sim$4%), the neutrino beam direction is required to be controlled within 1 mrad ($\sim 0.06°$) with respect to the beam-axis. This is because the 1 mrad shift of $\theta_{\rm OA}$ changes the peak position of the neutrino energy spectrum by 10-20 MeV and it results in a 2-3% uncertainty in determining $|\Delta m^2_{32}|$. Namely, uncertainty in the

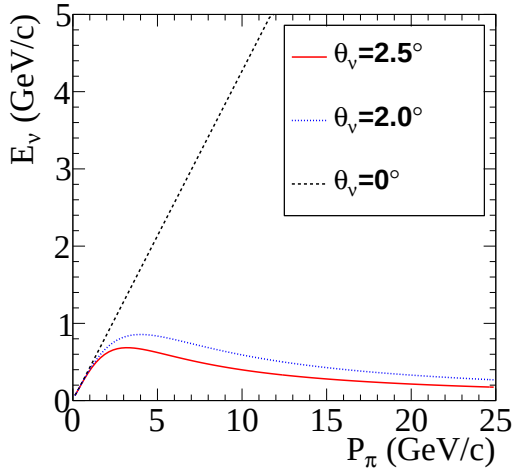

Figure 2.15.: Neutrino energy as a function of the pion momentum for different neutrino angles with respect to the parent pion direction.

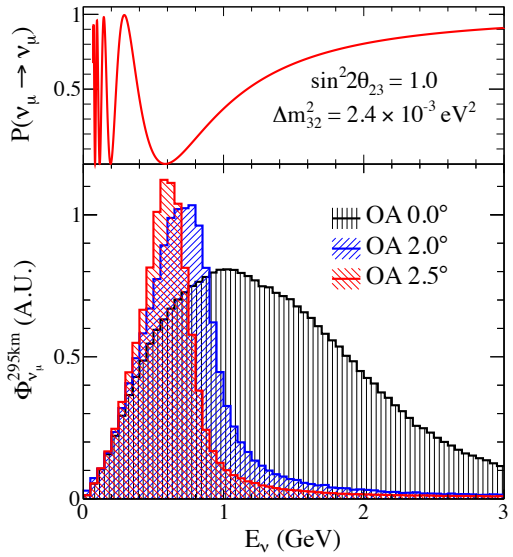

Figure 2.16.: Muon neutrino survival probability ($\nu_\mu \rightarrow \nu_\mu$) at 295 km and neutrino fluxes for different off-axis angles [42].

beam direction could be a dominant error source in our target precision. Therefore, the stringent control of the neutrino beam direction is highly important to precisely measure the neutrino oscillation parameters in the T2K experiment.

2.3. History of the T2K experiment

T2K began operation in January 2010 and has accumulated 7.39×10^{20} protons on target (p.o.t.) as of June 2014, which is about 9% of our target p.o.t. (7.8×10^{21} p.o.t.). Table 2.3 summarizes the status of T2K beam operation since the start of physics data taking. There have been five data taking periods (RUN 1-5) until June 2014. We have just resumed data taking (RUN 6) in October 2014 and it is also listed in Table 2.3. The repetition cycle of the proton beam has been reduced over the course of beam operations and 2.48 s was achieved from RUN 4. All three magnetic horns were operated at 250 kA except for RUN 3b and a part of RUN 5. In RUN 3b, the horn currents were set to 205 kA for the most part of operation. In RUN 5, a polarity of the horn currents was set o be opposite (-250 kA) to produce antineutrino beam in preparation for the measurement of CP violating phase: δ_{CP}. T2K intends to focus on the measurement of δ_{CP} from RUN 6 where the horn currents are set to -250 kA for the most part of operation. Figure 2.17 shows the history of the total accumulated p.o.t., as well as the beam power including RUN 6.

Table 2.3.: Summary of the status of the beam operation in T2K. The second and third column show the repetition cycle of the proton beam and the horn current, respectively. The accumulated number of p.o.t. obtained in each run is shown in the last column.

	Period	Rep. cycle (sec)	Horn curr. (kA)	Accum. p.o.t.
RUN 1	Jan. 2010 – Jun. 2010	3.52	250	3.28×10^{19}
RUN 2	Nov. 2010 – Mar. 2011	3.2 [3]	250	1.12×10^{20}
RUN 3b	Mar. 2012	2.92	250/205	2.15×10^{19}
RUN 3c	Apr. 2012 – Jun. 2012	2.56	250	1.37×10^{20}
RUN 4	Oct. 2012 – May 2013	2.48	250	3.60×10^{20}
RUN 5 (ν mode)	May 2014 – June 2014	2.48	250	6.88×10^{20}
RUN 5 ($\bar{\nu}$ mode)	June 2014	2.48	-250	5.09×10^{19}
RUN 6 (ongoing)	Oct. 2014 –	2.48	250/-250	—
		Total (until RUN 5)	ν mode	6.88×10^{20}
			$\bar{\nu}$ mode	5.09×10^{19}
			$\nu + \bar{\nu}$ mode	7.39×10^{20}

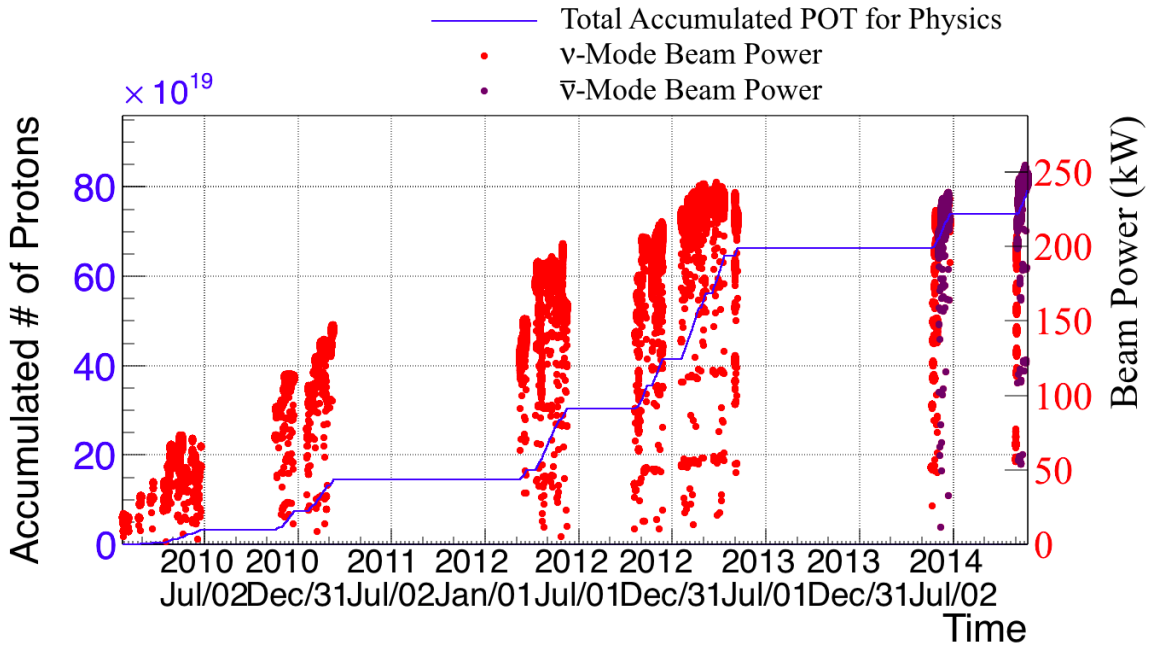

Figure 2.17.: History of total accumulated protons and beam power. The solid line shows the accumulated p.o.t. The dot points show the beam power.

[3] 3.04 sec from March 7th 2011 to March 11th 2011

2.4. Status of the T2K experiment

The primary goals of the T2K experiment were to accomplish following measurements with data of 7.8×10^{21} p.o.t.

- Discovery of $\nu_\mu \to \nu_e$ oscillation (ν_e appearance)

  Establishment of nonzero value of θ_{13} with a sensitivity down to $\sin^2 2\theta_{13} \simeq 0.008$ (90% C.L.).

- Precise measurement of oscillation parameters in $\nu_\mu \to \nu_x$ (ν_μ disappearance)

  Measurement of $\sin^2 2\theta_{23}$ and $|\Delta m^2_{32}|$ with a precision of $\delta(\sin^2 2\theta_{23}) \sim 0.01$ (1%) and $\delta(|\Delta m^2_{32}|) \sim 10^{-4}$ eV^2 (4%), respectively.

In 2011, an indication of the nonzero value of θ_{13} was reported by T2K (us) for the first time. In 2013, we reported an observation of ν_e appearance from the ν_μ beam using data which has been collected until the end of RUN 4 [49]. We detected 28 ν_e events at Super-K whereas the predicted number of events is 4.92 ± 0.55 in the case of $\sin^2 2\theta_{13} = 0.0$ as shown in Table 2.4. With this observation, $\sin^2 2\theta_{13} = 0$ was excluded with a significance of 7.3σ. The observed number of events are even larger than the expectation with $\sin^2 2\theta_{13} = 0.095 \pm 0.010$ (24.6 events) which is the average value derived from the reactor measurements in PDG2012 [50]. This may indicate that there is a contribution from the δ_{CP} term in the $\nu_\mu \to \nu_e$ oscillation. Figure 2.18 left shows the allowed 68% and 90% C.L. regions for $\sin^2 2\theta_{13}$ as a function of δ_{CP}. In this figure, a yellow band presents 1σ band of $\sin^2 2\theta_{13} (= 0.095 \pm 0.010)$ obtained from the PDG2012. Figure 2.18 right shows $-2\Delta \ln L$ distributions as a function of δ_{CP}, for the normal mass hierarchy (NH) and inverted mass hierarchy (IH) cases, where L is the likelihood function for observed e-like events. The 90% C.L. exclusion was measured to be between 0.35π and 0.63π (0.09π and 0.90π) rad. for the NH (IH) case. Our result shows that the combined T2K and reactor measurement prefer $\delta_{CP} = -\pi/2$ and performs the first constraint on δ_{CP} in the lepton sector.

We also performed a measurement of the neutrino mixing parameter θ_{23} from ν_μ disappearance [17]. In this oscillation mode, 120 ν_μ events are observed at Super-K while 450 ν_μ events are expected in the case of no oscillation. Figure 2.19 shows obtained 68% and 90% confidence regions for $\sin^2 \theta_{23}$ and Δm^2_{32} for the NH and IH cases. As seen in the figure, we perform the most precise measurement of $\sin^2 \theta_{23}$ which is measured to be $0.514 \pm^{0.055}_{0.056}$ for NH and 0.511 ± 0.055 for IH.

Table 2.5 summarizes uncertainties in the predicted number of ν_μ and ν_e candidates at Super-K. As shown in the table, some of the error sources are constrained by the measurement of ND280. Statistical uncertainties dominate T2K's error in both ν_e appearance and ν_μ disappearance measurements. We have only collected 8% of our target p.o.t. until May in 2013. The measurement can be statistically improved by a factor of 3.5 when we accumulate 7.8×10^{21} p.o.t., which is the full T2K statistics. As shown in Table 2.5, some of the uncertainties in the neutrino cross section are not constrained

Table 2.4.: Expected number of events for each event category in the case of $\Delta m^2_{21} = 7.5 \times 10^{-5}$ eV^2, $\Delta m^2_{32} = 2.4 \times 10^{-3}$ eV^2, $\sin^2 2\theta_{21} = 0.306$, and $\sin^2 \theta_{32} = 0.5$. The estimation is done for $\sin^2 2\theta_{13} = 0.0$ (no oscillation) and $\sin^2 2\theta_{13} = 0.095$ [50]. These numbers are estimated at 6.57×10^{20} p.o.t. [51]

	The predicted number of events	
	$\sin^2 2\theta_{13} = 0.0$	$\sin^2 2\theta_{13} = 0.095$
Total	4.97	21.06
ν_e signal ($\nu_\mu \to \nu_e$)	0	16.55
background	4.97	4.51

Table 2.5.: Uncertainties in the predicted number of ν_μ and ν_e candidates at SK for each error source [51].

Error source	$\delta n^{exp}_{\nu_\mu}/n^{exp}_{\nu_\mu}$	$\delta n^{exp}_{\nu_e}/n^{exp}_{\nu_e}$
Flux & ν interaction (ND280 constrained)	2.7%	3.1%
ν interaction (ND280-independent)	5.0%	4.7%
SK detector	4.0%	2.7%
Hadronic interaction in Oxygen	3.0%	2.4%
Total	7.7%	6.8%

by ND280 since a different nuclear target (carbon) is used as for now. This could be an obstacle to our target precision for the oscillation parameter measurements, θ_{13}, θ_{23}, and Δm^2_{32}, and search for the δ_{CP} under the full T2K statistics. Therefore, understanding of the neutrino interaction mechanism is now a key issue in the neutrino oscillation experiment. Figure 2.20 shows the fractional error of the neutrino flux at Super-K. The total error is dominated by the uncertainties in hadronic interactions. The uncertainties in the proton beam optics and off-axis angle of the neutrino beam direction actually give non-negligible effect on the neutrino flux around 0.7 GeV, at which the neutrino energy spectra has a peak in the case of $\theta_{\rm OA} = 2.5^\circ$ (see Fig. 2.16). A precise control of the beam direction is, therefore, as important as understanding of the neutrino interaction mechanism.

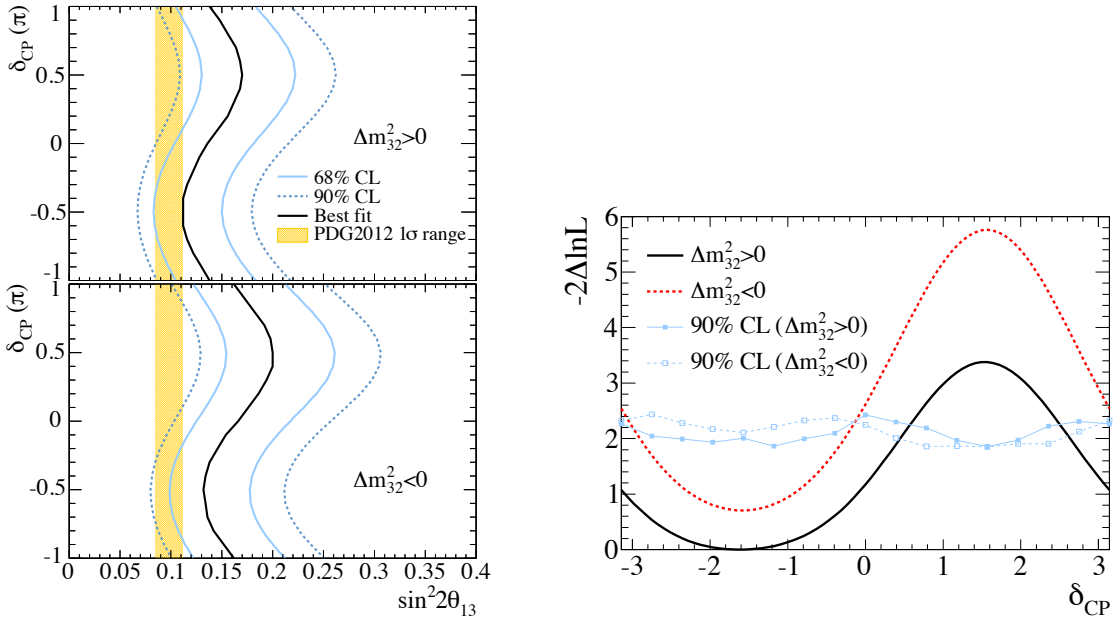

Figure 2.18.: Left: The 68% and 90% C.L. regions for $\sin^2 2\theta_{13}$ as a function of δ_{CP} for normal (top) and inverted (bottom) mass hierarchies [49]. The solid line represents the best fit $\sin^2 2\theta_{13}$ value for given δ_{CP} values. A yellow band presents the average θ_{13} value obtained from the PDG2012 [50]. Right: $-2\Delta \ln L$ distributions as a function of δ_{CP} for normal (solid line) and inverted (dotted line) mass hierarchies, where L is the likelihood function for observed e-like events. The 90% C.L. limit is represented as the solid (dotted) line with markers for the normal (inverted) mass hierarchy.

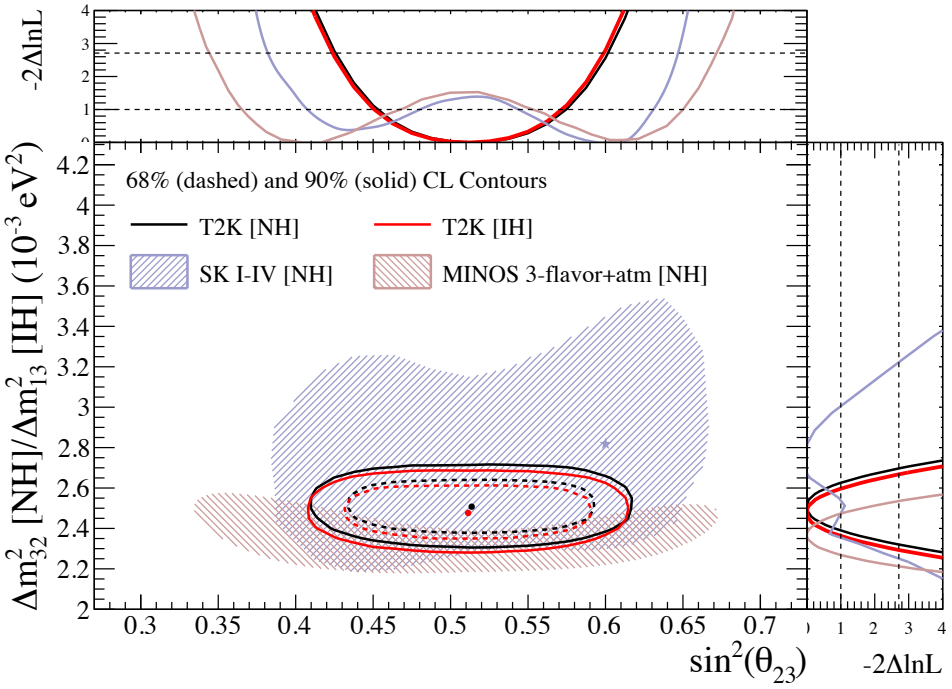

Figure 2.19.: The 68% and 90% C.L. confidence regions for $\sin^2\theta_{23}$ and Δm^2_{32} (normal mass hierarchy) or Δm^2_{13} (inverted mass hierarchy) [17]. The SK [52] and MINOS [19] 90% C.L. regions for the normal mass hierarchy are also shown.

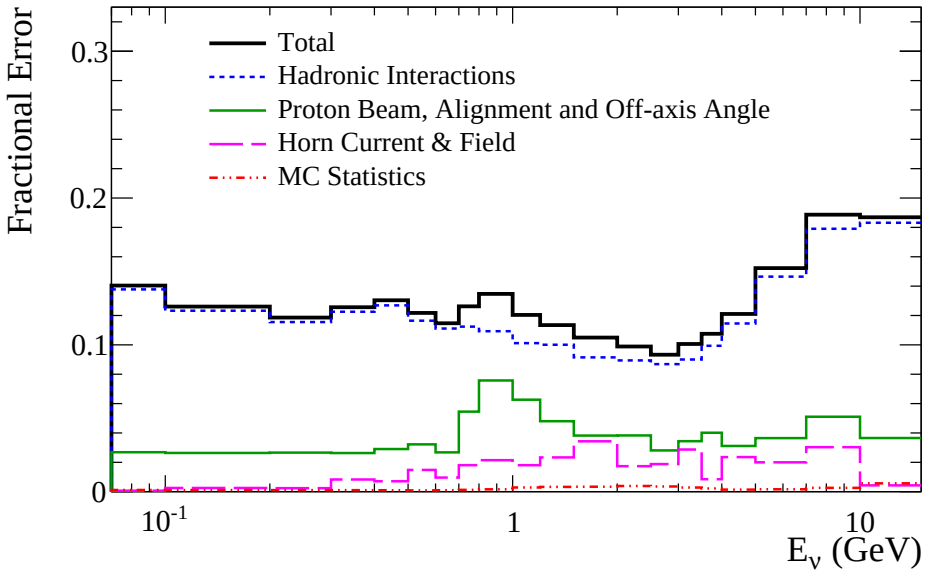

Figure 2.20.: Fractional error of the neutrino flux at Super-K, including all the uncertainties.

Chapter 3

Muon and neutrino beam monitoring

As we emphasize in Sec. 2.4, understanding of the neutrino beam direction is important in the T2K experiment. The beam direction has to be monitored with a good precision and controlled well to reduce the uncertainty for the oscillation parameters. It is also important to monitor the stability of the neutrino beam intensity to ensure that all the components in the beamline work stably and to secure long term operation. In order to fulfil these requirements, T2K employs proton beam monitors in the beam-line as described in Sec. 2.1, and two other beam monitors: the muon monitor and INGIRD. The muon monitor measures the muon beam, which is produced together with the neutrino beam from the decays of pions. INGRID measures the neutrino beam directly by accumulating neutrino events to reconstruct the neutrino beam direction and intensity. In the T2K experiment, measurements of these two monitors are complementary and are used to ensure the quality of the neutrino beam.

3.1. Muon monitor

The muon monitor [53] is located 118 m downstream of the target and just downstream of the beam dump. The purpose of the monitor is to detect the muon beam which is produced together with the neutrino beam from the pion decay, and to measure the direction and intensity of the muon beam spill-by-spill. In this way, the direction and intensity of the neutrino beam can be confirmed indirectly with spill-by-spill basis. The muon monitor can be used to monitor the status and healthiness of beam components in the beamline. For example, a sudden drop in the horn currents or deterioration of the target may arise during operation, affecting quality of the neutrino beam. These malfunctions can be probed promptly by the muon monitor.

The thickness of the beam dump located upstream of the muon monitor is chosen to minimize the hadron flux while retaining the sensitivity in the measurement of the muon beam direction: muons with energy above 5 GeV can pass through the beam dump and reach the muon monitor. A left plot in Fig. 3.1 shows a schematic view of the muon monitor. The monitor consists of two independent detectors: an array of ionization chambers and another array of silicon PIN photodiodes. Each detector array has $7 \times 7 = 49$ sensors at 25 cm intervals and covers an area of 150×150 cm^2 with respect to the beam-axis. There is also an additional silicon PIN photodiode mounted on a small moving stage behind the silicon array (see Fig. 3.1 right) for the calibration purpose.

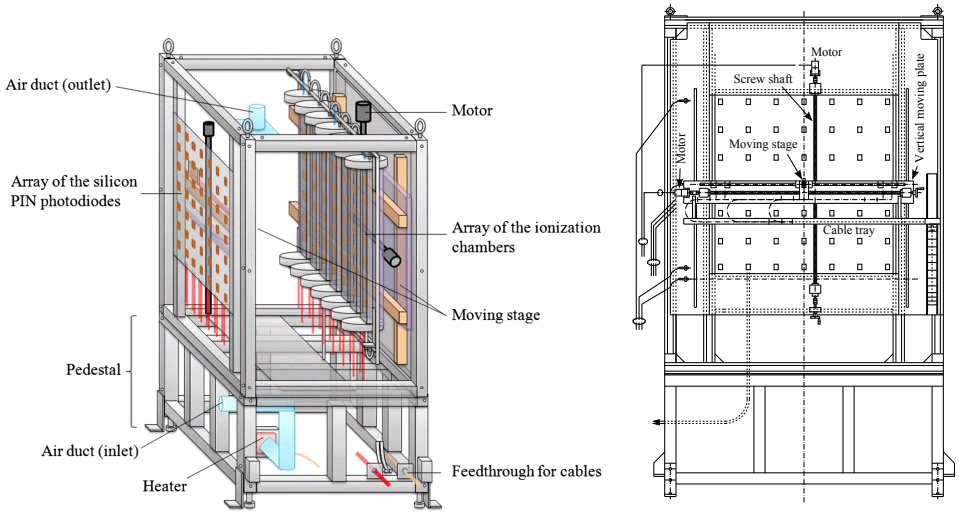

Figure 3.1.: Left: Schematic view of the muon monitor. The monitor consists of arrays of ionization chambers and silicon PIN photodiodes. The muon beam passes through the array of the silicon PIN photodiodes first and then the ionization chambers [53]. Right: Moving stage for the calibration silicon PIN photodiode, as viewed from downstream.

Our strategy is to monitor the muon beam direction with a precision of 0.3 mrad for every beam spill, in order to control the neutrino beam well for the neutrino oscillation measurement.

3.1.1. Silicon PIN photodiode

In the T2K experiment, silicon PIN photodiodes, HAMAMATSU® S3590-08, are used as the semi-conductor devise for the detection of the muon flux. In a semi-conductor device, an ionization process of charged particle leads to a generation of electron-hole (e-h) pairs. These carriers drift toward the electrodes under the electric field. The signal is then induced by the drift of these carriers and the charged particle can be detected.

Table 3.1 shows the specification of the silicon PIN photodiode. The sensor has an active area of 10×10 mm^2 and a depletion layer thickness of 300 μm. The silicon layer is mounted on a ceramic base. In order to fully deplete the layer, a bias voltage of 80 V is applied. The photodiode is put on a PEEK^{TM} base fixed to the support enclosure and is covered by an aluminum base.

Table 3.1.: Specification of the silicon PIN photodiode (S3590-08).

Effective area	10×10 mm^2
Depletion layer thickness	300 μm
Reverse voltage (max.)	100 V

3.1.2. Ionization chamber

There are $7 \times 7 = 49$ sensors and each of the 7 sensors are contained in one ionization chamber. The sensors are set on a 1929 mm long aluminum tray at an interval of 250 mm. The tray is inserted into 1956 mm^3 aluminium tube. A drawing of the sensors is shown in Fig. 3.2. Each of the sensors consists of two parallel 100×100 mm^2 ceramic plates separated by 3 mm. One of the two parallel plates has a signal electrode which has a dimension of 75×75 mm^2 and is surrounded by ground electrodes. A bias voltage of 200 V is applied to a 93×93 mm^2 electrode on the other plate and a uniform electric field is created through a 75×75 mm^2 area between the two electrodes. Thus, ionization pairs generated only in the $75 \times 75 \times 3$ mm^3 volume contribute to the signal. All the conductive parts except the electrodes are covered with insulator made of PEEK or a ceramic.

Signal of the ionization chamber is induced by movements of electrons and ions, which are created by the ionization process of charged particles (muons). In the T2K experiment, each of the bunches has an interval of 581 ns (see Table 2.1). In order to avoid pileup of the signal pulse with a faster response, the signal induced by the electrons' drift are used and the one by the ions' drift (about 1000 times slower) are disregarded. Two kinds of gas mixtures are chosen for operation in order to get wide dynamic range: (98% Ar and 2% N_2) and (99% He and 1% N_2). At the standard condition, the ionization yields for a minimum ionization particle are 95.6 cm^{-1} and 7.80 cm^{-1} for Ar and He, respectively [54]. Namely, the signal size with the He gas is about 10 times smaller than that with the Ar gas. Ar is used for a beam intensity below 2.3×10^{13} protons per bunch (p.p.b.). For higher beam intensity, He is used instead. In both of the gas systems, N_2 is used as a quencher and to render the signal size insensitive to the amount of impurities in the gas via the Jesse effect [55]. A space charge effect, which is caused by the slow ions' drift velocity, leads to a recombinations of electrons and ions and hence, non-linearity of the detector response. We had tested the effect of the recombination using an electron beam [53] and confirmed that linearity is guaranteed up to 1.8×10^{13} p.p.b. for Ar+N_2 and 3.0×10^{14} p.p.b. for He+N_2.

In order to get stable response of the ionization chamber, pressure, temperature and purity of the gas are controlled. A diagram of the gas system for the chamber is shown in Fig. 3.3. The gas is feed by five out of ten gas cylinders (7 m^3). The pressure in the entire gas line is kept at 130 ± 0.2 kPa (absolute) by a solenoid control valve at the most downstream of the gas line and is monitored by five pressure transducers (PTs). The gas temperature is controlled to be kept at 34.0 ± 1.5°C by a heater which is placed at

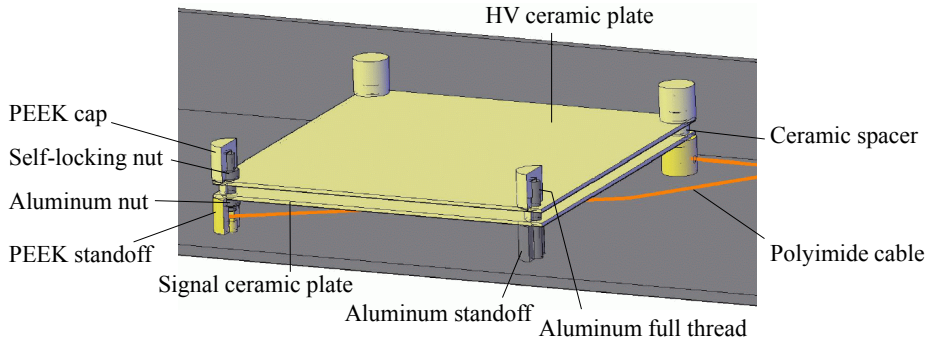

Figure 3.2.: Drawing of a sensor of the ionization chamber [53].

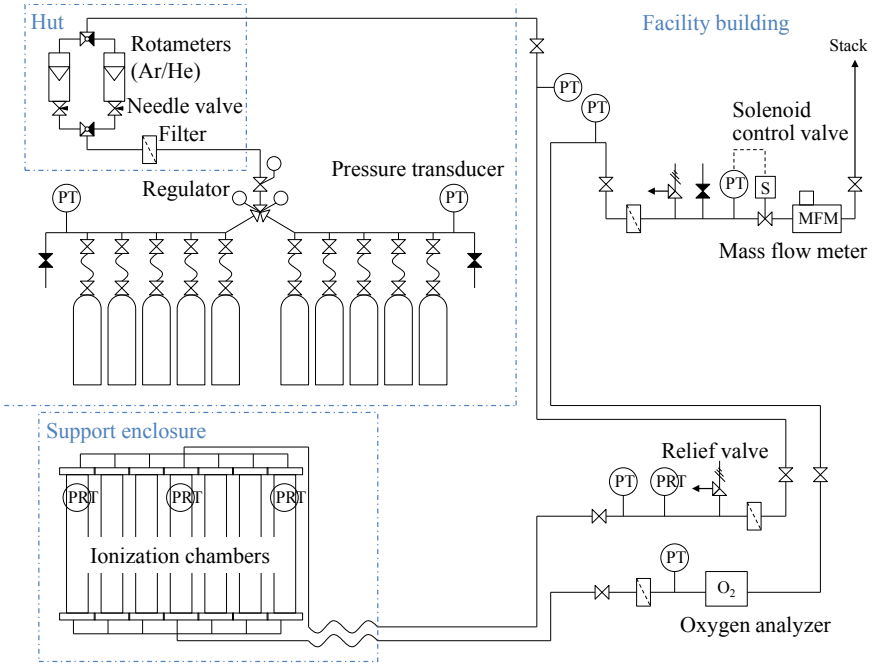

Figure 3.3.: Diagram of a gas system for the ionization chamber. PT and PRT stand for a pressure transducer and Pt100 resistance thermometer, respectively [53].

the pedestal of the muon monitor (see Fig. 3.1) and is monitored by Pt100 resistance thermometers (PRTs) which are mounted inside the aluminum tubes. The contamination of O_2 is always monitored by an oxygen analyzer placed just downstream of the chamber since it leads to loss of drifting electrons by attachment to oxygen, resulting in depletion of the signal. According to a past report [56], 100 ppm of the O_2 contamination causes 1% depletion of the signal. In order to reduce the contamination less than 100 ppm, the flow rate of gas is set at approximately 100 cc/min. During operation, the O_2 contamination has been always kept at 10-20 ppm using these systems.

3.1.3. Electronics

Voltage for the silicon PIN photodiode (ionization chamber) is provided by a 80 V (200 V) power supply via a voltage divider and about 70 m co-axial cables, which run through the muon pit underground to an electronics hut on the surface. The divider consists of two systems as shown in Fig. 3.4. In the pre-divider, zenor diodes are used to prevent excessive voltage being applied to the sensors. The 10 kΩ registor in the pre-divider and 1 μF capacitor in the rear divider work as a low-pass filter for the power supply. The 51 Ω registors in the rear divider is inserted to match the impedance to the co-axial cables and to prevent the pulses from sensors to reflect.

Figure 3.5 shows an illustration of the readout system, which is placed at the electronics hut. A timing signal synchronised to the beam is generated from the MR radio frequency (RF) clock and is distributed to the neutrino beamline as the trigger singal. The trigger is transported via an optical fiber and is received by a transceiver module at the hut, which converts the signal into a NIM pulse. The pulse timing and width are adjusted by a digital gate generator and is used as the gate signal. The delay in the gate generator is set to 30.57 μs, which is optimized from calculations of the time delay of the cables in the beamline and time-of-flight of the proton and muon beam. Signals from both the ionization chamber and silicon PIN photodiodes are transmitted to the electronics hut by about 70 m of co-axial cables. The signals are digitized by Flash-ADC modules (FADC) of the COPPER system [57] developed by KEK. Table 3.2 shows a specification of the FADC. The sampling rate is externally handled by a clock generator and is set to 65 MHz. The full scale of the FADC is $\pm$1V and the resolution is 12 bit. The pulse is shaped with 52.8 ns time constant with a registor (2.4 kΩ) and capacitance (22 pF) in the integrator (see Fig 3.6). The value of the time constant was chosen as small as possible so as to avoid pileup of the pulse on following ones but not to make the pulse discontinuity due to the finite ADC sampling step (=65 MHz). For the ionization chamber, the gain in the FADC is set to 5. On the other hand, unity gain is set for the photodiodes since the size of the signal is about 30 times larger than that of the signal from the ionization chambers. The signal from the photodiode is attenuated by 0, 15, and 30 dB depending on the beam intensity.

The system is calibrated with the CAMAC charge/time (QT) generator (Phillips 7120) before every operation. The calibration covers:

- attenuation due to the signal transmission in the 70 m cable,
- attenuation of the signal in the readout electronics (attenuator and FADC).

The conversion factor from ADC counts to charge (pC) is obtained for every channels by this calibration with 1% precision.

Table 3.2.: Specification of the Flash-ADC module of the COPPER system.

Range	±1V
Sampling rate	65 MHz
Resolution	12 bit
Shaping time	52.8 ns

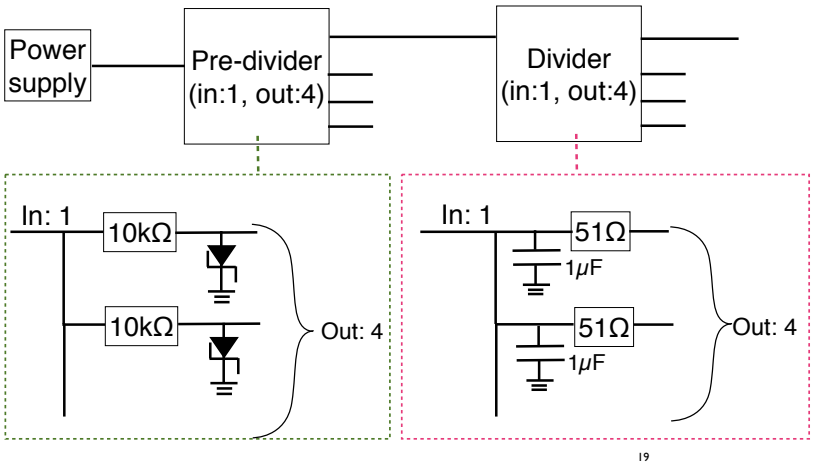

Figure 3.4.: Schematic diagram of the divider system for the power supply of the muon monitor.

3.2. INGRID detector

3.2.1. Detector overview

INGRID [58] consists of 14 independent modules which are composed of iron plates and scintillator planes. The modules are installed at positions in cross shape whose center is on beam-axis. An overview of the INGRID detector is shown in Fig. 3.7. We also assign "ID" to identify the modules as shown in Fig. 3.7. Each module has 9 iron target plates and 11 plastic scintillator tracking planes. The iron plate and the tracking plane is aligned alternately and it makes the sandwiched structure as shown in Figure 3.8. Each of the iron plates has an area of 124×124 cm^2 and thickness of 6.5 cm, providing a total iron mass of 7.1 ton per module. A scintillator tracking plane consists of two scintillator layers: one for the horizontal and the other one for vertical tracking respectively. Each of the layer has 24 scintillator bars, which construct a plane of 120×120 cm^2 and 1.0 cm along the beam direction. The module is surrounded by VETO planes, each of which has 22 scintillator bars and detects charged particles coming from outside of the module.

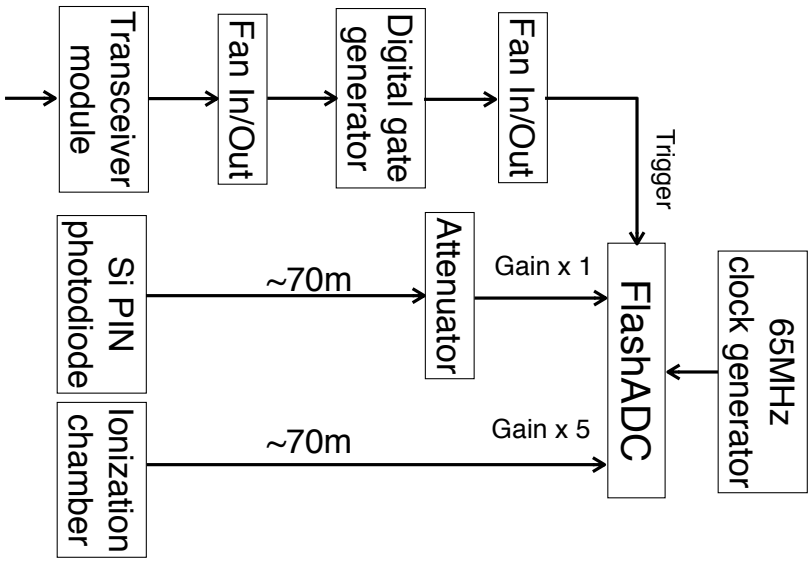

Figure 3.5.: Schematic diagram of the readout system for the Si PIN photodiode and ionization chamber.

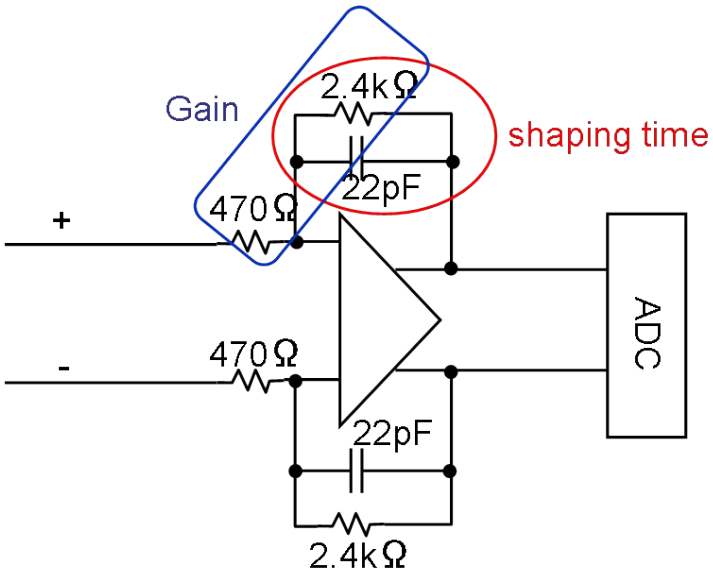

Figure 3.6.: Diagram of the input part of the FADC module.

3.2.2. Tracking plane

In the INGRID analysis, tracks of charged particles are reconstructed from the signals of the tracking planes. An exploded view of the tracking plane is drawn in Fig. 3.9. All the scintillator bars were produced by extrusion in the shape of rectangular (1.0 cm×5.0 cm) at Fermilab [59]. The scintillator bar is made of polystyrene and is infused with two

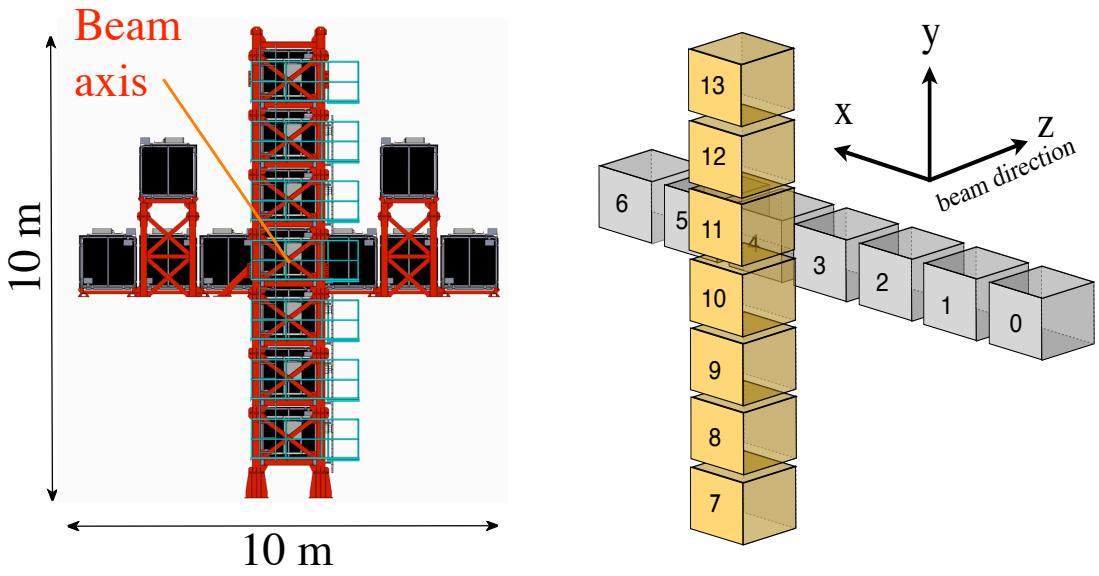

Figure 3.7.: Left: INGRID detector. The modules are arranged to cover 10 m x 10 m region to monitor the neutrino beam profile and the event rate stability. Two separated modules located at off-axis position are not used in this analysis. Right: Module ID used to identify the modules.

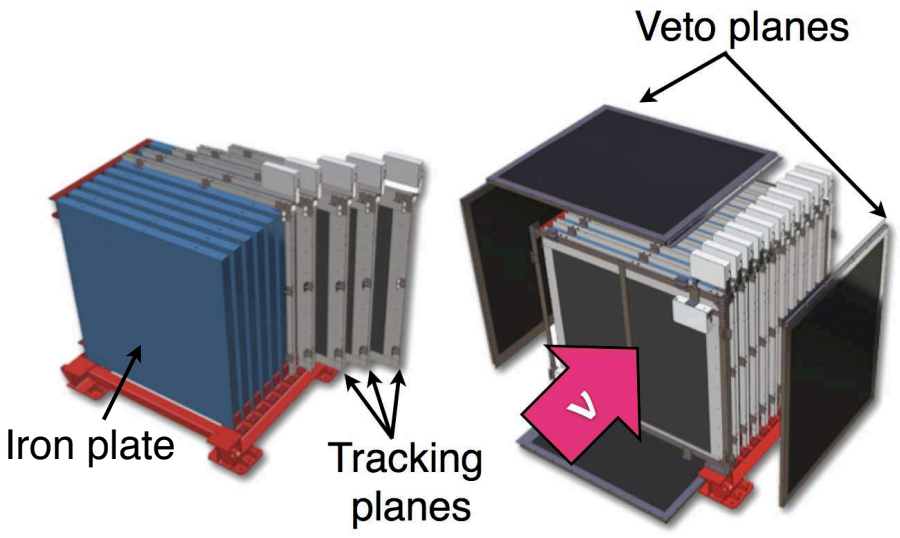

Figure 3.8.: Schematic drawing of the INGRID module. The module has 9 iron target plates and 11 tracking planes, which is covered by VETO planes.

kinds of fluorescence dopants: PPO (1%) as a primary dopant and POPOP (0.03%) as a secondary dopant. The bar is coated with TiO_2 infused in polystyrene. Each of the scintillator bar for the tracking plane has a length of 120.3 cm. A hole of 3 mm in diameter at the center of the scintillator bar allows the insertion of a wavelength shifting

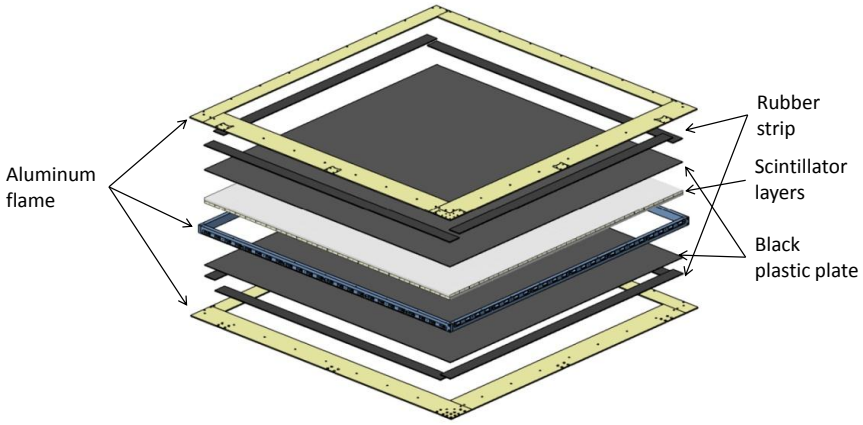

Figure 3.9.: Exploded view of the tracking plane.

(WLS) fiber for light collections, which is described later. In total, 8369 scintillator bars are used in INGRID. Each of the tracking planes is built by glueing a vertical and horizontal scitillator layer together using expoxy resin with aluminum frame and black plastic plates (see Fig. 3.9). The rubber strips are attached between the aluminum frames and the plastic plate in order to avoid the light leak.

The WLS fiber, Y11(200) developed by Kuraray, is inserted into the hole in order to collect the scintillation light. The light is absorbed by Y11 flour and then re-emitted. An absorption and emission spectrum of Y11 is centered at 420 nm and 476 nm, respectively, as shown in Fig. 3.10. One edge of the fiber is connected to a MPPC(Multi Pixel Photon Counter) [60] (S10362-13-050C) developed by HAMAMATSU, while the other one is polished and coated with TiO_2.

The MPPC has an active area of 1.3×1.3 mm^2 and is composed of 667 pixels of Avalanche PhotoDiode (APD). The MPPC is operated in Giger-mode, at which the diode is reverse-biased beyond the electrical breakdown voltage (typically $\sim$70 V). At above the voltage, a gain of the MPPC is approximately 5×10^5.

Detection of charged particles consists of following three steps.

1. An incoming charged particle excites atoms in the polystyrene bar and the excitation energy is transferred to the primary dopant (PPO), which emits light of wavelength (λ) $\sim$340 nm. This process is then followed by an excitation of the secondary dopant (POPOP), emitting light at $\lambda \sim 400$ nm.

2. The WLS fiber collects the light and shifts the wavelength to 476 nm.

3. The light is detected by the MPPC. The signal from the MPPC is digitized at the electronics, details of which is given in Sec. 3.2.4.

This process is illustrated in in Fig. 3.11.

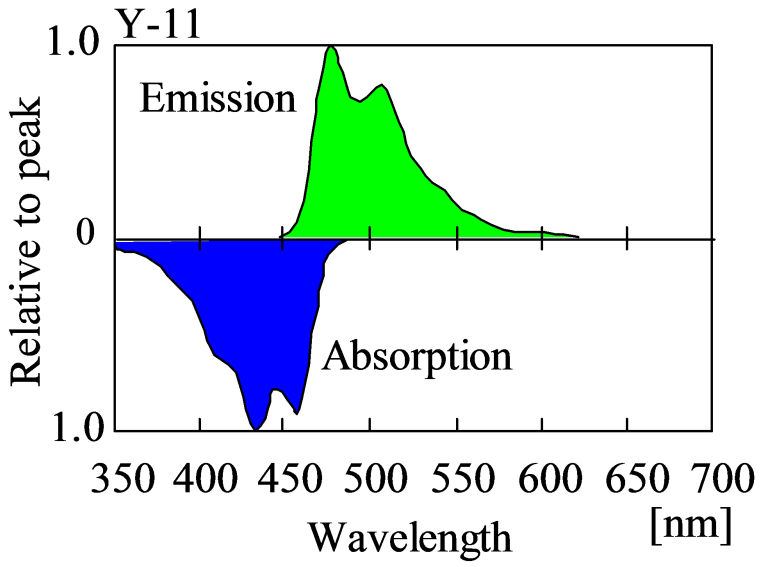

Figure 3.10.: Absorption and emission spectra of Y11 WLS tiber.

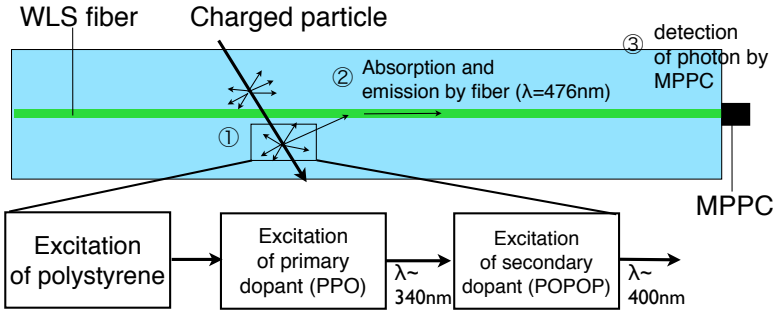

Figure 3.11.: Illustration for detection of a charged particle with the scintillator in INGRID.

3.2.3. Iron palte

The iron plates were fabricated in France. The designed mass of each plate was 785 kg and was measured with a precision of 1 kg after the fabrication. Table 3.3 shows the measured mass of nine iron plates for each module. The difference between measured and designed value is used for correction for observed number of neutrino events.

3.2.4. Electronics and data acquisition

Readout electronics of INGRID is composed of one front-end board called Trip-t front-end Board (TFB), and three kinds of back-end boards (BEBs): Readout Merger Module

Table 3.3.: Mass of iron plates for each module. The design value is 7065 kg (785 kg×9 plates).

Module	0	1	2	3	4	5	6
Weight (kg)	7124	7081	7065	7076	7059	7094	7114
Module	7	8	9	10	11	12	13
Weight (kg)	7041	7063	7094	6987	7079	6979	6988

(RMM), cosmic trigger Module (CTM), and a timing module. The diagram of the TFB and BEBs are shown in Fig. 3.12.

TFB [61] has four Trip-t chips, two 10-bit dual channel ADC chips (AD9201), eight 8-channel 8-bit DACs (AD5308), a FPGA (Xillinx Spartan 3) and so on. Each of the INGRID module has 13 TFBs (182 TFBs in total). Trip-t integrates charge of the signal from MPPCs and AD9201 digitized that charge. Signals from AD9201 is brought to a discriminator, which is a part of the Trip-t, providing timing information. The TDC data is recorded with a time resolution of 2.5 nsec. AD5308 provides programmable trim voltage (0-5 V) to each MPPC. The TFB operation is controlled by FPGA. Each TFB reads out MPPCs in one tracking plane or MPPCs in two veto planes.

All BEBs are developed on the same hardware platform with a high-end Vertex II Pro FPGA from Xillinx. RMM is connected to TFB via Cat 5e cables and all BEBs are connected to each other via their RocketIOs. The timing module distributes the beam trigger to TFB via RMM. It also distributes the cosmic-ray trigger signal generated by CTM. The CTM generates the cosmic-ray trigger from the primitive signal from TFBs. These BEBs are connected to the DAQ PCs by optical Gigabit Ethernet cables.

Figure 3.13 shows the timing diagram of DAQ. As with the muon monitor, the trigger timing is provided from the MR RF. The time window of the integration and the rest is set to 530 ns and 50 ns, respectively. Each of the integration time window is called "cycle". The timing is adjusted so that the first bunch timing is in the middle of fifth cycle. The INGRID DAQ then starts to take data and record the data of 23 cycles.

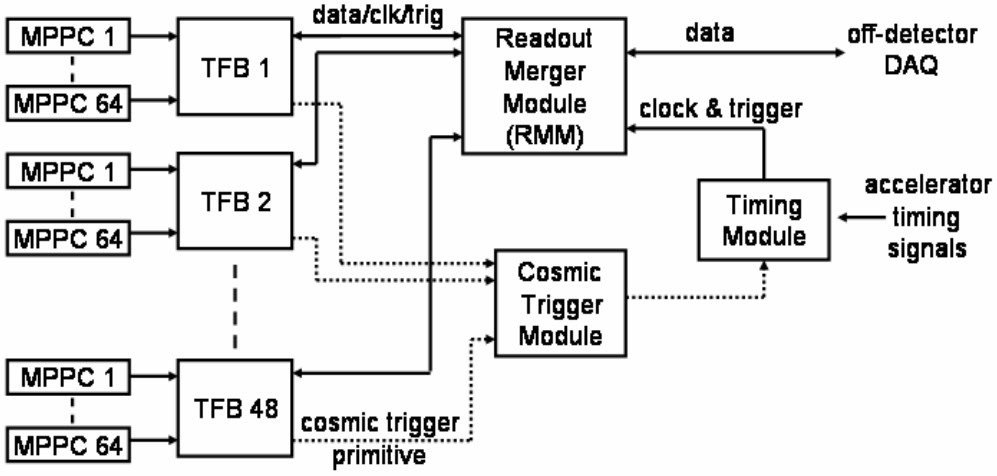

Figure 3.12.: The Trip-t based front-end board (TFB) and the back-end boards (BEBs) [61].

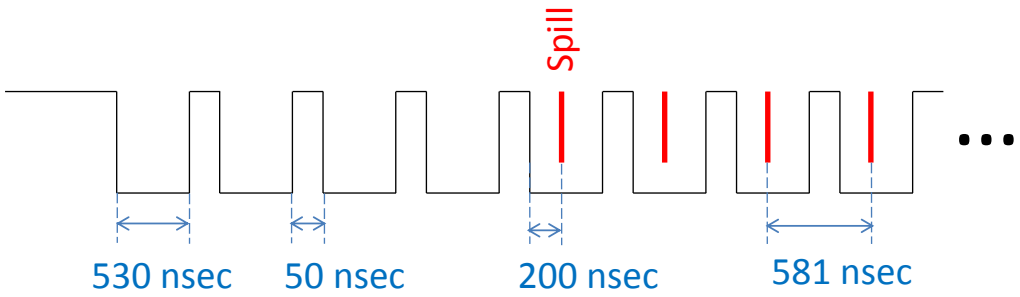

Figure 3.13.: Timing diagram of the data acquisition. The time window of the integration and the rest is set to 530 ns and 50 ns, respectively. Each of the integration time window is called "cycle". The timing is adjusted so that the first bunch timing is in the middle of fifth cycle.

Part III.

Muon beam properties

Chapter 4

Overview of the muon beam measurement

Muon monitors were used in the various long baseline neutrino experiments to control the neutrino beam direction [62–64]. In the T2K experiment, the neutrino beam direction is required to be within 1.0 mrad to reduce the additional uncertainty on the measurement of the neutrino oscillation parameters. Tasks of the T2K muon monitor is to measure the muon beam direction with a precision of 0.3 mrad and to control the neutrino beam direction to within 0.3 mrad with respect to the beam-axis. In this part, we describe properties of the muon beam, which are the direction and intensity of the muon beam, and the absolute muon flux, and provide the world-first quantitative measurements in the accelerator-produced neutrino experiments.

Chapter 5 describes an analysis method for reconstruction of the muon beam profile with the muon monitor. In this chapter, we also introduce the T2K beam simulation and the detector calibration system. Chapter 6 then describes results of the muon beam measurement in T2K beam operation. In this chapter, the measurement of the absolute muon flux by the emulsion detector is also described. The result is then compared to the prediction by the beam simulation. This comparison is important to ensure the detector response of the muon monitor and hence the validity of the beam control by the muon monitor.

Chapter 5

Analyses with the muon monitor

In this section, we focus on an analysis method of the beam data with the muon monitor. We first describe how to reconstruct the muon beam profile and measure the beam direction in Sec. 5.1. The beam simulation is prepared for the prediction of the muon flux: simulation of hadronic interactions inside and outside of the target and calculation of the particle decay in the decay volume. Section 5.2 explains the simulation in more detail. The sensors are calibrated using the actual beam at the beginning of each beam operation period as described in Sec. 5.3.

5.1. Reconstruction of the muon beam profile

In the measurement of the muon beam with the muon monitor, the signal from each of the sensors in the silicon and ionization chamber arrays are read out by the FADC. The signal is then integrated to calculate the collected charge after subtracting the baseline. The typical waveforms recorded during beam operation are shown in Fig. 5.1. These waveforms were obtained at a beam intensity of 1.3×10^{13} protons per bunch (p.p.b.) where the attenuator level was set to 30 dB for the signal from the silicon sensors. In the analysis, the integration windows are set to each bunch and the profile of the muon beam can be reconstructed bunch-by-bunch. In this way, it is possible to measure the muon beam direction and intensity for each bunch. The single bunch measurement is affected by bunch-by-bunch fluctuation in the proton beam direction and intensity. Therefore, the muon beam direction and intensity are also reconstructed for an entire spill by summing the collected charge over all bunches in that spill. We monitor this spill-by-spill beam direction and intensity and check those for corresponding bunches when issues are found for some spills. For the beam measurement, we usually use the muon beam profile measured with the silicon arrays as the size of the signal is about 30 times larger than that of the signal from the ionization chambers, providing a better signal-to-noise ratio. Figure 5.2 shows the charge distribution measured by the silicon PIN photodiodes, which is obtained by summing the distribution over all bunches. In order to extract the profile of the muon beam, the charge distribution is fitted by a two-dimensional Gaussian function with 5 fitting parameters $\{A, x_0, y_0, \sigma_x, \sigma_y\}$:

$$f(x, y) = A \exp\left[-\frac{(x - x_0)^2}{2\sigma_x^2} - \frac{(y - y_0)^2}{2\sigma_y^2}\right] , \tag{5.1}$$

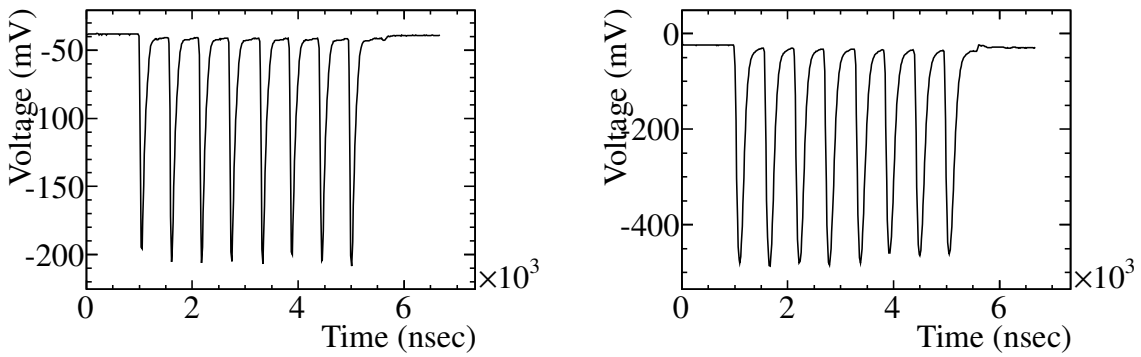

Figure 5.1.: Waveform of the signal from the silicon PIN photodiode (left) and ionization chamber (right), digitized by the FADC. Both of the signals are from sensors placed at the center of the arrays and recorded when the beam intensity is 1.3×10^{13} p.p.b. The attenuator level was set to 30 dB for the signal from the silicon sensors.

where A is a normalization parameter; x_0 and y_0 represent centers of the beam profile in the horizontal and vertical direction, respectively; σ_x and σ_y represent widths of the beam profile in the horizontal and vertical direction, respectively. Here the x_0 and y_0 are positions relative to the designed beam-axis at the muon monitor. In the beam direction measurement, we apply corrections of effect from the tilted beamline and mis-alignment of the monitor, which are described in Secs. 6.2.2 and 6.3.1, respectively.

An example of the reconstructed profile obtained from a fit of the two-dimensional Gaussian is shown on the right in Fig. 5.2. Figure 5.3 shows profiles of the muon beam for the horn currents of 0 kA and 250 kA. The peak charge collected at 250 kA operation is about 4 times larger than that collected at 0 kA operation. Table 5.1 summarizes the center and width of the reconstructed profile for the data and MC simulation when the horns are operated at 250 kA. The muon beam-axis direction $\{\theta_x, \theta_y\}$ is then calculated using parameters $\{x_0, y_0\}$ and distance $(= L)$ between the target and muon monitor:

$$\theta_x = x_0/L, \qquad \theta_y = y_0/L \qquad (L = 118 \text{ m}) \,. \tag{5.2}$$

Here we use an approximation of $\tan\theta_{x(y)} \simeq \theta_{x(y)}$, as $\theta_{x(y)} \ll 1$.

5.2. Monte Carlo simulation

The T2K beam simulation consists of two processes: a simulation of the hadronic interaction in the graphite target, and propagation of the particles until they interact or decay. For the simulation of the hadronic interaction in the target, several simulators

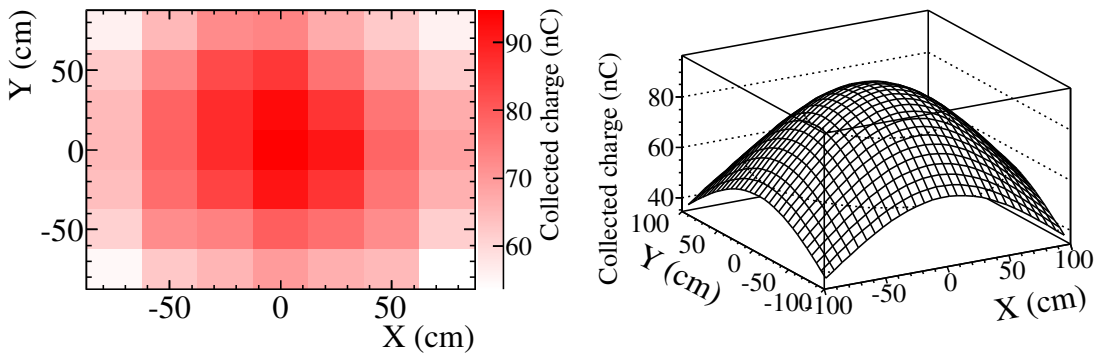

Figure 5.2.: Obtained charge Charge distribution (left) and reconstructed profile (right) of the muon beam measured by the silicon array. The collected charge is obtained for each sensor by integrating the waveform of all of the bunches (i.e spill) read out by the FADC. This is a beam event when the intensity is 1.3×10^{13} p.p.b.

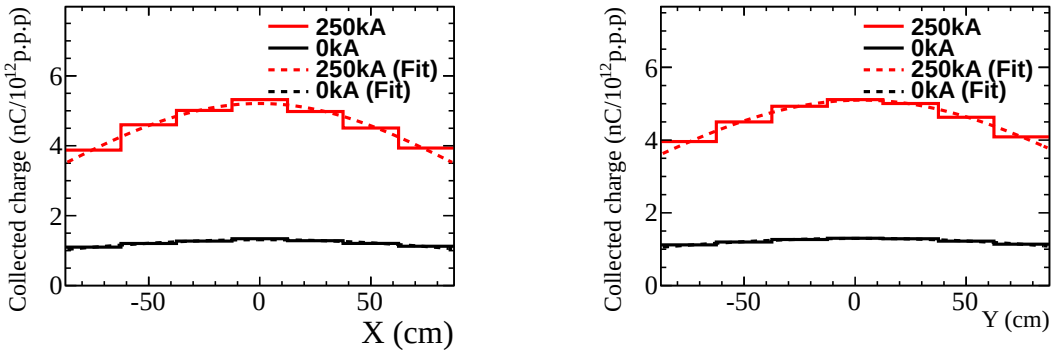

Figure 5.3.: Charge distribution (solid) and reconstructed muon beam profile (dashed) obtained with the silicon array when horns are operated at 0 kA (black) and 250 kA (red). The horizontal (vertical) profile is shown in left (right).

were tested and compared with the hadronic production data. Finally FLUKA2008 [65] was chosen, which was found to be in good agreement with the data[1,2]. Kinematic information for particles emitted from the target is saved and transferred to the JNUBEAM simulation [42] JNUBEAM is a GEANT3 [66] simulation of the secondary beamline including the muon monitor. The geometry of these components is modeled based on the final mechanical drawings of the constructed beamline. Hadronic interactions are modeled by GCALOR [67] in JNUBEAM. Table 5.2 shows the MC estimation of flux of particles penetrating the muon monitor at the 250 kA horn current setting. The muons are accompanied by soft components such as gammas and δ-ray electrons. The

[1]Recently FLUKA2011 is found to be the best agreement with external hadron production data.
[2]The hadron interactions are further tuned with the external experiment data in Sec. 6.4.2

Table 5.1.: Comparison of the center and width of the beam profile between the data and MC prediction at 250 kA horn operation. In the MC simulation, the position and width of the proton beam at the baffle are matched with the measured values. The errors on the numbers are the MC statistical ones.

	Fitted profile center		Fitted profile width	
	x (cm)	y (cm)	wx (cm)	wy(cm)
Data	-0.1	-1.0	98.2	108.5
MC	-0.2 ± 0.3	-0.2 ± 0.3	97.7 ± 0.6	105.8 ± 0.8

particles contributing to the signal at the muon monitor are also estimated using the MC simulation where argon gas is used for the ionization chamber and all horn currents are set to 250 kA. The result is shown in Table 5.3. In both the silicon and ionization chamber arrays, the muons account for about 80% of the total signal. The subsequent contribution to the signal comes from δ-rays, accounting for about 10% of the total. A breakdown of the muon flux by the parent particles ($\pi^{\pm}$, $K^{\pm}$ and K^0_L) is shown in Table 5.4. As listed in the table, 92% (95%) of total μ^+ (μ^-) production is attributable to parent π^+ (π^-) decays. Table 5.5 shows the breakdown of parent particles ($\pi^{\pm}$ and $K^{\pm}$) generated at each of the materials in the secondary beamline. Most of the pions contributing to the muon flux are generated at the graphite target. The subsequent contributions from pions come from interactions at the beam dump (carbon) which is placed just in front of the muon monitor.

Figure 5.4 shows the p-θ phase space of the production of the parent π^+'s contributing the muon flux at the muon monitor and the neutrino flux at INGRID where p is the momentum and θ is the polar angle with respect to the beam-axis. These are estimated for the 250 kA horn setting. As seen in the figure, the muon monitor measures the muons from the forward-angle pions with high momenta (>5 GeV/c). This is because only muons with energy above 5 GeV can pass through the beam dump and reach the muon monitor. On the other hand, the parent pion for the neutrino flux at INGRID has lower momentum ($\langle p_\pi \rangle$ =4.4 GeV/c) than that for the muon flux at the muon monitor. Namely, the phase space covered by the muon monitor has small overlap with that for the neutrino flux. This implies that the muon beam direction measured by the muon monitor might be different from the neutrino beam direction when the direction is largely shifted from the designed beam-axis. Therefore, it is highly important to keep the beam direction close to the design axis, to understand the response of the muon monitor and to confirm the neutrino beam direction by INGRID.

Table 5.2.: Breakdown of the particles ($/10^{13}$ p.o.t.) arriving at the muon pit and going through the area covered by the muon monitor (150×150 cm^2). These are estimated by the MC simulation with 250 kA horn current settings.

Particle type	Particles at the silicon array		Particles at the chamber array	
μ^+	2.39×10^{10}	(49.3%)	2.20×10^{10}	(52.0%)
μ^-	0.18×10^{10}	(3.7%)	0.17×10^{10}	(3.9%)
e^-	0.32×10^{10}	(6.7%)	0.26×10^{10}	(6.3%)
e^+	0.03×10^{10}	(0.6%)	0.02×10^{10}	(0.6%)
γ	1.92×10^{10}	(39.6%)	1.56×10^{10}	(37.0%)
others	$< 0.01 \times 10^{10}$	(0.1%)	$< 0.01 \times 10^{10}$	(0.2%)
Total	4.84×10^{10}	(100%)	4.22×10^{10}	(100%)

Table 5.3.: Breakdown of the particles ($/10^{13}$ p.o.t.) contributing to the signal at the muon monitor. The number listed in the table is estimated for particles going through the area covered by the monitor (150×150 cm^2). In this MC estimation, argon gas is used for the ionization chamber and horn currents are set to 250 kA.

Particle type	Particles at the silicon array		Particles at the chamber array	
μ^+	2.39×10^{10}	(82.2%)	2.19×10^{10}	(83.4%)
μ^-	0.18×10^{10}	(6.1%)	0.17×10^{10}	(6.3%)
e^-	0.30×10^{10}	(10.2%)	0.25×10^{10}	(9.3%)
e^+	0.03×10^{10}	(0.9%)	0.02×10^{10}	(0.9%)
γ and others	0.02×10^{10}	(0.6%)	$< 0.01 \times 10^{10}$	(<0.1%)
Total	2.90×10^{10}	(100%)	2.63×10^{10}	(100%)

5.3. Detector calibration

The relative gain of sensors are calibrated using beam at the beginning of each beam operation period. The ionization chamber is calibrated by moving the entire chamber array by ±25 cm, which corresponds to the sensor spacing, in both the horizontal and vertical direction and measuring the muon profile at 9 different configurations. These 9 measured profiles should be the same on the assumption that the muon beam profile itself does not change over the course of the measurements. After the measurement of the muon profile at the 9 different configurations, at most 9 collected charge are obtained with the 9 different sensors at each position. The relative gain of the sensors are then estimated

Table 5.4.: Breakdown of the μ^+/μ^- flux by the parent particles ($\pi^\pm$, $K^\pm$ and K^0_L) for the 250 kA horn current setting.

Parent particle	μ^+	μ^-
π^+	85.3%	-
π^-	-	6.6%
K^+	7.7%	-
K^-	-	0.4%
K^0_L	<0.1%	<0.1%

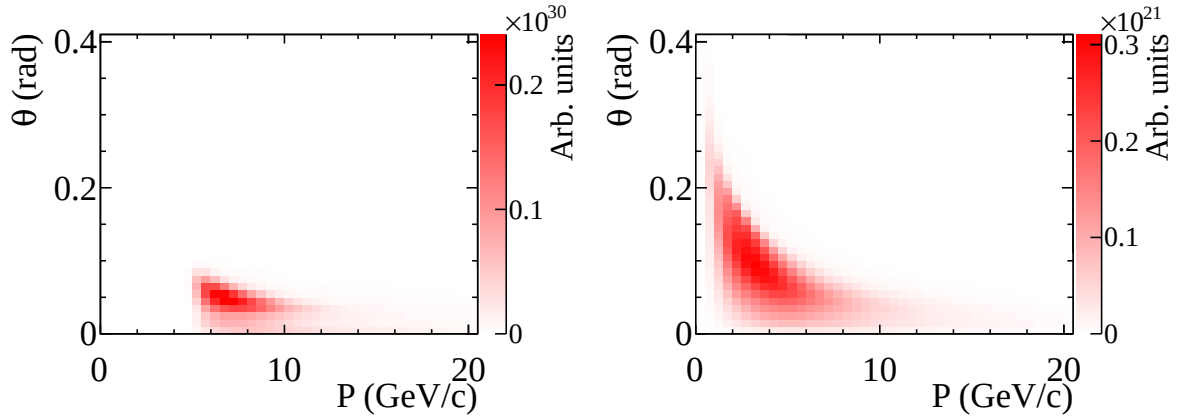

Figure 5.4.: p-θ phase spaces of the parent π^+'s contributing the muon flux at the muon monitor (left) and the neutrino flux at INGRID (right), where p is the momentum and θ is the polar angle with respect to the beam-axis at the time of the production. These phase spaces are estimated for the 250 kA horn setting. The same p.o.t. (1.0×10^{21} p.o.t.) is used for the normalization in both the left and right plots.

by comparing these charges and the correction factors for the gain are determined so that the charges match. In order to estimate the uncertainty on the correction factors, these 9 measurements, together with one more measurement at the nominal position, are subdivided into two data sets (5 measurement for each). The correction factors are determined with each data set in the same way as above (Fig. 5.5 top). The root mean square (RMS) of the differences of 49 correction factors between two data sets is taken as the uncertainty of the correction factor (Fig. 5.5 bottom).

The silicon PIN photodiodes are calibrated sensor-by-sensor by measuring the muon beam with an extra calibration sensor mounted on small moving stage behind the silicon array (see Fig. 3.1). The calibration sensor is placed behind each sensor and the ratio of the charge collected by the calibration sensor to that of the fixed signal sensors is

Table 5.5.: Breakdown of the muon parent particles generated at each material for the 250 kA horn setting. The last column shows the breakdown for the total flux. A symbol in a parenthesis denotes the main material element.

Material	π^+	π^-	K^+	K^-	Total
Graphite target (C)	94.0%	64.0%	89.8%	53.9%	91.6%
Horn (Al)	1.5%	3.9%	1.2%	1.0%	1.7%
Decay volume (He)	1.2%	6.7%	1.0%	3.3%	1.6%
Decay volume (Fe)	0.4%	3.9%	0.7%	2.8%	0.6%
Beam dump (C)	2.4%	20.8%	7.2%	38.4%	4.1%
Other materials	0.5%	0.6%	0.3%	0.5%	0.5%
	100%	100%	100%	100%	100%

calculated:

$$R_i = Q_i/Q_{ref} \quad (i = 1, 2, .., 49) \ , \tag{5.3}$$

where Q_{ref} and Q_i are the collected charges obtained by the extra calibration sensor and i^{th} signal sensor, respectively (see Fig. 5.6). The correction factor is then calculated for each sensor using the mean of the charge ratios:

$$G_i = \langle R \rangle / R_i \ . \tag{5.4}$$

This correction is then applied to each sensor. The uncertainty in the correction factor is due to the statistical error on the collected charge and it determines the precision of this calibration.

For the ionization chamber, all of the sensors are calibrated with a precision of 0.4% which is determined from the difference in the correction factors between the two data sets as described above. For the silicon PIN photodiodes, the calibration is done with a precision of 0.1% which originates from the statistical fluctuation of the measured collected charge.

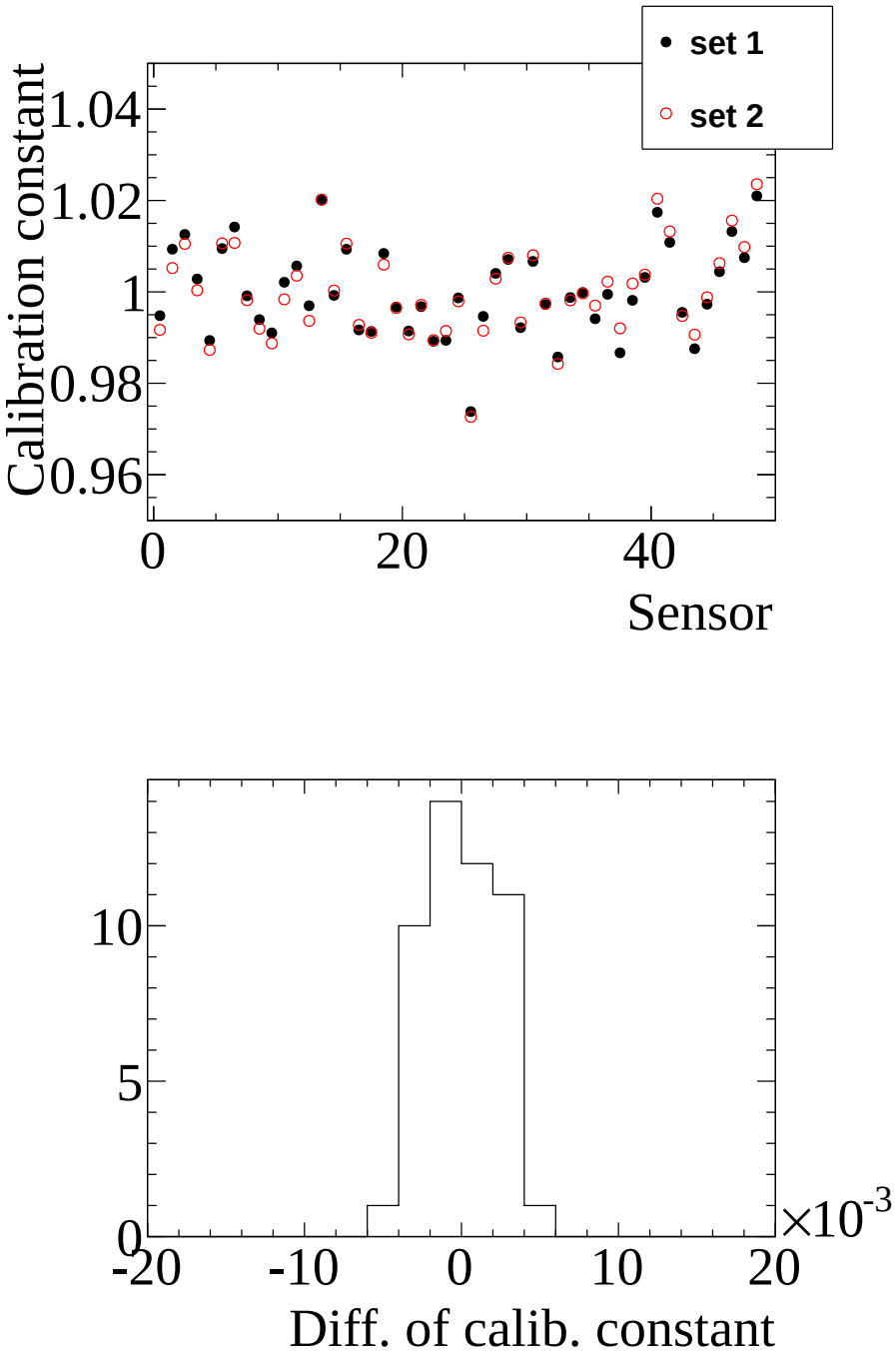

Figure 5.5.: Top: Obtained correction factor of each sensor of the chamber array for different two data sets. Bottom: Distribution of the difference in the correction factor between two data sets. The RMS of the distribution is taken as the uncertainty of the correction factor.

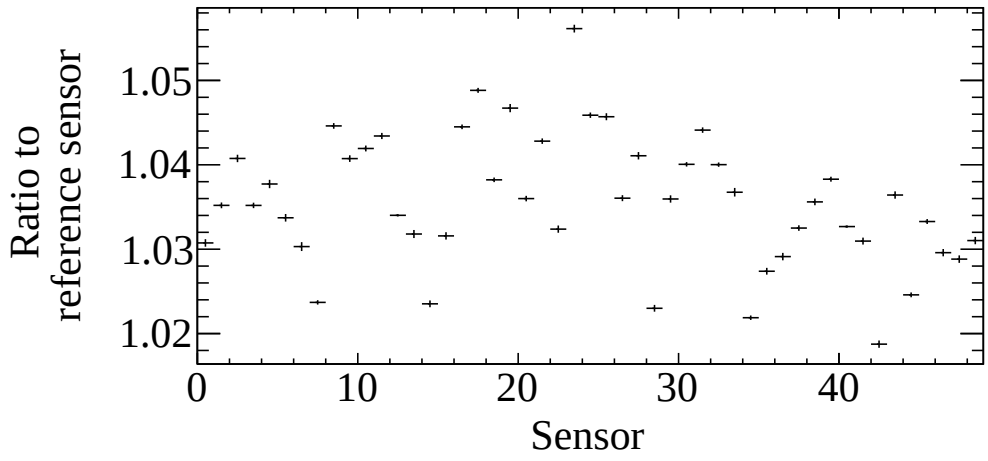

Figure 5.6.: Distribution of the ratio of the charge collected by the SI calibration sensor to that of the fixed signal sensors. The error bar is the statistical one.

Chapter 6

Muon beam measurements in T2K beam operation

This chapter describes the results of the muon and neutrino beam measurement during beam operations including those at the commissioning stage. The data collected until RUN 4 (May 2013) is used for the analysis (see Table 2.3). Hereafter we first describes the measurement at the commissioning stage in Sec 6.1. The systematic error in the muon beam direction is discussed in Sec. 6.2. Section 6.3 then shows beam direction and intensity of the muon and neutrino beam measured by the muon monitor and INGRID during beam operation. In this section, we also describe resolution of the variation in the direction and intensity measurement by the muon monitor. Understanding of the absolute muon flux is important to understand the detector response and hence to verify the beam control by the muon monitor. The muon flux was measured with the emulsion during beam operation and the result was then compared with the prediction, which are described in Sec. 6.4. Finally a summary of the measurement of the muon beam is given in Sec. 6.5.

6.1. Measurements at the beamline compromising

The muon monitor has played an important role during the commissioning of the experiment. At the commissioning stage, proton beam is tuned with the muon monitor so that the muon beam profile is centered at the muon monitor. Horn currents are varied to check the dependence of the muon flux on the horn current, In addition, the monitor was used as a tool for a survey of the components in the secondary beamline. It gives useful information for understanding the actual configuration of the baffle and target.

6.1.1. Proton beam tuning with the muon monitor

Figure 6.1 shows a schematic view of the configuration of the components in the secondary beamline, the proton-beam monitor, and the muon monitor. Before hitting the target, the proton beam passes through the proton-beam monitors. Using the SSEMs and OTR measurements, the beam position upstream of the baffle (target) is reconstructed with an accuracy better than 0.7 mm (0.6 mm). Data at various beam positions were taken in order to investigate the correlation between the proton beam position at the target

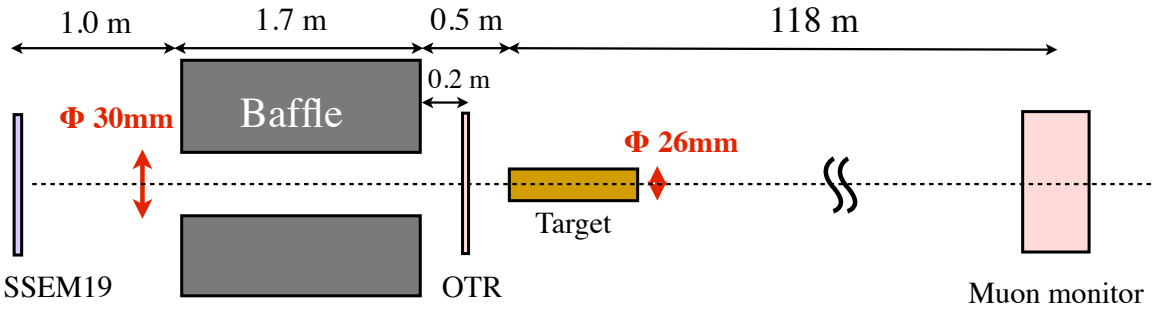

Figure 6.1.: Configuration of the components in the secondary beamline with SSEM19 and the muon monitor.

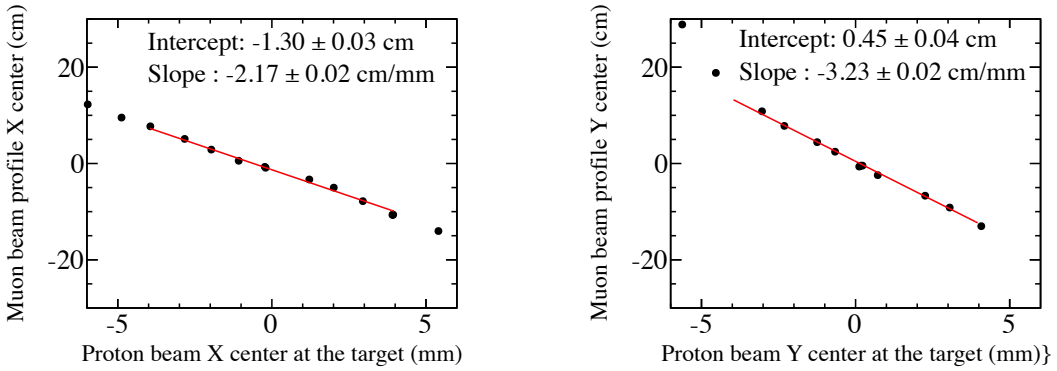

Figure 6.2.: Correlation between the profile center at the muon monitor and the proton beam position at the target in the horizontal (left) and vertical (right) direction. The position of the proton beam is extrapolated at the target using the measurement of the SSEMs and OTR. Fitted lines (red lines) and the results of the fit are shown in the figures. The errors on the fitted parameters are only statistical ones. The data was taken when all the horn currents were set to 250 kA.

and the profile center of the muon beam at the muon monitor. As shown in Fig. 6.2, the profile center measured by the muon monitor is very sensitive to the position of the proton beam at the target: 1 mm change of the proton beam at the target results in -2.17 cm (-3.23 cm) shift of the profile center at the muon monitor in the horizontal (vertical) direction. For the physics data taking, the angle and position of the proton beam are tuned such that a shift of the profile center of the muon beam is less than 2 cm at the muon monitor in order to keep the beam direction well within 0.3 mrad during long term beam operation.

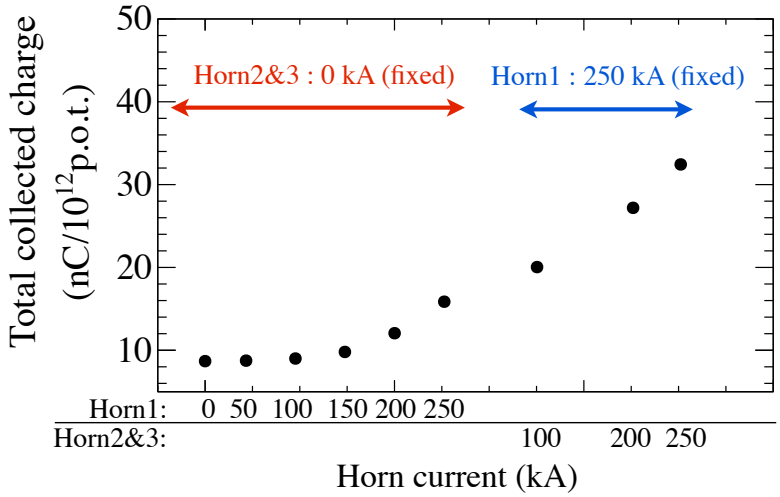

Figure 6.3.: Dependence of the total collected charge of the muon monitor for different combination of horn currents. Since a common power supply was used for the Horn2 and Horn3, these horn currents were simultaneously changed.

6.1.2. Dependence of the muon yield on the horn current

Increasing the horn currents results in focusing more charged pions and producing more intense muon and neutrino beams. The focusing of pions can be confirmed by the charge of muon flux. During beam operation, we tested how the collected charge changes by varying the horn currents from 0 kA to 250 kA. Figure 6.3 shows the total collected charge measured by the silicon array for various horn currents. Since a common power supply was used for the Horn2 and Horn3, these horn currents were simultaneously changed. When all of the horns are operated at 250 kA, the collected charge are increased by a factor of 4 compared with the case of 0 kA horn current setting[1]. We also varied the horn current by ±1% (2.5 kA) and checked the effect on the collected charge. This result is shown in Fig. 6.4. When the Horn1 current was varied by ±1 kA from 250 kA while fixing the Horn2 and Horn3 currents at 252 kA, the collected charge measured by the silicon array varied by 0.40% (left in Fig. 6.4). Subsequently, Horn2 and Horn3 currents were simultaneously varied by ±1% from ∼250 kA while fixing the Horn1 current at 248 kA. This resulted in a 0.33%/kA change in the collected charge (right in Fig. 6.4). As described in Sec. 6.3.2, the muon monitor has a resolution of 0.1% in the beam intensity measurement. Thus, the monitor is sensitive to variations of ∼0.3 kA in either Horn1, or Horn2 and Horn3 combined. These results show that the muon monitor is also useful for monitoring the horn currents.

[1]The neutrino flux at Super-K is increased by a factor of ∼17 at the spectrum peak energy (∼0.7 GeV).

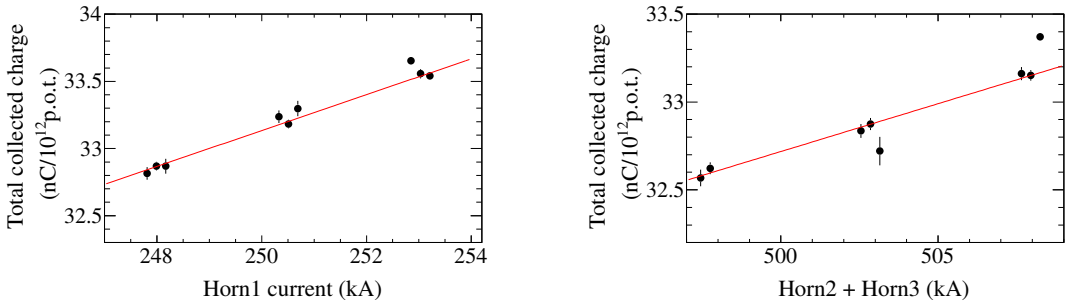

Figure 6.4.: Dependence of the total collected charge on the horn current variation. Left: the Horn1 current was changed by ±1% (2.5 kA) from the nominal value (250 kA) while fixing the Horn2 and Horn3 currents at 252 kA. Right: the Horn2 and Horn3 currents were simultaneously changed by ±1% (2.5 kA) from the nominal values while fixing the Horn1 current at 248 kA.

6.1.3. Survey of the secondary beamline after the earthquake

During beam-off span, a level of the beamline was surveyed and it turned out that there was a sinking of the ground. The configuration of the components in the beamline might be changing due to the the ground sinking. In addition, the Grate East Japan Earthquake in 2011 resulted in movement of many components [42]. The muon monitor has also played an important role in confirming the alignment of the secondary beamline. Ideally the relative center positions should be consistent between the baffle and target. If there is a difference in the relative center positions between these two components, the proton beam may hit the baffle (collimator) and may not produce secondary particles in the target effectively. In addition, the miss-steered beam, which is not collimated properly by the baffle, would result in hitting downstream components other than the target. However, it is impossible to survey the instruments with a visual inspection because they are inside the helium gas volume enclosed in the helium vessel. We therefore conducted the survey using the proton beam during operation just after the recovery work for the earthquake. In this measurement, we moved the proton beam position at the target from one end to the other in steps of ∼1mm. If such an off-centered beam hits the target, thermal shock in the target is not axisymmetric and expansion occurs anisotropically. This thermal damage increases as the intensity of the proton beam increases and would cause cracks inside the target. In addition to that, many protons would hit instruments other than the target such as a container of the target and the horn conductor. Therefore, the intensity of the proton beam was kept as low as possible (4×10^{11} p.p.b.) in order to minimize the damage to any components in the beamline. The proton beam size was set 2.3-2.8 mm during the survey run while the nominal size is ∼4 mm. As shown in Fig. 6.1, the baffle has a beam hole of 30 mm, while the target has a diameter of 26 mm. Namely, there is a radial gap of 2 mm between the baffle and target. If the alignments of these two instruments are perfect, the proton beam interacts less with the target when passing through the gap. Then the contribution of the muons from interactions at the

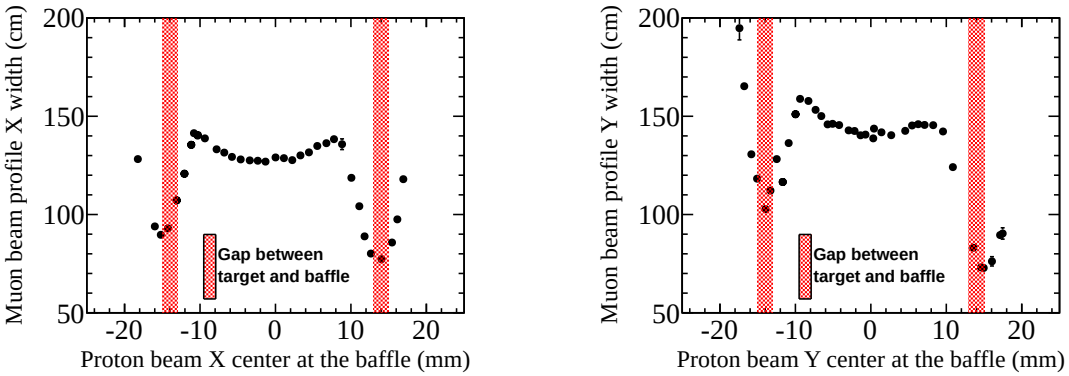

Figure 6.5.: Profile width of the muon beam at the silicon array obtained by scanning the proton beam at the baffle in horizontal (left) and vertical (right). The expected position of 2 mm gap between the baffle and target is expressed as the red shaded region ($-15 \sim -13$ mm and $13 \sim 15$ mm). All of the horn currents are set to 0 kA during the data taking.

Table 6.1.: Fitted gap position between the baffle and target. The error is statistical.

	Scan in horizontal		Scan in vertical	
	$x < 0$	$x > 0$	$y < 0$	$y > 0$
Fit result (mm)	-15.0 ± 0.04	13.7 ± 0.04	-14.1 ± 0.03	14.9 ± 0.11
Fit range (mm)	$-17.0 \sim -13.0$	$11.5 \sim 15.5$	$-16.0 \sim -13.0$	$13.0 \sim 16.5$

dump increases. This results in a narrower muon beam at the muon monitor. Figure 6.5 shows the profile width of the muon beam at the silicon array, obtained by scanning the proton beam position at the baffle in horizontal (left) and vertical (right) axes. The expected position of the 2 mm gap between the baffle and target is expressed as the red shaded region ($-15 \sim -13$ mm and $13 \sim 15$ mm) in the figure. As shown in Fig. 6.5, the profile widths have minimums around the gap in both horizontal and vertical axes. Fitting to these dips with a quadratic function was performed to extract the actual gap position. The fitted dips are situated within the expected position of the 2 mm gap between the baffle and target. In conclusion, we confirmed that the center position of the baffle consistent with that of the target for physics data taking.

6.2. Systematic error in the beam direction measurement

The systematic error in the beam direction comes from:

1. uncertainty of the structure of the upstream materials,
2. δ-ray contamination in the muon beam,
3. uncertainty in the relative calibration of the sensors,
4. alignment error of the muon monitor,
5. effect from the tilted beamline.

The first three sources cause a distortion in the observed beam profile and lead to an uncertainty in the beam direction. The error in the alignment between the target and muon monitor causes the error on the beam direction. The beam-axis is tilted by 3.637 degrees downward and this results in an vertically asymmetric profile at the muon monitor. A correction factor was estimated using the MC simulation for the measurement.

6.2.1. Profile distortion

The muon beam profile is reconstructed by fitting the collected charge distribution assuming it has a form of perfect Gaussian. However, the profile can be deviated from the ideal Gaussian form reflecting the geometrical shape of the upstream materials. In addition, the secondary particle, such as δ-ray, generated at the nearby materials could further distort the observed beam profile.

The beam dump consists of multiple components as shown in Fig. 6.6. Any deviation of the thickness or density of these objects from their design values causes a non-uniformity of the path length of muons and may distort the muon profile. This effect was estimated with a MC simulation. In the simulation, as an extreme case study, both the density (ρ) and thickness (d) of one half (positive side in the horizontal direction) of each dump component are adjusted up/down by their listed errors. The obtained profile centers are then compared to the nominal one. Table 6.2 summarizes the adjusted components of the beam dump and the resultant shifts of the profile center from the nominal values. In total, a value of 0.38 cm (0.032 mrad) was assigned to the systematic error of the profile center (beam direction)[2].

[2] For this error estimation, we consider an extreme case in which both the density and thickness of one half of each dump component are changed. Even though this is a conservative estimation, the obtained error size here is not dominant one in the total systematic error.

The other source of distortion of the profile is soft secondary particles (δ-rays and γs) from nearby materials. We have evaluated the effect of profile distortion due to surrounding materials in two ways. The muon monitor covers an area of 150×150 cm^2 transverse to the beam-axis while the actual profile width (1σ) of the muon beam is typically 100-110 cm at the monitor when the horns operate at 250 kA. Namely, the muon monitor covers $\sim$50% of the profile region. In order to check how the actual profile deviates from the ideal Gaussian shape, the ionization chamber arrays were moved by $\pm$25 cm to take the tail of the profile into account. Then, the fit was done for the different portions of the same profile. If the profile has a perfect Gaussian shape, the fitted result will always be same at different positions of the array. However, the result showed that there are differences in the fitted values. The maximum differences among the fitted profile centers are 1.25 cm (0.106 mrad) for the horizontal direction and 1.12 cm (0.095 mrad) for the vertical direction. During beam operation, a discrepancy of the profile center has been observed between the chamber and silicon arrays (0.55 cm in the horizontal direction and 1.77 cm in the vertical direction). This discrepancy is considered to be due to the difference of the nearby structures in-between the chamber and silicon arrays, causing the profile to be distorted differently at the chambers and silicon arrays. The structure most likely to cause the discrepancy is the silicon moving stage just behind the silicon array (see right in Fig. 3.1). Figure 6.7 shows the profile center measured by the chamber array during the calibration of the silicon array where the stage of the calibration sensor was moved to be positioned at each of the silicon sensors. When the silicon moving stage is positioned behind the top corner sensors, the profile center in the vertical direction measured by the chamber array shifts by -1.4 cm from the nominal case in which the stage is lowered to the bottom. This suggests nearby materials affect the beam profile at the muon monitor. The shift observed in two condition, 1.25 cm for different chamber array positions and 1.77 cm for the difference in the profile center between the silicon and chamber arrays, are taken as the systematic error. Even though part of the shift may be caused by the dump core structure, we conservatively add these errors since we cannot distinguish the effects.

As discussed in Sec. 5.3, the gain of the sensors are relatively calibrated with a precision of 0.4% for the ionization chambers and 0.1% for the silicon PIN photodiodes. The uncertainty in this calibration was propagated to the error in the beam direction. As a result, 0.08 cm (0.007 mrad) and 0.30 cm (0.026 mrad) for the horizontal and vertical directions respectively, were assigned to the systematic error for the profile center (beam direction).

In conclusion, the total systematic error in the beam direction due to the profile distortion was estimated to be 2.20 cm in the horizontal direction and 2.22 cm in the vertical direction. These correspond to 0.187 mrad (horizontal) and 0.188 mrad (vertical) beam direction errors.

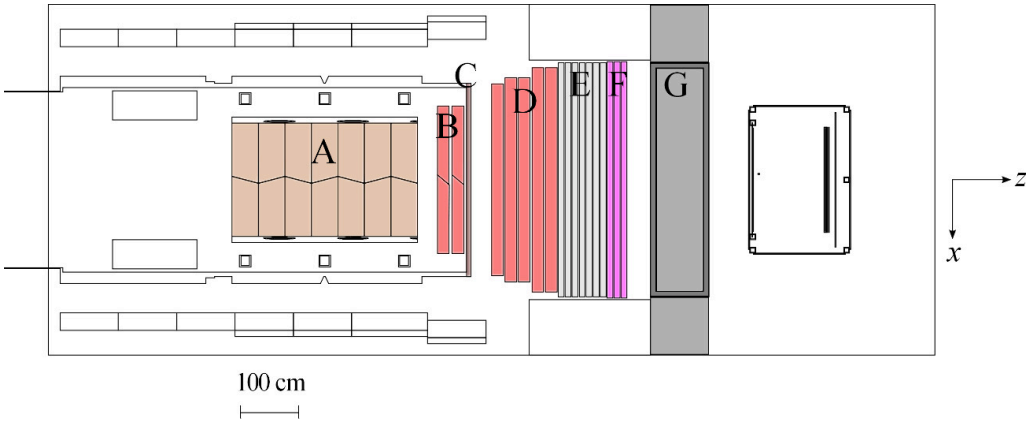

Figure 6.6.: Top view of the beam dump. A: graphite core. B-F: Fe plates. G: concrete wall. The beam enters from the left side.

Table 6.2.: Density (ρ), thickness (d) and their uncertainties of the dump graphite core, Fe plates and concrete wall (see Fig. 6.6). The errors marked with $*$ are obtained from JIS G3193 and the tolerance listed in the document is taken as 3σ error for this analysis. The other errors are from measurements. The shift of the profile center is estimated for the case ρ and d of one half of each component are adjusted by their errors.

	Material	ρ (g/cm^3)	d (cm)	Profile center shift (cm)
A	Graphite	1.707 ± 0.009	45.001 ± 0.003	Negligible
B	Fe	7.83 ± 0.03	$20.00^{+0.24}_{-0.12}$ *	0.107
C	Fe	7.85 ± 0.02 *	$8.00^{+0.17}_{-0.09}$ *	0.054
D	Fe	7.83 ± 0.03	$20.00^{+0.24}_{-0.12}$ *	0.169
E	Fe	7.8435 ± 0.0083	10.083 ± 0.033	0.083
F	Fe	7.85 ± 0.02 *	$10.00^{+0.23}_{-0.11}$ *	0.126
G	Concrete	2.30 ± 0.023	100	0.276
			Total	0.38

6.2.2. Effect of the tilted beamline against the beam dump

The beamline is tilted by 3.637 degrees vertically and the level of the beam dump is even with the ground. (see bottom in Fig. 2.3). This results in asymmetric path lengths of the muons going through the beam dump with respect to the beam-axis. Thus, an asymmetric profile of the muon beam is observed at the muon monitor. This causes 1.35 cm profile center shift in the vertical direction, which was estimated using MC simulation where the center of the proton beam was set to the center of the target and

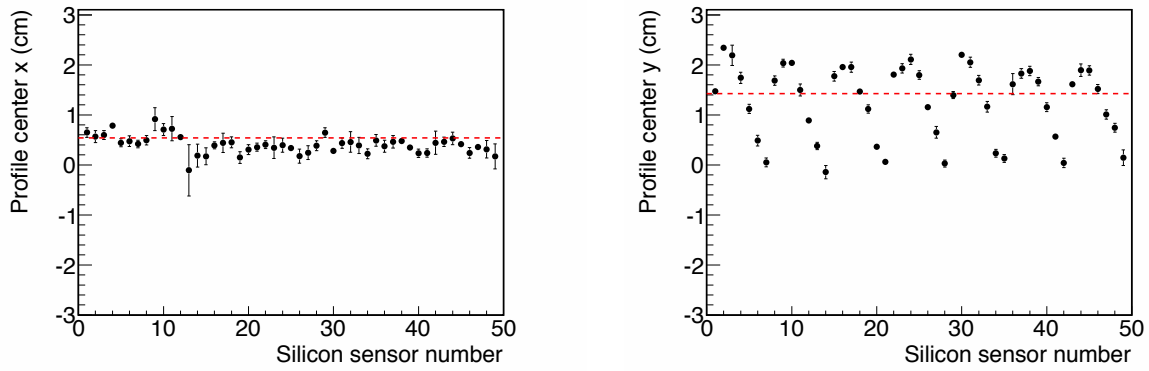

Figure 6.7.: Variation of the muon beam profile center measured by the chamber array during the calibration of the silicon PIN photodiodes. The dashed line shows the profile center for the same beam condition when the silicon moving stage is lowered at the bottom (nominal position).

parallel to the beam-axis. This shift is used for the correction in the beam direction measurement and a MC statistical error of 0.22 cm (0.019 mrad) was assigned to the systematic error of the profile center (beam direction).

6.2.3. Alignment error of the muon monitor

For the systematic error in the beam direction measurement, alignment accuracy between the muon monitor and target is also taken into account. The alignment error mainly comes from the measurement error of the relative position of reference points between the target and muon pit, determined to be 6.1 mm for the horizontal position and 6.3 mm for the vertical position. In addition, alignment error also comes from the setting of the muon monitor (1 mm) and the target (< 1 mm). The total alignment error of the muon monitor relative to the target is therefore 6.3 mm (horizontal) and 6.5 mm (vertical). Thus, the systematic error of the muon beam direction was 0.054 mrad in the horizontal direction and 0.055 mrad in the vertical direction.

6.2.4. Summary of the systematic error on the beam direction measurement

Table 6.3 summarizes the systematic error for each source. Some of these systematic errors may come from the same origin, but we conservatively take quadratic sum of these as the total systematic error. The total systematic error on the measurement of the beam direction was estimated to be 0.28 mrad ($= \sqrt{0.19^2 + 0.20^2}$). Thus, the performance of the muon monitor fulfills our requirement of 0.3 mrad.

Table 6.3.: Summary of the systematic error for the beam direction measurement.

Error source	Profile center		Beam direction	
	Δx (cm)	Δy (cm)	$\Delta\theta_x$ (mrad)	$\Delta\theta_y$ (mrad)
Profile distortion	2.20	2.22	0.187	0.188
Tilted beam	–	0.22	–	0.019
Alignment	0.63	0.65	0.054	0.055
Total	2.3	2.3	0.19	0.20

6.3. Result of beam operation in physics data taking

6.3.1. Stability of the beam direction and intensity

As described in Sec. 6.1.1, the proton beam is tuned using information from the muon monitor and always controlled such that the muon beam and hence the neutrino beam are on the beam-axis. Figure 6.8 (A) shows the stability of the measured total collected charge. The ratio of the total charge collected by the silicon array to that collected by the chamber array is also shown in Fig. 6.8 (B). As seen in the figure, the ratios are different among the run periods. In Run 2, the observed ratio are 3-5% larger than the RUN 1 and RUN 3 periods. This was caused by lower signal of the ionization chamber (see Table. 6.4). Although the signal of the chamber has a dependency on the gas pressure, temperature and any other gas settings, which could affect the signal size, the ratio has been stable for each run period: RUN 1, RUN 2, and RUN 3. The large ratio is observed at the beginning of RUN 4. This is due to the fact that He gas was mistakenly allowed to flow into the chambers where it mixed with the Ar gas. Before a start of RUN 4 operation, all of the silicon PIN photodiodes were replaced with new ones. At the beginning of RUN 4, it was observed that their signal sizes gradually decreased and then stabilized. This also affects the stability of the ratio of the total collected charged around the beginning of the RUN 4 operation and is currently under investigation. The profile center measured by the silicon and chamber arrays is shown in Fig. 6.8 (C) and (D), respectively. In the figure, lines of 0.3 mrad (blue) and 1.0 mrad (pink) represent the requirement for the control of the muon beam direction and the target requirement for the neutrino beam direction in T2K, respectively. As shown in the history of the beam direction, most of the events lie within 0.3 mrad except for RUN 1 and RUN 3b. After the RUN 1 operation, we found that the center position of the muon monitor was mistakenly mis-aligned by -2.5 cm in the vertical direction. This mis-alignment was taken into account for the beam tuning from the RUN 2 operation onwards. The magnetic horns were operated at 205 kA during the RUN 3b operation. During this time the profile center of the muon beam was shifted even though the proton beam was tuned to the center at the target using the correlation obtained at 250 kA operation, which is shown in Fig. 6.2. The reason might be due to a mis-alignment in the horns, which results in

focusing the beam direction in the deviated direction. Since the focusing strength at 205 kA is weaker, a tendency of the deviation could be different between the 205 kA and 250 kA operation. The measured muon beam direction at 205 kA operation is also discussed in Sec. 6.3.3.

The direction and intensity of the neutrino beam have also been measured by INGRID and the result is shown in Fig. 6.9, with the neutrino event rate having been stable over the majority of the run period. Details of the reconstruction of the neutrino eventsand the neutrino beam profile with INGRID are described in Chapter 8 and Appendix C, respectively. As seen in the figure, there is a clear correlation in the vertical beam direction measurement between INGRID and the muon monitor over RUN 1 and RUN 2. As described above, the mis-alignment of 2.5 cm of the muon monitor was not taken into account in the beam tuning during RUN 1. After tuning the proton beam with this correction, both of the measurements then give vertical position close to 0 from RUN 2. On the other hand, the beam direction measured by INGRID shows a different tendency from that of the muon monitor during the RUN 3b operation. As shown in Fig. 5.4, the p-θ phase space of the parent pions contributing to the muon flux at the muon monitor is different from that contributing to the neutrino flux at INGRID. Therefore, the secondaries for the neutrino beam are considered to be focused by horns differently from that for the muon beam. This difference could result in the different tendency in the beam direction observed at INGRID and the muon monitor. However, all of the spills were within 1.0 mrad for both the muon and neutrino beams. In addition, most of the spills were controlled well within our 0.3 mrad requirement.

Table 6.4 summarizes the average and RMS of the spill-by-spill fluctuations of the profile center and total collected charge measured by the muon monitor. At the beginning of the RUN 3b, the horn current were operated at 250 kA and the proton beam intensity was gradually increased from very low value (4.0×10^{11} p.p.b.). This results in a larger RMS of the spill-by-spill fluctuations in the measurement by the chamber array due to the low signal-to-noise ratio. However, this is still within the requirement and we achieved good stability in the beam direction over the entire period. The total collected charge was also kept stable with the RMS less than 1.0% for most of the span of beam operation. The neutrino beam direction measured by INGRID is summarized in Table 6.5. As seen in the table, the neutrino beam direction has been kept within 0.3 mrad.

6.3.2. Resolutions of spill-by-spill measurements for the direction and intensity of the muon beam

The resolution of the variation in the direction and intensity measurement by the muon monitor was estimated by comparing two independent detectors, i.e. the silicon and chamber arrays in order to reduce the effects from intrinsic beam fluctuations. The measurement was done for a short period ($\sim$1 hour) in beam operation, in which beam conditions were stable. For the beam direction, we took the difference in the measured

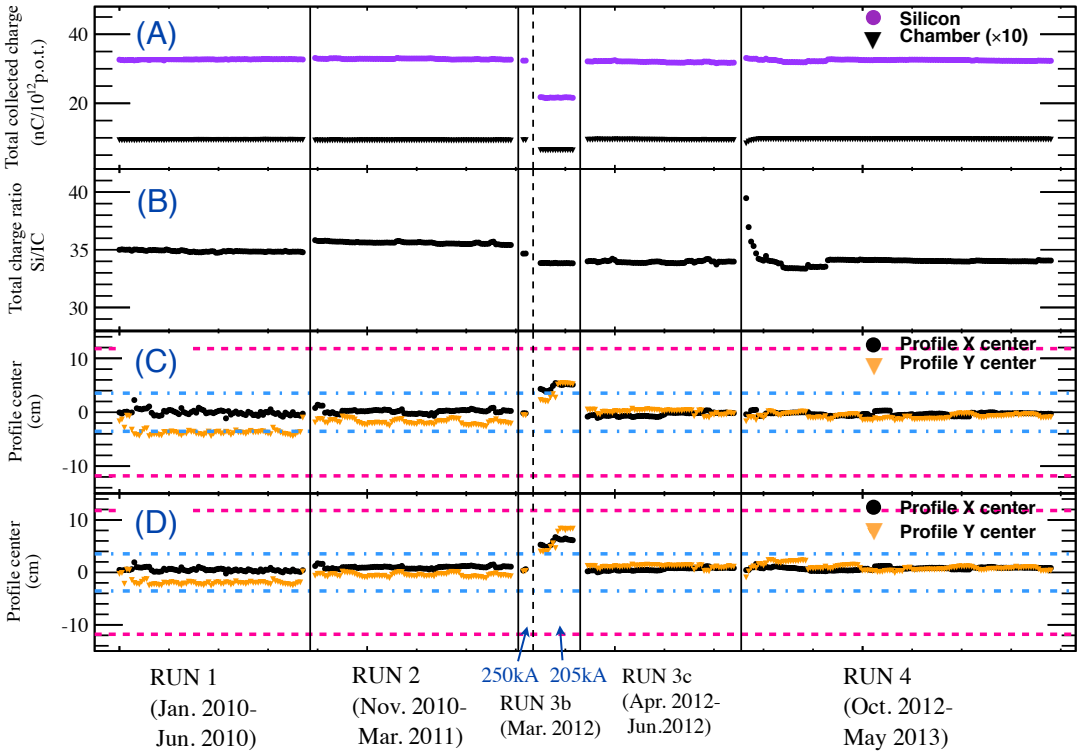

Figure 6.8.: Daily stability of the muon beam measured by the muon monitor. (A): The total collected charges measured by the silicon and chamber (scaled up by a factor of 10) arrays. (B): The ratio of the total charged collected by the silicon array to that collected by the ionization chamber one. (C): The profile center measured by the silicon array. (D): The profile center measured by the ionization chamber array. In the plots (C) and (D), lines of 0.3 mrad (blue) and 1.0 mrad (pink) represent the requirement for the control of the muon beam direction and the target requirement for the neutrino beam direction in T2K, respectively.

profile center between the silicon and chamber arrays (see left in Fig. 6.10). For the beam intensity, we took a ratio of the total collected charge measured by the silicon array to that measured by the chamber array (see the right in Fig. 6.10). The resolution obtained in this way are actually a (quadratic) sum of those from the ionization chamber and silicon sensors. As the size of a signal from the silicon array is 34 times larger than that from the ionization chambers (see Table 6.4), the resolution at lower intensity is limited by the resolution of the ionization chambers. The resolutions become better as the proton beam intensity increase. For the beam intensity above 0.5×10^{13} p.p.b., resolutions of < 3.0 mm for the beam direction and $< 0.1\%$ for the beam intensity are achieved.

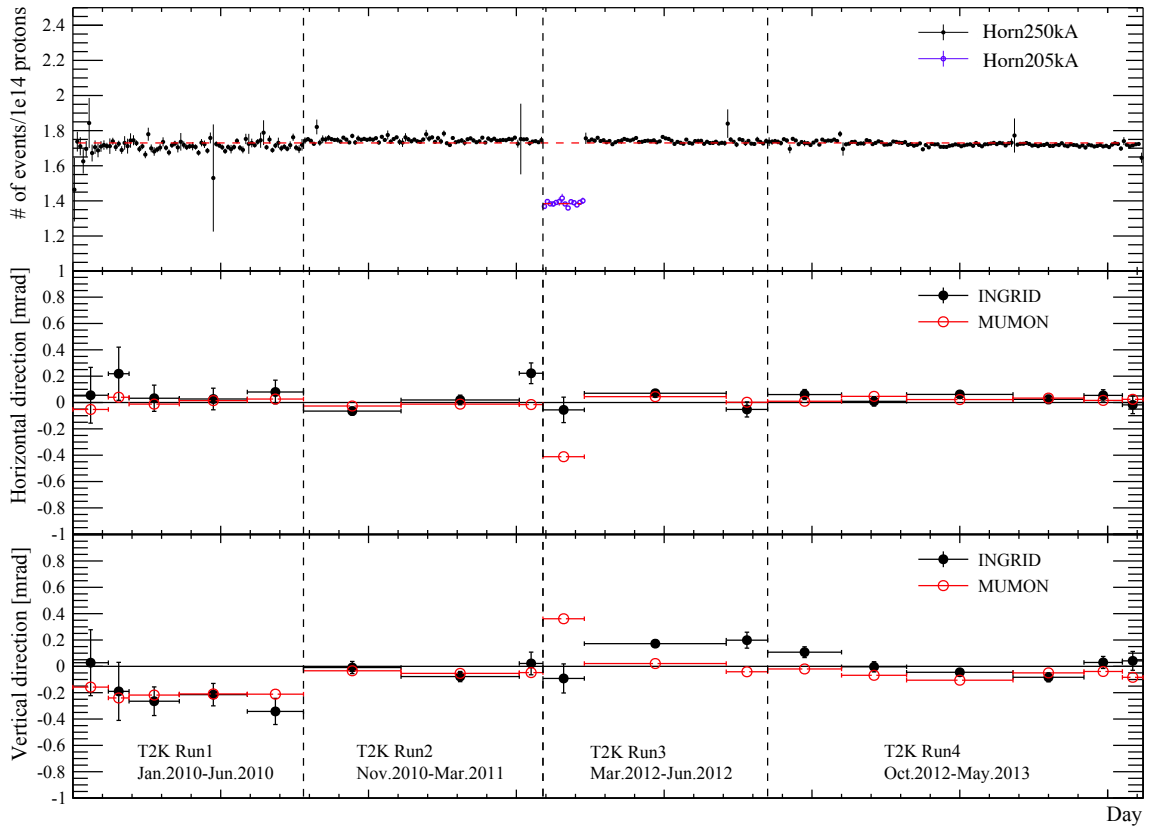

Figure 6.9.: Top: Neutrino event rate per 10^{14} p.o.t. measured by INGRID (points) with the mean value (dashed line). Middle and Bottom: Beam direction measured by the muon monitor (red open circle) and INGRID (black circle) in the horizontal and vertical direction respectively. The error bar represents the statistical error. In this figure, a sign is reversed for the horizontal direction measured by the muon monitor so that the x-coordinate for the muon monitor matches that for INGRID.

Table 6.4.: Average beam profile center and total collected charge as measured by the muon monitor for each T2K run period. The numbers in parentheses denote the RMS of the spill-by-spill fluctuations.

	Silicon array			Ionization chamber array		
	Profile center		Total collected charge	Profile center		Total collected charge
Period	X (cm)	Y (cm)	(nC/10^{12} p.o.t.)	X (cm)	Y (cm)	(nC/10^{12} p.o.t.)
RUN 1	-0.1 (0.62)	-3.8 (0.53)	32.7 (0.7%)	0.4 (0.47)	-2.0 (0.47)	0.939 (0.7%)
RUN 2	0.2 (0.42)	-1.9 (0.48)	32.8 (0.8%)	1.0 (0.45)	-0.5 (0.46)	0.922 (0.7%)
RUN 3b (250 kA)	-0.2 (0.19)	-0.6 (0.19)	32.4 (0.5%)	0.5 (3.06)	0.2 (2.01)	0.934 (1.6%)
RUN 3b (205 kA)	4.8 (0.60)	4.2 (1.52)	21.7 (0.7%)	5.9 (1.11)	6.7 (2.18)	0.640 (0.7%)
RUN 3c	-0.4 (0.38)	0.1 (0.41)	32.0 (0.7%)	0.6 (0.44)	1.1 (0.46)	0.942 (0.6%)
RUN 4	-0.3 (0.33)	-0.8 (0.47)	32.4 (0.8%)	0.8 (0.34)	0.9 (0.66)	0.954 (1.0%)
Total (250 kA)	-0.2 (0.47)	-1.2 (1.30)	32.5 (1.2%)	0.7 (0.45)	0.3 (1.23)	0.943 (1.5%)
(250 kA+205 kA)	0.0 (1.02)	-1.0 (1.63)	-	0.9 (1.05)	0.5 (1.7)	-

Table 6.5.: Neutrino beam direction measured with INGRID for each T2K run period. Only the statistical errors are shown. The X coordinate is opposite to that for the muon monitor.

	X (mrad)	Y (mrad)
RUN 1	0.057 ± 0.049	-0.250 ± 0.052
RUN 2	0.011 ± 0.026	-0.041 ± 0.028
RUN 3b	-0.056 ± 0.097	-0.092 ± 0.110
RUN 3c	0.049 ± 0.023	0.177 ± 0.025
RUN 4	0.043 ± 0.015	0.013 ± 0.016

6.3.3. Muon beam direction at 205 kA operation

In order to understand the large shift of the muon beam direction during the 205 kA operation, we scanned the proton beam at the target and compared the result with that obtained during 250 kA operation. Figure 6.11 shows the correlation between the profile center at the silicon array and the proton beam position at the target. As seen in the figure, the correlation is negative at the 250 kA operation, whereas it is positive at the 205 kA operation. The reason is considered as follows. An off-center proton beam produces secondary particles asymmetrically with respect to the beam-axis because of different path lengths through the target. In the case of 0 kA horn current setting, particles emitted to the direction opposite to the proton beam displacement are more absorbed in the target (see left in Fig. 6.12). The muon beam would then be biased towards the proton beam displacement side, resulting in the positive correlation. When the horn currents are turned on and the focusing becomes stronger, particles emitted to the same direction as the proton beam displacement experience a Lorentz force longer.

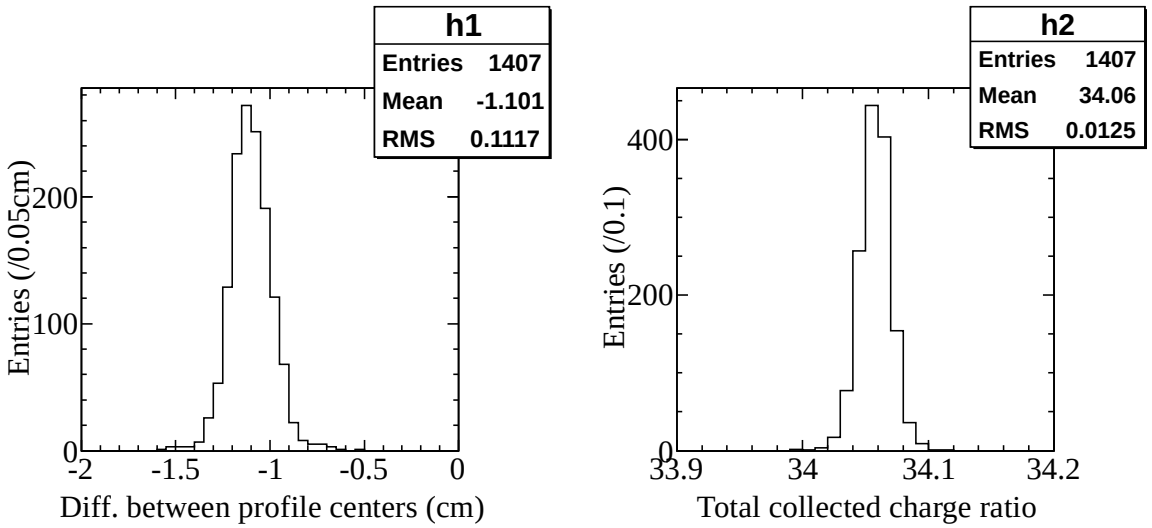

Figure 6.10.: Resolution obtained as the variation in the direction (left) and intensity (right) measurement by the muon monitor. For the beam direction, the differences in the measured profile center between the silicon and chamber arrays are plotted. For the beam intensity, we took a ratio of the total collected charge measured by the silicon array to that measured by the chamber array. These results were obtained using beam data with 1 hour operation and 1.3×10^{13} p.p.b. of the proton beam intensity.

This results in the negative correlation between the profile center at the muon monitor and the proton beam position at the target (see right in Fig. 6.12). The MC simulation was also used to confirm the dependence of the profile center position of the muon beam on the proton beam position at the target with different horn currents. The result also showed the correlation is positive at the 205 kA operation. In addition, correlation is lost for some horn current value between 205 kA and 250 kA. This means that it is impossible to conduct the physics data-taking for some horn current between 205 kA and 250 kA since the profile center of the muon beam is no longer sensitive to the proton beam position at the target at those horn currents.

6.3.4. Summary of the beam operation

The muon monitor performs the spill-by-spill measurement of the muon beam with good resolution, which enables us to keep the beam stable and control the direction within 0.3 mrad for most of the span of beam operation. Thus, the neutrino beam direction has also been kept stable within 0.3 mrad and this was, indeed, confirmed by the INGRID measurement. These beam measurements provided by the muon monitor have guaranteed good quality beam data for use as an input to the neutrino oscillation measurements.

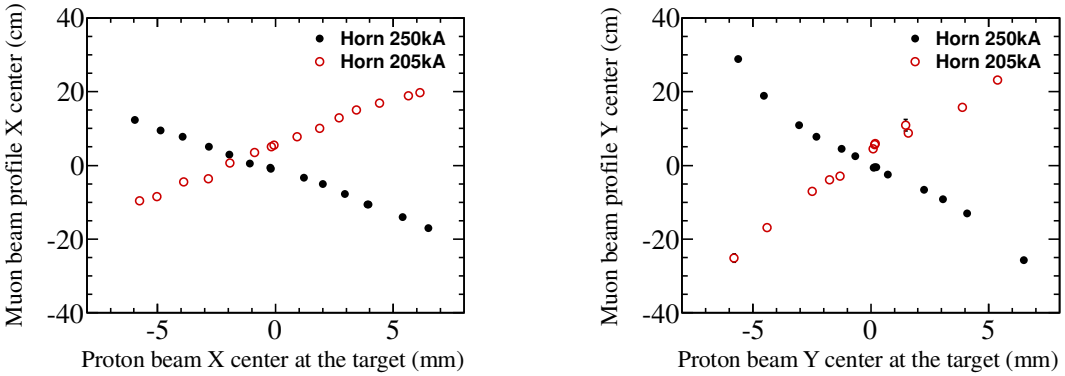

Figure 6.11.: Correlation between the profile center at the silicon array and the proton beam position at the target for the 250 kA (black) and 205 kA (red) operation.

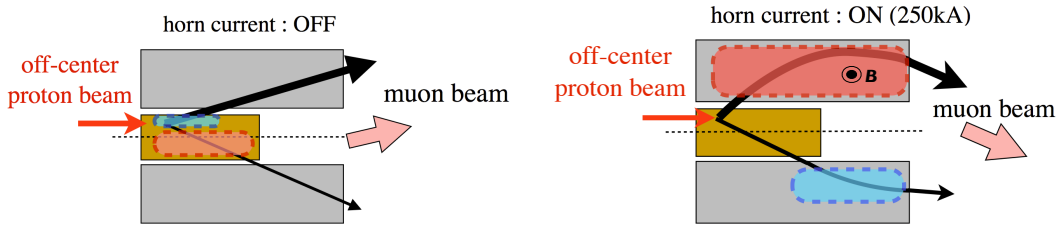

Figure 6.12.: Explanation of changes in the direction of the muon beam when the horn current is turned off (left) and on at 250 kA (right).

6.4. Measurement of the absolute muon flux

6.4.1. Absolute muon yield measurement by emulsion detector

The particles arriving at the muon monitor are expected to be a mixture of muons and some lower energy components, namely electrons and gammas as shown in Table 5.2. Since the standard detectors of the muon monitor, the silicon detectors and the ionization chambers, are designed to obtain the profile of the muon beam by measuring the integrated ionization in their active volumes, the measured profile is a convolution of all components in Table 5.2. In order to ensure that the beam flux arriving at the muon monitor is composed of muons, it is very important to measure the absolute muon flux at the muon monitor and to compare it with the prediction. Namely, the understanding of the absolute muon flux is important for understanding the detector response of the muon monitor and, therefore, to verify its use for proton beam control. In order to complement the muon monitor measurement and to diagnose the absolute muon flux, a set of emulsion detectors was temporarily inserted during the period of commissioning.

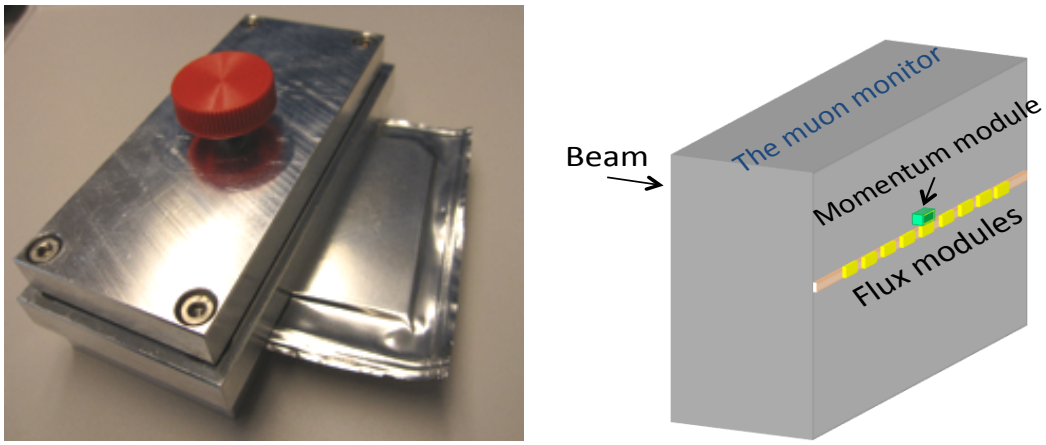

Figure 6.13.: Left: A picture of flux module with 8 emulsion films vacuum-packed in an aluminum laminated film and a mechanical support to keep high flatness. Right: Schematic of emulsion detector setup.

The emulsion detector has a high spatial resolution, down to tens of nano-meters, allowing a 5D reconstruction of particle trajectories, 3 positions (X, Z, Y) and 2 angles ($\tan\theta_x$, $\tan\theta_y$), for particle densities of up to 10^6 particles/cm^2. Furthermore, by employing a proper detector structure, it can successfully reject the low energy components with their multiple Coulomb scattering inside the detector materials.

The emulsion film used for this measurement is the recent standard emulsion film, so-called OPERA film [68], which has two sensitive 44 μm emulsion layers on both sides of a plastic base (205 μm thick) and the thickness of the film in terms of radiation length is 0.003 X_0. In order to reduce the background tracks accumulated in the emulsion film, a *refreshing* treatment [68] was previously applied. An emulsion detector module (see left in Fig. 6.13) consists of eight 6 cm $\times$ 5 cm films. A horizontal array of seven modules (separated by 25 cm) centered on the neutrino beam-axis just downstream of the muon monitor ionization chambers measures the absolute muon yield as shown on the right in Fig. 6.13.

The data readout of the emulsion films is performed with the OPERA scanning microscopes [69] and the tracks crossing several films are reconstructed by the FEDRA emulsion data analysis framework [70].

The performance of the detector module for the flux measurement is also checked with a Geant4-based MC simulation (G4). The flux input, described in Sec. 6.4.2, is propagated through the detector by G4 with the detection efficiency described later.

The energy distributions of the input fluxes and the reconstructed particles are shown in Fig. 6.14 on the left. An application of the angular acceptance of $\tan\theta < 0.3$ (where θ is the angle from the normal vector of the film surface) can effectively reduce the low energy components because the track angles of low energy components have less

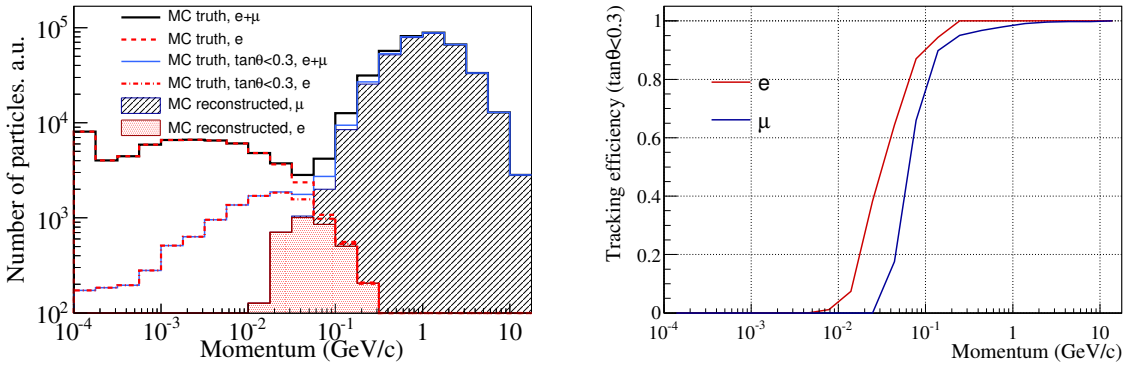

Figure 6.14.: Left: Momentum distribution of the input fluxes and the reconstructed particles. The true distribution for the electron+muon and electron are shown as black solid and red dashed lines, respectively. The true distribution for electron+muon and electron with an angular acceptance cut ($\tan\theta$ <0.3) are shown as blue solid and fine dashed lines, respectively. The reconstructed distributions for muon and electron are shown as stacked histograms with black and red, respectively. Right: Tracking efficiency for electron (red) and muon (blue) in the angular acceptance of $\tan\theta < 0.3$.

correlation with the beam angle. The reconstructed tracks which have at least 4 hits out of 8 films, with the most upstream hit existing among the first 4 films are selected for the flux measurement, and shown as a filled stacked histogram; the additional reduction of low energy components is achieved via their multiple Coulomb scattering in the 8 films by requesting a stringent angular matching between the films. The track reconstruction efficiencies for muons and electrons are given in Fig. 6.14 on the right, as a function of their momenta. The overall detection efficiency for muons is estimated to be 98.0% with respect to the muons in the angular acceptance or 94.2% for muons in all angular space. The contamination by electrons is expected to be as small as 1.0% with respect to the number of muons reconstructed in the angular acceptance, which is estimated from the MC simulation.

The emulsion detectors were exposed to a low intensity beam twice with the different horn current settings, see Table 6.6. In the table, we assign 2.6% error on the p.o.t. measurement, which is determined from calibration accuracy of the beam monitor and uncertainty in the analysis technique. The films were then photo-developed.

For each film, the data is taken from a 2 cm^2 area at the center of film. The relative alignments between the films are found by using the beam tracks themselves with sub-micron precision. After the track reconstruction, an effective area of 1 cm^2 at the center of film is used to compute the flux and an angular acceptance ($\tan\theta < 0.3$) is applied. An example of the reconstructed tracks is shown in Fig. 6.15 on the left, and the angular distribution on the right.

Table 6.6.: Horn current, the number of spills, and p.o.t. for each exposure time. A systematic error of 2.6% is assigned to the p.o.t. measurement, which is determined from calibration accuracy of the beam monitor and uncertainty in the analysis technique.

Exposure	Horn current	# of spills	($\times 10^{11}$) p.o.t
A	250 kA	1	1.95 ± 0.05
B	0 kA	2	$1.98 + 1.95 = 3.93 \pm 0.10$

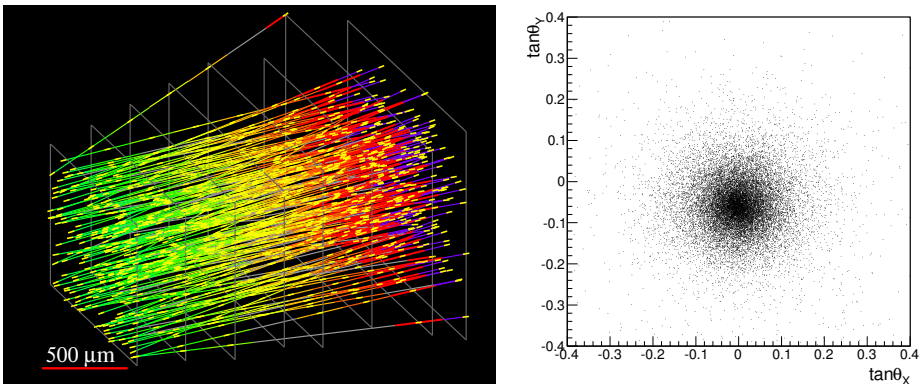

Figure 6.15.: Left: Example of reconstructed tracks entering a 1×1 mm^2 surface in the center module when the horn is operated at 250 kA. The color of lines shows the depth in the module. Right: The measured angular distribution in the same detector. Each dot corresponds to the individual track angle.

The detection efficiencies of each film and module are measured using the reconstructed tracks in the module, counting the number of missing hits in the film for the tracks crossing the film, these are shown in Fig. 6.16. The tracking efficiency of each module is then computed by taking account of the efficiencies of individual films in the module and the track selection criteria with the angular acceptance. Since a track can be reconstructed if it has at least 4 hits out of 8 films, the tracking efficiency is higher than the single film efficiencies.

The tracking efficiencies for high energy particles, where multiple Coulomb scattering does not contributes towards the inefficiency, are calculated to be higher than 99.5% for all modules. The flux data is corrected by the tracking efficiency module-by-module and used in later analysis.

For each flux module, we add the systematic uncertainty of 2% which was estimated from the measurement reproducibility test[3]. The flux data is then fitted with a Gaussian function as shown in Fig. 6.17. The muon fluxes at the profile center are obtained as $(1.09 \pm 0.01 \pm 0.03) \times 10^4$ tracks/cm^2/4×10^{11} p.o.t. when the horns are not operated and $(4.06 \pm 0.05 \pm 0.10) \times 10^4$ tracks/cm^2/4×10^{11} p.o.t. when the horns are operated

[3]Two flux modules were placed one after the other and exposed to the beam. The difference of number of muons between those modules was assigned to the systematic error.

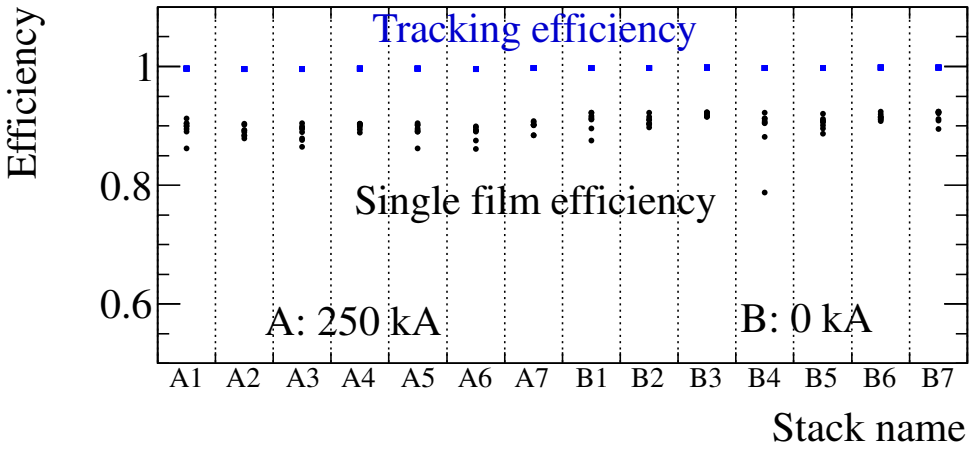

Figure 6.16.: Single film and tracking efficiencies for all films and modules. The efficiency is computed using all tracks with the angular acceptance of $\tan\theta < 0.3$.

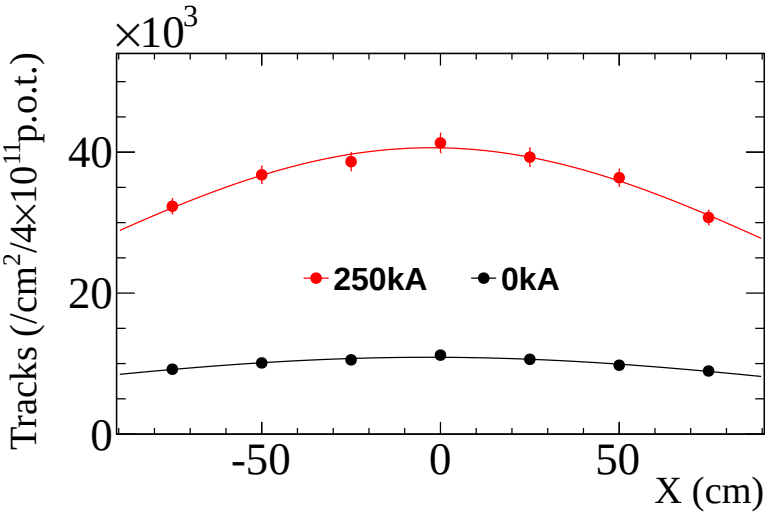

Figure 6.17.: Measured muon fluxes for the 250 kA (red) and 0 kA (black) operation. Fitted lines are represented as solid curves. Error bars denote statistical and systematic ones.

at 250 kA. Here the first error denotes the error in the flux measurement due to the statistical error and the systematic uncertainty for each module. The second comes from the systematic uncertainty in the p.o.t measurement (2.6%). The 1σ widths of the flux profiles are measured to be 122.4± 6.5 cm and 105.6 ± 4.1 cm, respectively. The obtained fluxes and profiles are compared to the predictions and the result is shown in Table 6.9.

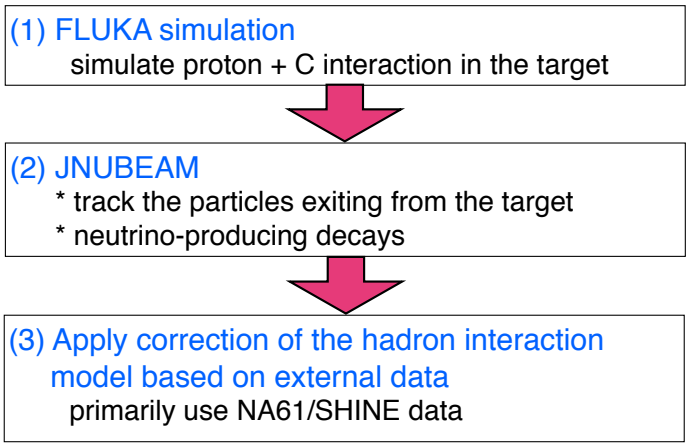

Figure 6.18.: Flow diagram of the flux prediction.

6.4.2. Comparison of the muon yield with prediction based on tuned-simulation

As described in Sec. 5.2, T2K uses FLUKA2008 for the simulation of the hadronic interaction in the graphite target and the kinematic information for the particles is then transferred to the JNUBEAM simulation. Hadronic interactions in the JNUBEAM simulation are treated with GCALOR. For a precise prediction of the neutrino and muon flux, T2K corrects the model based on hadron interaction data provided by external experiments, primarily relying on the NA61/SHINE measurements [71]. A flow diagram for the precise estimation of the muon flux is shown in Fig. 6.18. This section first describes how the muon flux is predicted. Systematic errors of the prediction are then summarized. Finally, the result is compared with the measurement from the emulsion data.

Correction of the muon flux

In order to make a prediction based on the external hadron-interaction data, we use the method developed for the T2K flux prediction [42]. Here, we briefly summarize the procedure. The following quantities modeled in FLUKA2008 and GCALOR are corrected based on the external data,

1. interaction rates for p, $\pi^{\pm}$ and $K^{\pm}$, and
2. differential production of $\pi^{\pm}$, $K^{\pm}$ and K^{0}_{L} in the interaction of protons on the target.

The NA61/SHINE measurement provides both the differential production and the interaction rate [72, 73], which are primarily used for the prediction of the neutrino and muon flux. Other experimental data are used to compensate for the measurement of NA61/SHINE [74–76].

The hadronic interaction rate is given by a so called production cross section ($\sigma_{\rm prod}$) which is calculated by subtracting the cross section for the quasi-elastic scattering process ($\sigma_{\rm qe}$) from the total inelastic cross section ($\sigma_{\rm inel}$):

$$\sigma_{\rm prod} = \sigma_{\rm inel} - \sigma_{\rm qe} \tag{6.1}$$

Most of the data provides $\sigma_{\rm inel}$. In order to extract $\sigma_{\rm prod}$, $\sigma_{\rm qe}$ is estimated from hadron+nucleon scattering data using a method based on [77] and is subtracted from $\sigma_{\rm inel}$. The production cross section is also estimated from both FLUKA2008 and GCALOR. The simulated cross sections are then compared to the data. The prediction of FLUKA2008 was found to be in good agreement with the data. Therefore, the correction of $\sigma_{\rm prod}$ using the data is applied only for GCALOR.

Figure 6.19 shows the phase space of the parent π^+ contributing to the muon flux at the muon monitor when the horn currents are set at 250 kA (left) and 0 kA (right). Most of the phase space is covered by the NA61/SHINE data for the 250 kA operation. When the horns are operated at 0 kA, the coverage by the NA61/SHINE data falls in 30%. Most of the K^+s contributing to the muon flux are not covered by the NA61/SHINE data [4]. The differential production cross section depends on the incident particle momentum, p_{in}, and target nucleus, A. For secondary $\pi^{\pm}$s produced by 31 GeV/c protons in the phase space covered by NA61/SHINE data, corrections are directly applied using the NA61/SHINE data. The corrections for tertiary pion production from secondary particles and for the production at materials (A) other than graphite are obtained with extrapolations from the NA61/SHINE data assuming momentum and A-dependent scaling [77–80].

The correction for the production of K^+ and K^- in the phase space not covered by the NA61/SHINE data is estimated with other experimental data [74, 75]. For the hadrons in phase space uncovered by any experimental data, the corrections are no longer applied.

As a result of the correction the absolute muon flux is increased by about 20% (1.9% by the production cross section, 14.8% by the pion and 3.1% by the kaon production tuning).

Systematic error on the flux prediction

The systematic error on the muon flux prediction originates from uncertainty in the hadron production and measurement error of the proton beam, horn current, and alignment of the target. A detailed description of the estimation for the flux uncertainties can be found in [42]. This section briefly explains the flux error sources and methods to estimate the errors.

[4] The correction of the flux was performed using results from the NA61/SHINE measurement in 2007. NA61/SHINE also collected data in 2009, where statistics increased by an order of magnitude as compared to the 2007 data and a phase space coverage was enlarged. Therefore the flux is expected to be predicted more precisely with the 2009 data.

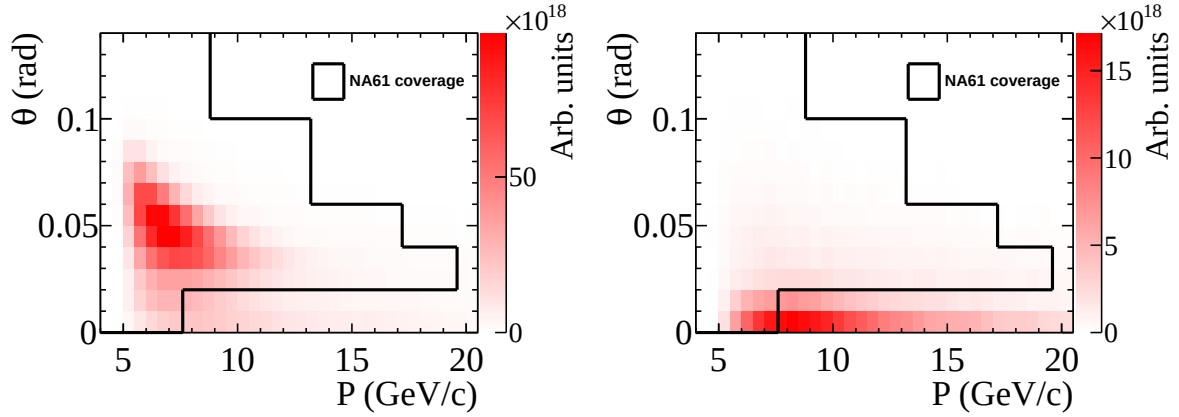

Figure 6.19.: Phase space of the parent π^+s contributing muon flux at the muon monitor when the horn currents are operated at 250 kA (left) and 0 kA (right). The same p.o.t (=4.0×10^{11} p.o.t.) is used for the normalization in both the left and right plots. The measurement of NA61/SHINE in 2007 covers the left sides in the figures. Different scales are used for the z-axes in these two figures.

Uncertainty in the hadron production

The systematic error on the production cross section is dominated by the uncertainty of the quasi-elastic subtraction. This assumption is based on discrepancies in the production cross section data among data sets [42].

The systematic error of the pion or kaon differential production comes from:

1. measurement error of the pion/kaon differential production,
2. uncertainty in the momentum or target scaling,
3. uncertainty from the pion/kaon production in the phase space not covered by data.

In addition to uncertainties listed above, the systematic error on the muon flux also arises from uncertainty in secondary nucleon production. The error is primarily estimated using other experimental data sets [74, 75]. For the secondary nucleon production by protons with a small momentum transfer, we assign 100% error due to the lack of relevant data.

The muon flux is also produced by the decay of the mesons which are generated at the beam dump (C) and this contributes about 4% of the total flux as shown in Table 5.5. We have not corrected the hadronic interaction at the beam dump because of the small contribution to the total interactions. When it is corrected, it results in decrease of the muon flux by 0.7%. The change of 0.7% is assigned to the systematic error on the muon flux.

Table 6.7.: Systematic errors on the muon flux due to uncertainty in the hadron production.

Error source	Error size
Pion production	9.0%
Kaon production	1.3%
Production cross section	9.1%
Secondary nucleon production	3.6%
Dump interaction	0.7%
Decays from Λ, Σ, and quaternary particles	1.2%
Total	13.4%

The muon flux is also generated from decays of Λ, Σ or other particles whose productions are not corrected. According to the MC simulation, 0.6% of the muons come from such particles. Since there is no relevant data for such production, we conservatively assign a 100% error to the production in these cases. In addition, 0.6% of muons come from decays of quaternary particles, which are not corrected at this stage because of the small contributions to the muon flux. A 100% error is conservatively assigned in this case.

In total, we attribute 13.4% of the systematic error in the muon flux to uncertainty in the hadron production and summarize those errors in Table 6.7.

Uncertainty in the proton beam measurement

The trajectory and optics of the proton beam are measured by the proton-beam monitors placed in the primary beam line. In the MC simulation, the parameters of the proton beam are varied within those errors attributed to the measurement errors from the proton beam monitors. The resultant variation of the muon flux (0.9%) is then estimated at the muon monitor and is taken as the systematic error on the muon flux.

Uncertainty in the absolute horn current

During beam operation, the monitored values of the horn current were found to drift by up to 2%, 5 kA. The drift is considered to be mainly due to the temperature dependence in the hardware monitoring. In the MC simulation, the horn currents are varied by 5 kA from the nominal values (=250 kA). The variation of the muon flux, 3.6%, is then taken as the systematic error on the muon flux.

Uncertainty in the target alignment

The rotation of the target with respect to the horn-axis was surveyed and was measured to be 1.3 mrad (0.1 mrad) in the horizontal (vertical) direction. The effect of the target alignment is estimated by rotating the target in the simulation according to the measured values described above. The resultant variation of the muon flux, 0.5%, is assigned to the systematic error.

Table 6.8.: Summary of the systematic error on the absolute muon flux.

Error source	Error size
Hadron production	13.4%
Proton beam	0.9%
Absolute horn current	3.6%
Target alignment	0.5%
Horn skin effect	2.0%
MC statistics	0.3%
Total	14.1%

Skin effect in the magnetic horns

Since the horn current is applied as pulses of about 1 ms, the current would flow only around the surface of the conductor due to the skin effect. However, the present MC simulation assumes a flat current density. To estimate the size of the skin effect, the magnetic field in the simulation is modified by taking the skin depth into account. The modification results in decreasing the muon flux by 2.0%. The change is assigned to an additional systematic error.

Summary of the systematic error on the absolute muon flux

Table 6.8 summarizes the systematic error on the absolute muon flux prediction. Finally we assigned a total of 14.1% error to the absolute muon flux. In the case of 0 kA horn current setting, the systematic error cannot be fully evaluated because the phase space of pions (kaons) is poorly covered by data. This may result in a large error size for the muon flux. From these reasons, we evaluated the systematic error only for the 250 kA operation.

Comparison with the emulsion measurement

Figure 6.20 and Table 6.9 show the comparison between the measurement and prediction for the reconstructed profile of the muon flux at the emulsion detector, where the hadron production is corrected as described in Sec. 6.4.2. In the case of the 250 kA operation, the ratio of the measured muon flux to the prediction is 0.97 ± 0.14. The data and prediction agrees quite well. The measured muon profile by the emulsion and the prediction are also in agreement within those error sizes. In case of the 0 kA operation, there is about a 10% discrepancy in the flux between the measurement and prediction. This is because the phase space of secondary pions contributing to the muon flux at the emulsion is less constrained by the external data. In summary, the measured absolute muon flux and profile are consistent with the predictions for the 250 kA horn setting, which supports our understanding of the muon, and hence neutrino, production for physics data taking at 250 kA operation.

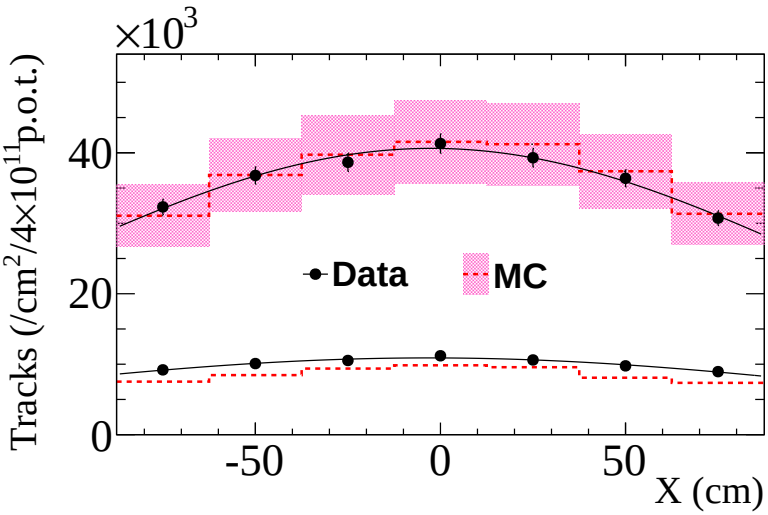

Figure 6.20.: Comparison of the reconstructed fluxes at the emulsion between the measurement and prediction for the 250 kA (top) and 0 kA (top) operation. The error band represents the uncertainty of the flux prediction at 250 kA and is not drawn for the prediction at 0 kA.

Table 6.9.: Comparison of the reconstructed flux at the emulsion detector between the measurement and prediction. The fluxes are normalized to 4×10^{11} p.o.t. For the measured flux, the first error is due to the statistical error and the systematic uncertainty of each module and the second one comes from the 2.6% systematic uncertainty of the p.o.t measurement.

	0 kA			250 kA		
	flux tracks /cm^2	flux ratio (Data/MC)	fitted profile width (cm)	flux tracks /cm^2	flux ratio (Data/MC)	fitted profile width (cm)
Data	$10892 \pm 126 \pm 283$	-	122.4 ± 6.5	$40628 \pm 468 \pm 1056$	-	105.6 ± 4.1
T2K MC	9682	1.12	100.3	41833 ± 5898	0.971 ± 0.140	98.7

6.5. Summary of the muon beam measurement

Through Chapter 5 and this chapter, we described the properties of the muon beam measured by the muon monitor and the emulsion detector. The systematic error of the beam direction measurement with the muon monitor was estimated to be 0.28 mrad. This fulfills our requirement of < 0.3 mrad. The result of the measurement of the muon beam profile center for the entire run period is (X,Y) = $(0.0 \pm 2.3, -1.0 \pm 2.3)$ cm, and its root mean square (RMS) of the spill-by-spill fluctuation is (X,Y) = $(1.0, 1.6)$ cm. The result of measurement of the total collected charge for 250 (205) kA horn operation is 32.5 (21.7) nC/10^{12} p.o.t., and its RMS of the spill-by-spill fluctuation is 1.2% (0.7%). Here

we quote the results from the measurement of the silicon array. Accordingly, we have controlled the muon beam direction within 0.3 mrad with the muon monitor for most of the span of beam operation. The total collected charge is also kept stable with the RMS of 1%. Thus, the neutrino beam direction has also been kept stable and controlled within 0.3 mrad with respect to the designed beam-axis, guaranteeing good quality beam data. The absolute muon flux was measured with the emulsion detector and compared with the prediction in order to confirm the detector response of the muon monitor and hence to verify the beam control by the muon monitor. As a result, we obtained good agreement between the data and prediction. This result supports our understanding of the detector performance of the muon monitor and confirms the validity of the beam control by the muon monitor.

Part IV.

Neutrino-nucleus CC inclusive cross section on iron

Chapter 7

Charged current neutrino-nucleus interaction

From this chapter, we report the measurement of the CC inclusive ν_μ cross section on iron. The measurement is conducted using the T2K neutrino beam, which is well controlled and understood by the measurements of the muon monitor.

CC total (or CC inclusive) cross section is a sum of several CC interaction modes. A summary of the CC inclusive cross section measurements is shown in Fig. 7.1. In this section, each CC interaction mode is briefly explained in Sec. 7.1 - 7.4. Section 7.5 introduces one of the neutrino event generator, NEUT, which is primarily used in the T2K experiment. Then, the importance of the measurement of the CC inclusive cross section is discussed in Sec. 7.6. Finally, the measurement of the CC inclusive cross section on iron, is introduced in Sec. 7.7 with our motivation of the measurement.

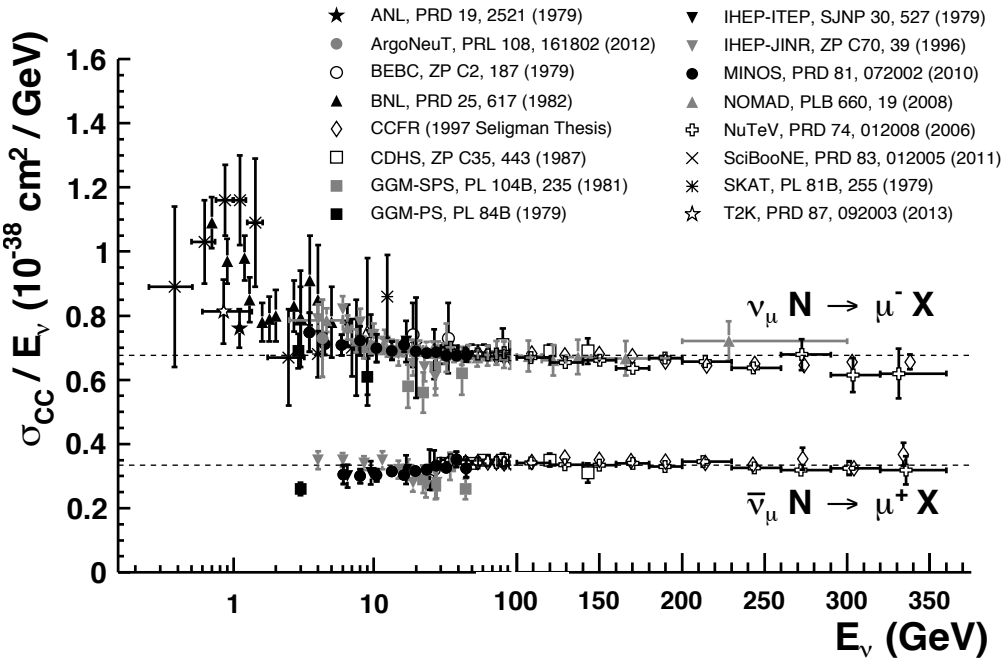

Figure 7.1.: Summary of measurements of ν_μ and $\bar{\nu}_\mu$ CC inclusive scattering cross section divided by neutrino energy. This figure is taken from [81].

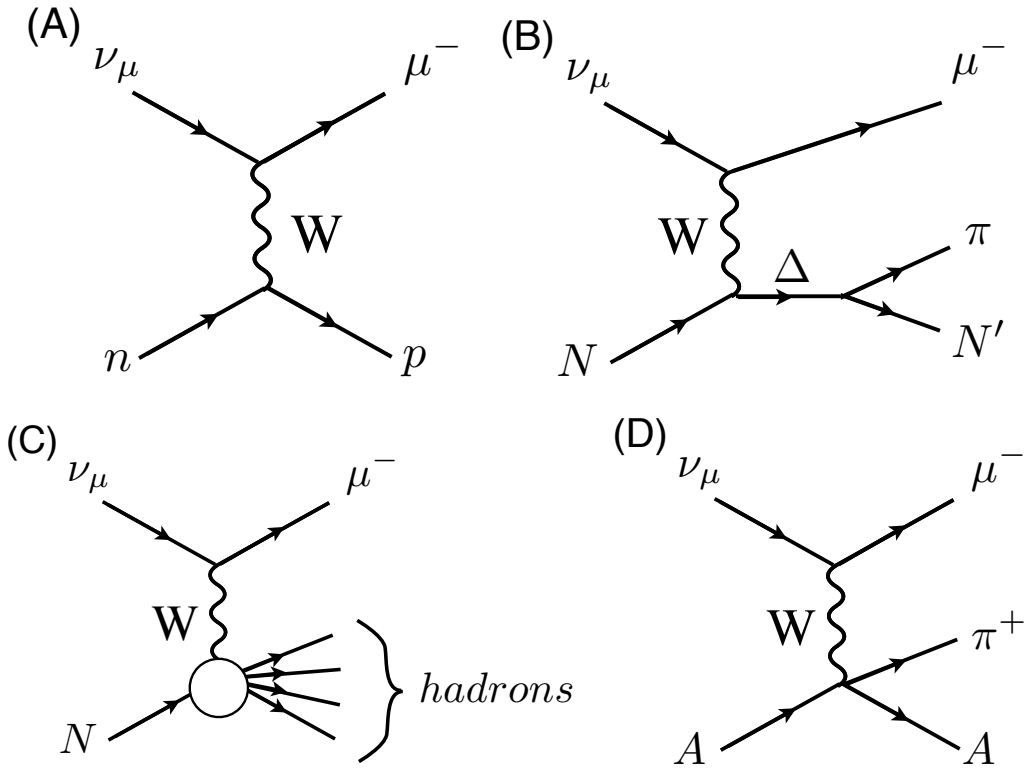

Figure 7.2.: Diagrams of ν_μ CC interactions. (A) CCQE ($\nu_\mu + n \to \mu^- + p$). (B) CC1$\pi$ ($\nu_\mu + N \to \mu^- + \Delta \to \mu^- + \pi + N'$). (C) CC DIS ($\nu_\mu + N \to \mu^-$ + hadrons). (D) CC coherent pion production ($\nu_\mu + A \to \mu^- + \pi^+ + A$). Here N and A represent the nucleon and nucleus, respectively.

7.1. Charged current quasi-elastic scattering: CCQE

CCQE ($\nu_\mu + n \to \mu^- + p$) is a two body reaction (Fig. 7.2 A) and is used as a signal mode in the T2K experiment. In this reaction, the target nucleons (neutrons) are bound inside the nuclei.

We consider a muon neutrino in the energy region of sub-GeV interacts with a neutron for the cross section of CCQE. In this energy region, the 4-momentum squared, defined in the following equation, transferred to the nucleon is much smaller than the intermediate vector boson mass:

$$q^2 \equiv (E_\mu - E_\nu)^2 - (\vec{P_\mu} - \vec{P_\nu})^2 \,, \tag{7.1}$$

where $E_\nu(E_\mu)$ and $P_\nu(P_\mu)$ are the energy and momentum of the incoming neutrino (outgoing muon), respectively. Under this condition, the cross section can be calculated

to be

$$\frac{d\sigma}{dq^2} = \frac{1}{32\pi}\frac{1}{E_\nu^2 m_n^2} G_F^2 \cos^2\theta_c L_{\alpha\beta} H^{\alpha\beta} \ , \tag{7.2}$$

where m_n is neutron mass; E_ν is incoming neutrino energy; $L_{\alpha\beta}$ and $H^{\alpha\beta}$ are the leptonic and hadronic tensors, respectively. H represents the structure of the neutron and it contains six form factors: F_S, F_V, F_T, F_P, F_A, and F_M. F_S and F_T are known as scalar and tensor form factors, respectively, and these are vanished on the assumption of T invariance and charge symmetry. F_P is a psudo-scalar tensor. This factor is always multiplied with m_μ^2 (a squared mass of muon) and is negligible for higher neutrino energy. Therefore, H can be expressed by the vector (F_V), axial-vector (F_A), and weak magnetism (F_M) form factors. Using Eq. (7.2) and assumption described above, the CCQE cross section is calculated to be [82]

$$\begin{aligned}\frac{d\sigma}{dq^2} =& \frac{G_F^2}{4\pi}\cos^2\theta_c \Bigg\{ (F_V + F_M + F_A)^2 + (F_V + F_M - F_A)^2 (1 + \frac{q^2}{2E_\nu m_n})^2 \\ &+ \left[F_A^2 - (F_V + F_M)^2\right] \frac{(-q^2)}{2E_\nu^2} \\ &+ \left[F_M^2 \frac{(-q^2 + 4m_n^2)}{4m_n^2} - 2(F_V + F_M)F_M\right] \left[2 + \frac{q^2(m_n + 2E_\nu)}{2E_\nu^2 m_n}\right] \Bigg\} \ . \end{aligned} \tag{7.3}$$

The three form factors, F_V, F_A, and F_M, have the q^2 dependence and are expressed as

$$F_V(q^2) = \left(1 - \frac{q^2}{4m_n^2}\right)^{-1} \left[G_E^V(q^2) - \frac{q^2}{4m_n^2} G_M^V(q^2)\right] \ , \tag{7.4}$$

$$F_A(q^2) = (g_A/g_V)\left(1 - \frac{q^2}{M_A^2}\right)^{-2} \ , \tag{7.5}$$

$$F_M(q^2) = \left(1 - \frac{q^2}{4m_n^2}\right)^{-1} \left[G_M^V(q^2) - G_E^V(q^2)\right] \ , \tag{7.6}$$

where M_A is known as the axial-vector mass ($\equiv M_A^{QE}$) and g_A/g_V is measured to be $\sim$1.267 from β decay. G_E^V and G_M^V are the electromagnetic form factors of the neutron and are expressed as

$$G_E^V(q^2) \simeq (1 - \frac{q^2}{M_V^2})^{-2} \ , \tag{7.7}$$

$$G_M^V(q^2) \simeq (1 + \mu_p - \mu_n)\left(1 - \frac{q^2}{M_V^2}\right)^{-2} \ , \tag{7.8}$$

where μ_p and μ_n are magnetic moment of proton and neutron, respectively. M_V is a vector mass and its value is measured to be 0.84 GeV from electron scattering off protons [83]. Therefore, equation (7.3) can be parametrized by q^2 and M_A^{QE}.

7.2. Charged current single pion production : CC1π

CC1π (Fig. 7.2 B) is a reaction producing one pion in the final state:

$$\nu_\mu + N \to \mu + N' + \pi \ , \tag{7.9}$$

where N represents the nucleon (n or p) bound inside the nucleus. In the energy range of a few-GeV, the amplitude of the reaction is dominated by a weak excitation of the $\Delta(1232)$ resonance ($\nu N \to \mu\Delta$) and its subsequent decay ($\Delta \to N\pi$). Then, the cross section can be calculated by modifying the hadronic tensor in Eq. (7.2):

$$H^{\alpha\beta} = \langle\Delta|V^\alpha - A^\alpha|N\rangle\langle\Delta|V^\beta - A^\beta|N\rangle^* \ . \tag{7.10}$$

The vector form factors in $N\Delta$ transition are fixed from the analysis of pion electroproduction data while the axial-vector couplings are determined using PCAC (partially conserved axial vector current) [84]. The cross section is actually dominated by the axial-vector contribution and can be expressed as

$$\frac{d\sigma}{dq^2} \simeq \frac{G_F^2 \cos\theta_c}{12\pi} \frac{s - m_\Delta^2}{s - m_N^2} \left(\frac{m_\Delta + m_N}{m_\Delta}\right)^2 |C_5^A(q^2)|^2 \ , \tag{7.11}$$

where m_Δ and m_N are the mass of Δ and a nucleon, respectively; s is a Mandelstam variable ($s = 2m_N E_\nu + m_N^2$). C_5^A is one of the axial-vector form factors and is parametrized by q^2 and the axial-vector mass ($\equiv M_A^{RES}$), as well as F_A in the CCQE cross section. In most of the MC generators, the single pion production (or meson production) via resonance is calculated using the Reign-Sehgal model [85] , which includes all of the possible baryon resonances with mass less than 2 GeV.

CC1π mimics the CCQE interaction if the charged pion in the final state is not detected. In fact, this interaction is a main background for the ν_μ disappearance in the neutrino oscillation experiments.

7.3. Deep inelastic scattering : DIS

At higher neutrino energy, the nucleon fragments into multi-hadrons: $\nu_\mu + N \to \mu +$ hadrons (Fig. 7.2 C). In this interaction, neutrinos are assumed to interact with "quarks" in a nucleon, This process is called "DIS". In the calculation of this process, the parton model is used. The cross section of DIS is obtained by summing up contributions from each quark with the weight of the parton distribution

$$\frac{d^2\sigma}{dxdy} = \frac{G_F^2 m_N E_\nu}{\pi} \left[(1 - y + \frac{1}{2}y^2 + C_1)F_2(x) + y(1 - \frac{1}{2} + C_2)(xF_3(x))\right] \ . \tag{7.12}$$

Here we used following expressions:

$$C_1 = \frac{m_\mu^2(y-2)}{4m_N E_\nu x} - \frac{m_N xy}{2E_\nu} - \frac{m_\mu^2}{4E_\nu^2} \,, \tag{7.13}$$

$$C_2 = -\frac{m_\mu^2}{4m_N E_\nu x} \,, \tag{7.14}$$

$$x = -\frac{q^2}{2m_N(E_\nu - E_\mu)} \,, \tag{7.15}$$

$$y = \frac{E_\nu - E_\mu}{E_\nu} \,, \tag{7.16}$$

where E_μ and m_μ are energy and mass of the muon. F_2 and F_3 are composed of parton distribution functions (PDFs) $Q(x)$ and $\bar{Q}(x)$:

$$F_2(x) = 2x(Q(x) + \bar{Q}(x)) \,, \quad xF_3(x) = 2x(Q(x) + \bar{Q}(x)) \,. \tag{7.17}$$

The MINOS experiment [18] uses the neutrino beam whose energy has a peak at around 3 GeV. In this energy region, the DIS interaction is a dominant mode and is actually used for the signal mode in the MINOS experiment.

When the DIS interaction on a heavier nuclear target is considered, one has to pay attention to a difference in the structure function (F_2) between free and bound nucleons. This anomaly was first reported by the European Muon Collaboration [86] who measured the structure functions of deuteron and iron through deep inelastic muon scatterings. The corresponding nuclear correction factor has to be evaluated and applied to the PDF in order to calculate the DIS cross section. The study on the nuclear correction is being done using neutrino and charged lepton data [87][1].

7.4. Charged current coherent pion production

The coherent pion production is an interaction where the nucleus recoils as a whole (Fig. 7.2 D). This interaction occurs when the squared momentum transfer ($= q^2$) to the nucleus is very small. A specific formula of this interaction was made by Rein and Sehgal [89] through Adler's theorem [90]; In the limit of small angle scattering where the final-state lepton is parallel to the incoming neutrino, the scattering amplitude of the reaction, $\nu + \alpha \to l + \beta$, is proportional to divergences of the vector and axial-vector currents:

$$|\mathcal{M}|^2 \propto \langle \beta | \partial_\mu (V^\mu + A^\mu) | \alpha \rangle |^2 \,. \tag{7.18}$$

[1] The MINERνA experiment conducted the measurement of ratios of the ν_μ CC inclusive cross section on different nuclear targets in order to check the effects from the different nuclei on the PDFs. The result does not reproduce the data of the charged lepton-nucleus scattering and the prediction by any MC generators [88].

If the conservation of vector current (CVC) is true, i.e. $\partial_\mu V^\mu = 0$, only the axial-vector current contributes to the amplitude. In addition to that, the PCAC hypothesis can relate the neutrino coherent scatterings with the pion-nucleus elastic ones. Finally the cross section can be calculated to be

$$\frac{d^2\sigma}{dxdy} = \frac{G_F^2 m_N E_\nu}{\pi^2} f_\pi^2 (1-y)\sigma_\pi \ , \tag{7.19}$$

$$y = \frac{E_\nu - E_l}{E_\nu} \ , \tag{7.20}$$

where f_π is known as the pion decay constant, E_l is energy of final-state lepton, and σ_π denotes the pion-nuclues elastic scattering cross section. The cross section for coherent pion production had been successfully explained by the PCAC for high neutrino energy ($E_\nu > 2$ GeV). For the lower energy region, however, the model was found to overestimate the cross sections for both NC and CC coherent pion production. Recently, the alternative model called "microscopic model" was developed to explain the cross section in the lower energy region [91, 92].

7.5. Neutrino event generator: NEUT

In the T2K experiment, NEUT [40] is being used as the primary event generator. With the given neutrino energy and cross section, NEUT determines the interaction mode of an event and calculate kinematics in the final state. Re-interactions of the particles within the nucleus, which is called "Final State Interaction (FSI)" is also simulated prior to their escapes. This FSI effect is considered only for the particles which interact via the strong force. Following interaction modes are provided for both CC and NC interactions by NEUT:

- quasi-elastic scattering ($\nu N \to lN'$),
- single meson production ($\nu N \to lN'm$),
- coherent π production ($\nu A \to l\pi A$),
- deep inelastic scattering ($\nu N \to lN'hadrons$),

where N and N' are the nucleons, l is the lepton, m is the meson and A is the nucleus. Figure 7.3 shows schematics of the NEUT simulation for the neutrino-nucleus (^{56}Fe) interaction of CCQE (left) and CC1π (right). The cross section predicted by NEUT is also shown in Fig. 1.6.

CCQE

CCQE is a dominant interaction mode at the neutrino energies around 1 GeV. NEUT adopts the Smith and Moniz model [93] for the CCQE interaction: a relativistic Fermi gas

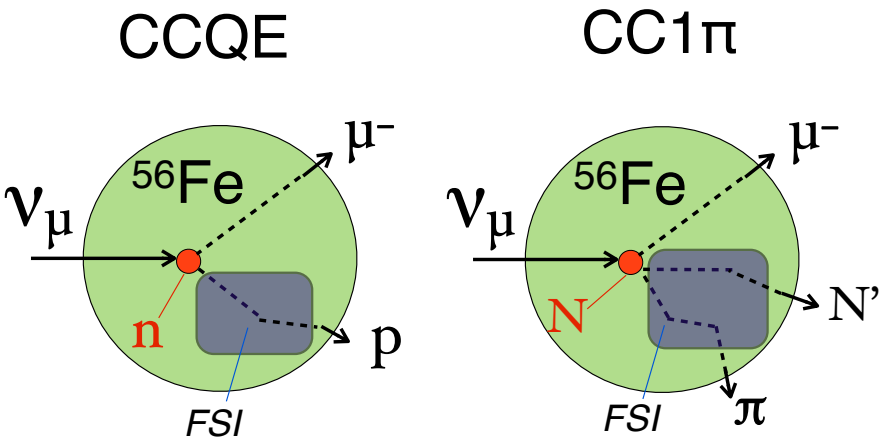

Figure 7.3.: Schematics of the NEUT simulation for the neutrino interaction inside a nucleus (^{56}Fe). Left: CCQE ($\nu_\mu + n \to \mu^- + p$). Right: CC1$\pi$ ($\nu_\mu + N \to \mu^- + N' + \pi$).

(RFG) model is used for modeling a neutrino-nucleus interaction, which is characterized by a global Fermi momentum (p_F) and a constant binding energy (E_b). In this model, a knocked-out nucleon is required to have a momentum larger than p_F due to Pauli blocking effect. The axial-vector mass M_A^{QE} is determined from the measurement of the neutrino-nucleus interaction and is set to be 1.21 GeV.

CC1π

CC1π becomes a dominant mode in the energy range of 2-3 GeV. The amplitude of this reaction in this energy range is dominated by the $\Delta(1232)$ resonance. NEUT uses the Rein-Sehgal model for this reaction. The axial-vector mass M_A^{RES} is set to be 1.21 GeV as well as M_A^{QE}.

CCDIS

CCDIS becomes important for $E_\nu >\sim 3$ GeV. NEUT uses a formula of Eq. 7.12 for the calculation of the cross section with GRV98 PDF [94]. In addition, the corrections are applied to the PDFs in the small q^2 region using the method developed by Bodek and Yang [95].

Meson (pion) multiplicities for DIS are determined according to the hadronic invariant mass W:

$$W^2 = m_N^2 + 2\{E_N(E_{\nu_\mu} - E_\mu) - \vec{p}_N \cdot (\vec{p}_{\nu_\mu} - \vec{p}_\mu)\} + q^2 \ , \tag{7.21}$$

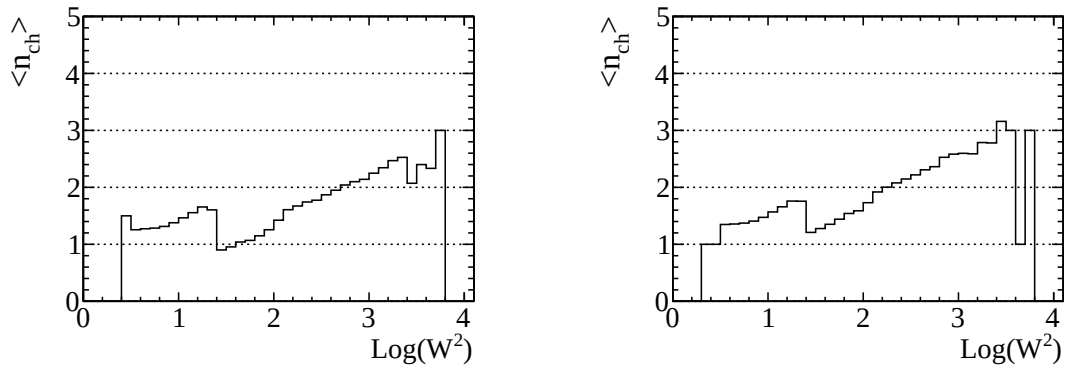

Figure 7.4.: Mean of the charged pion multiplicity as a function of $\log W^2$ for the neutron (left) and proton (right) target. Dips at $\log W^2 \sim 1.5$ are due to the transition from the internal custom model to PYTHIA/JETSET [97].

where $E_{\nu_\mu}(\vec{p}_{\nu_\mu})$, and $E_\mu(\vec{p}_\mu)$ denote energy (3-momentum) of ν_μ, and μ, respectively; $\vec{p}_N$ denotes the Fermi momentum of the nucleon and E_N is the corresponding energy[2]. For $W < 2$ GeV, NEUT uses an approximation formula for a mean of the pion multiplicity ($\equiv \langle n \rangle$):

$$\langle n_\pi \rangle = A + B \log W \ . \tag{7.22}$$

A and B are determined from the past multiplicity measurement [96] to be 0.09 and 1.83, respectively. For $W > 2$ GeV, the multiplicity model in NEUT changes over from the internal custom model to PYTHIA/JETSET [97]. Figure 7.4 shows the mean of the charged pion multiplicity as a function of $\log W^2$ for the neutron (left) and proton (right) target. There are dips in the distribution at $\log W^2 \sim 1.5$ where the transition of the models occurs.

CC coherent pion

NEUT computes the cross section using the model developed by Rein and Sehgal (see Eq. 7.20). The cross section of the pion-nuclues scattering is determined from [89].

Final state interaction

When hadrons are created by the neutrino interaction, re-interactions of these particles inside the nucleus, FSI, need to be taken into account. In particular, the pion FSI is treated more carefully because it has a significant effect on the CCQE events in Super-K or ND280. NEUT uses a microscopic cascade model for the pion FSI. In the

[2] $\vec{p}_N$ vanishes when a free-proton is used as the target.

model, the probabilities of various interactions are calculated for each step based on Δh (Delta-hole) model [98] for p_π <500 MeV/c, and measurements of the π-nucleon (or π-deutron) scattering for p_π >500 MeV/c. In later stage of analysis, the pion FSI are corrected using the measurements of the π-nucleus scattering. The pion momentum region below 500 MeV/c is called Δ-region where the scattering cross section with the nucleon is very large. In this region, there are three important channels for the pion interaction, which can be categorized according to the number and type of the pions in the final state:

Quasi-elastic scattering
: The pion interacts inelastically with the nucleon, but only one pion, which is the same type as the incoming pion, exists in the final state.

Absorption
: The incident pion is absorbed by the nucleus, resulting in there being no pions in the final state.

Single charge exchange
: There is only one π^0 and no other type of the pions in the final state.

Figure 7.5 shows the pion inelastic scattering cross sections on iron with the prediction by NEUT. As seen in the figure, these three reactions contribute dominantly to the total inelastic cross section in the Δ-region. As the pion energy increases, multi-π production becomes important.

7.6. Importance of the CC inclusive cross section measurement

As discussed in Sec. 2.4, understanding of the neutrino interaction models is one of key issues for the measurement of the neutrino oscillation parameters. In order to model the neutrino interaction, the exclusive cross section measurements, such as CCQE, are very important. However, the precise measurement of these exclusive channels suffers from uncertainty in the nuclear medium effect such as a multi-nucleon interaction and final state interaction. On the other hand, the CC inclusive channel is less affected by the uncertainty in the nuclear medium effect. The precise measurement of this channel could be helpful for understanding the neutrino interaction mechanism. In this section, we first briefly describe current issues and difficulties in determining the cross section exclusively. Then, the motivation of the measurement of the CC inclusive cross section is described.

Discrepancy in the CCQE cross section

As described in Sec. 7.1, the CCQE cross section has a free parameter of M_A^{QE}. The value was determined in early CCQE measurements on deuterium and hydrogen targets

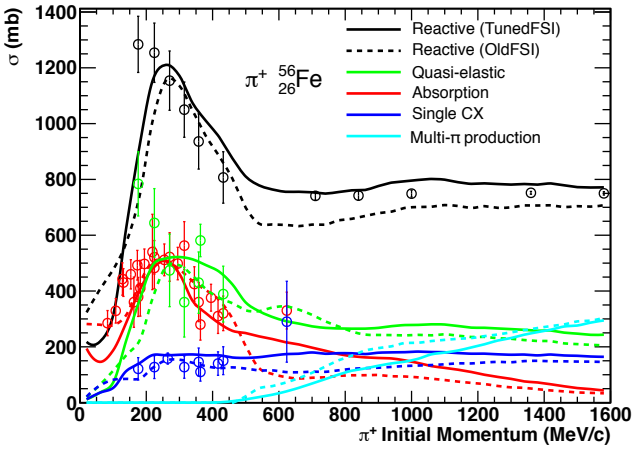

Figure 7.5.: Pion inelastic scattering cross section on iron with the prediction by NEUT. Solid (dashed) lines represent the corrected (non-corrected) FSI cross sections in the NEUT simulation. In the Δ-region, the scatterings of the quasi-elastic, absorption, and single charge exchange (single CX) contribute largely to the total inelastic cross section. As the higher pion energy, the multi-π production becomes important. The reactive cross section is defined as a sum of any of the inelastic cross sections.

to be $M_A^{QE} = 1.016 \pm 0.026$ GeV [99] from the neutrino event rate. Later the K2K experiment [100] conducted the measurement of the CCQE cross section on oxygen. The M_A^{QE} of 1.20 ± 0.12 GeV was extracted from the Q^2 ($\equiv -q^2$) distribution [101]. The result is larger as compared to that obtained in the early experiments. Subsequently the MINOS experiment measured the CCQE cross section on the iron target [102]. They measured M_A^{QE} to be around 1.2 GeV from the Q^2 distribution, which is consistent with the K2K's result. The MiniBooNE experiment [103] made the situation more complicated. They collected a large amount of data using the mineral-oil (CH_2) target and measured the CCQE cross section. The M_A^{QE} was extracted from the Q^2 distribution and measured to be 1.35 ± 0.17 GeV [104]. The result was larger than that obtained by K2K and MINOS[3] In fact, the discrepancy of $\sim$20% in M_A^{QE} between these measurements is conservatively taken as the systematic error for M_A^{QE} in the T2K experiment.

The differences in the measurements of M_A^{QE} are generally thought to be due to uncertainty in the nuclear medium effect. Both of the measurements on the deuteron and hydrogen targets use "light" nucleus for their targets and the prediction of the neutrino cross section is less affected by the uncertainty in the nuclear effect. In the case of the heavier nuclear target, the interaction process becomes more complicated. As atomic weight of the nuclear target increases, two or more nucleons are involved in the reaction. This process is called a multi-nucleon interaction [107] (see Fig. 7.6). This interaction

[3] Among the recent experiments, NOMAD and MINERνA showed that measured M_A^{QE}s are in agreement with $\sim$1.0 GeV [105, 106].

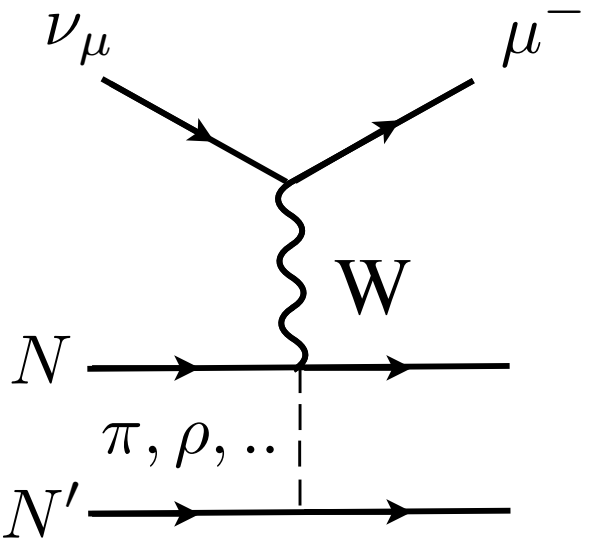

Figure 7.6.: Diagram of the mechanism of the the multi-nucleon interaction. The dashed line represents an exchange of mesons between the nucleons.

has not been modeled in the event generators until just recetnly[4,5]. According to this interaction, multi-nucleons are ejected by the neutrino interaction. This process mimics the CCQE interaction if only one of the nucleons is detected and would overestimate size of the CCQE cross section. It, therefore, would result in increasing M_A^{QE}[6].

Most of the present event generators [40, 109, 110] use the RFG model. Recently, an alternative model called "Spectral function (SF)" is considered for modeling the neutrino-nucleus scattering [111] since the SF model well describes the results of the electron scattering data [112]. Unlike RFG, SF takes into account for a strong nucleon-nucleon (NN) correlation. Figure 7.7 shows the momentum distribution, $n(p)$, of the nucleon bound in oxygen for the RFG and SF models. In RFG, there is a hard momentum cut-off at p_F. This is because the nucleons are filled in all energy levels up to the Fermi surface energy. In SF, on the other hand, $n(p)$ has a long tail and is extended to the higher momentum region. This tails comes from the correlated pair of nucleons. The nucleon in this region leads to the emission of a second nucleon, resulting in a reduction of the order of 15% in the "pure" CCQE cross section. Namely, replacing RFG with SF results in more increasing M_A^{QE} to compensate the reduction of the cross section. Hence, there are many possibilities of combination of the "correct" models to describe the CCQE interaction. This fact makes it difficult to depict the CCQE model.

[4]In addition to the multi-nucleon interaction, the event generators start to take account of the medium polarization effect with the random phase approximation (RPA) [108] .

[5]In this thesis, both the multi-nucleon interaction and RPA are not taken into account because the event generator used in our analysis is not up to date.

[6]K2K, MINOS, and MinibooNE measured the Q^2 distribution for the extraction of M_A^{QE}. All the experiments observed a deficit of the event in the small Q^2 region. This also results in increasing the M_A^{QE}.

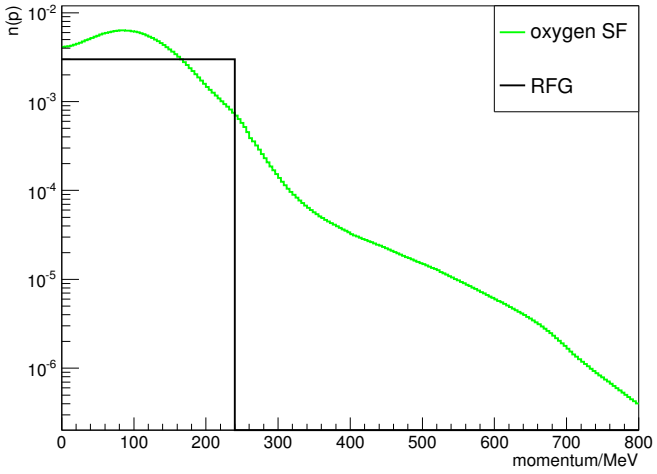

Figure 7.7.: Momentum distribution of the nucleon ($n(p)$) bound in oxygen. The black and green lines represent $n(p)$ for RFG and SF, respectively.

Discrepancy in the single pion production measurements

The MinibooNE experiment measured differential cross sections for the single pion production channel (CC1π) with a large amount of data [113, 114]. They provided the CC1π cross section as a function of the reconstructed neutrino energy, which is shown in Fig. 7.8. They used NUANCE [110] as their neutrino event generator, where the Rein-segal model is used for the calculation of the CC1π cross section. In addition, FSI of the pion is taken into account. As seen in the figure, there is a large discrepancy in the cross section between the data and prediction by NUANCE including the effect of FSI. This difference gives a large uncertainty in the CC1π cross section in the T2K experiment.

The difficulty in the measurement of the CC1π cross section comes from the uncertainty of FSI. Pions can be absorbed during its way out of the nucleus and the reaction would mimic the CCQE interaction. In addition, pions can be inelastically scattered inside of the nucleus and change the momentum and angles. Hence, the FSI alters the signature of the event. The model, hence, needs to simulate these pictures correctly to extract the correct cross section.

Verification of the model via the CC inclusive cross section measurement

As described above, the extraction of the exclusive cross section suffered from the uncertainty in the nuclear medium effect. Benefit of the CC inclusive cross section is that this channel is less affected by these uncertainties because we can identify this interaction mode only by detecting outgoing lepton (muon). Therefore, the total uncertainty of the

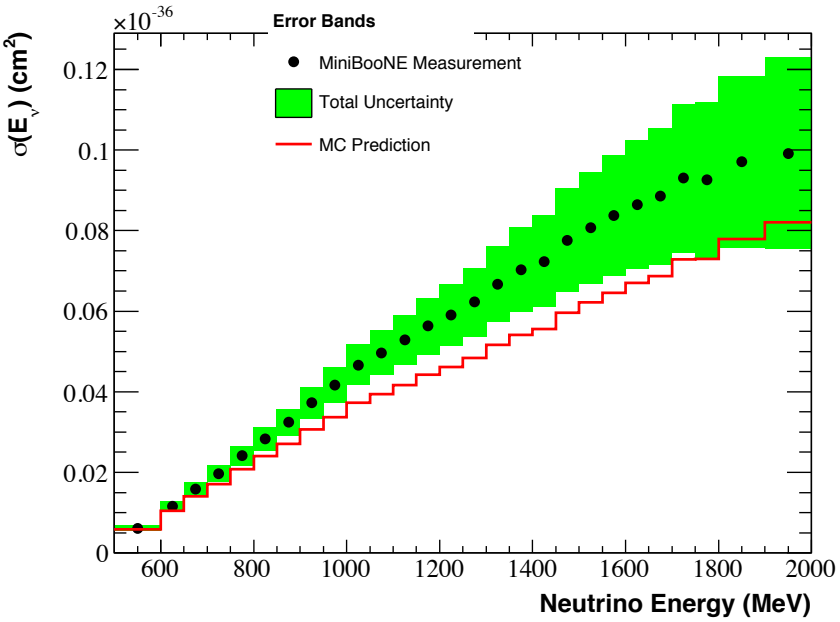

Figure 7.8.: CC1π^+ cross section measured in the MinibooNE experiment [113]. A red line shows the prediction by NUANCE [110] including the effect from FSI.

CC inclusive cross section measurement is expected to be much smaller than that of the exclusive ones and the precise measurement becomes possible.

In the T2K experiment, an neutrino event generator, GENIE [109], is used for the reference: the obtained cross section results are compared with predictions by NEUT and GENIE. Both NEUT and GENIE use the same models for calculations of the exclusive cross sections. However, for example, NEUT sets M_A^{QE} to be 1.21 GeV while GENIE uses 0.99 GeV as a default value of M_A^{QE}, resulting in about 20 % difference in the CCQE cross section between these two generators. The precise measurement of the CC inclusive cross section enable us to test the models. In addition, the precise measurement provides a strong constraint for a sum of exclusive channels and could also be helpful for the exclusive cross section measurement.

7.7. Motivation of the measurement of the CC inclusive cross section on iron

Table 7.1 shows a summary of the published results on the ν_μ inclusive cross section on various neutrino targets. ArgoNeuT [115], MINERνA [88], MINOS [116], and NOMAD [117] experiments measured the CC inclusive cross section above $E_\nu > 3$ GeV. The

Table 7.1.: Summary of the publish results on the ν_μ inclusive cross section.

Experiment	$\langle E_\nu \rangle$	neutrino target
ArgoNeuT [115]	3.3	Ar
MINERνA [88]	3.3	C, O, Fe, Pb
MINOS [116]	3.3	Fe
NOMAD [117]	26.0	C
SciBooNE [118]	0.8	CH
T2K (off-axis beam) [119]	0.85	CH
T2K (on-axis beam) [120]	1.51	CH, Fe

CC inclusive cross section at lower neutrino energies were measured by SciBooNE and T2K. To date, there are two measurements of the ν_μ-Fe CC inclusive cross section[7]:

- a measurement with the near detector in the MINOS experiment [116],
- a measurement with INGRID [120].

The MINOS collaboration used a ν_μ beam from the NuMI beamline at Fermilab [121]. The beam has a broad band peaking between 3 and 4 GeV with a long tail in the high energy region. The CC inclusive cross section on iron in the energy range of 3-50 GeV was measured through the DIS scattering of neutrinos. They used the tracking calorimeter composed of magnetized iron and plastic scintillator to measure energies of hadrons and a muon which are produced by a neutrino interaction. A sum of these two energies gives the incoming neutrino energy. In this way, the cross section was measured as a function of neutrino energy with a precision of 2-8%.

In the T2K experiment, the CC inclusive ν_μ cross section on iron was measured with the INGRID horizontal center module (module 3). In this measurement, the CC inclusive cross section on CH was also measured with the Proton Module and the cross section ratio on Fe to CH was obtained. In the event selection for INGRID, the criteria described in Sec. 8.2 were used to select CC events[8]. Finally, the flux-averaged CC inclusive cross section on Fe were measured at a mean neutrino energy of 1.51 GeV with a precision of $\sim$10 %.

The results of the ν_μ CC inclusive cross section on Fe from MINOS and T2K are shown in Fig. 7.9. Predictions by two different MC generators, GENIE and NEUT, are overlaid in the same figure. GENIE was initially developed by the MINOS collaborator and the model has been re-developed for the MINOS analyses. As seen in Fig. 7.9,

[7] The MINERνA collaboration also measured ν_μ-Fe CC inclusive interaction but reported only the cross section ratio on Fe to CH [88].

[8] An acceptance cut is also applied to the INGRID event selection in order to minimize the difference in the selection efficiency between INGRID and the Proton Module , which could enlarge the systematic error on the measurement of the cross section ratio.

NEUT overestimates the CC inclusive cross section for higher neutrino energy region. For the lower energy region, the result from T2K is consistent with both NEUT and GENIE. In the energy range of 2-3 GeV, the CC inclusive cross section on iron has never been measured. Therefore, the cross section in that energy region will be important input for modeling the neutrino interaction mechanism. The measurement covering the energy range of 1-3 GeV is useful to check the consistency between the T2K and MINOS measurements. As described in Sec 7.6, the measurement of the CC inclusive cross section is less affected by the uncertainty in the nuclear medium effect than that of the exclusive cross section, and hence can help the measurement of the exclusive channel.

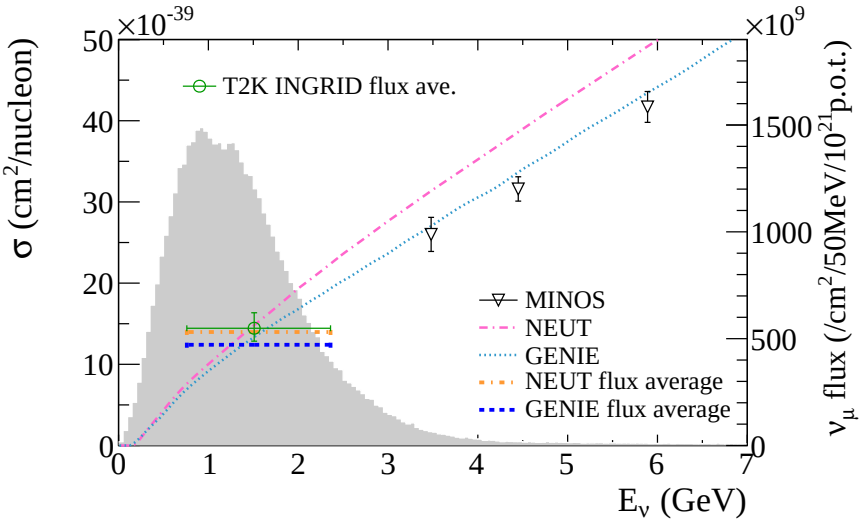

Figure 7.9.: Summary of the measurements of the ν_μ CC inclusive cross section on iron. The energy dependent cross section with the MINOS near detector [116] and the flux-averaged cross section with INGRID [120] are shown with the NEUT and GENIE predictions. The T2K ν_μ flux at on-axis is shown in grey.

Chapter 8

Event reconstruction in INGRID

The primary role of INGRID is to measure the direction and intensity of the neutrino beam. A high-statistics data can be collected for the neutrino-iron scattering, and can also be used for studying the neutrino-nucleus (iron) interaction. This chapter first describes the MC simulations used in the INGRID analysis. Then we explain methods for reconstruction of the neutrino events in Sec. 8.2. In order to operate the detectors stably, quality of the detector performance has been always checked, details of which is given in Sec. 8.3.

8.1. Monte Carlo simulation

The MC simulation in the INGRID analysis consists of following three steps:

1. generation of the neutrino flux at the INGRID modules,
2. simulation of the neutrino-nucleus interactions in the iron target (^{56}Fe),
3. simulation of the particle passages through the detector and its response.

The neutrino flux at INGRID is simulated in the same way as described in Sec. 5.2. We then simulate the neutrino-nucleus interaction using NEUT which provides kinematics of the particles in the final state. Finally, the kinematic information is propagated through the detector simulation.

8.1.1. Neutrino flux

The neutrino flux at INGRID is calculated using FLUKA2008 and JNUBEAM as well as the muon flux at the muon monitor. The flux is then corrected using hadron interaction data[1]. Figure 8.1 shows the obtained neutrino flux for a given flavor at one of the center modules (module 3, see Fig. 3.7) when all the horn currents are set to 250 kA. As shown in the figure, the neutrino flux has a peak around 1 GeV and a wider band compared to the flux at off-axis (see Fig. 2.16). Table 8.1 shows the fraction of the integrated flux by flavour in each energy range, at the module 3. As seen in the table, ν_μ accounts for

[1]Section 6.4.2 details the correction applied to the muon flux. The same correction is also applied to the neutrino flux.

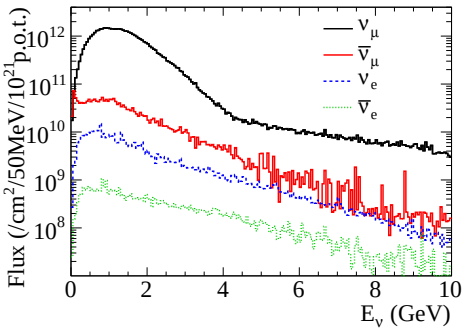

Figure 8.1.: Neutrino flux at module 3 for a given flavor. These fluxes are estimated when all the horn currents are set to 250 kA.

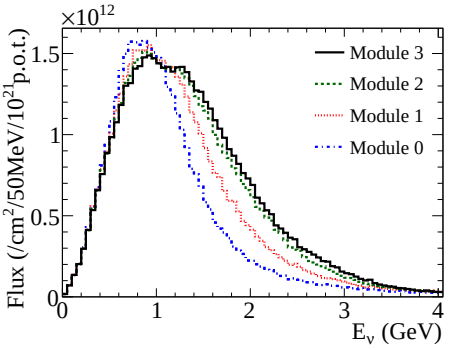

Figure 8.2.: Neutrino flux at the horizontal modules: module 0, 1, 2, and 3. These fluxes are estimated when all the horn currents are set to 250 kA.

Table 8.1.: Fraction of the integrated flux by neutrino flavour in each energy range at module 3. All of the horn currents are set to 250 kA.

	Neutrino energy range (GeV)				
Flavour	0–1	1–2	2–3	3–4	>4
ν_μ	94.2%	96.8%	95.4%	89.7%	86.5%
$\bar{\nu}_\mu$	4.8%	2.7%	3.8%	7.9%	9.3%
ν_e	0.9%	0.5%	0.7%	2.0%	3.5%
$\bar{\nu}_e$	0.1%	0.0%	0.1%	0.3%	0.6%
Total	100%	100%	100%	100%	100%

$>\sim$95% of the total flux for $E_\nu < 3$ GeV. The ν_μ contamination is then down to less than 90% for $E_\nu >3$ GeV, and $\bar{\nu}_\mu + \nu_e$ account for $>\sim$10% of the total flux for $E_\nu > 3$ GeV.

Figure 8.2 shows the ν_μ flux at the the horizontal modules: module 0,1,2, and 3. As seen in the figure, a peak of the neutrino energy at module 0 slightly shifts in the lower energy region compared to the flux at module 3. This is because the module is located at θ_{OA} =1.2° from on-axis, and a peak of the neutrino energy at the module shifts in the lower energy due to the off-axis beam effect (see Sec. 2.2).

8.1.2. Neutrino event generator

Neutrino interactions are simulated using the neutrino flux as an input. In the INGRID analysis, the event generator NEUT [40] is used for the simulation of the interaction with the iron target as it is a primary generator in T2K (see Sec. 7.5 for detail). In the INGRID analysis, we simulate the interaction only for Fe and assume the cross section per a nulceon for the other target (mainly CH) is equal to that on Fe. This is because the contribution of the interaction from CH is only $\sim 4\%$ and effects from the difference in the cross section between CH and Fe are considered to be small.

8.1.3. Detector simulation

Information of kinematics provided by NEUT is propagated into the detector simulation build with a GEANT4 framework [122]. In the simulation, all the detectors' components, geometries, and structures are modeled and particles are tracked step-by-step. The energy deposit of the particle at the scintillator is converted into the number of photo-electrons with a given conversion factor determined from a comparison of the peak position of photo-electron (PE) distribution obtained with the beam induced muon events (Fig. 8.3). A non-linear response of the scintillator by a high ionization density along the track of the charged particle is calculated using the Birks' formula [123]:

$$\frac{dE'}{dx} = \frac{dE/dx}{1 + K_B \cdot dE/dX} \ , \tag{8.1}$$

where dE/dx is the energy loss calculated with the Bethe-Bloch formula and K_B is the adjustable parameter. For the INGRID detector simulation, we use $K_B = 0.0208$ cm/MeV which was determined from the proton beam irradiation test. The effect of collection and attenuation of the light in the scintillator and the WLS fiber were measured with a electron beam [124] and the results are used in the simulation. The non-linearity of the MPPC response is also taken into account.

Particles generated in the upstream wall of the INGRID detectors are also propagated into the detector simulation and are treated as the background sources. The neutrino interaction at the wall is simulated with CH as the target using NEUT. Figure 8.4 shows the geometry of the upstream wall reproduced in the GEANT4 simulation.

For the hadronic interaction modeled in GEANT4, following physics lists are considered.

QGSP_BERT

QGSP_BERT consists of: a GEANT4 Bertini cascade model (BERT) below 9.9 GeV; a low energy parametrization (LEP) model, which is based on a GEISHA model [125] used in GEANT3, between 9.5 and 25 GeV; and a Quark-Gluon-String [126] with a pre-compound model [127] (QGSP) above 12 GeV. QGSP_BERT is valid for charged pions, kaons, and proton/neutron. On the other hand, all other hadrons

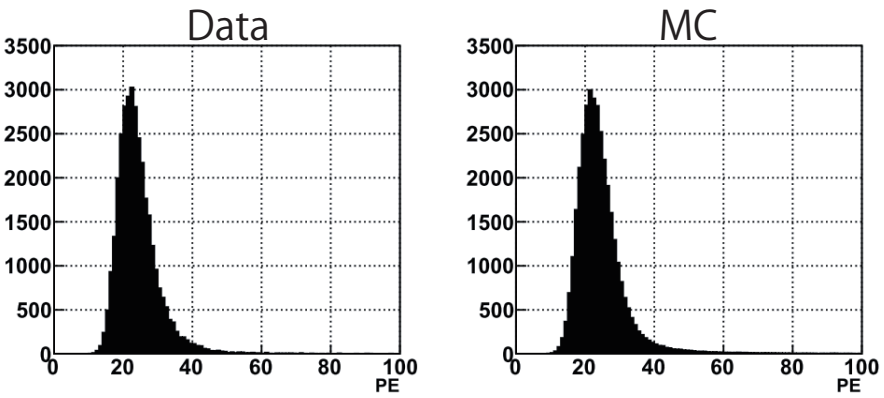

Figure 8.3.: Photo-electron (PE) distribution of the sand muon events for the real data (left) and MC simulation (right).

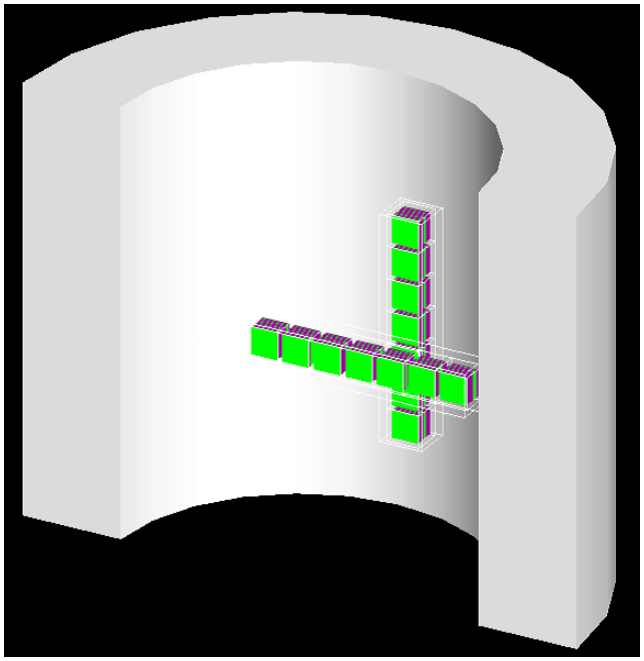

Figure 8.4.: Upstream wall of the INGRID detectors reproduced in the GEANT4 simulation, viewed from downstream.

are handled by a low and high energy parametrisation (LHEP). In the T2K energy range, almost only the GEANT4 Bertini cascade model is used. This model is based on a re-engineering of the INUCL code [128], which includes the Bertini intra-nuclear cascade model [129, 130].

FTFP_BERT

FTFP_NERT consists of: a GEANT4 Bertini cascade model (BERT) below 5 GeV;

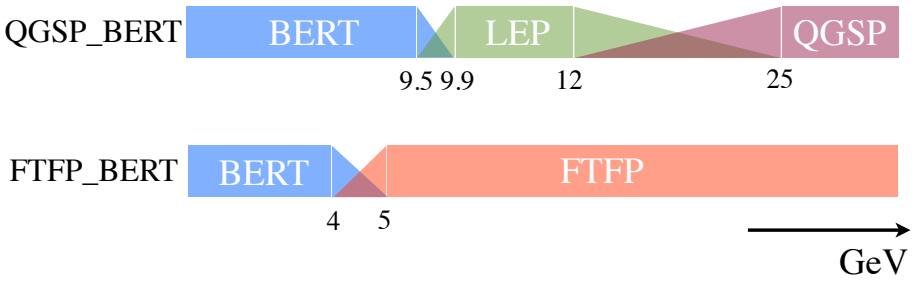

Figure 8.5.: Illustration for the physics lists: QGSP_BERT and FTFP_BERT.

Fritiof[131] with the pre-compound model (FTFP) above 5 GeV. As with QGSP_BERT, FTFP_BERT is valid for charged pions, kaons and proton/neutron, and all other hadrons are treated by LHEP. This model uses the same total inelastic cross section as QGSP_BERT.

QGSP_BERT is chosen as the default physics list for the INGRID MC simulation[2]. As described in Chapter 9, FTFP_BERT is also used for a comparison of the results of the CC inclusive cross section measurement. Figure 8.5 summarizes energy regions for hadronic interaction models used in each of the physics lists.

8.2. Neutrino event selection

In order to select neutrino-interaction events, following selections are applied:

1. **Pre-selection**
   The channel, where the ADC signal have larger than 2.5 photo-electron, is defined as the "hit" channel. If there are more than three hit channels within 100 nsec in an INGRID module, hits concentrated within ±50 nsec from their average time are classified into a cluster. Then we count planes which have at least one coincidence hit cluster in both of X and Y planes. The plane is called "active plane". If the number of the active plane is larger than 2, then we apply "tracking" to reconstruct the charged particle as described below.

2. **2D track reconstruction**
   A tracking algorithm is applied for hits in X and Y planes to obtain tracks in the XZ view and YZ view respectively according to "Cellar automaton" algorithm [132].

3. **3D track matching**
   We check if the reconstructed tracks in the XZ view and YZ view originate from the

[2]In a past simulation, QGSP was used for the simulation of the hadronic interaction in GEANT4. In this analysis, $\bar{\nu}_\mu$ events are estimated using the old MC simulation, therefore QGSP is used for the event samples.

same vertex by looking at a difference in the most upstream layer hit between the two tracks. If the difference of the layer is more than 2 planes, the event is rejected.

4. Vertexing

If two or more tracks are found after the 3D track matching, then we check if all the tracks originates from the same vertex. First, distances between vertices in the X and Y direction are summed up. If this sum is less than 150 mm, a difference of the Z position of the vertices of the two 3D tracks is calculated for XZ view (ΔZ_x) and YZ view (ΔZ_y) separately. If the sum of ΔZ_x and ΔZ_y is less than 3 planes, two tracks are recognized that they are originate from the same vertex.

5. Timing cut

This cut is only applied to the data. Since the T2K neutrino beam has eight pulsed-beam structures, a timing of the selected events are required to be within 100 ns from the expected one in each bunch (Fig. 8.6). The expected timing is calculated from the timing when proton beam hits the target and time-of-flight of the neutrinos from the target to INGRID.

6. VETO cut

The VETO cut is applied in order to reduce the incoming charged particles. Hits in the VETO planes are searched for position extrapolated from the track. If there are such hits, those events are rejected (Fig. 8.7).

7. Fiducial volume cut

The FV is defined as a cubic volume which has $(\pm 50)\times(\pm 50)$ cm^2 transverse area, corresponding to the area composed of scintillator bars from 3rd to 22nd channels in X and Y, and from tracking plane#1 to 8. We check if the vertices are in the fiducial volume or not as shown in Fig. 8.8.

A typical event display of a neutrino event is shown in Fig. 8.9. As beam power increases, the probability of event-pileup, where more than one neutrino events are detected in a same bunch and at a same module, increases. If one of those tracks piles up with another track, vertices may fail to be reconstructed and a loss of events may happen. The correction factor for the event-pileup is given as a linear function of the beam intensity, which was estimated by using pseudo high-power data made by combining real data [132]. Table 8.2 summarizes the results of the event selection for MC and the data to which the correction for the pileup-event is applied. The reconstructed events contain $\bar{\nu}_\mu$, ν_e and BG events which consist of sand muon, neutron and γ generated at the upstream wall of INGRID (hereafter beam-related BG). Since the contamination of $\bar{\nu}_e$ is negligible as shown in Table 8.1, it is not counted in MC. The distribution of the vertex position in the X and Y directions after all the event selections are shown in Fig. 8.10. The vertex position in the Z direction (vertex-Z) and angular distribution are shown in Fig. 8.11 and 8.12, respectively. Figure 8.13 shows the detection efficiency for each ν_μ interaction mode which is estimated from the MC simulation. We obtain >70% efficiency for the CC events in the energy range >1 GeV.

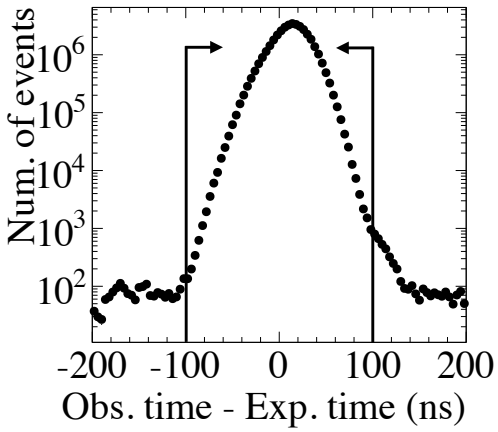

Figure 8.6.: Difference between the measured and expected timing. Events within ±100 ns are selected. Neutrino events summed over all modules are shown.

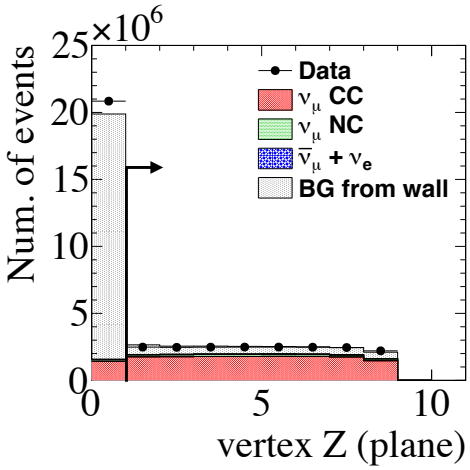

Figure 8.7.: Distribution of the vertex position in the Z (beam) direction. If there are hits at the upstream VETO plane, those events are rejected. Neutrino events summed over all modules are shown.

Figure 8.14 shows vertex-Z distributions for the neutrino events in which outgoing μ penetrates the most downstream plane. Such a event is called downstream (DS-) escaping event. These distribution are obtained from the data and are normalized by areas. As seen in the figure, there are more DS-escaping events at the upstream plane for module 3 when compared to module 0. As described in Sec. 8.1.1, a peak of the neutrino energy at module 0 shifts in the lower energy region due to the off-axis beam effect. Therefore, a more energetic μ is observed at the module 3. Such a μ can penetrate the most downstream plane even if it is created upstream. Different features in event topologies between modules are useful to determine the incoming neutrino energy. In fact, we use these features for an extraction of the energy dependent cross sections.

8.3. Basic detector performance

The performance of the INGRID detector has been monitored using the MPPC dark count and beam induced muons in order to ensure the long term stability in operation.

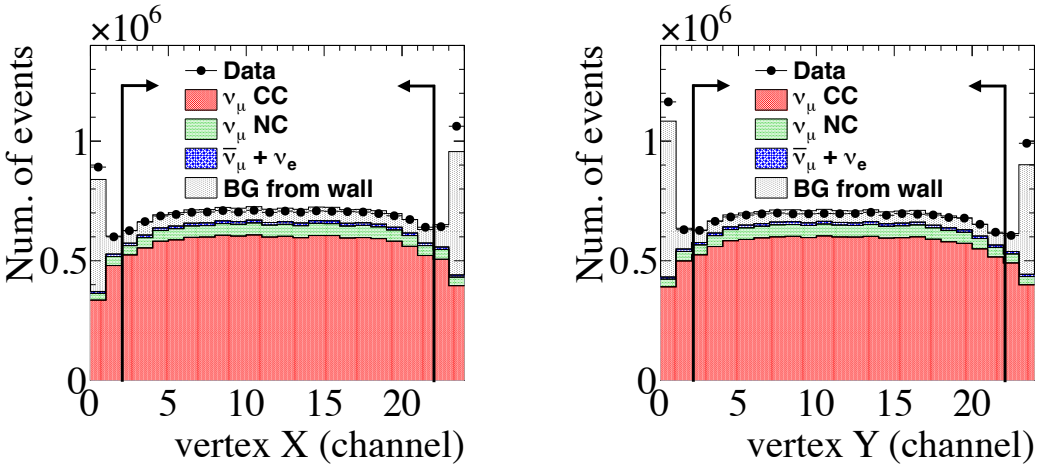

Figure 8.8.: Distribution of the vertice in the X (left) and Y (right) direction. The fiducial volume (FV) is defined as the cubic volume which has $(\pm 50)\times(\pm 50)$ cm^2 transverse area, corresponding to the area composed of scintillator bars from 3rd to 22nd channels in X and Y, and from tracking plane #1 to 8. Events having the vertices in FV are selected. Neutrino events summed over all modules are shown.

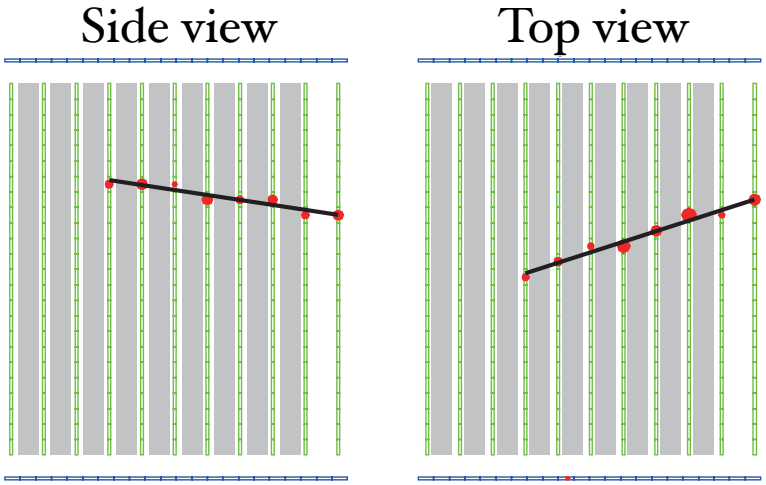

Figure 8.9.: Typical event display of the neutrino event from side (left) and top (right) view. The neutrino beam enters from the left. A size of the red circle denotes the size of the light yield at the scintillator planes.

8.3.1. Stability of the MPPC response

For each MPPC channel, the dark count spectra has been taken before and through the data-taking (beam-off) period. One of the MPPC dark count spectra is shown in Fig. 8.15.

Table 8.2.: Summary of the neutrino event selection. The p.o.t. used in the MC simulation is normalized to 6.25×10^{20} which is equivalent to an accumulated one over the periods of RUN 1, 2, 3c, and 4. The reconstructed events contains ν_μ, $\bar{\nu}_\mu$ and BG events which consist of sand muon, neutron and γ generated at the upstream wall of INGRID.

	Data	MC			
		ν_μ	$\bar{\nu}_\mu + \nu_e$	beam-related BG	Total
Vertexing	3.993×10^7	1.655×10^7	0.039×10^7	2.294×10^7	3.987×10^7
Timing cut	3.992×10^7	1.655×10^7	0.039×10^7	2.294×10^7	3.987×10^7
Veto cut	1.725×10^7	1.458×10^7	0.036×10^7	0.239×10^7	1.733×10^7
FV cut	1.103×10^7	1.098×10^7	0.027×10^7	0.006×10^7	1.131×10^7

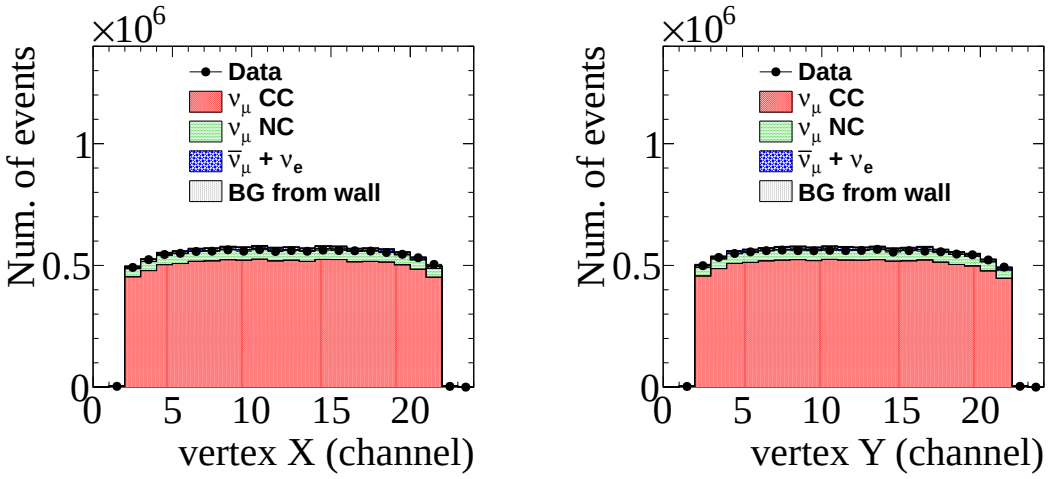

Figure 8.10.: Distribution of the vertice in the X (left) and Y (right) direction after all the event selections. Neutrino events summed over all modules are shown.

As seen in the figure, the ADC distribution has peaks corresponding to a pedestal and single (double) photo-electron. This is because MPPC has a capability of single photon counting and high dark noise rate of few hundreds Hz due to the thermal generation of carriers, which enable us to measure the single (double) photo-electron peaks without any light sources. A difference in the peak position between the pedestal and single photo-electron is defined as "gain". This MPPC gain is temperature dependent; as the temperature rises, vibration of the crystal lattice becomes stronger. This process increases the probability that carriers interact with the crystal before getting a sufficiency energy to occur the ionization process. This results in decreasing the gain. This decrease can be fixed by increasing the operation voltage applied to MPPC. In order to get a stable gain, the operation voltage has been adjusted for all the channels before the start

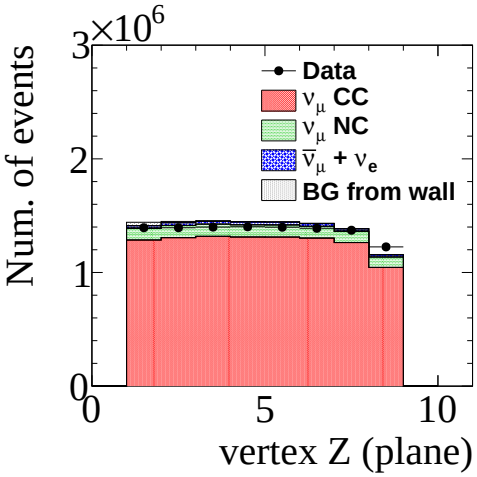

Figure 8.11.: Distribution of the vertex position in the Z (beam) direction after all the event selections. Neutrino events summed over all modules are shown.

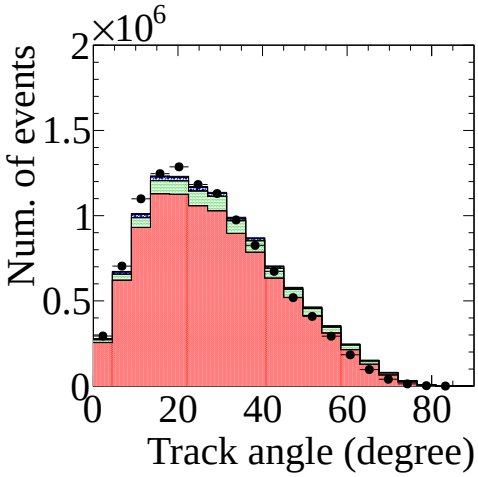

Figure 8.12.: Distribution of the reconstructed track angle after all the event selections. Neutrino events summed over all modules are shown.

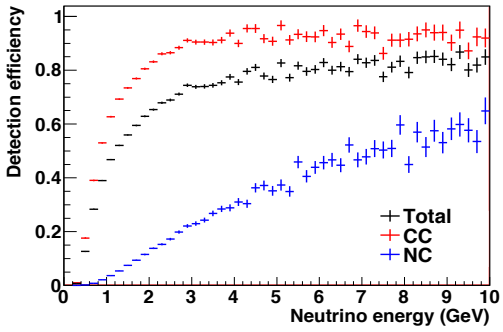

Figure 8.13.: Detection efficiency for CC (red), NC (blue), and CC+NC (black) events.

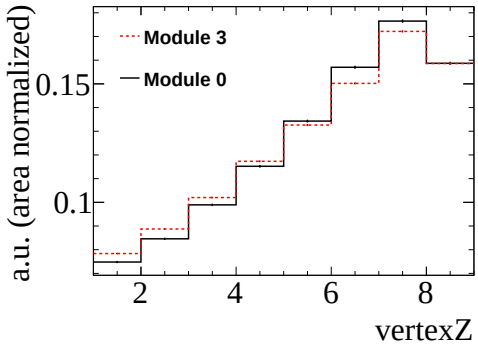

Figure 8.14.: Vertex-Z distributions of DS-escaping events for module 0 (black) and module 3 (red). These distribution are obtained from the data and are normalized by areas.

of beam operation. Figure 8.16 shows the stability of the MPPC gain for all the channels. As seen in the figure, a spread in the MPPC gain distribution is narrowed after tuning the operation voltage, which was done before a start of beam operation. In this way, we have tuned all the MPPC gains to ∼10 and have kept the variation within a 10% level.

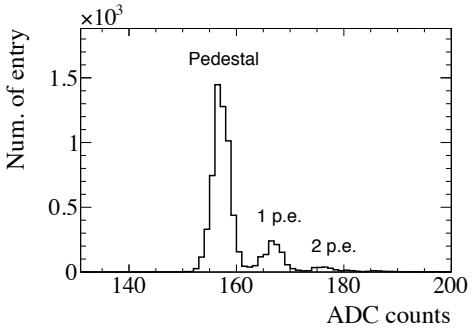

Figure 8.15.: ADC distribution of the MPPC dark count.

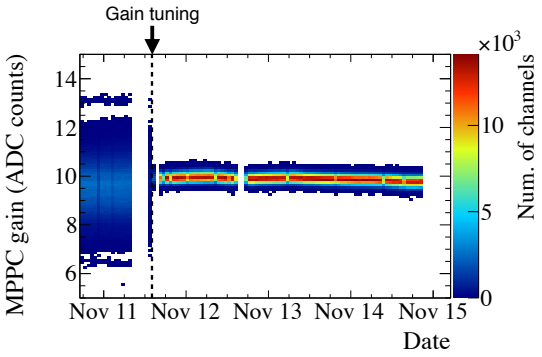

Figure 8.16.: Stability of the MPPC gain for all the channels. This data was taken before the start of RUN 2 operation.

8.3.2. Hit efficiency

A neutrino beam undergoes interactions in the upstream wall of INGRID (see Fig. 8.4), producing beam induced muons (sand muons). These muons are identified by searching hits at the upstream tracking plane in a module and are used to evaluate hit efficiency for each channel as follows. In each of the tracking plane except for the upstream and downstream ones, we check if the channel, which is expected to have hits from the track trajectory, has actual hits or not. The number of missed hits is then counted for the corresponding channel in order to calculate the hit efficiency. Figure 8.17 shows the obtained hit efficiencies for all the channels, which has an average of 98%. The 2% inefficiency is due to the fact that a muon with a small angle has a higher probability to go through a gap between scintillator bars and does not deposit the energy. Figure 8.18 shows the hit efficiency as a function of an angle of the reconstructed muon track with respect to the neutrino beam direction. As seen in the figure, the hit efficiency has a dependency on the track angle and a large inefficiency is observed around 5°, which is caused by the muon going through the gap as described above.

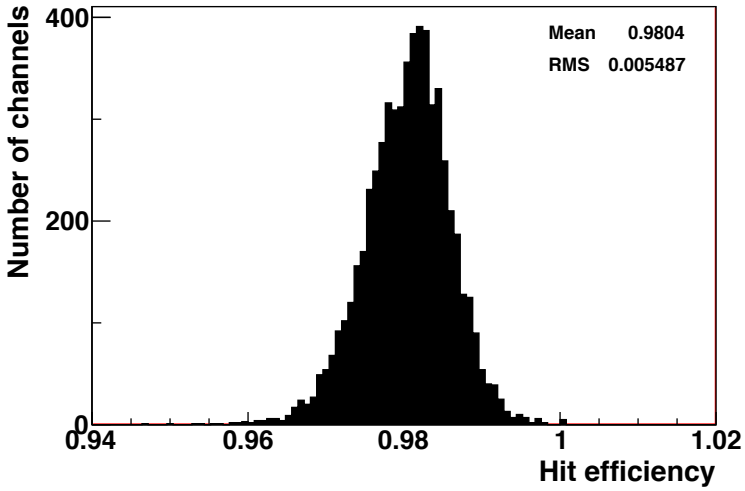

Figure 8.17.: Hit efficiencies for all the channels, which are measured with the sand muons.

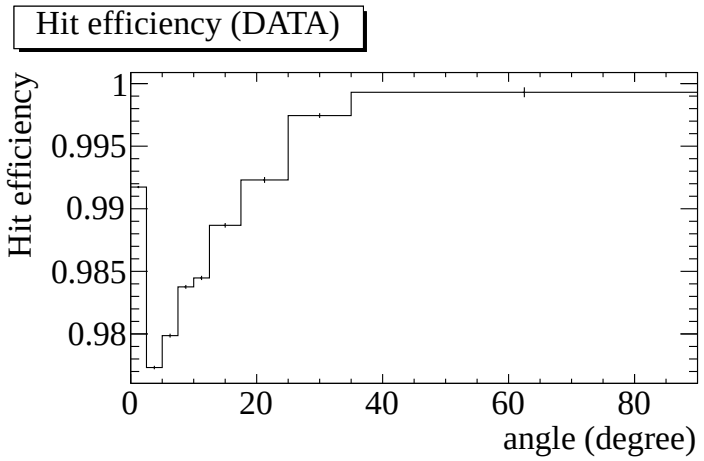

Figure 8.18.: Hit efficiency as a function of the track angle with respect to the beam direction, which are measured with the sand muons.

Chapter 9

Measurement of the energy dependent ν_μ CC inclusive cross section

The goal of this analysis is to measure the energy dependent ν_μ-Fe CC inclusive cross section with the INGRID detector in the energy range of 1-3 GeV. As described in Sec. 8.1, the neutrino energy spectrum has a dependence on the module position due to the off-axis beam effect. The difference of neutrino spectra at different modules can be used to extract the cross section at different energies. In addition, a usage of information of kinematics of the outgoing lepton (event topology) can enhance the sensitivity to the measurement. To derive the energy dependent cross section, we use the probability density function (PDF) of interaction rate at different positions and different event topologies for different energy regions. Details of the analysis method and the obtained PDF are described in Sec. 9.1. Section 9.2 shows the obtained samples and the predictions, which are categorized according to the module position and event topologies. Section 9.3 describes the systematic errors for this measurement. Finally we report the result of the measurement using the T2K data in Sec. 9.4. A summary and discussion of our result are given in Secs. 9.5 and 9.6, respectively.

9.1. Analysis method

9.1.1. Overview

The energy dependent cross section is measured by using a χ^2 fitting method. We use following information to construct the PDF for the χ^2. As described in Sec. 8.1.1, the peaks of the energy spectra of the neutrino fluxes are different between modules because each module covers different off-axis angle region. Figure 9.1 shows predicted energy spectrum of the reconstructed ν_μ event at the INGRID modules. The averaged energy of the neutrino beam is different for the different modules. Vertex position, track angle and number of iron layers penetrated by track are reconstructed during event selection. These event topologies can also be used to extract energy dependent cross section. By combining the information, difference energy spectrum at difference modules and event topologies, the PDF is constrcuted. A binning of the neutrino energy in the PDF is optimized so that sensitivity to the measurement becomes as high as possible. In the course of building the χ^2, the fit parameters for the cross section are required to be

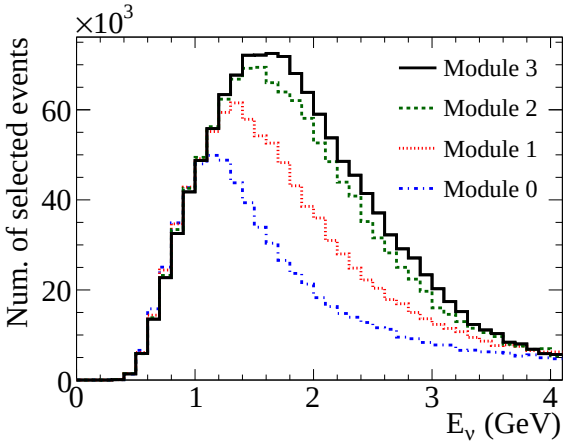

Figure 9.1.: Predicted energy spectrum of the reconstructed event at the INGRID modules.

continuous at each of the energy boundaries. The final cross sections are then measured by taking average of the neighbouring fit parameters, giving the cross section at 1.1, 2.0, and 3.3 GeV.

9.1.2. Event topology

After the neutrino event selection described in Sec. 8.2, the selected events are categorized according to following two topologies.

1. Downstream (DS-) escapingvertex-Z
2. Nondownstream (NonDS-) escaping

If one of the tracks from the neutrino interaction penetrates the most downstream plane as shown in Fig. 9.2 (a), that event is categorized into the DS-escaping. Other than the DS-escaping event, i.e. both of side escaping and fully contained events (see Fig. 9.2 (b)) are categorized into the NonDS-escaping. Events are then categorized according to vertex-Z position. Here, the vertex-Z is defined as the most upstream active plane number and ranges from 1 to 8. Figure 9.3 shows a schematic view of one of the INGRID modules. Each module has 11 tracking planes. In this analysis, events whose vertex-Z is in the range of 1-7 are used [1].

In total, there are 14 topologies;

- DS-escaping: vertex-Z=1-7
- NonDS-escaping: vertex-Z=1-7

[1] We found events where the vertex-Z is at downstream planes are largely affected by hadron production models in GEANT4 and decided not to use the topology of vertex-Z=8.

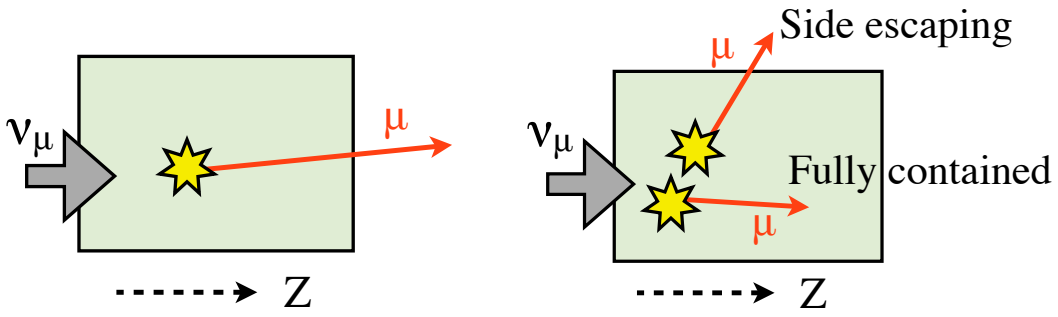

(a) DS-escaping (b) NonDS-escaping

Figure 9.2.: Event topology. If a track penetrates the most downstream plane, the event is categorized as DS-escaping (a). The other events are categorized as NonDS-escaping (b).

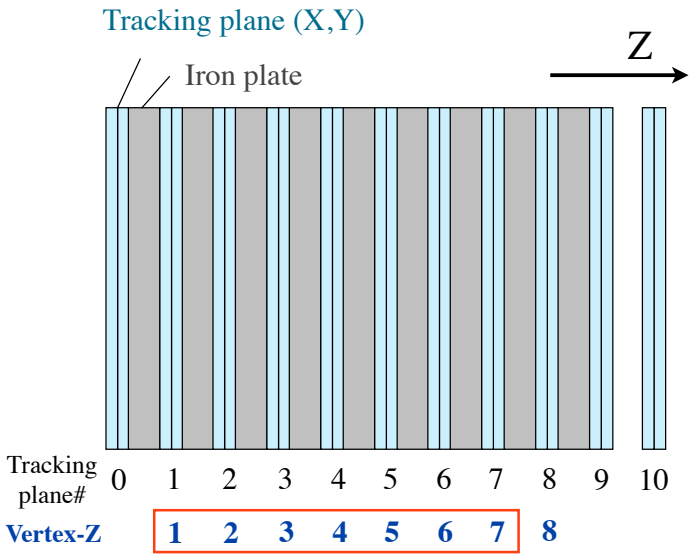

Figure 9.3.: Schematic side view of an INGRID module. A module has 11 tracking planes and 8 iron plates. vertex-Z is defined as the most upstream active plane number. In this analysis vertex-Z 1-7 are used.

Figure 9.4 shows the energy spectra of "DS-escaping & vertex-Z=1" events and "NonDS-escaping & vertex-Z=7" events for different modules (module 0 and 3). The former has a more energetic μ track and hence higher energy neutrino. On the other hand, the latter has a larger μ angle or a shorter track and hence lower energy neutrino.

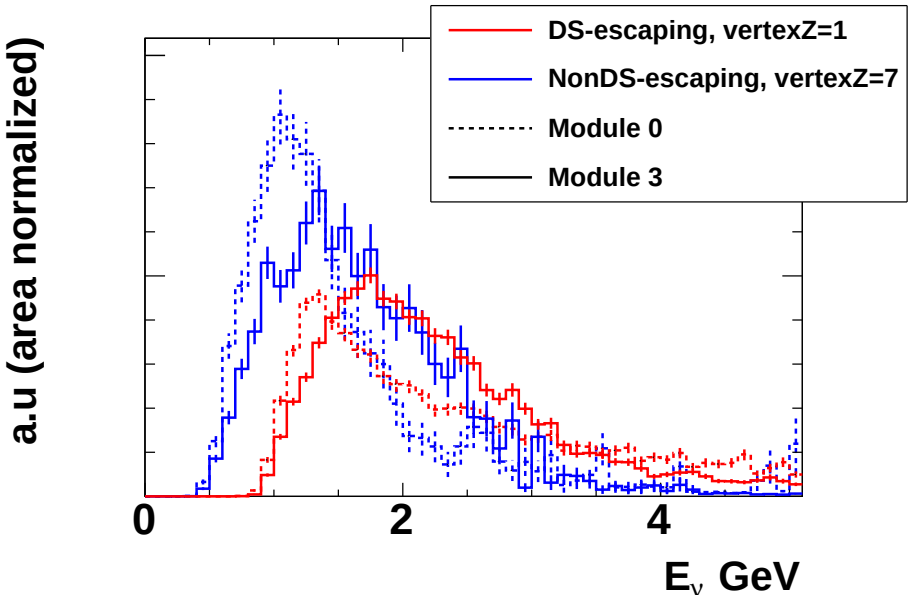

Figure 9.4.: Neutrino energy spectra for "DS-escaping & vertex-Z=1" (red) events and "NonDS-escaping & vertex-Z=7" (blue) events. The energy spectra for module 0 (dashed line) and 3 (solid line) are shown. Both spectra are normalized by the areas.

9.1.3. Grouping two modules

A shift of the neutrino beam direction changes the peak of the neutrino energy spectra at the INGRID modules. In order to reduce this effect, we group two modules at beam-axis symmetric positions in horizontal and vertical direction separately. This results in 7 module groups in total. The definition of the module group is shown in Table 9.1. Then the number of selected events for each module group and each topology is defined as,

$$N_{jg} = \frac{N_{jm} + N_{jm'}}{2} , \tag{9.1}$$

where index of j and g denote the j^{th} topology and the g^{th} module group ($g = 1, 2, .., 7$), respectively. The index of m and m' stand for the module numbers corresponding to this group.

Table 9.1.: Definition of the module groups

Module group	Module #	Distance from the beam axis (cm)	Horizontal or Vertical
1	0, 6	450	Horizontal
2	7, 13	450	Vertical
3	1, 5	300	Horizontal
4	8, 12	300	Vertical
5	2, 4	150	Horizontal
6	9, 11	150	Vertical
7	3, 10	0	(Center)

9.1.4. Extraction of the cross section

This analysis uses a χ^2 fitting to the observed number of selected events at each module group (g^{th} bin) and for each event topology (j^{th} bin):

$$\chi^2 = \sum_j \sum_g \chi^2_{jg} = \sum_j \sum_g \frac{(N^{obs}_{jg} - N^{exp}_{jg})^2}{(\sigma_{N^{obs}_{jg}})^2} \ , \tag{9.2}$$

The N^{obs} and $\sigma_{N^{obs}}$ are the observed number of events and its statistical error, respectively. N^{exp} is the number of events predicted by MC and is decomposed as follows.

$$N^{exp} = N^{cc} + N^{nc} + N^{bg} \ , \tag{9.3}$$

where N^{cc}, N^{nc}, and N^{bg} are the number of CC events, NC events, and BG events, respectively. The BG events are induced by

- sand muons and neutral particles (n and γ) generated by neutrino interactions at the upstream wall,
- $\bar{\nu}_\mu$ components in the beam flux, and
- ν_e components in the beam flux.

The expected number of CC events at g^{th} module group and for j^{th} event topology is expressed as:

$$N^{cc}_{jg} = \sum_i (1 + \Delta f_i) \cdot \phi_{ig} \cdot \sigma^{cc}_i \cdot \epsilon^{cc}_{ij} \cdot T \ . \tag{9.4}$$

where the index of i denotes the i^{th} energy bin; ϕ, σ^{cc}, and ϵ^{cc} are the ν_μ flux, ν_μ CC cross section[2], and the detection efficiency, respectively; T is the number of the nucleons in the target, i.e. fiducial volume of the INGRID module; Δf is a parameter to represent the fractional deviation of the CC inclusive cross section and used as a fit parameter for the cross section model. In order to include the systematic parameters on the signal, equation (9.4) is modified as follows.

$$N^{cc}_{jg} = (1+\Delta f^d_j)\cdot(1+\Delta f^{cc}_j)\sum_i (1+\Delta f^b_{ig})\cdot(1+\Delta f_i)\cdot\phi_{ig}\cdot\sigma^{cc}_i\cdot\epsilon^{cc}_{ij}\cdot T\ , \tag{9.5}$$

where Δf^d_j and Δf^{cc}_j are the parameters representing the uncertainty in detector response and CC interactions for the j^{th} topology bin, respectively. In fact, these uncertainties change the detection efficiency as a function of neutrino energy, resulting in variation of the number of j^{th} topology. Therefore, the systematic parameter is introduced as the uncertainty on the expected number of j^{th} topology and the covariance matrix is constructed as described in Sec. 9.3. Since differences in these uncertainties between the module groups were found to be very small, only the difference between the event topologies are taken into account. Δf^b_{ig} is a flux uncertainty for the i^{th} energy bin for the g^{th} module. The Δf^d_j, Δf^{cc}_j and Δf^b_{ig} are parametrized as the fractional deviation from a nominal value and change the number of events in each category. Details of these systematic errors are described in Sec. 9.3.

Likewise, the number of NC events which is our major BG is expressed as,

$$N^{nc}_{jg} = (1+\Delta f^d_j)(1+\Delta f^{nc}_j)\sum_i (1+\Delta f^b_{ig})\cdot\phi_{ig}\cdot\sigma^{nc}_i\cdot\epsilon^{nc}_{ij}\cdot T\ , \tag{9.6}$$

where Δf^{nc}_j is the normalization error which attributes to NC interaction systematic errors for the j^{th} topology. Since a fraction of the NC events is very small, the NC events are summed over the entire energy region and a following averaged flux systematic parameter is used:

$$\Delta\bar{f}^b_g = \sum_i \Delta f^b_{ig}\cdot\frac{\phi_{ig}}{\sum_{i'}\phi_{i'g}}\ . \tag{9.7}$$

Then, equation (9.6) becomes,

$$N^{nc}_{jg} = (1+\Delta f^d_j)(1+\Delta\bar{f}^b_g)(1+\Delta f^{nc}_j)\sum_i \phi_{ig}\cdot\sigma^{nc}_i\cdot\epsilon^{nc}_{ij}\cdot T\ . \tag{9.8}$$

The number of BGs are obtained by summing up those from the wall, ν_e and $\bar{\nu}_\mu$ for each module and for each topology (N^{bg}_{jg}). The contamination of BG is less than 5% according to Table 9.3. The size of flux and detector systematic error are 15% and 3%, respectively

[2]We do not take account of ν_μ CC interaction with CH in this analysis. Here we assume event rate per unit weight on CH is equal to that on Fe. Effects of the CH interaction is summarized in Appendix G. As described in this chapter, we can ignore the effect on our final results.

according to Table 9.4. That is to say, the effect on the total number of events due to the systematic error of BG is less than 1%. Therefore, we neglect the error of BG.

Finally, we obtain,

$$\chi^2 = \sum_j \sum_g \frac{\left\{ N_{jg}^{obs} - (N_{jg}^{cc} + N_{jg}^{nc} + N_{jg}^{bg}) \right\}^2}{(\sigma_{N_{jg}})^2} + \sum_k \Delta(\vec{f}^k)^t (V_k)^{-1} \Delta \vec{f}^k \ , \tag{9.9}$$

where N_{jg}^{obs} is the observed number of selected events in the j^{th} topology bin and the g^{th} module. The denominator in the χ^2 statistical term is,

$$\sigma_{N_{jg}} = \sqrt{N_{jg}^{obs} + \left(\sigma_{N_{jg}^{mc}}\right)^2 + \left(\sigma_{N_{jg}^{det}}\right)^2} \ , \tag{9.10}$$

where $\sigma_{N_{jg}^{mc}}$ and $\sigma_{N_{jg}^{det}}$ are the MC statistical error and the uncorrelated detector systematic error, respectively. $\Delta\vec{f_k}$ and V_k are the systematic parameter and the covariance for the k^{th} error source (flux, neutrino interaction, and detector systematic error), respectively. The second term gives a prior constraint for these parameters.

9.1.5. Energy binning

At each of the neutrino energy bin (i.e. i^{th} bin in Eq. 9.5), the cross section is given from Δf_i obtained by fitting to data with χ^2 as described in Sec. 9.1.4. The binning of the neutrino energy is optimized in order to keep sensitivity to the cross section measurement as high as possible. We also require the cross section to be continuous at bin boundaries and Eq. 9.5 is modified as follows:

Table 9.2.: Summary of the energy range of the global bin, bin size of each local bin, and the number of the local bins

Energy range of global bin (GeV)	Bin size of each local bin (MeV)	Number of local bins (L_i)
0-0.5	500	1
0.5-0.8	100	3
0.8-1.4	100	6
1.4-2.6	100	12
2.6-4.0	100	14
4.0-30.0	26000	1

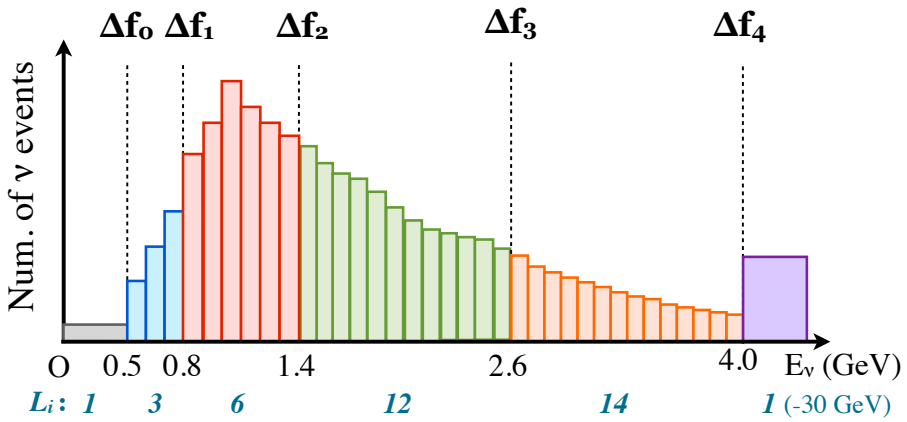

Figure 9.5.: Position of normalization factors for the cross section and the binning of the "local bin". L_i denotes the number of local bins for the i^{th} energy bin.

$$N^{cc}_{jg} = (1+\Delta f^d_j)\sum_i (1+\Delta f^b_{ig}) \cdot \sum_{l=0}^{L_i} \left(1 + \Delta f_i + \frac{\Delta f_{i+1} - \Delta f_i}{L_i} \cdot l\right) \cdot \phi_{ilg} \cdot \sigma^{cc}_{il} \cdot \epsilon^{cc}_{ilj} \cdot T \ . \tag{9.11}$$

Each i^{th} energy bin is divided into fine bins ($l = 0, 1, .., L_i$). We define the i^{th} energy bin as "global bin" and the l^{th} energy bin as "local bin", respectively. The definition of energy range of the "global bin" and the binning of the "local bin" are summarized in Table 9.2. The Δf_is are set at 0.5, 0.8, 1.6, 2.4, and 4.0 GeV as shown in Fig. 9.5. Finally the energy dependent CC inclusive cross sections are extracted as follows. After deriving the fit parameters by the least χ^2 method, we take an average of neighboring parameters: $\frac{\Delta f_1+\Delta f_2}{2}$, $\frac{\Delta f_2+\Delta f_3}{2}$, and $\frac{\Delta f_3+\Delta f_4}{2}$. This is because we apply a linear interpolation between the neighbouring Δf_is as in Eq. 9.11. As a result, the cross sections at 1.1, 2.0, and 3.3 GeV are measured. Δf_0 is not used for the final result. This is because the detection efficiency rapidly rises up at ∼0.5 GeV region and detection systematic errors can affect this energy region. As for $E_\nu > 4.0$ GeV, there is only a small difference in the neutrino energy spectra between modules. Therefore, sensitivity to the measurement of the cross section for $E_\nu > 4.0$ GeV is expected to be worse as compared to the other energy region. From these reasons, we use Δf_1-Δf_4 to measure the cross sections at 1.1, 2.0, and 3.3 GeV.

In this analysis, fitting parameters are set to cover the entire energy region and then the linear interpolation is applied as described above. In this way, the final error on the cross section is reduced since anti-correlations between the fitted parameters are cancelled out after taking average of the neighbouring Δf_is.

9.1.6. PDF

Figures 9.6 and 9.7 show the probability density function (PDF) of CC events for each energy region. Here "fraction" in the figure is obtained for each energy region by dividing the number of CC events in each bin by the total number of CC events. As shown in Fig. 9.6, at lower neutrino energy, most of the CC events is selected at the downstream vertex-Z for DS-escaping. At the higher energy, the CC events is then uniformly distributed at any vertex-Z. For NonDS-escaping, the CC events are selected at any vertex-Z for low energy neutrinos and tend to be selected at the upstream vertex-Z for high energy neutrinos. In addition, more high energy neutrino events are selected at modules closer to the beam-axis.

9.2. Data and MC comparison

T2K RUN 1, 2, 3c, and 4 data sets were used (see Table 2.3) in this analysis. The corresponding accumulated p.o.t is 6.27×10^{20}. Table 9.3 summarizes the observed and predicted numbers of events for RUN 1+2+3c+4 data set. The numbers are those obtained by summing over all module groups. The distribution of the event topology is shown in Figure 9.8. As seen in the figure, the number of observed events for NonDS-escaping is 3-10% smaller than the expectation.

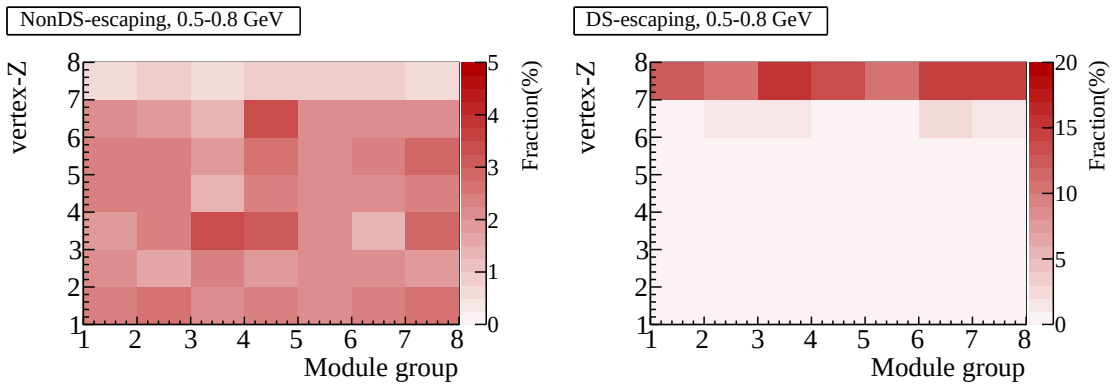

(a) E_ν =0.5-0.8 GeV

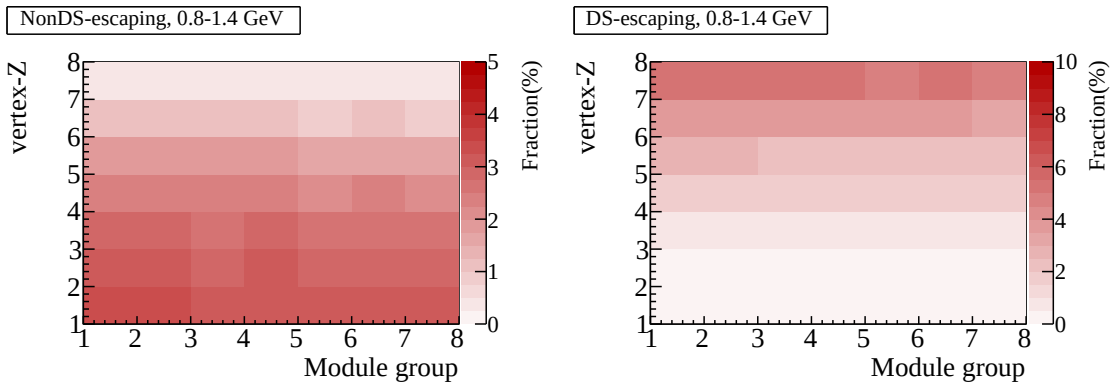

(b) E_ν =0.8-1.4 GeV

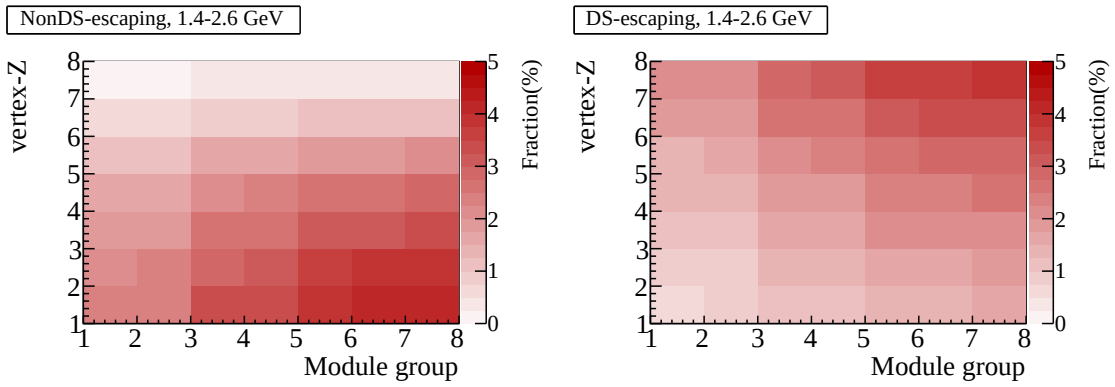

(c) E_ν =1.4-2.6 GeV

Figure 9.6.: Probability density function (PDF) for the energy region of 0.5-0.8 GeV, 0.8-1.4 GeV, and 1.4-2.6 GeV.

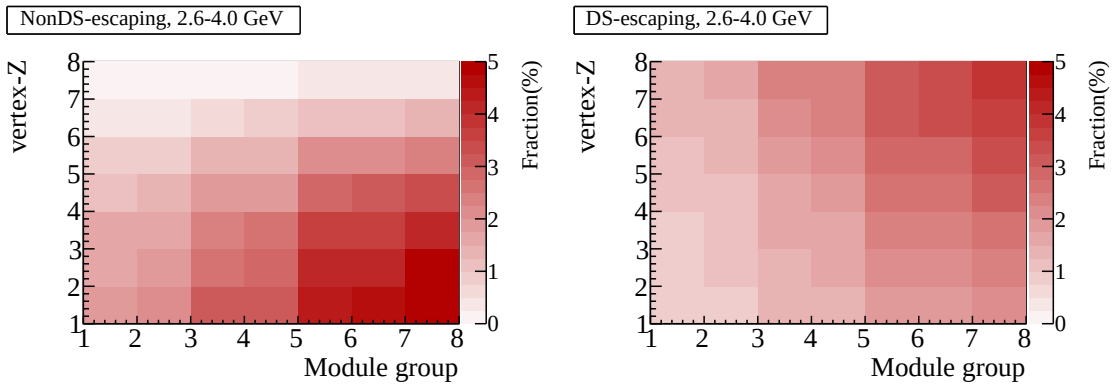

(a) E_ν =2.6-4.0 GeV

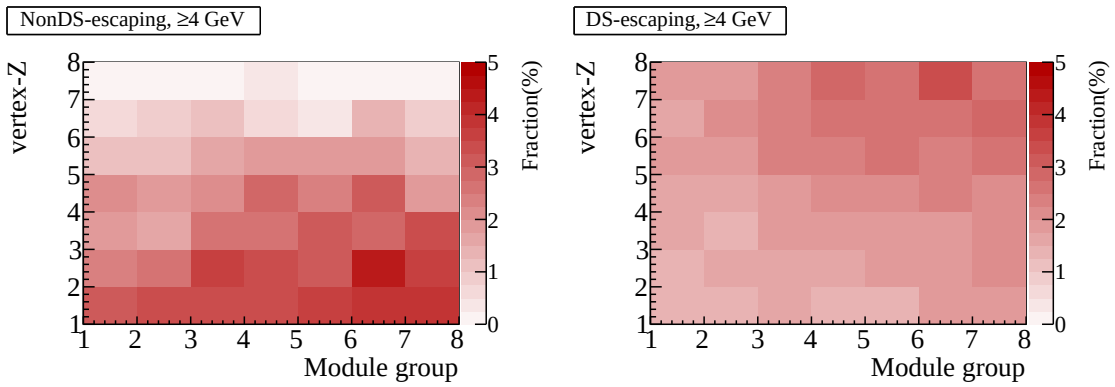

(b) E_ν ≥4.0 GeV

Figure 9.7.: Probability density function (PDF) for the energy region of 2.6-4.0 GeV and >4.0 GeV.

Table 9.3.: Observed predicted number of events for each event topology for RUN 1+2+3c+4 data set. Here FTFP_BERT in GEANT4 is used for the prediction. Each number in this table is the sum of all module groups.

			MC			
Escaping type	vertex-Z	Data	Total	CC	NC	other BG
Non-Downstream	1	411057	438803.1	365407.3	49155.2	24240.5
	2	371859	403381.7	338873.3	50319.0	14189.4
	3	319134	354731.8	295553.5	47548.7	11629.7
	4	266306	295332.9	242181.1	42792.4	9399.0
	5	199991	216384.0	176340.5	33546.1	6497.4
	6	118434	120620.5	98297.5	19188.2	3134.8
	7	30603	31491.0	26987.6	3900.0	603.4
Downstream	1	287951	283622.9	273230.1	1991.8	8401.0
	2	333175	326215.8	314437.5	3659.3	8119.0
	3	372833	378758.0	363744.0	6212.9	8801.1
	4	427482	437337.4	415742.5	11332.5	10262.5
	5	492671	517036.9	483886.6	20377.6	12772.7
	6	572959	603779.9	555383.9	33221.9	15174.1
	7	656318	667995.4	604778.7	46096.5	17120.3

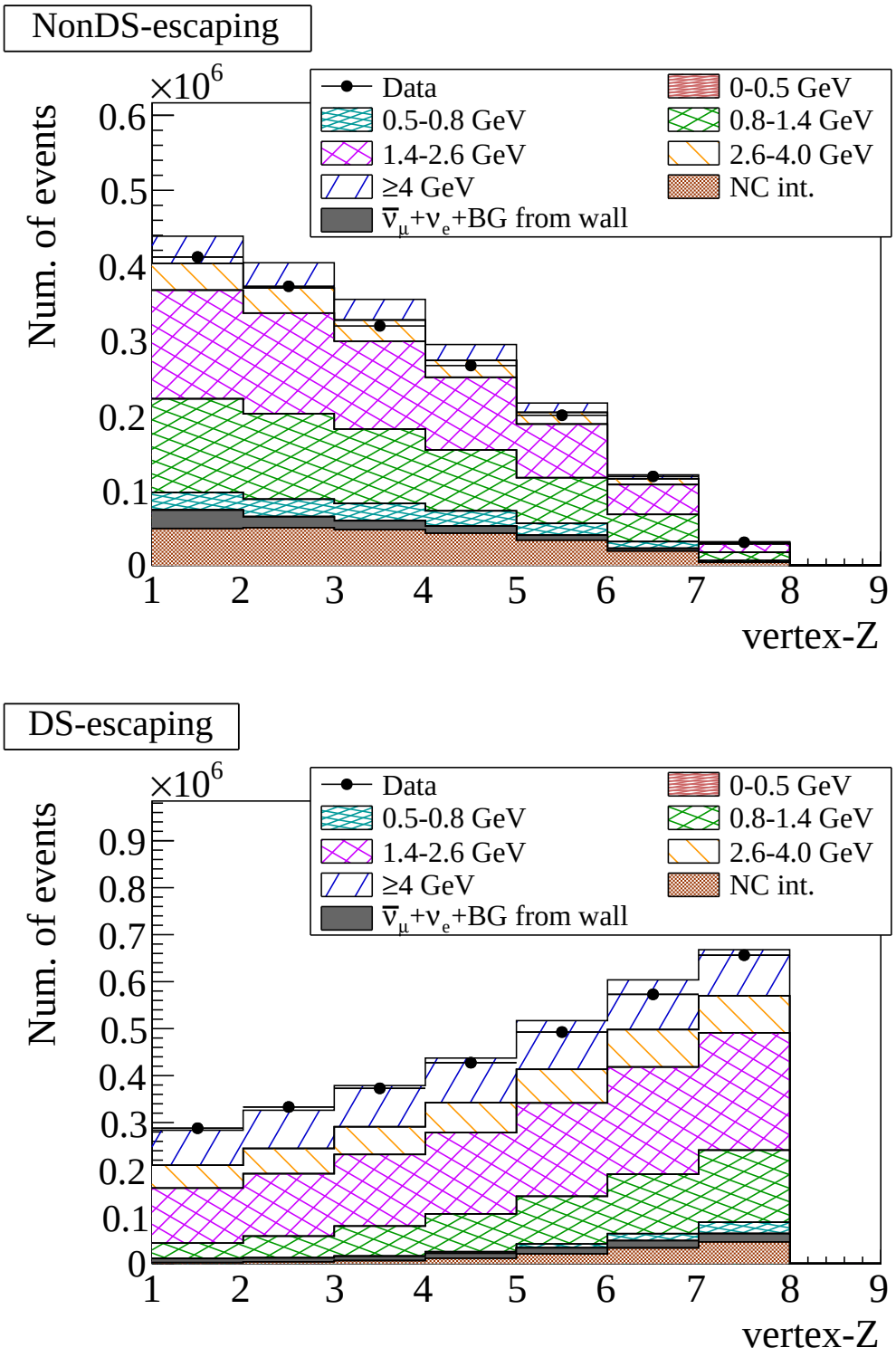

Figure 9.8.: Topology distribution for NonDS-escaping (top) and DS-escaping (bottom) of Run 1+2+3c+4 data set. They are the sum over all module groups. The predicted events are categorized according to CC events, NC events, and beam $\bar{\nu}_\mu + \nu_e$ and BG from wall, and shown as a stacked histogram. The CC events are subdivided into those in 6 true neutrino energy regions.

Table 9.4.: Systematic error sources and the maximum error size among topology bins.

Error source		Error size (at maximum)
Flux		15%
Detector	uncorrelated error	2%
	correlated error	3%
Neutrino interaction	NC interaction	5%
	CC interaction	3%
Pion FSI		After data fit
Pion multiplicity		After data fit
Pion SI		After data fit

9.3. Systematic errors

Table 9.4 summarizes the systematic error source and the error size on the number of selected events. The systematic errors arise from uncertainties in the neutrino flux, detector response, and neutrino interaction. We also take account of uncertainties in the pion final state interaction (FSI), multiplicity, and secondary interaction (SI). The error size of these three uncertainties are estimated after the fit to data is done. In this section, we explain each of the error sources.

9.3.1. Neutrino flux

As we describe in Sec. 6.4.2, the hadron production cross section and multiplicity at p+C interaction were tuned so that it matches to external measurements. The systematic error of the neutrino flux was estimated by using those measurement errors. Uncertainties from primary beam optics, horn focusing, and alignments in the beam-line were also taken into account. Details of the flux error estimation can be found in [42]. In this analysis, we also take account of the uncertainty in the neutrino beam direction which is estimated from the measurement by INGRID. Figure 9.9 shows the fractional error of the neutrino flux at module group 6. In this figure not only the total error but also a breakdown of the flux errors are shown. The total error size is 10-15% for $E_\nu < 4$ GeV. The flux covariance matrix, which gives correlations among module groups and energies, was constructed and implemented into the χ^2. The obtained correlation matrix is shown in Figure 9.10. The energy binning used in the covariance matrix is same as "global bin" defined in Table 9.2.

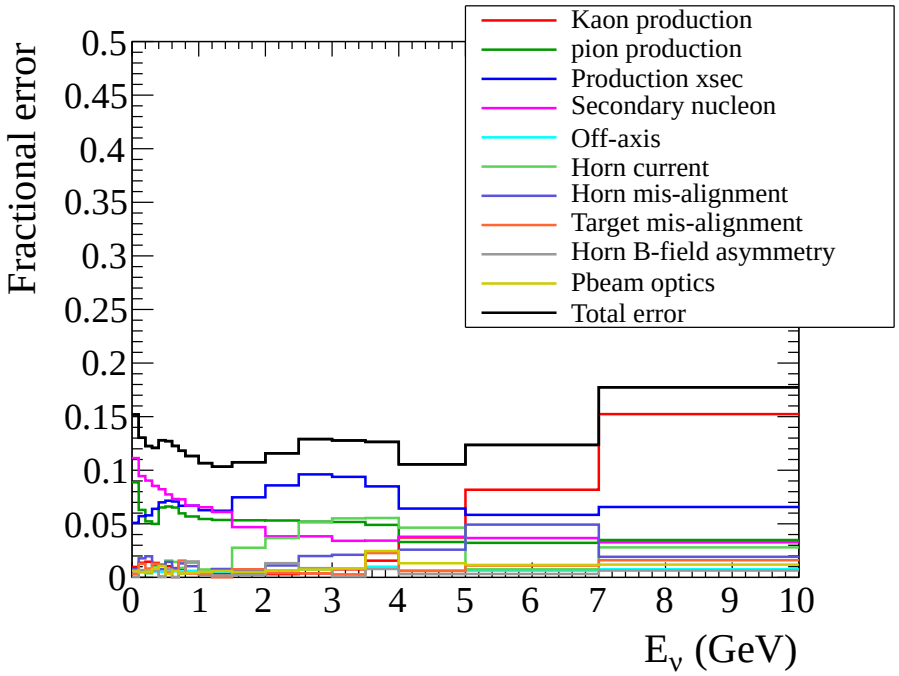

Figure 9.9.: Fractional flux error for each error source.

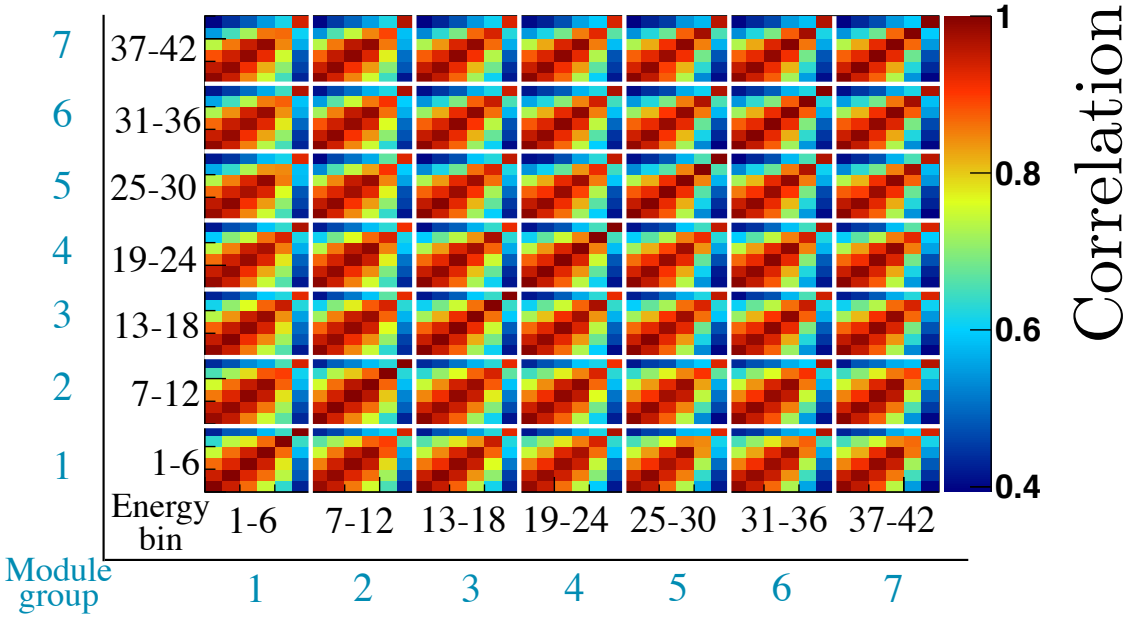

Figure 9.10.: Correlation matrix between module groups for the flux error. The energy binning used in this matrix is same as "global bin" defined in Table 9.2.

9.3.2. Detector response

In this analysis, the correlation between event topologies for each error source needs to be taken into account. We categorize each error source into two types by seeing if it gives correlation among topology bins or not. The correlation types and sources of the systematic error are summarized as follows:

- Uncorrelated error
  - Mass of iron plate
  - Pileup correction
- Correlated error
  - Event selection
  - Accidental MPPC noise rate

For the correlated error source, a covariance matrix for topology bins averaged over all modules was constructed. For the uncorrelated error source, we did not construct the covariance. Instead we calculated the error size for each topology and for each module group and inserted it into the denominator of the χ^2 statistical term ($\sigma_{N_{jm}^{det}}$ in Eq.(9.10)).

Uncorrelated error

Iron mass

An error of 0.09% is assigned to the number of selected events, which attributes to a measurement error of the mass of each iron plate and the machining tolerance for the plate area.

Pileup correction

As described in Sec. 8.2, the number of selected events is corrected to avoid a loss of events due to the event pileup. The uncertainty on the correction factor is estimated and the error of 0.5-2% is assigned to the number of selected events.

The systematic error from "Iron mass" and "Pileup correction" are summed up quadratically and the total error is inserted into the denominator in χ^2 statistical term ($\sigma_{N_{jm}^{det}}$ in Eq. (9.10)).

Correlated error

Accidental MPPC noise

Accidental MPPC noise hit sometimes results in mis-reconstruction of vertex or miscounting of the number of active planes, which results in variation of the neutrino event selection efficiency. In the nominal MC simulation, 4 hits/module/cycle is

used for the MPPC noise rate. On the other hand, the maximal measured noise rate for RUN 1-4 is 5.84 hits/module/cycle. The number of selected events for each topology with the measured maximal rate is estimated using MC. The effect of the difference of the noise rate is 1% at maximum. This difference is taken as the systematic error of the accidental MPPC noise.

Event selection

The systematic errors from all event selections are evaluated by varying each selection threshold and by comparing the resultant fractional variation ($\equiv \Delta N/N$) in the number of selected events for the data and MC. We pick up the loosest or the tightest criterion. Such a change from the nominal criterion to the loosest (tightest) criterion is defined as "$+1\sigma(-1\sigma)$ change". Difference in $\Delta N/N$ between the data and MC is then calculated to be:

$$\Delta_{i(j)} = \left(\frac{\Delta N_{obs}}{N_{obs}}\right)_{i(j)} - \left(\frac{\Delta N_{exp}}{N_{exp}}\right)_{i(j)} , \tag{9.12}$$

where index of $i(j)$ denotes the $i(j)^{th}$ topology bin. The covariance is then constructed using Δ_i. If both of the $+1\sigma$ and -1σ change of the event selection are estimated, following covariance is calculated:

$$V_{ij} = \frac{1}{2}\left\{(\Delta_i \cdot \Delta_j)_{+1\sigma} + (\Delta_i \cdot \Delta_j)_{-1\sigma}\right\} . \tag{9.13}$$

If only the $+1\sigma$ change of the event selection is estimated, the covariance is,

$$V_{ij} = \Delta_i \cdot \Delta_j . \tag{9.14}$$

The statistical error of Δ_i is also calculated and added to Eq. (9.13) (or Eq. (9.14)). In this error estimation, uncertainties in following event selections are taken into account:

- 3D track matching
- Vertexing
- VETO cut by the surrounding VETO planes
- FV cut

Other systematic errors

Following uncertainties are not taken into account because they are negligible in this analysis.

Hit efficiency

The uncertainty in the hit efficiency was estimated from a comparison between the

Table 9.5.: Detector systematic error type and its error size.

Error type	Error size (at maximum)
Correlated error	3%
Uncorrelated error	2%

data and MC. Variation of the number of selected due to the uncertainty in the hit efficiency was estimated be less than 0.5%.

Beam-related BG

The contamination of the beam-related BG was estimated using the BG simulation which generates particles from the neutrino interaction at the upstream wall of the INGRID detectors. The systematic error of the number of selected events due to the uncertainty in the BG was estimated to be around 0.2%.

Upstream VETO cut

The hit inefficiency of the upstream VETO plane leads to an increase of sand muon events and it affects the number of neutrino events. We estimated that the uncertainty in the hit efficiency gives only 0.03% variation in the number of events.

Tracking effieincy

Uncertainty in the tracking efficiency was estimated from a comparison between the data and MC. We checked the effect of the uncertainty on the final result and found that it gives less than ∼1% changes in the cross section normalizations. Therefore, we neglect this error.

Summary of detector systematic error

For correlated errors, the total covariance is calculated by summing up each covariance. Figure 9.11 shows the obtained total error matrix (top) and correlation matrix (bottom). Table 9.5 summarizes the size of the detector systematic error for each error type.

9.3.3. Neutrino interaction systematic error

Table 9.6 summarizes the parameters used for modeling the neutrino interaction in NEUT. The systematic parameters listed in the table were used in the previous analyses of neutrino oscillation in T2K [133, 134]. These are categorized into following four types:

M_A^{QE}, M_A^{RES}, Fermi momentum, binding energy, and spectral function

These parameters are used for modeling CCQE, CC1π, and the nuclear model for the CCQE interaction. The 20% error is assigned for uncertainty in the axial mass vector from a comparison among external data sets. The uncertainty on Fermi

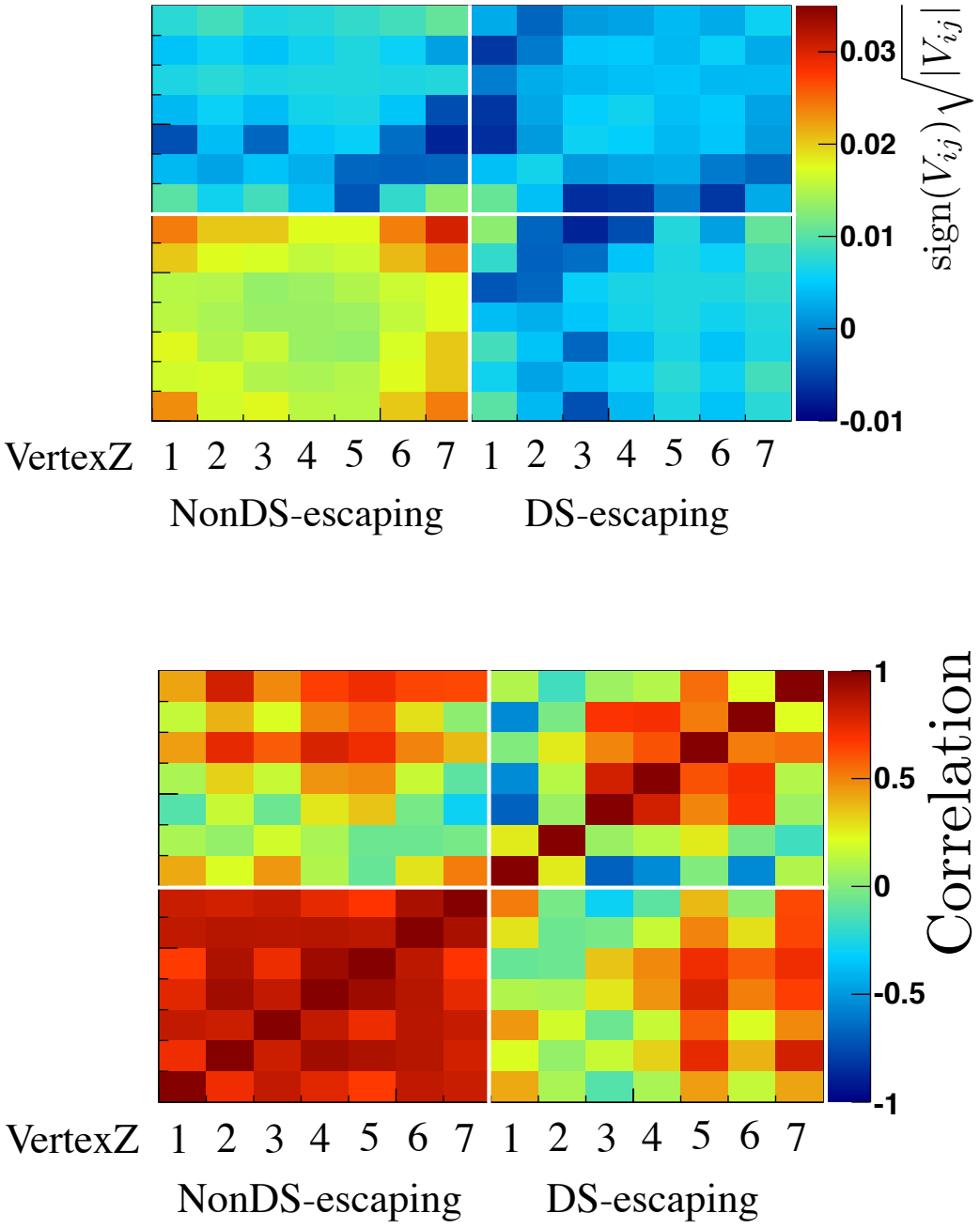

Figure 9.11.: Total error matrix (top) and the correlation matrix (bottom) for the detector correlated errors. In both of the matrices, the binning on the y-axis is identical to that on the x-axis.

momentum and binding energy are estimated from electron scattering data [93]. The error from the RFG model is estimated by alternating the model with the spectral function model.

π-less Δ decay and W shape

These parameters are empirically introduced. In the resonant pion production process, baryon resonances, mainly Δ, can interact with other nucleons and disappear without pion emissions. The π-less Δ decay parameter is introduced to take into account uncertainties on this process. The W shape parameter is introduced in order to modify the shape of the momentum distribution of pion produced by the NC single pion production process so that it matches MinibooNE data [135].

Normalization paramaters

Normalization parameters are used to change an overall normalization of the cross section. The normalizations for CCQE and CC1π are defined separately for different energy region. Uncertainty on the normalizations are mostly determined from the MiniBooNE data. A parameter of the CC other shape is introduced as an energy dependent uncertainty. The error size is estimated from external data [116] and is defined as:

$$\sigma_{CCother} = \frac{0.4 \text{ GeV}}{E_\nu} , \tag{9.15}$$

where E_ν is the neutrino energy in GeV. The interactions have a threshold energy of approximately 0.6 GeV and the uncertainty is an order of 10% at 4 GeV. A parameter of the 1π E_ν shape is a weighting factor as a function of neutrino energy and is applied to the CC1π cross section in order to make the data [136] and prediction agree. In the nominal NEUT, this weighting is not taken into account ("off" as in Table 9.6). A half size of the weighting factor (50%) is used for the uncertainty on this parameter.

Pion final state interaction

There are three final-state interactions (FSIs) of interest in the T2K energy range: absorption, charge exchange, QE scattering (see Sec. 7.5). In addition to these interactions, we also considered a process of particle production defined as "inelastic scattering", which is a dominant process at the higher pion energy. Uncertainties on these errors are estimated using external data sets.

In this analysis, the systematic error from the uncertainty in the CC interaction and NC interaction are evaluated separately.

Table 9.6.: Neutrino interaction systematic parameters, nominal values, uncertainties (1σ), and interaction types (CC, NC or CC+NC). First, second, and third groups represent the model parameters, the ad hoc parameters, and the pion FSI parameters. The 1 or 0 in the nominal value means the effect of the systematic parameter is implemented or not implemented by default, respectively [133, 134].

Parameter	Nominal value	Uncertainty (1σ)	Interaction type
M_A^{QE}	1.21 GeV	0.20 GeV	CC
M_A^{RES}	1.21 GeV	0.20 GeV	CC+NC
Fermi momentum (Fe)	250 MeV/c	30 MeV/c	CC
Binding energy (Fe)	33 MeV	9 MeV/c	CC
Spectral function	0 (off)	1 (on)	CC
π-less Δ decay	0.2	0.2	CC + NC
W shape	87.7 MeV	45.3 MeV	CC+NC
CCQE normalization ($E_\nu \leq 1.5$ GeV)	1	0.11	CC
CCQE normalization ($1.5 \leq E_\nu \leq 3.5$ GeV)	1	0.30	CC
CCQE normalization ($E_\nu \geq 3.5$ GeV)	1	0.30	CC
CC1π normalization ($E_\nu \leq 2.5$ GeV)	1	0.21	CC
CC1π normalization ($E_\nu \geq 2.5$ GeV)	1	0.21	CC
CC coherent normalization	1	1.0	CC
CC other shape	0 GeV	0.4 GeV	CC
NC $1\pi^0$ normalization	1	0.31	NC
NC coherent *pi* normalization	1	0.30	NC
NC $1\pi^\pm$ normalization	1	0.30	NC
NC other normalization	1	0.30	NC
1π E_ν shape	0 (off)	0.50	CC + NC
Pion absorption	1	0.5	CC+NC
Pion charge exchange ($P_\pi < 500$ MeV/c)	1	0.5	CC+NC
Pion charge exchange ($P_\pi > 400$ MeV/c)	1	0.3	CC+NC
Pion QE scattering ($P_\pi < 500$ MeV/c)	1	0.5	CC+NC
Pion QE scattering ($P_\pi > 400$ MeV/c)	1	0.3	CC+NC
Pion inelastic scattering	1	0.5	CC+NC

NC interaction systematic error

The uncertainty of the NC interaction on each bin is expressed by the normalization parameter:

$$f_{jg}^{nc} \equiv \frac{N_{jg}^{\prime nc}}{N_{jg}^{nc}} \ , \tag{9.16}$$

where N_{jg}^{nc} is the predicted number of NC events for j^{th} topology and g^{th} module group. $N_{jg}^{\prime nc}$ is the same but for the case one of the NC systematic parameters is changed by 1σ. The number of events is changed not only by the change of the cross section but also

by the change of the detection efficiency. Same normalization error, f^{nc}_{jg}, is used for all module groups

$$N^{nc}_{jg} \to f^{nc}_{j} \cdot N^{nc}_{jg} \qquad (f^{nc}_{j} = f^{nc}_{jg}) \; . \tag{9.17}$$

f^{nc}_{j} is estimated using NC events summed over all module groups. The fractional covariance for topology bins is calculated for each NC systematic parameter by varying $\pm 1\sigma$.

$$V^{nc}_{ij} = \frac{1}{2} \left\{ \left(\frac{N^{nc}_{i} - N^{nc,+1\sigma}_{i}}{N^{nc}_{i}} \cdot \frac{N^{nc}_{j} - N^{nc,+1\sigma}_{j}}{N^{nc}_{j}} \right) + \left(\frac{N^{nc}_{i} - N^{nc,-1\sigma}_{i}}{N^{nc}_{i}} \cdot \frac{N^{nc}_{j} - N^{nc,-1\sigma}_{j}}{N^{nc}_{j}} \right) \right\} \; , \tag{9.18}$$

where $N^{nc}_{i(j)}$ is obtained by summing over all module groups:

$$N^{nc}_{i} = \sum_{g} N^{nc}_{ig} \; . \tag{9.19}$$

Figure 9.12 shows the fractional error due to the NC interaction systematic uncertainty and the correlation matrix. The total error size for the number of NC events is 27-30%. It is then 5% for the number of total (CC+NC) events since the contamination of NC events is small. There is a strong correlation between topology bins. This is because the major systematic error of the NC interaction is "NC other normalization error" and the 1σ variation of the systematic parameter changes an overall normalization for the number of NC events. In particular, the total errors are fully correlated between "NonDS-escaping" bins. Therefore, the 7 bins of "NonDS-escaping" are merged into 1 bin.

CC interaction systematic error

The 1σ variation of interaction systematic parameters results in a change of the neutrino cross section and the detection efficiency. In this analysis, only the latter change is taken into account for the CC interaction systematic error because the cross section is the one we are measuring with this analysis. The predicted number of CC events is modified after the 1σ variation of the systematic parameters. A fractional covariance among topology bins is then calculated using the modified number of CC events ($N^{\prime cc}_{j}$) and the nominal one (N^{cc}_{j}):

$$V^{cc}_{ij} = \frac{1}{2} \left\{ \left(\frac{N^{cc}_{i} - N^{\prime cc,+1\sigma}_{i}}{N^{cc}_{i}} \cdot \frac{N^{cc}_{j} - N^{\prime cc,+1\sigma}_{j}}{N^{cc}_{j}} \right) + \left(\frac{N^{cc}_{i} - N^{\prime cc,-1\sigma}_{i}}{N^{cc}_{i}} \cdot \frac{N^{cc}_{j} - N^{\prime cc,-1\sigma}_{j}}{N^{cc}_{j}} \right) \right\} \; . \tag{9.20}$$

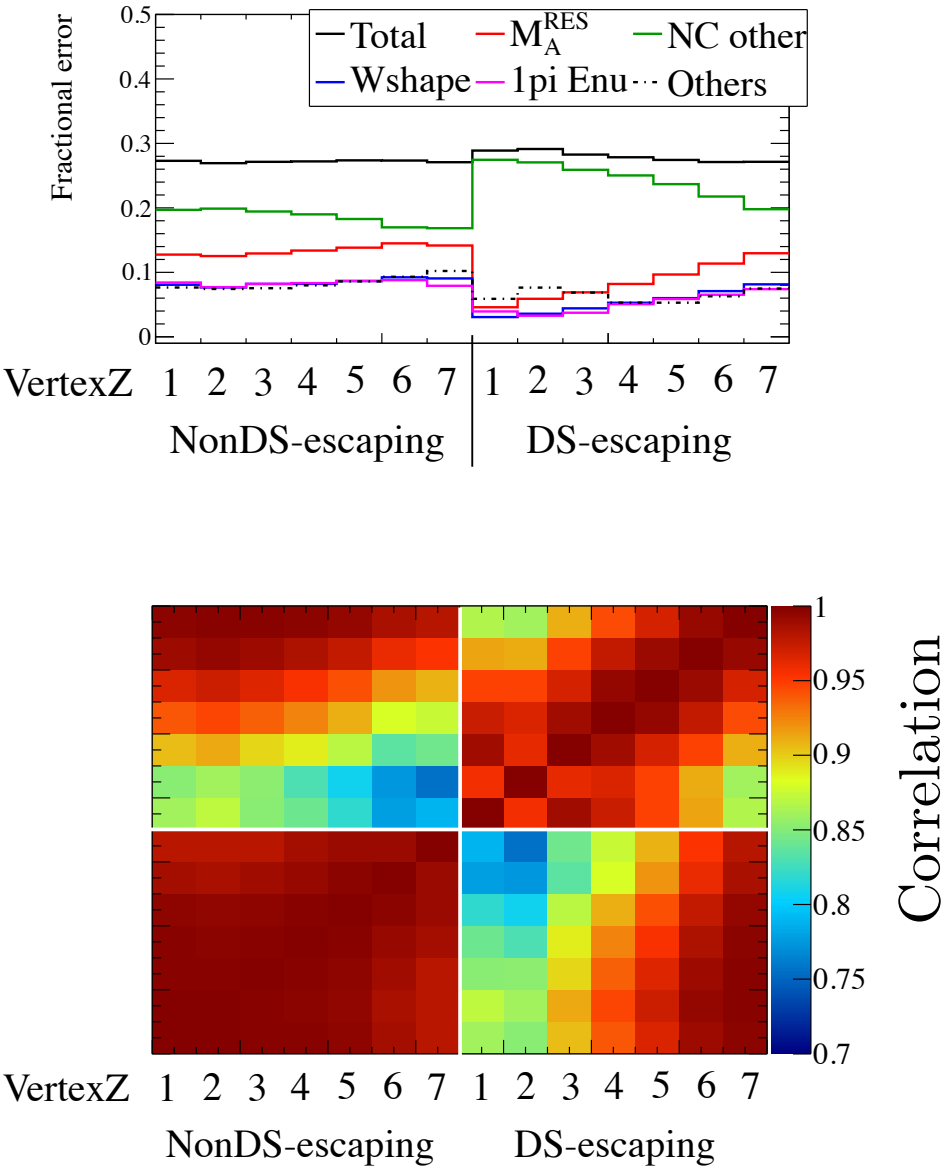

Figure 9.12.: Fractional error (top) and the correlation matrix (bottom) of the NC interaction. In the correlation matrix, the binning on the y-axis is identical to that on the x-axis. The total error size for the number of NC events is calculated to be 27-30%. There is a strong correlation between topology bins. This is because the 1σ variation of "NC other normalization error" which is the major systematic error changes an overall normalization for the number of NC events.

where $N^{cc}_{i(j)}$ is obtained by summing over all module groups:

$$N^{cc}_{i} = \sum_{g} N^{cc}_{ig} \ . \tag{9.21}$$

The total covariance for the CC interaction systematic error is calculated by summing up each of the covariances. The error matrix and correlation matrix are shown in Fig. 9.13.

For the systematic parameters of the pion FSI, uncertainties in the absorption, charged exchange, quasi elastic, and inelastic scattering of the pion are taken into account. These systematic errors are treated in a different way because there are correlations among the parameters; the data is fitted with N'^{cc} obtained by changing each FSI parameter and the difference of the fitted result is taken as the systematic error. The result is shown in Sec. 9.4.2. As described in this section, only the uncertainty in the pion absorption is taken into account since it gives a non-negligible effect on the final result.

9.3.4. Uncertainty in the pion multiplicity

In this analysis, the number of events are determined from the number of vertices, which sometimes fails to be reconstructed due to pile-up of tracks from neutrino events. Since those tracks could be from pions which are generated by neutrino interactions, the uncertainty in the pion multiplicity needs to be considered.

An extraction of the pion multiplicity for a given hadronic invariant mass is detailed in elsewhere [137]. Here we briefly describe the procedure. A relation between the mean multiplicity of charged hadrons (=$\langle n_{ch} \rangle$) and the hadronic invariant mass (=W) can be empirically expressed by

$$\langle n_{ch} \rangle = A + B \log W^2 \ , \tag{9.22}$$

where A and B are determined from a fit to data as described later. The mean of the total multiplicity including neutral hadrons (pions) $\langle n \rangle$ is calculated to be:

$$\langle n \rangle = 1.5 \times \langle n_{ch} \rangle \ . \tag{9.23}$$

Actual multiplicity distribution is parametrized by a Levy function (KNO scaling law [138]):

$$\mathrm{Levy}(z; c) = \frac{2e^{-c}c^{cz+1}}{\Gamma(cz+1)} \ , \tag{9.24}$$

where z=$n/\langle n \rangle$; c is determined from the fit to data as described later; Γ is a Gamma function. A, B, and c are then derived from a KNO standard fit to data using following

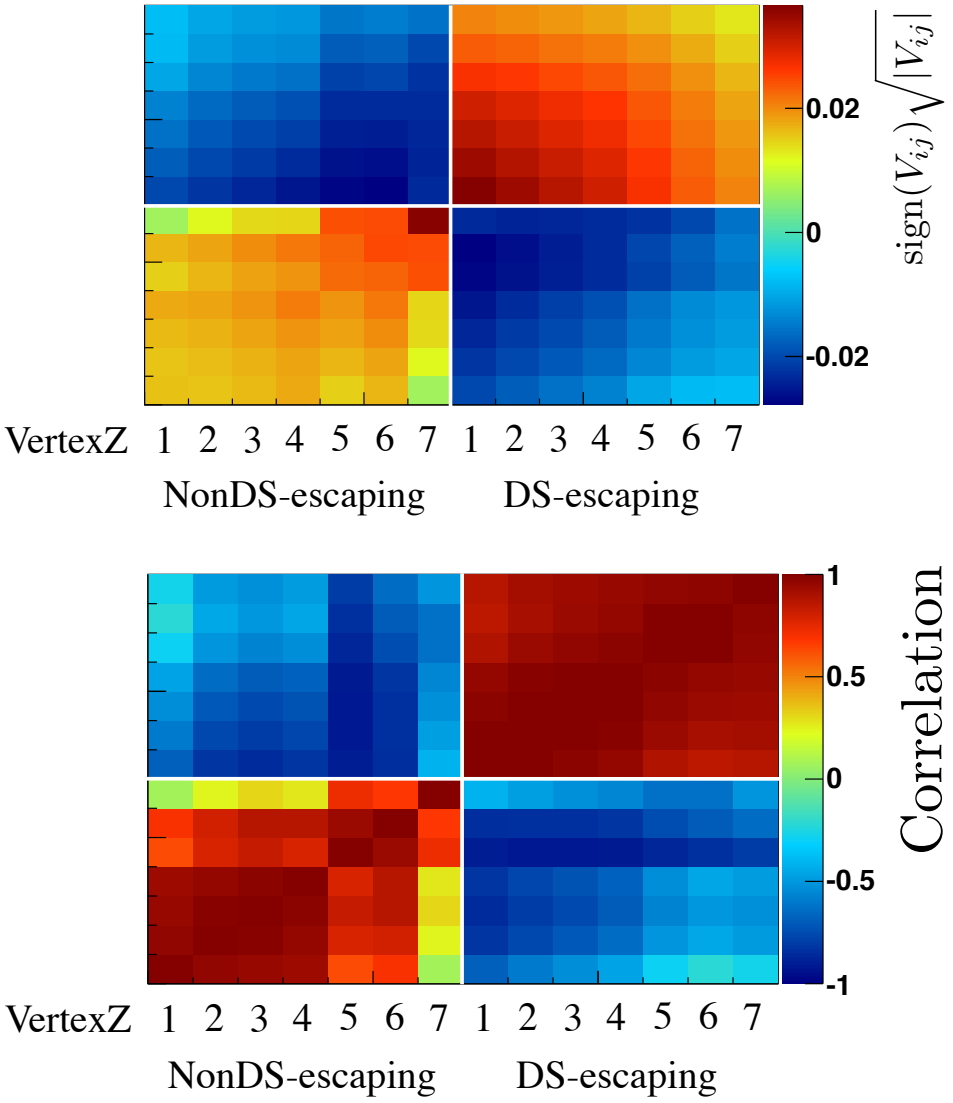

Figure 9.13.: Error matrix (top) and the correlation matrix (bottom) for the CC interaction systematic error. In these matrices, the binning on the y-axis is identical to that on the x-axis.

formula:

$$P(z; A, B, c) = \frac{1}{\langle n \rangle} \times Levy(z; c) \ . \tag{9.25}$$

The fit to data was performed using Fermilab data [139] as shown in Fig. 9.14. Fitted parameters are summarized in Table 9.7.

Another data set from the BEBC data [140] are used to test uncertainties of $\{A, B\}$. According to the BEBC measurement with a proton target, A and B in Eq. 9.22 are

Table 9.7.: Parameters determined from the KNO standard fit to the Fermilab data.

Parameters	A	B	Levy-c
ν-neutron	-0.05	1.38	5.21
ν-proton	0.68	1.36	7.98

0.37 ± 0.02 and 1.33 ± 0.02, respectively. The differences in A and B between the Fermilab and BEBC measurements are taken as the uncertainty in A and B: σ_A (=0.31) and σ_B (=0.03). Since neutron target data is missing in BEBC, for the ν-neutron data, the difference in ν-proton from the BEBC comparison is directly taken as the systematic errors on the A and B. Figure 9.15 shows average of the charged pion multiplicity as a function of $\log W^2$ for the prediction by the nominal NEUT and for two hadron multiplicity models: model 1 and model 2. Here "model 1" is the model in which parameters $\{A, B\}$ are used while parameters $\{A+\sigma_A, B+\sigma_B\}$ are used for "model 2". The deficit at $\log W^2 \sim 1.4$ (W=2.0 GeV) seen in the nominal NEUT is due to transition of the model inside NEUT. As seen in the figure, for the most part of $\log W^2$, difference of the mean of the charged pion multiplicity from NEUT is larger for model 2. Therefore, we use the model 2 for the evaluation of systematic error.

Prediction based on model 2 is made by applying weights to the NUET prediction. The weights are calculated as a function of $\{\log W^2, n_\pi\}$ from the 2D distribution of $\{\log W^2, n_\pi\}$ by NEUT and model2. Both of the distributions are normalized for each of the $\log W^2$ bins in order to make the probability density function of the charged π multiplicity for the given $\log W^2$, $P(\log W^2|n_\pi)$. The weight is then obtained by taking a ratio of the probability in model 2 to that in NEUT:

$$w(\log W^2, n_\pi) = P_{model2}(n_\pi|\log W^2)/P_{NEUT}(n_\pi|\log W^2)\ . \tag{9.26}$$

Figure 9.16 shows the obtained weight for the given $\log W^2$ and n_π. The weights are then used to re-weight events for CC multi-π and DIS mode in the default MC simulation. The re-weighted MC samples are used to fit data and fitted results are compared to the results with the nominal sample. Finally, the difference are taken as the systematics. The results are given in Sec. 9.4.2.

9.3.5. Secondary interaction

Hadrons produced by neutrino-nucleus interactions can interact with the other nucleus during their travels. This effect is called "secondary interaction (SI)". In the INGRID simulation, the pion SI is implemented by the physics list in GEANT4. As described in Sec. 9.4, FTFP_BERT is used for the final result. Since the hadronic interaction model, and hence SI, depends on a choice of the physics list, we use FTFP_BERT for

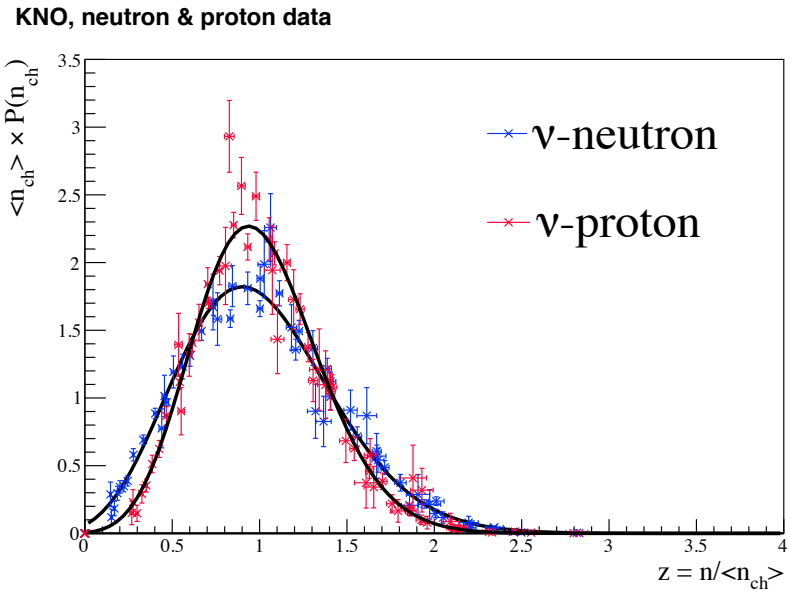

Figure 9.14.: Fit to the Fermilab data using Eq. 9.25 [138].

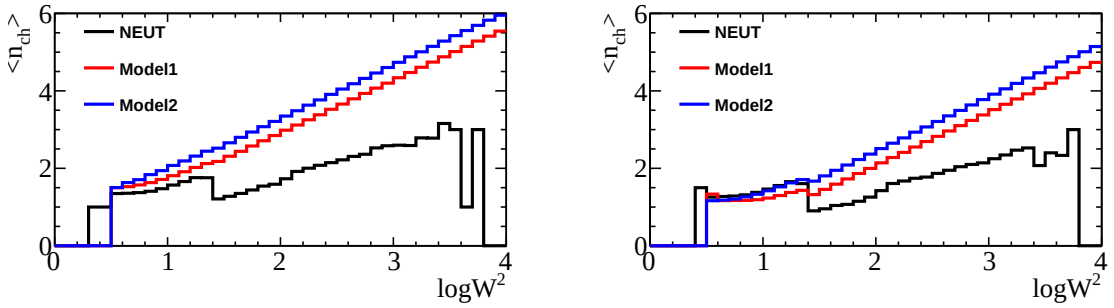

Figure 9.15.: Mean of the charged pion multiplicity as a function of $\log W^2$ for the prediction by the nominal NEUT (black) and by two hadron multiplicity models: model 1 (red), and model 2 (blue). The deficit at $\log W^2 \sim 1.4$ (W=2.0 GeV) seen in the nominal NEUT is due to transition of the model inside NEUT.

the evaluation of the systematic error from the SI uncertainty. The cross section by the model is extracted using a GEANT4 FTFP_BERT simulation. The uncertainty in the pion SI is then estimated by comparing the pion inelastic cross sections between the prediction and experimental data. Since the experimental data do not cover the whole pion energy region, we conducted case studies, details of which are described in Appendix F.

Finally, we assume 4 cases in total: case A1, case A2, case B1, and case B2. Thus, 4 sets of the MC samples are generated and a fit to the data is attempted for each case.

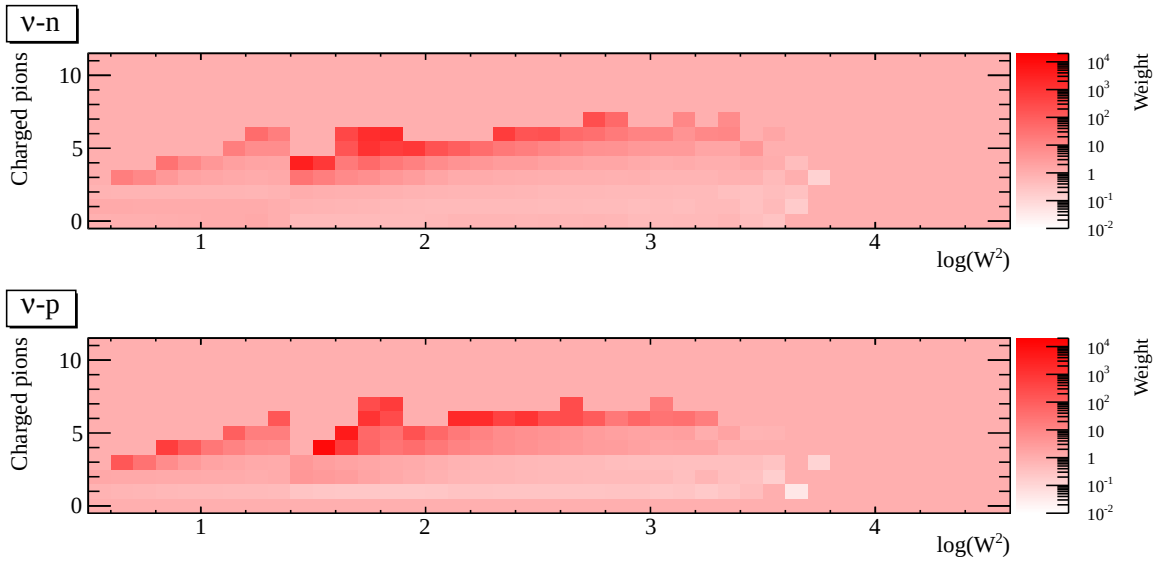

Figure 9.16.: Weighting factors for the given $\log W^2$ and n_π for the ν-neutron (top) and ν-proton (bottom) interactions. These weights are obtained from a comparison of the multiplicity between the nominal NEUT and model 2.

All the obtained results are then compared to the result with the nominal MC samples (nominal FTFP_BERT) in order to estimate the uncertainty from the pion SI.

9.3.6. Summary of systematic error

We described all the systematic errors and listed in Table 9.4. A major error for the number of total (CC+NC) events is the flux error and the error size is approximately 15%. The error from the uncertainty of the NC interaction is 5% for the number of total events. Since the errors from the uncertainties of the pion multiplicity, FSI and SI are estimated after the fitting is done, we do not write those error sizes in the table.

9.4. Result

We performed the data fit both with FTFP_BERT and QGSP_BERT as the GEANT4 physics hadronic interaction mode and decided to use FTFP_BERT for the final result because it gives a better χ^2 than QGSP_BERT. All the disributions in figures in this section are obtained with FTFP_BERT for MC. However, some of the systematic error evaluation, which are less dependent on the physics model, were done with QGSP_BERT because of a historical reason.

9.4.1. CC inclusive cross section fit

Table 9.8 shows parameters (f_0-f_4) obtained by fitting with T2K RUN 1+2+3c+4 data set. The topology distribution after the data fit is shown in Figs. 9.17 (module group 0) and 9.18 (module group 7). The fit results of the other systematic parameters, flux, detector, CC interaction, and NC interaction, are shown in Fig. 9.19. In order to derive the normalization factor for the cross section, we take the average of the neighboring fitted parameters. The obtained cross sections are:

$$\begin{aligned} f(1.1\text{ GeV}) &= \frac{f_1 + f_2}{2} \\ &= 0.980 \pm 0.115\ , \\ f(2.0\text{ GeV}) &= \frac{f_2 + f_3}{2} \\ &= 1.062 \pm 0.123\ , \\ f(3.3\text{ GeV}) &= \frac{f_3 + f_4}{2} \\ &= 0.756 \pm 0.136\ , \end{aligned}$$

9.4.2. Additional systematic errors

For the uncertainties in the pion FSI, multiplicity, and SI, we do the actual fitting to the data with PDF's corresponding to those systematic error variations.

Final state interaction

Following 6 systematic parameters are considered for the uncertainty of pion final-state interaction.

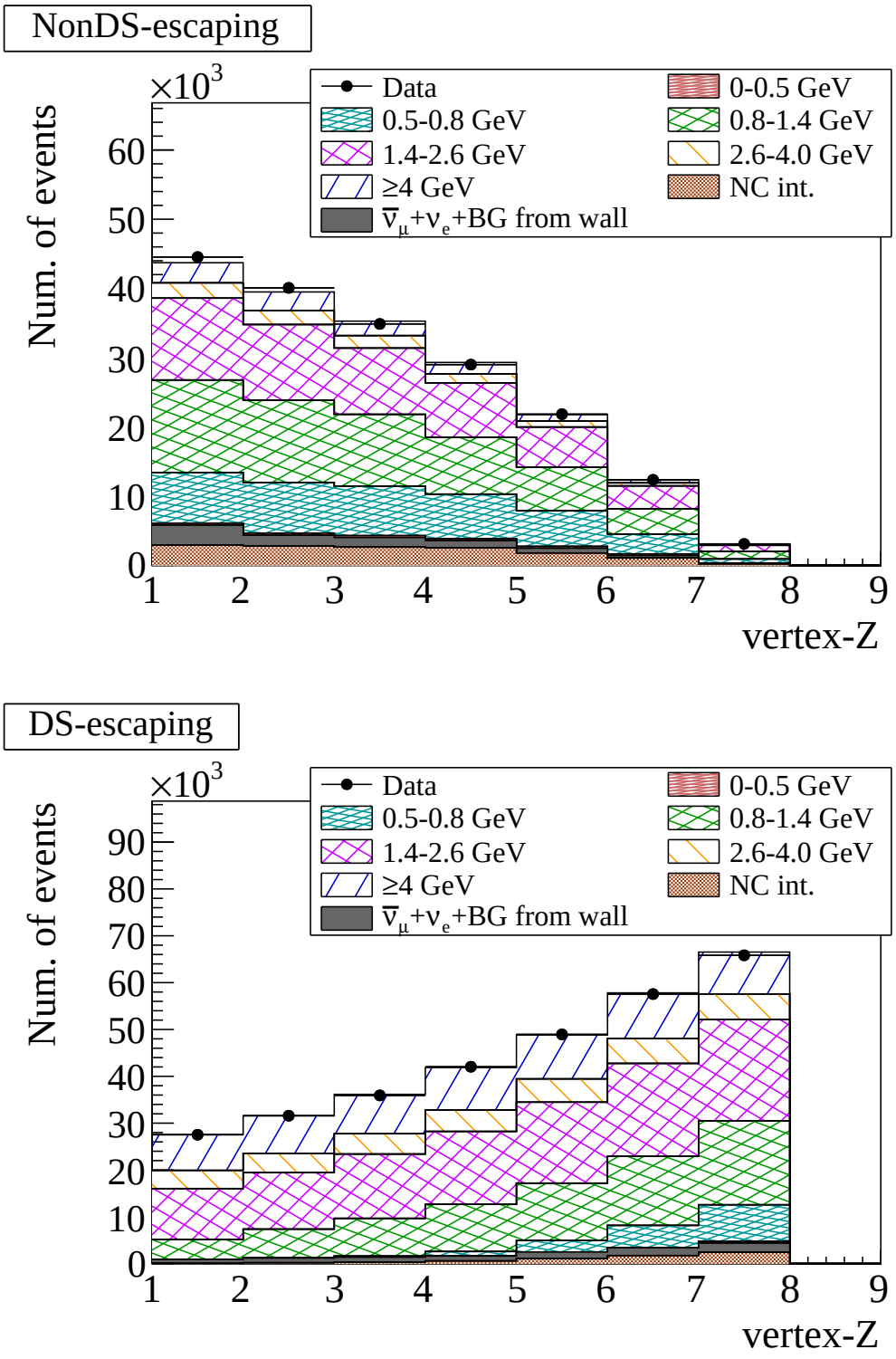

Figure 9.17.: Topology distribution for NonDS-escaping (top) and DS-escaping (bottom) for module group 1 after RUN 1+2+3c+4 data fit. The predicted events are categorized according to CC events, NC events, and beam $\bar{\nu}_\mu + \nu_e$ and BG from wall, and shown as a stacked histogram. The CC events are subdivided into those in 6 true neutrino energy regions.

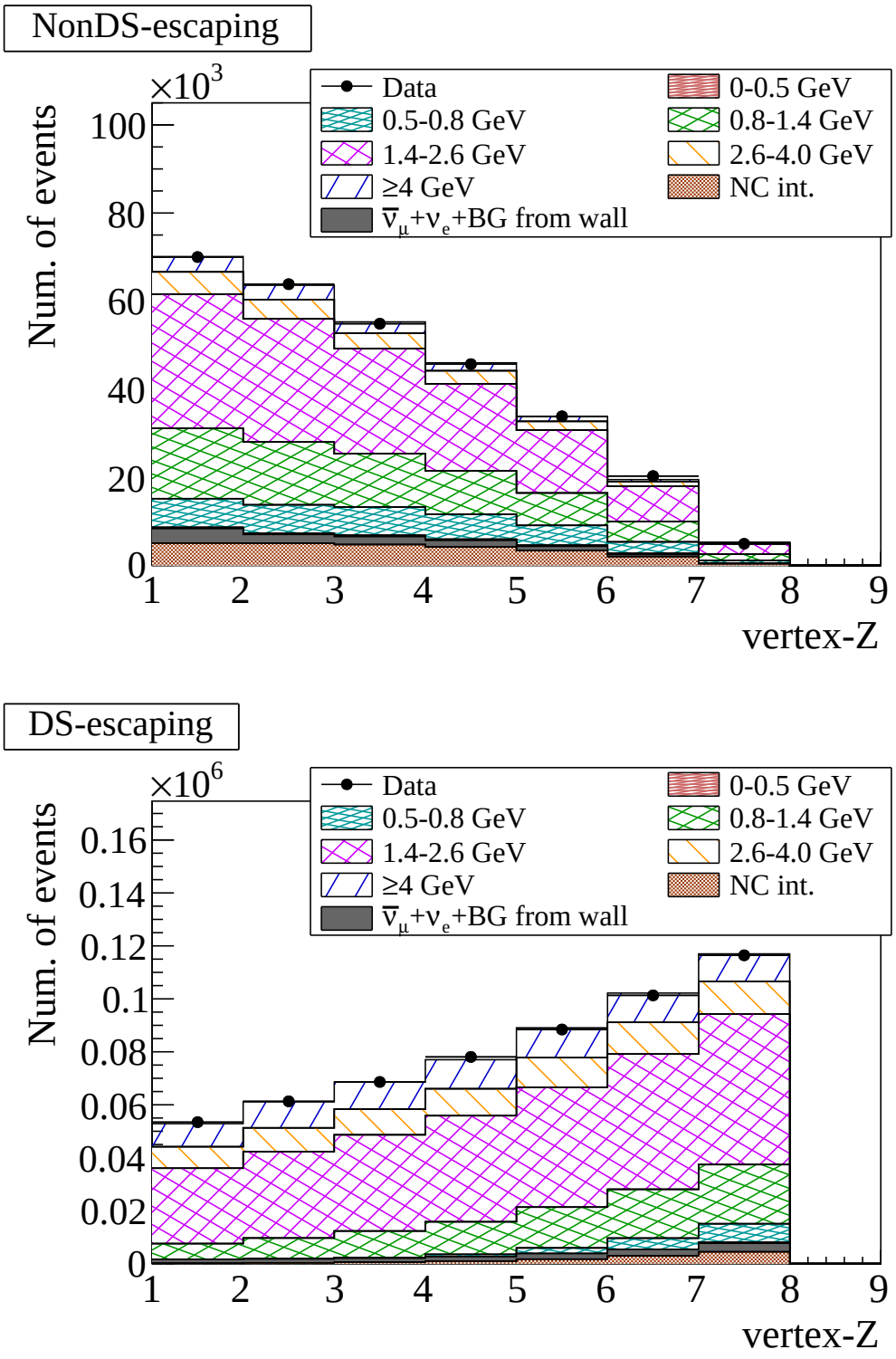

Figure 9.18.: Topology distribution for NonDS-escaping (top) and DS-escaping (bottom) for module group 3 after RUN 1+2+3c+4 data fit. The predicted events are categorized according to CC events, NC events, and beam $\bar{\nu}_\mu + \nu_e$ and BG from wall, and shown as a stacked histogram. The CC events are subdivided into those in 6 true neutrino energy regions.

Table 9.8.: Fit result of the normalization for the cross section with T2K RUN 1+2+3c+4 data set.

Fit parameter	Fit result
f_0 (0.5 GeV)	3.560 ± 0.508
f_1 (0.8 GeV)	0.637 ± 0.180
f_2 (1.4 GeV)	1.324 ± 0.181
f_3 (2.6 GeV)	0.800 ± 0.211
f_4 (4.0 GeV)	0.712 ± 0.120
χ^2	155.4

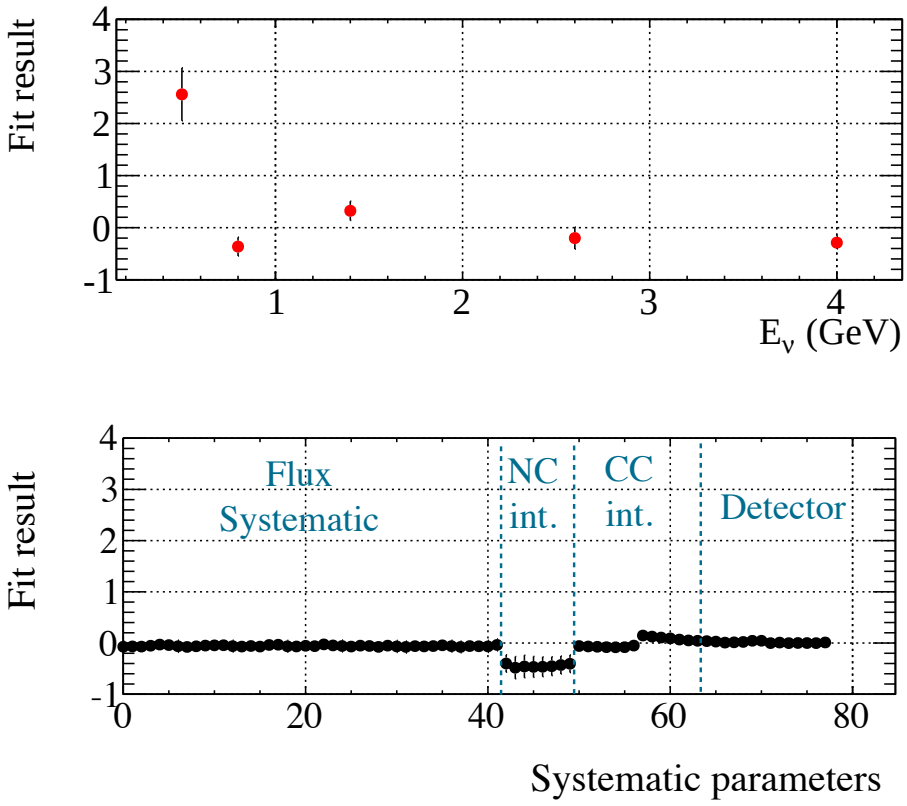

Figure 9.19.: Fit results for the normalization factors for the cross sections (top) and systematic parameters (bottom).

Table 9.9.: Normalizatoin factors for the cross sections obtained with $\pm 1\sigma$ variation of the FSI systematic parameters. The number inside of the parenthesis shows the fractional deviation from the nominal fit center. These numbers are estimated using QGSP_BERT for the physics list in GEANT4.

FSI parameters	1.1 GeV		2.0 GeV		3.3 GeV	
	$+1\sigma$	-1σ	$+1\sigma$	-1σ	$+1\sigma$	-1σ
FSI abs.	1.011 (+1.0%)	0.982 (-1.9%)	1.088 (-0.5%)	1.091 (-0.2%)	0.812 (-2.9%)	0.867 (+3.7%)
FSI ex (low energy)	1.002 (+0.1%)	1.002 (+0.1%)	1.093 (0.0%)	1.097 (+0.4%)	0.833 (-0.4%)	0.842 (+0.7%)
FSI ex (high energy)	1.007 (+0.6%)	0.993 (-0.8%)	1.094 (+0.1%)	1.091 (-0.2%)	0.830 (-0.7%)	0.846 (+1.1%)
FSI QE (low energy)	1.006 (+0.5%)	0.982 (-1.9%)	1.093 (0.0%)	1.079 (-1.3%)	0.832 (-0.5%)	0.838 (+0.2%)
FSI QE (high energy)	1.002 (+0.1%)	0.999 (-0.2%)	1.092 (-0.1%)	1.093 (0.0%)	0.832 (-0.5%)	0.840 (+0.5%)
FSI Inel.	1.006 (+0.5%)	0.995 (-0.6%)	1.095 (+0.2%)	1.090 (-0.3%)	0.834 (-0.3%)	0.838 (+0.2%)

- absorption (FSI abs.)
- charge exchange for pion with momentum below 500 MeV/c (FSI ex low)
- charge exchange for pion with momentum above 400 MeV/c (FSI ex high)
- quasi elastic scattering for pion with momentum below 500 MeV/c (FSI QE low)
- quasi elastic scattering for pion with momentum above 400 MeV/c (FSI QE high)
- inelastic scattering (FSI inel.)

The change of the detection efficiency for the CC interaction after the 1σ variation of the systematic parameter is used to correct the expected the number of CC events. Six sets of the PDF for CC events were prepared corresponding to these parameters and the data was fitted with each of them. Table 9.9 shows the result. For the final result, only the changes of the fitted center due to the variation of "FSI abs." are taken into account since effects from the 1σ variation of the other parameters are small and considered to be negligible.

Uncertainty in the pion multiplicity

As described in Sec. 9.3.4, weights to correct the pion multiplicities in CC multi-pi and DIS interactions in NEUT are obtained using external data. The MC sample is then re-weighted using the weights and is used to fit the data. The fitted results are then compared to that obtained with the nominal samples. Figure 9.20 shows a comparison in the fitted results between the re-weighted (red) and default (black) MC simulation where FTFP_BERT is used for the physics list in GEANT4. Table 9.10 summarizes the comparison in the normalization factor for the cross sections between the nominal and re-weighted MC samples. The difference from the nominal MC simulation is taken as the systematic error on this analysis.

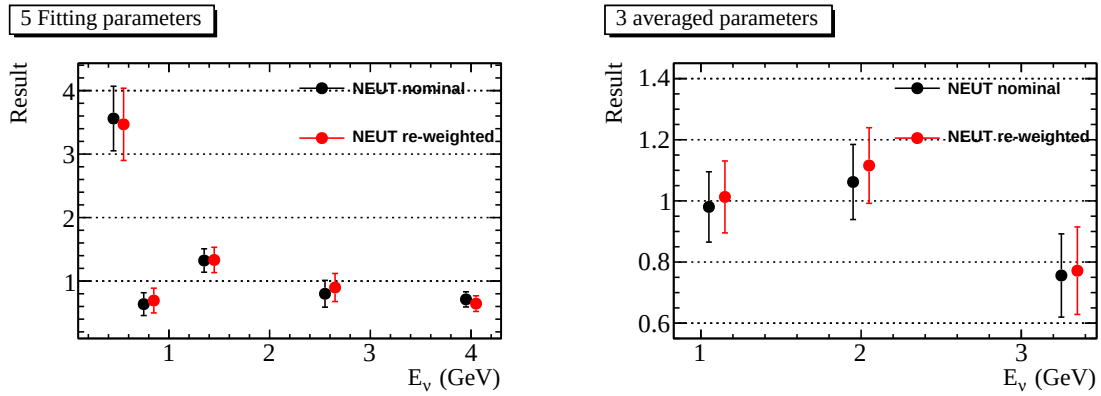

Figure 9.20.: Results for 5 fitting (left) and 3 averaged parameters (right). Black points are the nominal result while red points are obtained by re-weighting the CC multi-pi and DIS interactions in the MC simulation.

Table 9.10.: Comparison in the normalization factor for the cross section at 1.1, 2.0, and 3.3 GeV between the nominal and re-weighted MC simulation where the weight is applied to the CC-multi and DIS interaction mode. These numbers are estimated using FTFP_BERT for the physics list.

	1.1 GeV	2.0 GeV	3.3 GeV
Nominal MC	0.980	1.062	0.756
Re-weighted MC	1.013 (+3.3%)	1.116 (+5.1%)	0.772 (+2.1%)

Uncertainty in the pion SI

Effects from the uncertainty in the pion secondary interaction (SI) is estimated by changing the original cross section in GEANT4 (FTFP_BERT) according to the "case studies" described in Sec. 9.3.5. The obtained MC samples are then used to fit the data. Figure 9.21 shows the fitted results obtained using the corrected and nominal MC samples. Since four cases give similar size of difference, the error on the normalization factor is calculated as follows:

$$\Delta f_k = \sqrt{\frac{1}{4}\sum_{i=1}^{4}(f_k^{nom} - f_k^i)^2}\,, \tag{9.27}$$

where indices of k and i denote the k^{th} case and i^{th} energy bin for the normalization factor. From Eq. 9.27, final error sizes on the normalization factors due to the uncertainty in the pion SI are calculated to be 5.6%, 2.0%, and 6.9% at 1.1, 2.0, and 3.3 GeV, respectively.

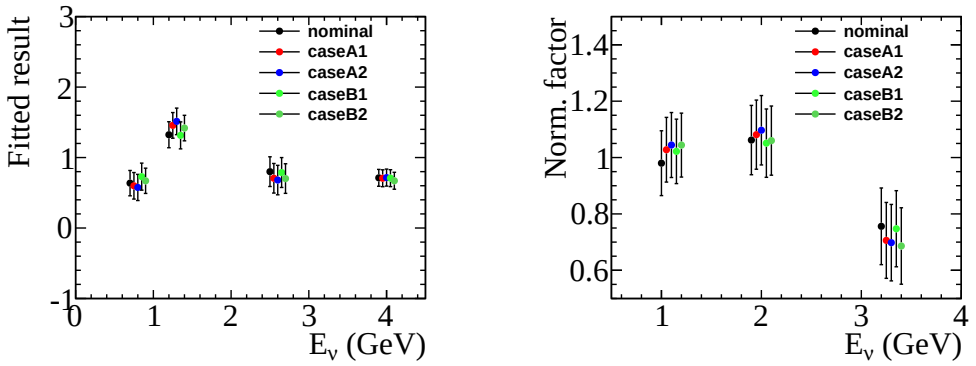

Figure 9.21.: Results for 5 fitting (left) and 3 averaged parameters (right) for each case where the pion cross sections are corrected in GEANT4. The results obtained from the nominal MC samples are also shown.

Table 9.11.: Contribution to the uncertainty on the fitted parameters (f_0-f_4) from each error source.

Error source	f_0 (0.5 GeV)	f_1 (0.8 GeV)	f_2 (1.4 GeV)	f_3 (2.6 GeV)	f_4 (4.0 GeV)
Statistical error	18.7%	6.0%	4.5%	4.8%	1.4%
Flux + Stat.	26.0%	7.9%	12.8%	14.5%	9.3%
Detector + Stat.	33.8%	10.0%	7.2%	7.0%	3.0%
Interaction (cc) + Stat.	30.6%	9.3%	6.8%	7.2%	3.8%
Interaction (nc) + Stat.	22.6%	6.6%	6.4%	5.8%	2.0%

9.4.3. Summary of the errors on the fitted parameters and cross sections.

Table 9.11 summarizes the uncertainty on the fitting parameters for the cross section normalizations for each error source. The error on the cross section normalization is then calculated for each uncertainty and is summarized in Table 9.12 in which the errors from pion FSI, multiplicity and SI uncertainties are also added. After taking an average, the dominant systematic error comes from the flux uncertainty which gives 8-9% error size for the cross section. This is because there is a strong positive correlation in the flux uncertainties between the energy bins and it results in a positive correlation among the fitted parameters (Δf_0-Δf_4). Therefore, the error size does not reduce even after taking an average of the neighbouring parameters.

Figures 9.22 and 9.23 show the error and correlation matrices for 5 fitted parameters (Δf_0-Δf_4) and the cross section normalization at 1.1, 2.0, and 3.3 GeV, respectively.

Table 9.12.: Contribution to the uncertainty on the cross section normalization at 1.1, 2.0, and 3.0 GeV from each error source including the pion FSI, multiplicity, and SI.

Error source	1.1 GeV	2.0 GeV	3.3 GeV
Statistical error	2.0%	0.6%	2.3%
Flux + Stat.	7.6%	9.0%	8.4%
Detector + Stat.	4.3%	0.9%	3.9%
Interaction (cc) + Stat.	3.7%	0.8%	4.8%
Interaction (nc) + Stat.	2.4%	0.9%	3.2%
pion FSI	$^{1.0\%}_{-1.9\%}$	0.5%	$^{+3.7\%}_{-2.9\%}$
pion multiplicity	3.3%	5.1%	2.1%
pion SI	5.6%	2.0%	6.9%

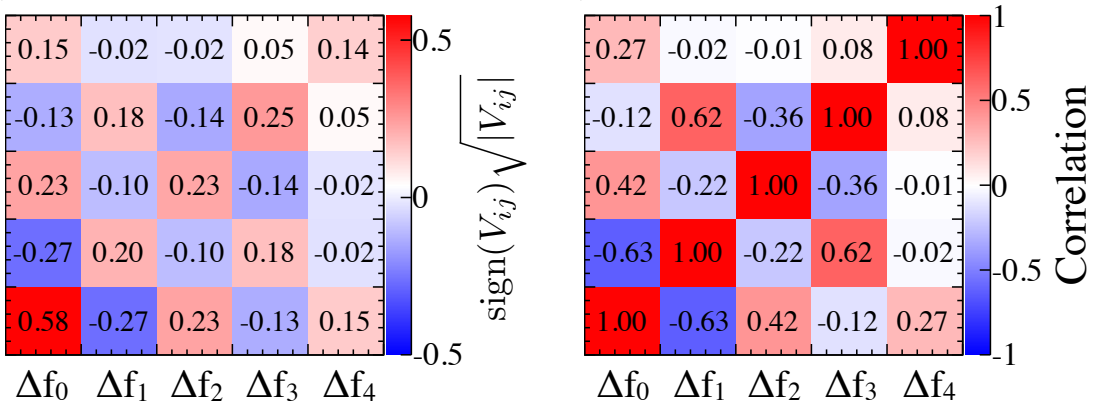

Figure 9.22.: Error (left) and correlation (right) matrices for the 5 fitted parameters. In both of the matrices, the binning on the y-axis is identical to that on the x-axis.

9.5. Summary

The result of the five individual fitting parameters (f_0-f_4) based on "FTFP_BERT" of the GEANT4 physics list is,

$$
\begin{aligned}
f_0 \ (0.5 \text{ GeV}) &= 3.56 \pm 0.58 \ , \\
f_1 \ (0.8 \text{ GeV}) &= 0.64 \pm 0.20 \ , \\
f_2 \ (1.4 \text{ GeV}) &= 1.32 \pm 0.23 \ , \\
f_3 \ (2.6 \text{ GeV}) &= 0.80 \pm 0.25 \ , \\
f_4 \ (4.0 \text{ GeV}) &= 0.71 \pm 0.14 \ .
\end{aligned}
$$

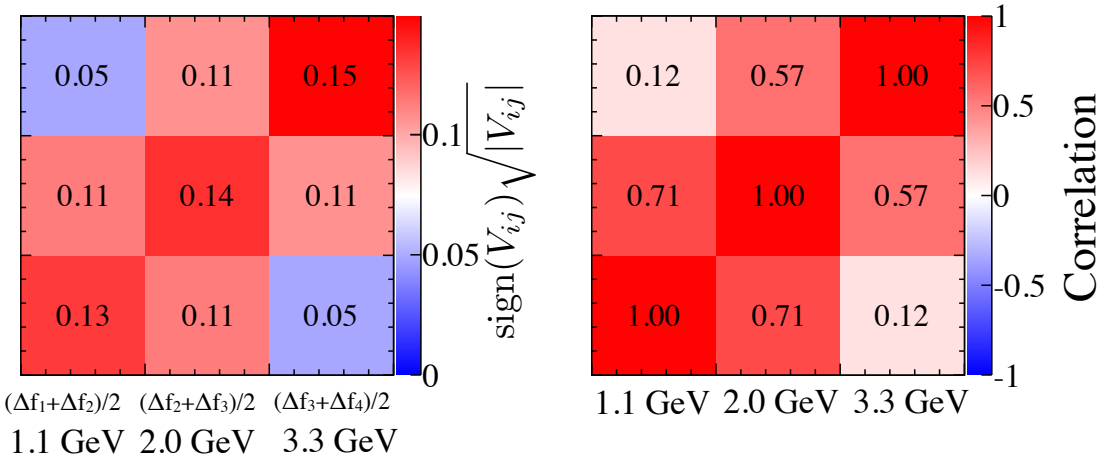

Figure 9.23.: Error (left) and correlation (right) matrices for the cross section normalization at 1.1, 2.0, and 3.3 GeV. In both of the matrices, the binning on the y-axis is identical to that on the x-axis.

These errors include the uncertainties the pion FSI, multiplicity and SI in addition to the fitting errors.

By taking an average of the neighboring fitting parameters, the normalization factors of CC inclusive cross section on Fe are calculated. Finally the results with the collected data for 6.27×10^{27} p.o.t. are:

$$\begin{aligned} f(1.1\text{ GeV}) &= \frac{f_1+f_2}{2} \\ &= 0.98 \pm 0.13\ , \\ f(2.0\text{ GeV}) &= \frac{f_2+f_3}{2} \\ &= 1.06 \pm 0.14 \\ f(3.3\text{ GeV}) &= \frac{f_3+f_4}{2} \\ &= 0.76 \pm 0.15\ , \end{aligned}$$

and the cross sections are,

$$\sigma^{cc}(1.1\text{ GeV}) = 1.10 \pm 0.15\ (10^{-38}\mathrm{cm}^2/\mathrm{nucleon})\ ,$$

$$\sigma^{cc}(2.0\text{ GeV}) = 2.07 \pm 0.27\ (10^{-38}\mathrm{cm}^2/\mathrm{nucleon})\ ,$$

$$\sigma^{cc}(3.3\text{ GeV}) = 2.29 \pm 0.45\ (10^{-38}\mathrm{cm}^2/\mathrm{nucleon})\ ,$$

at mean energies of 1.1, 2.0, and 3.3 GeV. Our measurement utilizes the different energy spectra at different off-axis angles to extract the energy dependent cross section and opens up a new technique to derive the energy dependent neutrino cross section.

Figure 9.24 shows these results with values from other measurements [116, 120] and the neutrino models, NEUT (v.5.1.4.2) and GENIE (v.2.8.0). Our measured cross sections are consistent with the energy dependent cross sections measured with the MINOS near detector and the flux-averaged cross section measured with INGRID. In neutrino energy range above 3 GeV, the prediction by NEUT is larger than our result and the MINOS measurement. This might suggest that GENIE chooses better neutrino interaction models than NEUT for the higher energy region. However, the differences in the cross section between NEUT and GENIE are within the errors of our results. Therefore, a reduction of the systematic error is necessary for a proper choice of the neutrino interaction model. As for now, our results support a current understanding of the neutrino interaction models which were used in the neutrino oscillation measurement. The prospect of our measurement is described in Sec. 9.6.1.

9.6. Discussion

9.6.1. Future improvements

We measure the ν_μ-Fe CC inclusive cross section in the energy range of 1-3 GeV with a precision of 13-20%. As seen in Fig. 9.24, our result is consistent with the previous measurements and with the predictions by NEUT and GENIE. In order to further study the neutrino interaction models, the reduction of the systematic error is necessary. The dominant error of our cross section result comes from uncertainties in the neutrino flux as shown in Table 9.12. Among them, the uncertainty in the hadronic production largely contributes to the error budget (see Fig. 9.9). The large error size is due to a lack of the production data. In the T2K flux simulation, the hadronic interaction rate are corrected using data from the NA61/SHINE experiment and the other external experiments. For this analysis, we use NA61/SHINE dataset taken in 2007, where a thin carbon target was used. In the datasets, only the data for $\pi^\pm$ and K^+ are available. NA61/SHINE also took data in 2009 with the thin target, where statistics increased by an order of magnitude as compared to the 2007 data. The new datasets allow to use the production of K^- and secondary protons. In addition, a coverage of the p-θ phase space is also enlarged thanks to some improvements in the experimental setup. With these additional datasets, the systematic error from the uncertainties in the hadronic production is expected to be reduced. NA61/SHINE also conducted the measurement with the T2K replica target and the analysis is now ongoing. Such a measurement with the long target will also be useful for the estimation of re-interactions of hadrons and will allow to reduce the systematic uncertainties. In conclusion, the systematic uncertainty in the neutrino flux could be reduced in the future analysis.

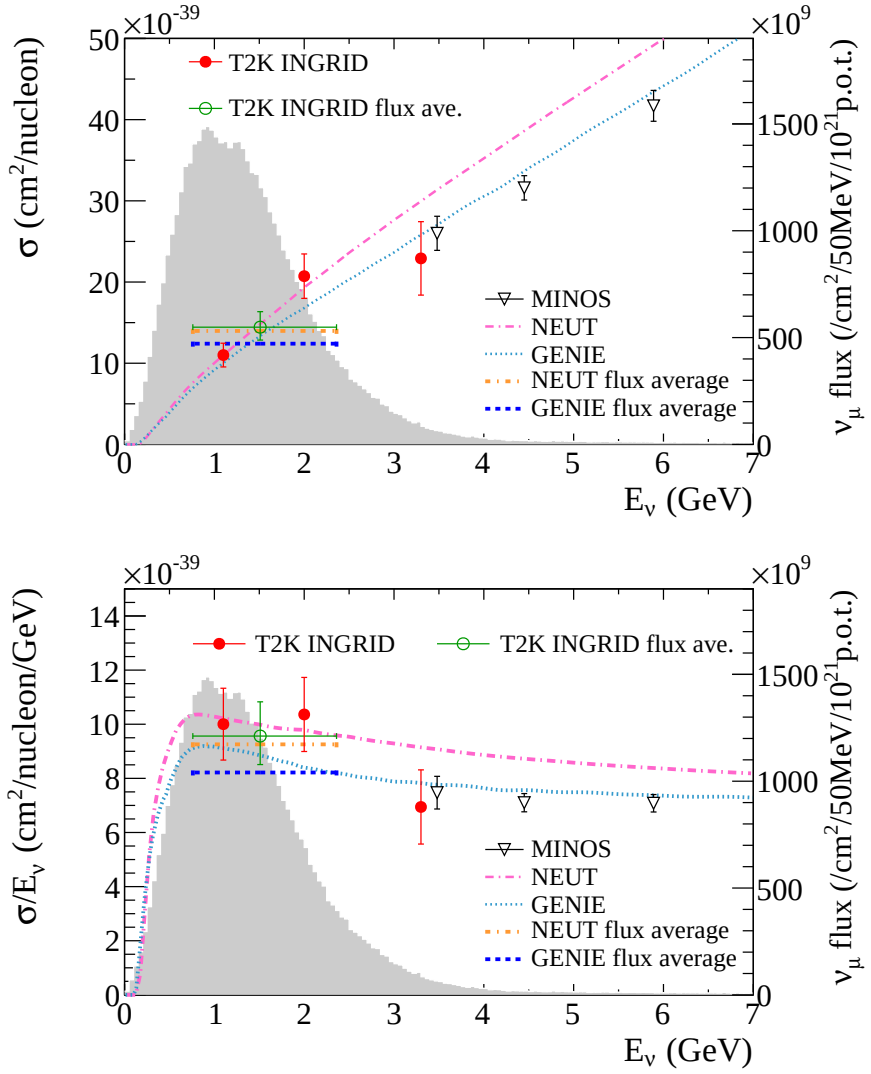

Figure 9.24.: Results of the ν_μ CC inclusive cross section on Fe; σ^{cc} (top) and σ^{cc}/E_ν (bottom). The energy dependent cross section with the MINOS near detector [116] and the flux-averaged cross section with INGRID [120] are shown with the NEUT (v.5.1.4.2) and GENIE (v.2.8.0) predictions. The T2K ν_μ flux at on-axis is also shown in grey. The result of the T2K flux-averaged cross section and this result are consistent with each other.

The subdominant errors come from the uncertainties on the pion SI and multiplicity. For these error sources, the difference in the fitted result between the "corrected" and "nominal" event samples is taken as the systematic error. Therefore, if we use the "corrected" event samples as nominal ones, the error can be reduced. In that case, the uncertainty on the "correction" has to be evaluated and further studies are required.

In this analysis, the obtained events are categorized according the event topology. This method introduces "model dependence" into the results. The uncertainty on the pion SI could affect the event signature and could cause additional uncertainty on the selected events in some topology bins. For example, an event having one or more hits at a downstream tracking plane is categorized into the "DS-escaping" event in our analysis. The hit might come from pion. If the pion is absorbed during its way before hitting the downstream tracking plane, the event signature migrates into the "NonDS-escaping" event. Therefore, sensitivity of this analysis to the cross section measurement is limited by the usage of the event topology.

9.6.2. New techniques to determine the energy dependent neutrino cross section

This analysis utilizes the fact that peaks of the energy spectra of the neutrino fluxes are different between modules, and opens up a new technique to derive the energy dependent neutrino cross section. In the current INGRID detector's configuration, however, the difference in the off-axis angle between the center and corner modules is only 1.2°. We checked the sensitivities with following two cases:

- [i] use only neutrino event rate at different modules,
- [ii] use both neutrino event rate at different modules and event topologies (i.e. our analysis method).

We estimated the expected error size for each fit parameter (f_0-f_4) using Toy MC data. Table 9.13 shows the results obtained without any systematics (Only statistical errors are taken into account). As seen in the table, the sensitivity for case(i) is bad for the determination of the energy dependent cross section. This is considered to be due to the small off-axis angle difference between the modules. Therefore, we use the final state kinematics of the particle to enhance the sensitivity in addition to the different off-axis angle technique for our analysis. Recently, a detector called "nuPRISM" is proposed as the new near detector for the T2K experiment and the T2HK project [141]. This detector is a water Cherenkov detector with a cylindrical water volume as shown in Fig. 9.25 and uses the same technology and analysis method as Super-K does. The height and diameter of the detector are 50-100 m and 6-10 m, respectively, and has an ability to measure the off-axis beam with θ_{OA} =1°-4° which corresponds to the neutrino energy range of 0.4-1.2 GeV. By dividing the detector into slices of off-axis angles based on the reconstructed vertex position, incoming neutrino energy can be inferred. Namely, the final state kinematics of the particles is not required to determine the neutrino energy

and "model-independent" cross section measurement can be done as a function of the neutrino energy covering the T2K and T2KHK neutrino energy range.

The off-axis neutrino beam has a strong potential to determine the energy dependent cross section as described above. Our analysis demonstrates the feasibility of the precise CC inclusive cross section measurement which could be useful for the neutrino oscillation experiment.

Table 9.13.: Expected fitting error size estimated from toy MC data. Case (i) is the results when only neutrino event rate at different modules is used. Case (ii) is the result when both of the event rate and event topologies are used. In this estimation, only the statistical error is taken into account.

Fit parameter	case (i)	case (ii)
f_0 (0.5 GeV)	4.069	0.167
f_1 (0.8 GeV)	0.891	0.055
f_2 (1.4 GeV)	0.167	0.042
f_3 (2.6 GeV)	0.117	0.044
f_4 (4.0 GeV)	0.330	0.013

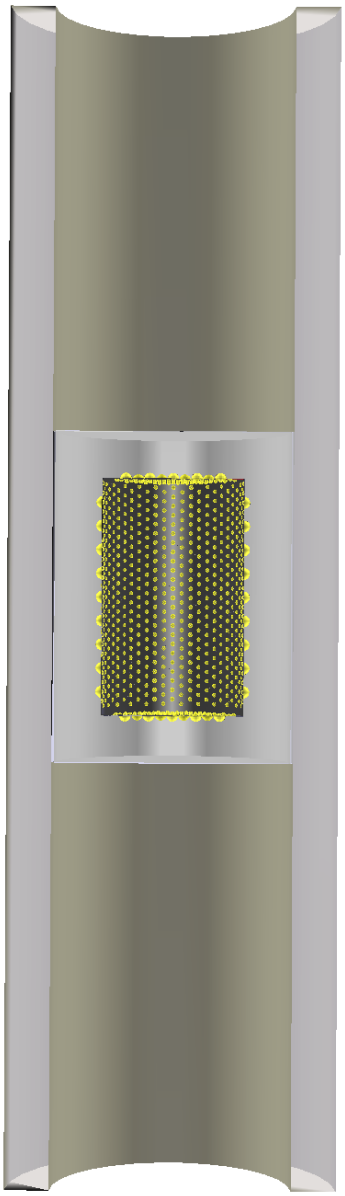

Figure 9.25.: The proposed configuration of the nuPRISM detector within the water tank is shown. This figure is taken from [141]

Part V.

Conclusion

Chapter 10

Conclusion

The T2K experiment aims to do a precise measurement of the oscillation parameters $\{\theta_{23}, \Delta^2 m_{23}, \theta_{13}\}$ and explore not-yet-known δ_{CP} using the off-axis muon neutrino beam. In order to achieve our goals, (1) a precise control of the neutrino beam and (2) understanding of the neutrino-nucleus interaction mechanism are essential.

In this thesis, we report the following two measurements:

- a measurement of the direction and intensity of the muon beam, and the absolute muon flux, and
- a measurement of the ν_μ-Fe CC inclusive cross section.

In the T2K experiment, both ND280 and Super-K are located 2.5 degrees from the beam-axis. In this way, the neutrino beam has a peak energy around 0.7 GeV at which neutrinos oscillate with near the maximum probability after traveling 295 km. However, a 1 mrad uncertainty in the beam direction measurement leads to a 2-3% uncertainty in the neutrino energy scale. Therefore, the precise control of the neutrino beam is highly important to measure the neutrino oscillation parameters precisely.

In the first half of this thesis, we described the measurement of the beam direction by the muon monitor. The systematic error of the beam direction measurement with the muon monitor was estimated to be 0.28 mrad, which fulfills our requirement of < 0.3 mrad. The results of the measurement of the muon beam profile center (cm) for each T2K run period are

	RUN 1	RUN 2	RUN 3b (250kA)	RUN 3b (205kA)	RUN 3c	RUN 4	Total
X :	-0.1 ± 2.3 (0.6)	0.2 ± 2.3 (0.4)	-0.2 ± 2.3 (0.2)	4.8 ± 2.3 (0.6)	-0.4 ± 2.3 (0.4)	-0.3 ± 2.3 (0.3)	0.0 ± 2.3 (1.0)
Y :	-3.8 ± 2.3 (0.5)	-1.9 ± 2.3 (0.5)	-0.6 ± 2.3 (0.2)	4.2 ± 2.3 (1.5)	0.1 ± 2.3 (0.4)	-0.8 ± 2.3 (0.5)	-1.0 ± 2.3 (1.6)

, where the numbers in parentheses denote RMS of the spill-by-spill fluctuation of the muon beam profile center. The results of the total collected charge (nC/10^{12} p.o.t.) for each T2K run period are

RUN 1	RUN 2	RUN 3b (250kA)	RUN 3b (205kA)	RUN 3c	RUN 4	Total (250 kA)
32.7 (0.7%)	32.8 (0.8%)	32.4 (0.5%)	21.7 (0.7%)	32.0 (0.7%)	32.4 (0.8%)	32.5 (1.2%)

, where the numbers in parentheses denote RMS of the spill-by-spill fluctuation of the total collected charge. Accordingly, the muon beam direction was kept within 0.3 mrad

with respect to the designed beam-axis for most of the span of beam operation, and the total collected charge was also kept stable with the RMS of 1%. Thus, the neutrino beam direction was kept stable within 0.3 mrad and this was, indeed, confirmed by the INGRID measurement. In order to confirm our understanding of muon beam and neutrino beam, the absolute muon flux was measured with the emulsion detector with a precision of 3%. It was then compared with prediction based on external hadron interaction data. As a result, we obtained good agreement between the data and prediction. This result supports our understanding of the detector response of the muon monitor and confirms the validity of the beam control by the muon monitor. In summary, all the beam measurements guaranteed good quality beam data, which was used for the neutrino oscillation measurements and our cross section measurement.

A proper choice of the neutrino interaction model is very important for the neutrino oscillation experiment. The precise measurement of the exclusive cross section, such as CCQE and CC1π, is essential for understanding the neutrino-nucleus interaction mechanism. However, the extraction of the exclusive cross section suffers from uncertainty in the nuclear medium effect. Advantage of the CC inclusive cross section is that this channel is less affected by the uncertainty than the exclusive channels and enable us to test neutrino interaction models. It would also guide the interpretation of the exclusive measurements. So far, the CC inclusive cross section on Fe was measured in the energy range of 3-50 GeV by MINOS, and was subsequently measured at a mean energy of 1.51 GeV by T2K. No measurement has been made in the energy range of 2-3 GeV. Therefore, the cross section in that energy region will be important input for modeling the neutrino interaction mechanism. The measurement covering the energy range of 1-3 GeV is also useful to check the consistency between the T2K and MINOS measurements.

In the later half of this thesis, we report the measurement of the ν_μ-Fe CC inclusive cross section in neutrino energy range of 1-3 GeV. The obtained cross sections are:

$$\sigma^{cc}(1.1\text{ GeV}) = 1.10 \pm 0.15\ (10^{-38}\text{cm}^2/\text{nucleon})\ ,$$

$$\sigma^{cc}(2.0\text{ GeV}) = 2.07 \pm 0.27\ (10^{-38}\text{cm}^2/\text{nucleon})\ ,$$

$$\sigma^{cc}(3.3\text{ GeV}) = 2.29 \pm 0.45\ (10^{-38}\text{cm}^2/\text{nucleon})\ ,$$

at mean energies of 1.1, 2.0, and 3.3 GeV. Our results are consistent with the past measurements and predictions by the neutrino event generators of NEUT and GENIE. In order to verify the neutrino interaction models, the reduction of the systematic error is necessary in the future analysis.

The measurement of the energy dependent cross section using neutrino beams with different off-axis angles is the first attempt in the world. If we fully bring out the potential of this technique, the measurement can be done in a "model-independent" way. Therefore, the precise measurement of the energy dependent CC inclusive cross section will be feasible with this technique and will be important input for the neutrino oscillation

measurement. Our cross section measurement opens up the new way to determine the energy dependent cross section.

Chapter A

Ideal horn design

The design of the horn is chosen so that pions, which under decays into neutrinos, can be collected with high efficiency. In order to simplify consideration, we adopt following approximations:

- the target is a point source and is placed upstream of the horn,
- the horn is short enough in the beam direction (the "thin lens" approximation),
- small angle approximation for production and deflection angles.

The situations with these approximations are illustrated in Fig. A.1. We consider that the magnetic horn with $B = \mu_0 I/2\pi r$ focuses a pion entering into it with an angle $\theta_{in}(= r/z)$, which then exits from horn with an angle θ_{out}. An averaged emission angle of the pion can be expressed:

$$\langle\theta_{in}\rangle \simeq \frac{\langle p_T\rangle}{p_\pi} \simeq \frac{0.3 \text{ GeV}}{p_\pi} , \tag{A.1}$$

where p_π and p_T are pion momentum and its transverse momentum, respectively. Here a typical $\langle p_T\rangle \simeq 0.3$ GeV off the target was assumed. The angular deflection of the pion in the magnetic field (the "p_T kick") is expressed as:

$$\Delta\theta = \theta_{in} - \theta_{out} \simeq \frac{eBl}{p_\pi} = \frac{e\mu_0 I}{2\pi r}\frac{l}{p_\pi} . \tag{A.2}$$

In an ideal case where all of the pions are collected, θ_{out} is zero and hence $\Delta\theta = \theta_{in}$. In the case of $\Delta\theta = \langle\theta_{in}\rangle$, using Eq. (A.1) and (A.2), we obtain:

$$l = \frac{2\pi r}{e\mu_0 I} \cdot 0.3 \text{ GeV} \propto r . \tag{A.3}$$

This means the path length of the pion in the horn should be proportional to the radius r: the ideal shape of the inner conductor should be a cone as shown in Fig. A.2.

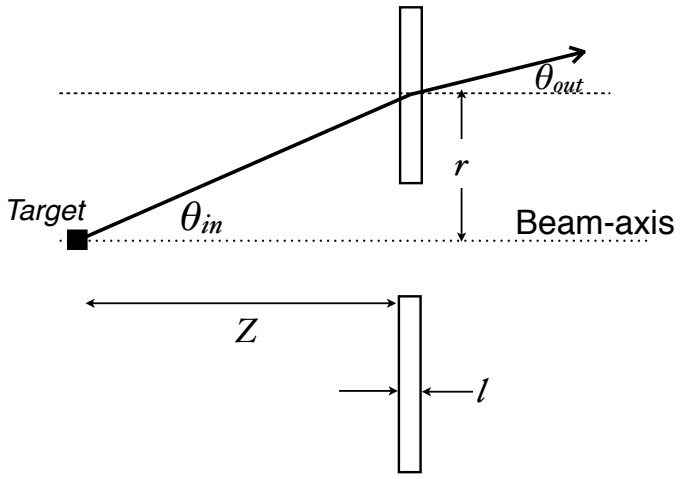

Figure A.1.: The horn system with the "thin lens" approximation.

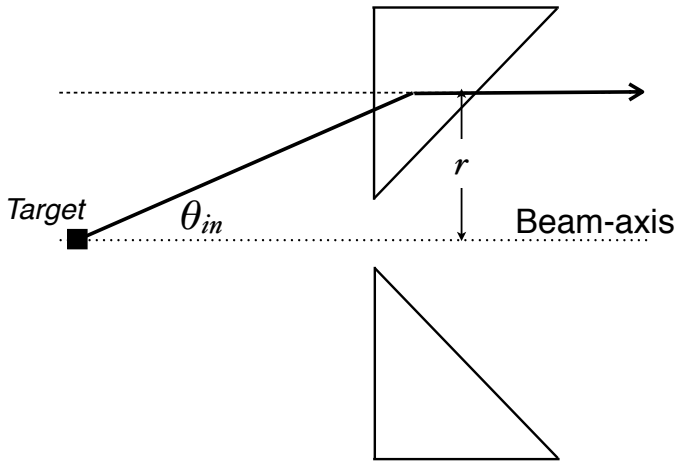

Figure A.2.: The ideal horn shape where the path length of the pion in the horn is proportional to the radius of the inner conductor.

Chapter B

Neutrinos from the two body decay

This section introduces formulas relating to the kinematics of the pion decay, resulting in generation of the neutrino flux. First we assume the pion decays into the muon and neutron in the rest frame. The transformation of daughter particles to the laboratory frame is then considered. Figure B.1 defines 4-momentum vectors for the daughter particles in the rest (P^*_ν, P^*_μ) and laboratory (P_ν, P_μ) frames. In order to simplify, the Lorentz boost is applied only for the Z direction which is in parallel to the parent pion's direction. At the rest frame, following conservations are hold:

$$E^*_\nu + E^*_\mu = m_\pi \ , \qquad \vec{P}^*_\nu + \vec{P}^*_\mu = \vec{0} \ ,$$

where m_π denotes pion mass. Since the neutrino is almost relativistic and its mass is very tiny, the absolute momentum is almost equivalent to the energy:

$$\begin{aligned} |P^*_\nu| &= E^*_\nu \\ \rightarrow |P^*_\mu| &= E^*_\nu = m_\pi - E^*_\mu \\ \rightarrow |P^*_\mu|^2 &= m^2_\pi - 2m_\pi E^*_\mu + (E^*_\mu)^2 \\ \leftrightarrow 2E^*_\mu &= \frac{(E^*_\mu)^2 - |P^*_\mu|^2}{m_\pi} \end{aligned}$$

Therefore, E^*_ν is calculated as:

$$E^*_\nu = \frac{m^2_\pi - m^2_\mu}{2m_\pi} \ , \tag{B.1}$$

Here $m_\mu = \sqrt{(E^*_\mu)^2 - |P^*_\mu|^2}$ denotes muon mass. The transformation of the neutrino to the laboratory frame is done by the Lorentz boost:

$$E_\nu = \gamma_\pi E^*_\nu (1 + \beta_\pi \cos\theta^*) \tag{B.2}$$

$$E_\nu \sin\theta = E^*_\nu \sin\theta^* \tag{B.3}$$

$$E_\nu \cos\theta = E^*_\nu \gamma_\pi (\cos\theta^* + \beta_\pi) \tag{B.4}$$

Here we use an approximation of $E_\nu = |P_\nu|$. β_π and γ_π are defined as:

$$\beta_\pi = \frac{|P_\pi|}{E_\pi} \ , \qquad \gamma_\pi = \frac{E_\pi}{m_\pi} \ , \tag{B.5}$$

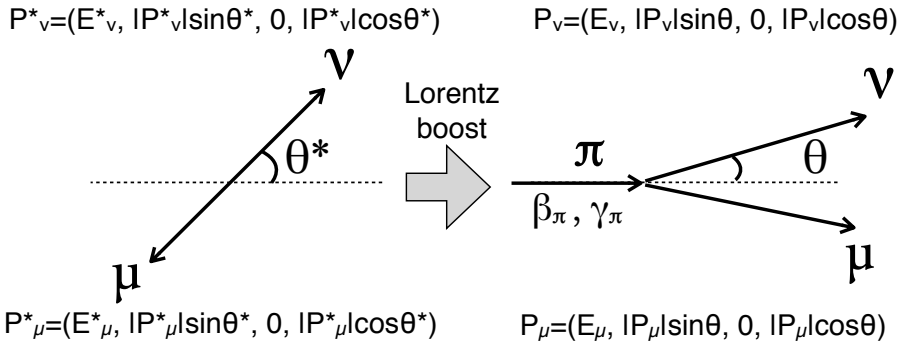

Figure B.1.: Illustration of the pion decay in the rest (left) and laboratory (right) frames, defining the momentums, energies, angles of the parent and daughter particles.

where P_π and E_π are the parent pion momentum and energy, respectively. With Eq. (B.5), the neutrino energy in Eq. (B.1) can be written as:

$$E_\nu = \frac{m_\pi^2 - m_\mu^2}{2m_\pi^2}(E_\pi + |P_\pi| \cos\theta^*) \ . \tag{B.6}$$

Equation (B.6) tells us the minimum and maximum neutrino energy which is available in the experiment:

$$E_\nu^{\min} = \frac{m_\pi^2 - m_\mu^2}{2m_\pi^2}(E_\pi - |P_\pi|) \simeq \frac{m_\pi^2 - m_\mu^2}{4E_\pi} \simeq 0 \ , \tag{B.7}$$

$$E_\nu^{\max} = \frac{m_\pi^2 - m_\mu^2}{2m_\pi^2}(E_\pi + |P_\pi|) \simeq \left(1 - \frac{m_\mu^2}{m_\pi^2}\right) \times E_\pi \ . \tag{B.8}$$

Here $E_\pi \gg m_\pi$ is used. In consequence, we can conclude that the available energy range of the neurone beam can be calculated to 0-0.427$\times E_\pi$. Kaons also contribute to the neutrino flux especially in the higher energy region. Since Eqs.(B.1)-(B.8) are valid for the kinematics of the two body decay, we can also relate the available energy range of the neutrino beam to the kaon energy (E_K): 0-0.954$\times E_K$. Since the pions and kaons are produced as secondary particles from the proton beam interaction, E_π and E_K strongly depends on the proton energy, i.e. the accelerator's individuality.

We then estimate an angular dependence of the neutrino flux Φ in the laboratory frame. Since the angular distribution of the decay is isotropic in the rest frame, we obtain:

$$\frac{d\Phi}{d\Omega^*} = \frac{1}{4\pi} \ , \tag{B.9}$$

where Ω^* denotes the solid angle in the rest frame. Therefore, the angular distribution of Φ in the laboratory frame can be calculated as:

$$\frac{d\Phi}{d\Omega} = \frac{d\Phi}{d\Omega^*} \cdot \frac{d\Omega^*}{d\Omega} \ . \tag{B.10}$$

The relation between $d\Omega$ and $d\Omega^*$ can be expressed using Jacobian of the transformation between the rest and laboratory frame:

$$\begin{aligned} d\Omega^* = d\cos\theta^* d\phi^* &= \mathcal{J}_{d\Omega^* \to d\Omega} \cdot d\cos\theta d\phi \\ &= \begin{vmatrix} \frac{\partial \cos\theta^*}{\partial \cos\theta} & \frac{\partial \phi^*}{\partial \cos\theta} \\ \frac{\partial \cos\theta^*}{\partial \phi} & \frac{\partial \phi^*}{\partial \phi} \end{vmatrix} \cdot d\cos\theta d\phi \ , \end{aligned} \tag{B.11}$$

where ϕ^* and ϕ are azimuthal angles in the rest and laboratory frames, respectively. The off-diagonal elements in the Jacobian are zero since we consider the Lorentz boosts in the Z direction. For the same reason, we obtain $\partial\phi^*/\partial\phi = 1$. $\cos\theta^*$ can be calculated using the transformation of the daughter particles to the rest frame:

$$E^*_\nu = E_\nu \gamma_\pi (1 - \beta_\pi \cos\theta) \tag{B.12}$$

$$E^*_\nu \cos\theta^* = E_\nu \gamma_\pi (\cos\theta - \beta_\pi) \tag{B.13}$$

Equations (B.12) and (B.13) give:

$$\cos\theta^* = \frac{\cos\theta_\nu - \beta_\pi}{1 - \beta_\pi \cos\theta_\nu} \ . \tag{B.14}$$

Finally we obtain the last remaining piece in the Jacobian using Eq. (B.14):

$$\frac{\partial \cos\theta^*}{\partial \cos\theta} = \frac{1 - \beta_\pi^2}{(1 - \beta_\pi \cos\theta)^2} \ . \tag{B.15}$$

Therefore, the angular distribution of Φ is expressed as a function of β_π and $\cos\theta$:

$$\frac{d\Phi}{d\Omega} = \frac{1}{4\pi} \cdot \frac{1 - \beta_\pi^2}{(1 - \beta_\pi \cos\theta)^2} \ . \tag{B.16}$$

In the long baseline neutrino experiment, the probability of the neutrino producing in the direction of the far detector can be estimated to be:

$$P = \frac{A}{4\pi L^2} \cdot \frac{1 - \beta_\pi^2}{(1 - \beta_\pi \cos\theta)^2} \ , \tag{B.17}$$

where A is a transverse area of the far detector and L is a distance between the production point and the detector. In the T2K experiment, the location of SK is far enough away from the production point. Thus, L can be regarded as the distance between the SK and target (=295 km).

Using Eqs (B.1) and (B.14), all the notations in Eq. (B.6) can be written as ones in the laboratory frame:

$$\begin{aligned} E_\nu &= \frac{m_\pi^2 - m_\mu^2}{2} \cdot \frac{E_\pi}{m_\pi^2} \cdot (1 + \frac{|P_\pi|}{E_\pi} \cdot \frac{\cos\theta - |P_\pi|/E_\pi}{1 - |P_\pi|/E_\pi \cos\theta}) \\ &= \frac{m_\pi^2 - m_\mu^2}{2} \cdot \frac{E_\pi}{m_\pi^2} \cdot \frac{E_\pi - |P_\pi|\cos\theta + (E_\pi \cos\theta - |P_\pi|) \cdot |P_\pi|/E_\pi}{E_\pi - |P_\pi|\cos\theta} \\ &= \frac{m_\pi^2 - m_\mu^2}{2} \cdot \frac{E_\pi}{m_\pi^2} \cdot \frac{(E_\pi^2 - |P_\pi|^2)/E_\pi}{E_\pi - |P_\pi|\cos\theta} \\ &= \frac{m_\pi^2 - m_\mu^2}{2(E_\pi - |P_\pi|\cos\theta)} \end{aligned} \tag{B.18}$$

Chapter C

Reconstruction of the neutrino beam profile

A profile of the neutrino beam is reconstructed from the number of the detected neutrino events at each module. A Gaussian function is then used to fit these profiles. Figure C.1 shows an example beam profile reconstructed using the selection in Sec. 8.2 when the beam power and horn current settings were 220 kW and 250 kA, respectively. These profiles shown in the figure are obtained with one day data. The fitted line of the Gaussian function is also shown in the figure as a dashed line.

Figure C.2 shows the expected statistical error on the measurement of the neutrino beam direction. As seen in the figure, the statistical error is typically 0.15 mrad with the beam power of 220 kW and the horn current of 250 kA. Although the measurement error is statistically improved as the beam power increases, we typically require one day to reconstruct the neutrino beam profile so that the neutrino beam direction can be monitored each day.

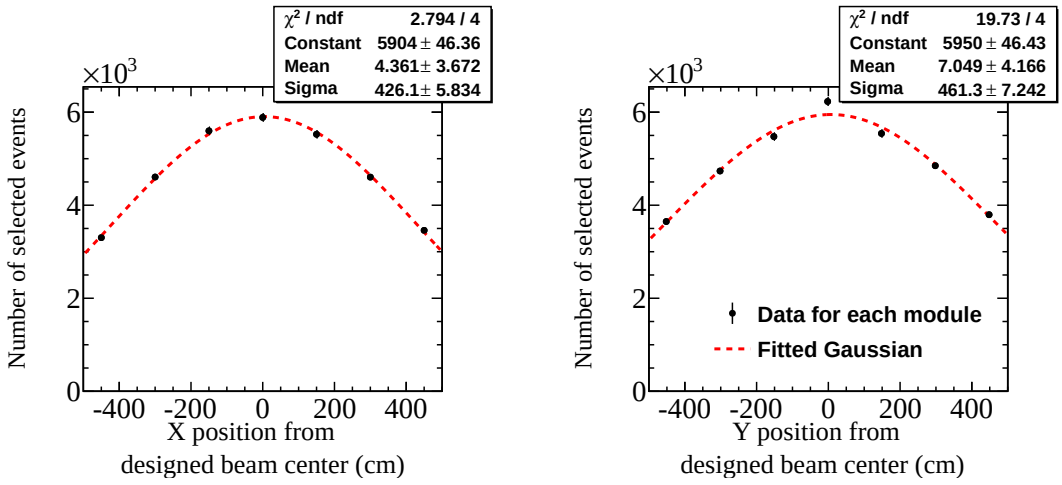

Figure C.1.: Obtained profiles of the neutrino beam with INGRID for the horizontal (left) and vertical (right) direction. They were obtained with data accumulated in one day at a 220 kW beam power. All of the horns were operated at 250 kA.

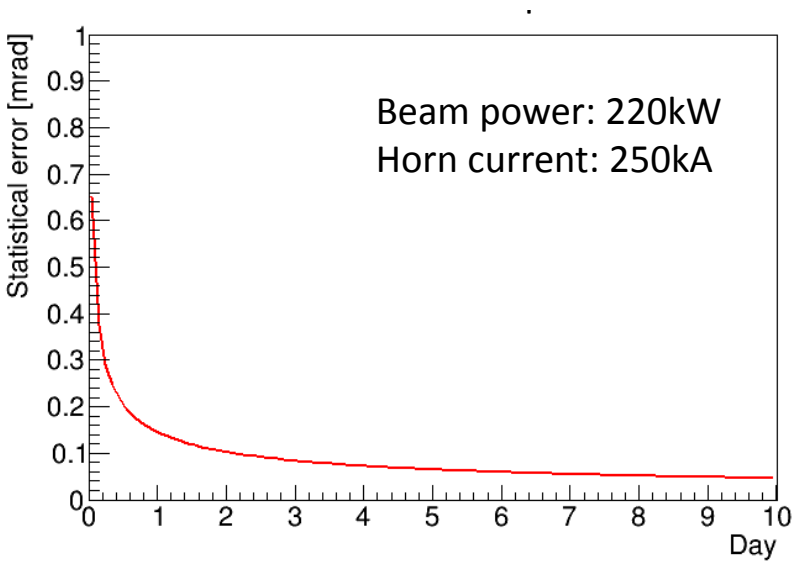

Figure C.2.: Expected statistical error on the measurement of the neutrino beam direction. In this study, the beam power and horn current setting are assumed to be 220 kW and 250 kA, respectively.

Chapter D

Final χ^2 formula

The χ^2 formula including all systematic parameters described in Sec. 9.3 is defined as follows.

$$\chi^2 = \sum_j \sum_g \frac{\left\{ N_{jg}^{obs} - (N_{jg}^{cc} + N_{jg}^{nc} + N_{jg}^{bg}) \right\}^2}{\sqrt{\left(\sigma_{N_{jg}^{obs,stat}}\right)^2 + \left(\sigma_{N_{jg}^{mc}}\right)^2 + \left(\sigma_{N_{jg}^{det}}\right)^2}} + \sum_k \Delta(\vec{f^k})^t (V_k)^{-1} \Delta\vec{f^k} \ , \quad \text{(D.1)}$$

where indices of j and g denote the j^{th} topology bin and the g^{th} module group, respectively; N^{obs}, N^{cc}, N^{nc}, and N^{bg} are the observed number of selected events, the predicted number of CC events, NC events, and BG events, respectively; $\sigma_{N^{mc}}$ and $\sigma_{N^{det}}$ are the MC statistical error and the uncorrelated error from the detector systematic errors, respectively; $\sigma_{N^{obs,stat}}$ is the statistical error. The last term in Eq .(D.1) is a constraint term for the systematic parameters:

- f_{ig}^b: Flux systematic error for the i^{th} energy bin of g^{th} module group
- f_j^d: Detector systematic error for the j^{th} topology bin
- f_j^{cc}: CC interaction systematic error for the j^{th} topology bin
- f_j^{nc}: NC interaction systematic error for the j^{th} topology bin

The predicted number of CC events and NC events are expressed as follows:

$$\begin{aligned}
N_{jg}^{cc} &= (1+\Delta f_j^d)(1+\Delta f_j^{cc}) \sum_i (1+\Delta f_{ig}^b) \cdot \sum_{l=0}^{L_i} \left(1 + \Delta f_i + \frac{\Delta f_{i+1} - \Delta f_i}{L_i} \cdot l\right) \cdot \phi_{ilg} \cdot \sigma_{il}^{cc} \cdot \epsilon_{ilj}^{cc} \cdot T \\
&\simeq \sum_i \sum_{l=0}^{L_i} \left(1 + \Delta f_i + \frac{\Delta f_{i+1} - \Delta f_i}{L_i} \cdot l + \Delta f_j^d + \Delta f_j^{cc} + \Delta f_{ig}^b\right) \cdot \phi_{ilg} \cdot \sigma_{il}^{cc} \cdot \epsilon_{ilj}^{cc} \cdot T \\
&= \sum_i \sum_{l=0}^{L_i} \left(1 + \Delta f_i + \frac{\Delta f_{i+1} - \Delta f_i}{L_i} \cdot l + \Delta f_j^d + \Delta f_j^{cc} + \Delta f_{ig}^b\right) \cdot n_{ijlg}^{cc} \ , \quad \text{(D.2)} \\
N_{jg}^{nc} &= (1+\Delta f_j^d)(1+\Delta \bar{f}_g^b)(1+\Delta f_j^{nc}) \cdot \sum_i \left(\phi_{ig} \cdot \sigma_i^{nc} \cdot \epsilon_{ij}^{nc} \cdot T\right) \\
&\simeq (1+\Delta f_j^d + \Delta \bar{f}_g^b + \Delta f_j^{nc}) \cdot \sum_i \left(\phi_{ig} \cdot \sigma_i^{nc} \cdot \epsilon_{ij}^{nc} \cdot T\right) \\
&= (1+\Delta f_j^d + \Delta \bar{f}_g^b + \Delta f_j^{nc}) \cdot n_{jg}^{nc} \ , \quad \text{(D.3)}
\end{aligned}$$

where index of l denotes l^{th} local bin; L_i is the number of local bins for the i^{th} energy bin. $\Delta\bar{f}_g^b$ in the expression of NC events is a flux averaged systematic parameter for NC interaction and is defined as follows:

$$\Delta\bar{f}_g^b = \sum_i \Delta f_{ig}^b \cdot \frac{\phi_{ig}}{\sum_{i'} \phi_{i'g}} \, . \tag{D.4}$$

Chapter E

Fitter validation

The fitter is validated by using a large number of pseudo data sets which are generaged by throwing the statistical parameters and the systematic parameters according to the covariances and fixing the parameters of the cross section normalization (Δf_0-Δf_4) to 0. The pull value for each toy MC experiment is defined as,

$$\text{Pull} = \frac{\tau_{fit} - \tau_{true}}{\sigma_{fit}} \tag{E.1}$$

where τ_{fit} is the best fit value for each fit parameter, τ_{true} is the true value for each fit parameter, and σ_{fit} is 1σ error for each fit parameter. Figure E.1 shows the pull distribution made with 3000 pseud experiments. A mean and width is derived from the distribution for each parameter. The results are shown in Figure E.2. In this figure, the fit parameters consist of:

- Cross section parameter (5)
- Flux systematic parameter (42)
- NC interaction systematic parameter (8)
- CC interaction systematic parameter (14)
- Detector systematic parameter (14)

The value in the parenthesis is the number of parameters. The pulls of all parameters are consistent with zero. The extracted width of the pull distribution for each parameter is also checked and it is consistent with 1.

We checked the chi-squared distribution for the fake data set. Figure E.3 shows the obtained chi-squared distribution. A degree of freedom is extracted by fitting the distribution with the chi-squared function which is prepared in ROOT (`ROOT::Math::chisquared_pdf`)

and it is 93.09 ± 0.25. In this analysis, the degree of freedom is calculated to be:

$$\begin{aligned} dof &= \{7 \text{ (Num. of vertex bins in DS-escaping)} \\ &+ 7 \text{ (Num. of vertex bins in NonDS-escaping)}\} \\ &\times 7 \text{ (Num. of module groups)} \\ &- 5 \text{ (Num. of fitted parameters)} \\ &= 14 \times 7 - 5 \\ &= 93 \end{aligned}$$

and it is in good agreement with the fitted value.

We also validated our fitter by using following 4 sets of the cross section parameters.

1. $\{\Delta f_0, \Delta f_1, \Delta f_2, \Delta f_3, \Delta f_4\} = \{-0.4, -0.2, 0, 0.2, 0.4\}$ (Parameter set 1)
2. $\{\Delta f_0, \Delta f_1, \Delta f_2, \Delta f_3, \Delta f_4\} = \{-0.2, -0.1, 0, 0.1, 0.2\}$ (Parameter set 2)
3. $\{\Delta f_0, \Delta f_1, \Delta f_2, \Delta f_3, \Delta f_4\} = \{0.2, 0.1, 0, -0.1, -0.2\}$ (Parameter set 3)
4. $\{\Delta f_0, \Delta f_1, \Delta f_2, \Delta f_3, \Delta f_4\} = \{0.4, 0.2, 0, -0.2, -0.4\}$ (Parameter set 4)

For each parameter set, 3000 pseudo experiments are used to make pull distributions for all fit parameters. The mean and width of the pull distribution for each parameter set are shown in Figure E.4 and E.5, respectively. (We used same random seeds for all parameter sets.) For parameter set 1, slight deviations of pull are seen for the cross section parameters, f_0-f_4. The maximum size of the deviation is 0.05. As described later, the size of the actual fitting error is around 20% for the cross section parameters. Namely, the correponding bias is 1% level and it is enough small. Hence, we confirm our fitter works well for any parameter sets.

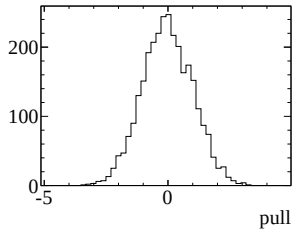

(a) Δf_0 (0.5 GeV)

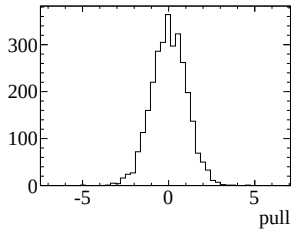

(b) Δf_1 (0.8 GeV)

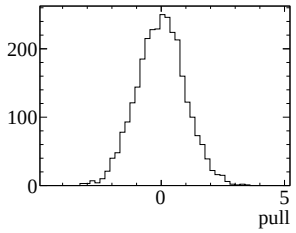

(c) Δf_2 (1.4 GeV)

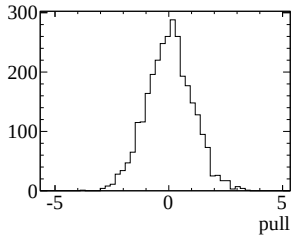

(d) Δf_3 (2.6 GeV)

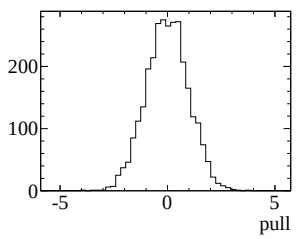

(e) Δf_4 (4.0 GeV)

Figure E.1.: Pull distribution for the parameters of the cross section normalization.

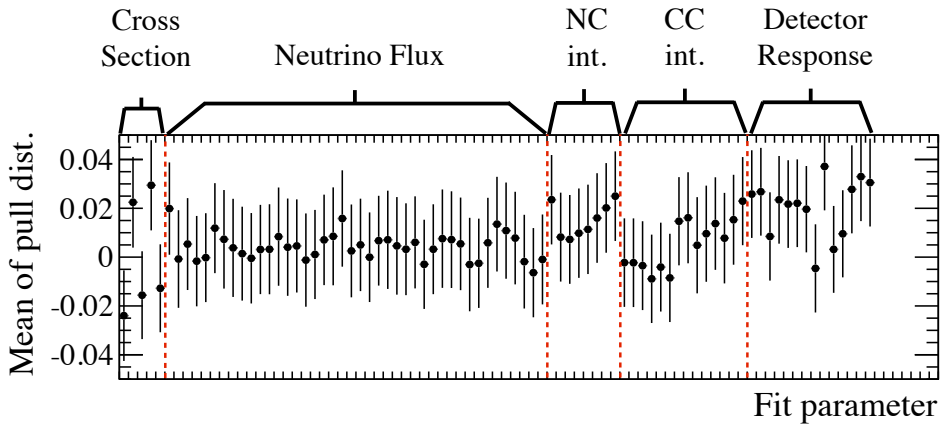

(a) Mean of pull distribution

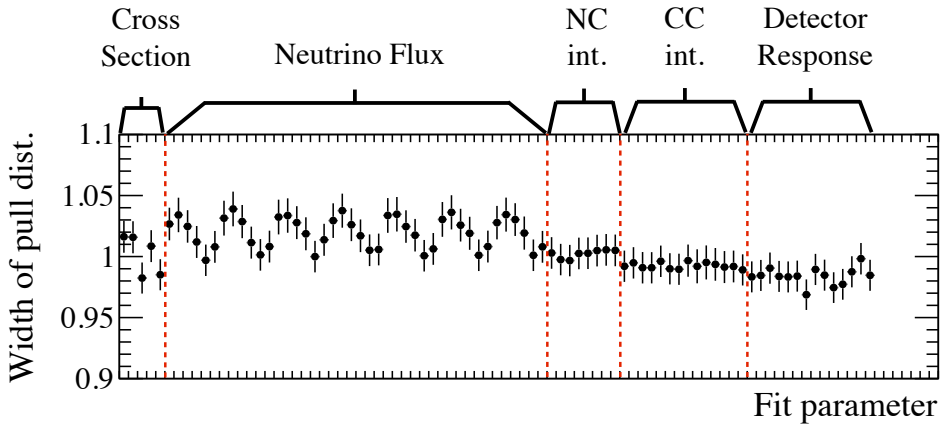

(b) Width of pull distribution

Figure E.2.: Mean (top) and width (bottom) of the pull distribution for each fit parameter. The vertical error bars for the mean and width distribution are the standard error of the mean (SEM) and root-mean-square error (RMSE), respectively.

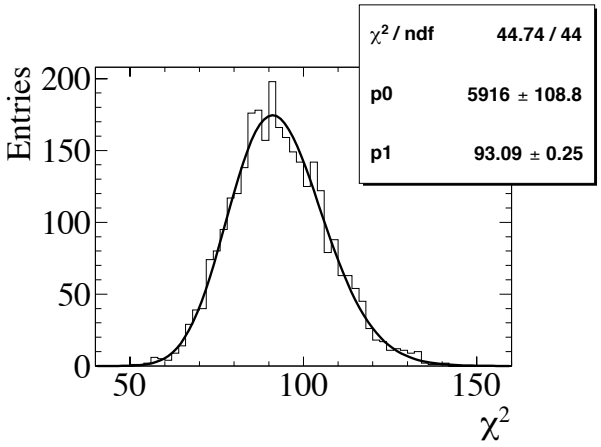

Figure E.3.: Best fit chi-squared distribution for the fake data set. A black line is the fitted distribution. The fitted dof is obtained from the fitted chi-squared and is 93.09 ± 0.25.

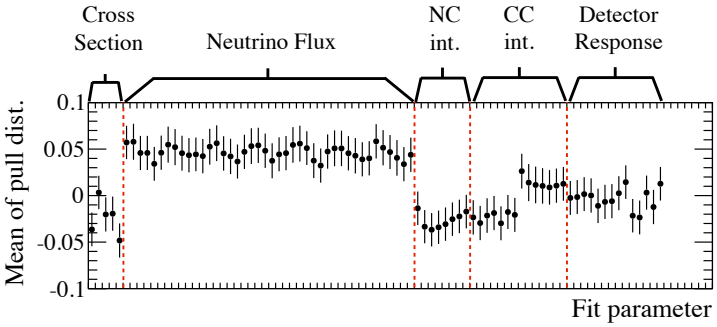

(a) Parameter set 1

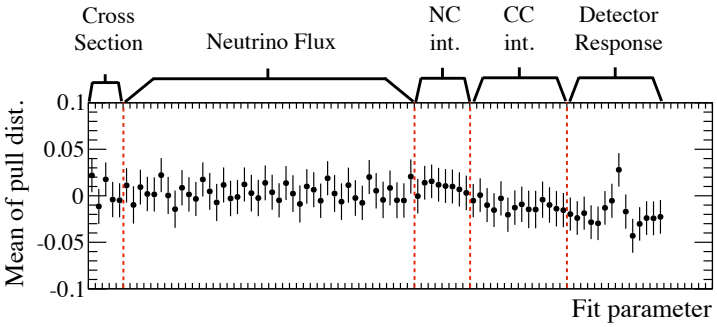

(b) Parameter set 2

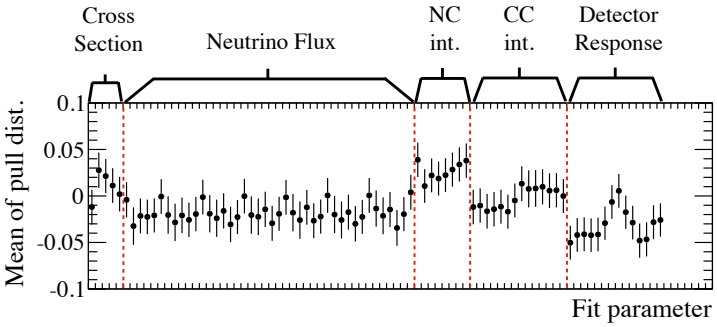

(c) Parameter set 3

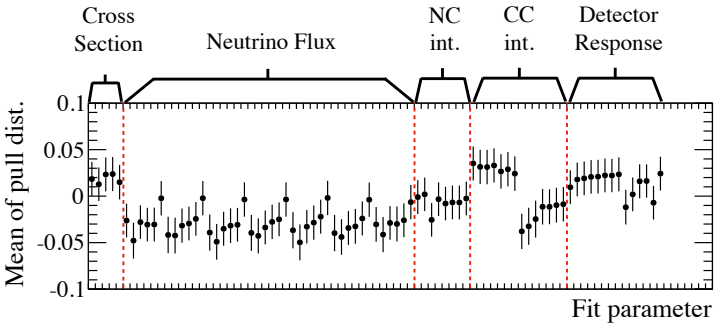

(d) Parameter set 4

Figure E.4.: Mean of the pull distribution for all fit parameters for each parameter set.

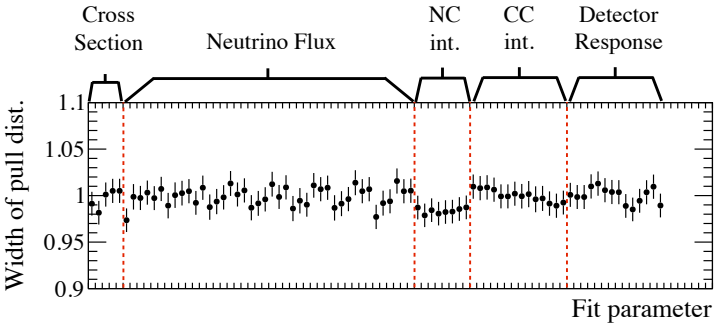

(a) Parameter set 1

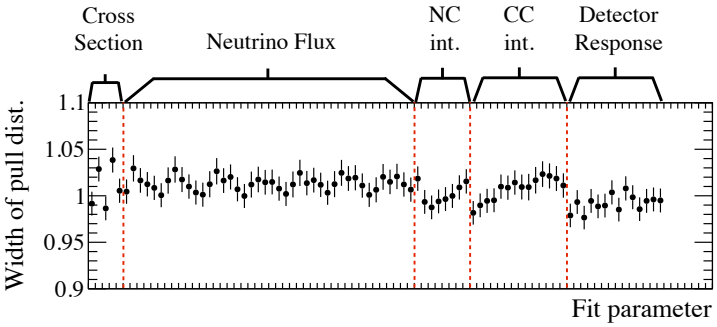

(b) Parameter set 2

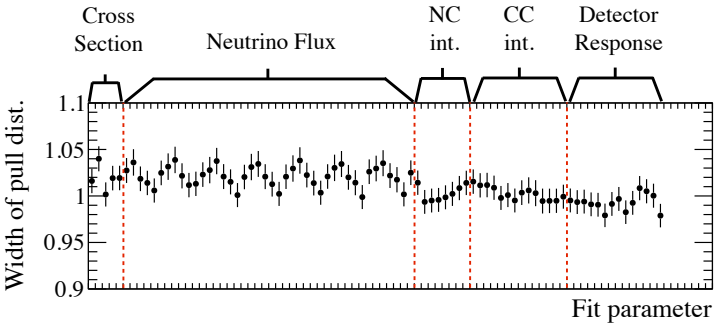

(c) Parameter set 3

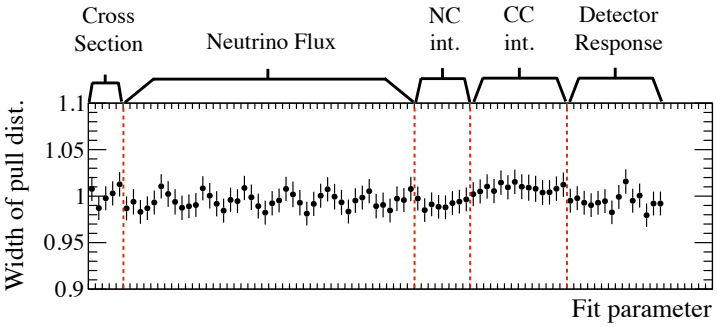

(d) Parameter set 4

Figure E.5.: Width of the pull distribution for all fit parameters for each parameter set.

Chapter F

Uncertainty in the secondary interaction

Hadrons produced by neutrino-nucleus interactions can interact with the other nucleus during their travels. This effect is called "secondary interaction (SI)". In the INGRID simulation, the pion SI is implemented by GEANT4 and following interaction modes are considered:

Quasi-elastic scattering (QEL)
A pion interacts inelastically with a nucleus, but only one pion, which is the same type as the incoming pion, exists in the final state.

Absorption (ABS)
The incident pion is absorbed by the nucleus, resulting in there being no pions in the final state.

Single charge exchange (SCX)
There is only one π^0 and no other type of the pions in the final state.

Double charge exchange (DCX)
A charged pion enters the interaction, and a pion of the opposite charge exits the interaction. Only one pion exits the interaction.

Multi-pion interaction (Multi-π)
The interaction produces more than one pions.

The uncertainty in the SI is considered for the first three interactions: QEL, ABS, and SCX because contribution from DCX and multi-pi are expected to be small. Here we only focus on the SI with the iron target because the contribution of the CH interaction to the total one is only $\sim$4%.

Experimental data, which is used for a comparison with the model, are collected and are summarized in Table F.1. In the table, the reactive cross section is defined as $\sigma_{\text{total}} - \sigma_{\text{elastic}}$, where σ_{total} is the total cross section and σ_{elastic} is the elastic cross section. As seen in the table, D. Ashery *et al.* provides various cross sections for various pion momenta and for various nuclear target including iron. However, the other data does not provide the cross section on the iron nucleus. For those data, material scaling is applied by referring [142] in order to extract the cross section on the iron nucleus (A=56).

Figure F.1 shows the comparison of the pion cross sections between the prediction from FTFP_BERT and compiled data. As seen in the figure, FTFP_BERT overestimates the size of the ABS for both π^+ and π^- around 100 MeV and largely underestimate the size of the QEL for π^+ below 300 MeV. The reactive cross sections, are found to be in agreement between the prediction and data in the high energy region.

To evaluate the systematic error from these disagreements between the model and data, we first tune the pion cross section in the momentum region covered by data. Second, for the lower energy region uncovered by data, the ABS $\pi^+(\pi^-)$ cross section in the lower energy region below 20(30) MeV are kept constant, which is motivated by the microscopic calculation based on [98][1]. The QEL cross section is extrapolated to 0 at 0 MeV for π^+[2]. For the higher energy region, "case studies" are conducted for both π^+ and π^-. In the "case studies", the size of the reactive cross section is conserved since the sections predicted by GEANT4 are in agreement with the experimental data in the high energy region.

Use results from Jones et al. (case A)
In this case, we tune both the ABS and SCX π^+ cross sections at 500 MeV. For the energy region above 500 MeV, we use same size of the correction at 500 MeV for both the ABS and SCX, which are estimated to be 30% and 100%, respectively. The QEL π^+ cross section is then tuned so as to keep the size of the reactive cross section.

Not use results from Jones et al. (case B)
This is motivated by the unknown error size on the SCX π^+ cross section. In this case, we do not tune both the ABS and SCX π^+ cross sections at 500 MeV. A discrepancy of the QEL π^+ cross section at 315MeV is estimated to be $\sim$100%. Thus, the 100% error on the QEL π^+ cross section is used for the correction of both the ABS and SCX for $T_\pi \geq$500 MeV so as to keep the reactive cross section.

For π^- in the higher energy region, a following "case study" is conducted. As seen in the left in Fig. F.1, FTFP_BERT overestimates the size of the ABS cross section by 30% as compared to the result from Nakai *et al.* (T_π=187, 233, 280 MeV). QEL (case 1) or SCX (case 2) is increased to compensate the decrease of ABS for $T_\pi >$165 MeV.

There are 4 cases in total: case A+case 1 (case A1), case A+case 2 (case A2), case B+case 1 (case B1), and case B+case 2 (case B2). Thus, 4 sets of the MC samples are generated in order to estimate the uncertainty from the pion SI. Figure F.2 and F.3 show the pion cross section after the tuning is applied in the case A1 and A2, and the case B1 and B2, respectively. After the generation of these MC samples, a fit to the data is attempted for each case. All the obtained results are then compared to the result with the nominal MC samples (nominal FTFP_BERT). Finally, the difference in the fit

[1]This model is also used for modeling the pion cross section for low energy region in NEUT.
[2]QEL for π^- for the lower energy region are linearly decreased at 0 MeV in FTFP_BERT. Therefore, we do nothing for the π^- QEL cross section.

Table F.1.: Summary of pion-nucleus scattering data. The reactive cross section is defined as a sum of any of the inelastic cross sections.

	Hadrons	Targets	P_{lab} (MeV/c)	interaction type
K. Nakai *et al.* [143]	π^+/π^-	Al, Ti, Cu, Sn, Au	83-395	ABS
D. Ashery *et al.* [142]	π^+/π^-	Li, C, O, Al, Fe, Nb, Bi	175-432	Reactive, Elastic, QEL, ABS, SCX
M.K. Jones *et al.* [144]	π^+	C, Ni, Zr, Sn, Pb	363-624	QEL, ABS, SCX
G.J. Gelderloos *et al.* [145]	π^-	Li, C, Al, S, Ca, Cu, Zr, Sn, Pb	479-616	Reactive
B.W. Allardyce *et al.* [146]	π^+/π^-	C, Al, Ca, Ni, Sn, Ho, Pb	710-2000	Reactive

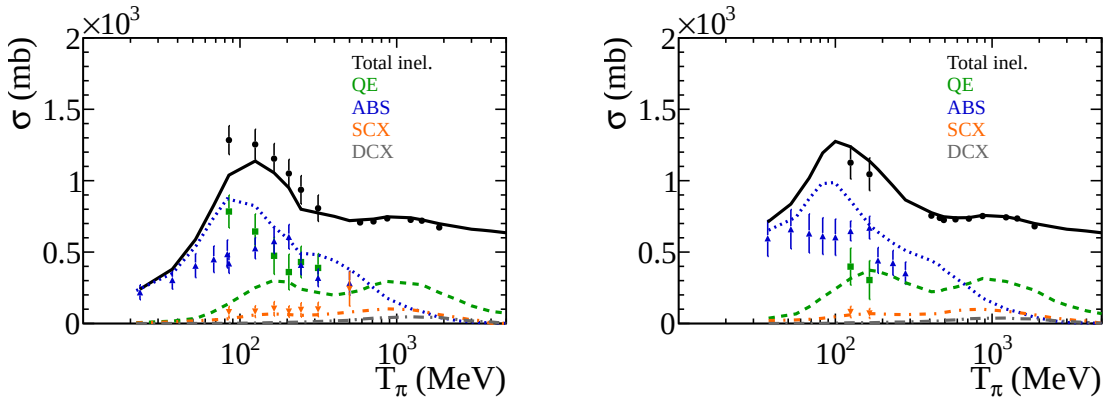

Figure F.1.: Comparison of the cross section for π^+ (left) and π^- (right) between the prediction from FTFP_BERT (lines) and compiled data (dots).

results from the nominal samples are used to the error calculation. The results are given in Sec. 9.4.2.

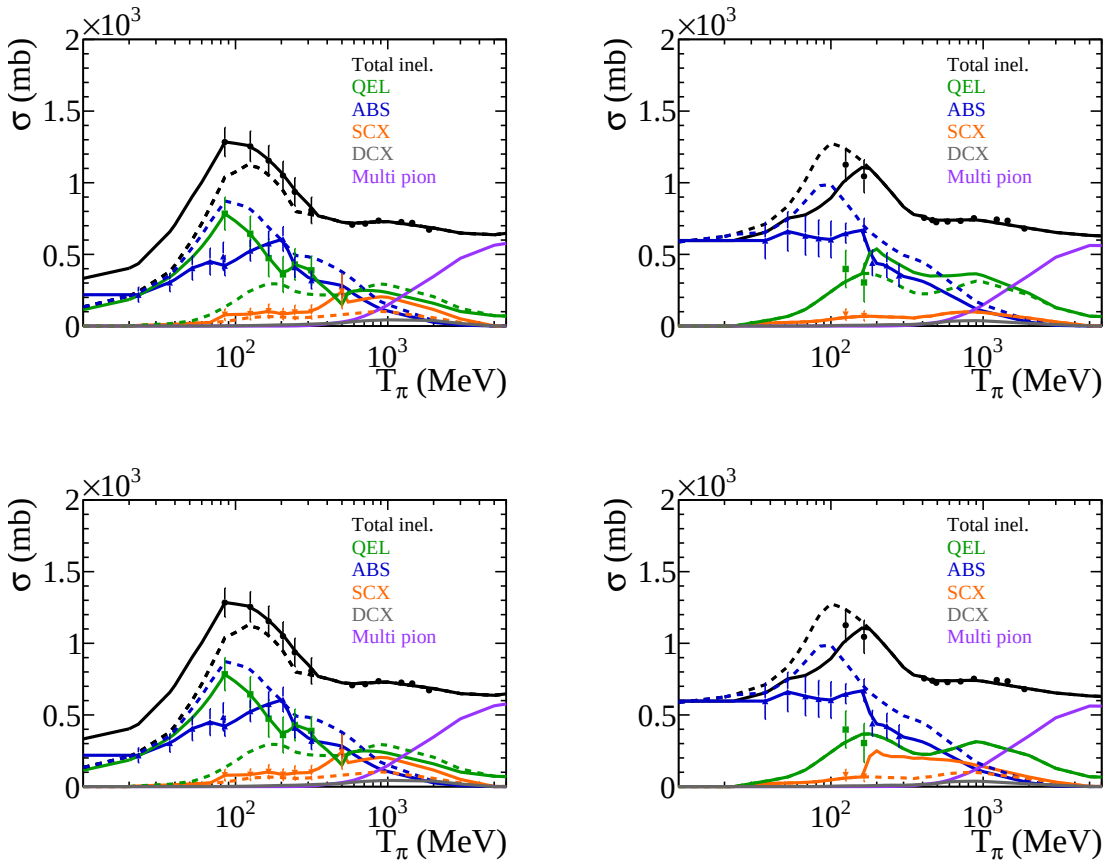

Figure F.2.: Nominal (dash) and tuned (solid) cross sections for π^+ (left) and π^- (right) with the compiled data. Top: caseA1. Bottom : caseA2.

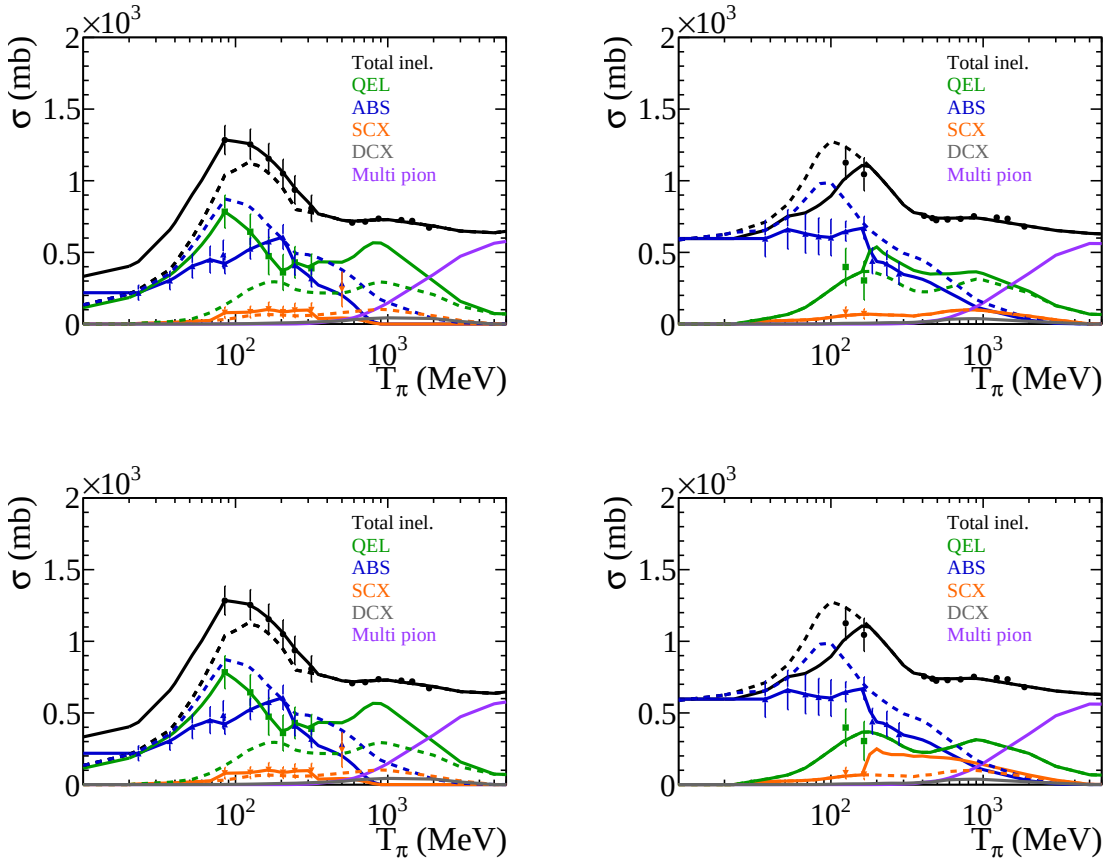

Figure F.3.: Nominal (dash) and tuned (solid) cross sections for π^+ (left) and π^- (right) with the compiled data. Top: caseB1. Bottom : caseB2.

Chapter G

Effect of the CH interaction

In current INGRID MC simulation, we assume ν_μ CC cross section (cm^2/nucleon) on carbon (CH) is equal to that on iron. Namely, we only produce NEUT files where we simulate ν_μ interaction with the iron target and not produce NEUT files for the interaction with CH. Those NEUT Fe files are then propagated to the INGRID detector simulation. Then we generate the position of the vertex (interaction) according to the probability of the mass of Fe and CH. In this analysis, we define the number of CC events as follows.

$$\begin{aligned} N_{jm}^{cc} &= \sum_i \phi_{im} \cdot \epsilon_{ij}^{cc} \cdot (\sigma_i^{cc,Fe} \cdot T^{Fe} + \sigma_i^{cc,CH} \cdot T^{CH}) \\ &\simeq \sum_i \phi_{im} \cdot \epsilon_{ij}^{cc} \cdot \sigma_i^{cc,Fe} \cdot (T^{Fe} + T^{CH}) \\ &= \sum_i \phi_{im} \cdot \epsilon_{ij}^{cc} \cdot \sigma_i^{cc} \cdot T \quad (T = T^{Fe} + T^{CH}) \end{aligned}$$

Here we assume $\sigma_i^{cc} = \sigma_i^{cc,Fe} \simeq \sigma_i^{cc,CH}$. Fitting and nuisance parameters are then applied as follows,

$$N_{jm}^{cc} = (1 + \Delta f_j^d) \cdot (1 + \Delta f_j^{cc}) \cdot \sum_i (1 + \Delta f_{jm}^b) \cdot (1 + \Delta f_i) \cdot \phi_{im} \cdot \epsilon_{ij}^{cc} \cdot \sigma_i^{cc} \cdot T$$

This means, we apply both of the cross section normalizations and the other systematic parameters to both of $\sigma^{CC,Fe}$ and $\sigma^{CC,CH}$. The contamination of CH interaction was estimated by using QGSP_BERT and is estimated to be 3.4-3.9% for each topology. The effect of the CH interaction is then checked by using modified formula for the number of CC interaction:

$$\begin{aligned} N_{jm}^{cc} &= (1 + \Delta f_j^d) \cdot (1 + \Delta f_j^{cc}) \sum_i (1 + \Delta f_{im}^b) \cdot (1 + \Delta f_i) \cdot \phi_{im} \cdot \sigma_i^{cc} \cdot \epsilon_{ij}^{cc} \cdot (T \cdot r_{Fe,j}) \\ &\quad + \sum_i \phi_{im} \cdot \sigma_i^{cc} \cdot \epsilon_{ij}^{cc} \cdot (T \cdot r_{CH,j}) \end{aligned}$$

where $r_{CH,j}$ and r_{Fe} are the fraction of CH and Fe interaction given in j^{th} topology bin, respectively. Here we assume there is no difference in the CH contamination between module groups. We also do not apply any systematic parameters to the number of CC events with CH because of its small fraction (4%). Even if 15% error (e.g. Flux systematic error) is applied to the number of CC events with CH, the effect is less than

1% level (4% × 15% = 0.6%). In this sense, we can safely ignore the effect of systematic errors for the number of CC events with CH. In this investigation, we also use same covariance matrices for detector and neutrino interaction systematic errors, which are used in this analysis.

Figure G.2 shows the results for 5 fitting and 3 averaged parameters with the physics list of QGSP_BERT (a), FTFP_BERT (b), and FTF_BIC (c). Black and red points in those figures are the results before and after the CH interactions are taken into account, respectively. As seen in those figures, the change of the center value is within the previous error size. The center values for the 5 fitting and 3 averaged parameters are also summarized in Table G.1 and G.2. The numbers in parentheses in the tables show fractional changes from the results before the CH interactions are taken into account. The difference is 0-5% level for the 5 fitting parameters and it is within the previous error size as already described. By taking the average, the size of the difference is reduced to $< 1\%$. In conclusion, the effect of CH interaction is small in this analysis.

The cross section of CH is actually different from that of Fe. Figure G.3 shows a ratio of the cross section of Fe to that of CH as a function of neutrino energy. As seen in the figure, the difference between σ^{Fe} and σ^{CH} is 3-5% for > 0.5 GeV where the detection efficiency starts to rise up. However, the fraction of CH interaction is 4% and the effect of the different cross section is 4%×3-5% = 0.1-0.2%. We can ignore the effect of different cross sections because of its small size.

Table G.1.: Fit results of 5 fitting parameters after the CH interaction is taken into account. The numbers in parentheses in the tables show fractional changes from the previous results.

Fit parameter	QGSP_BERT	FTFP_BERT	FTF_BIC
f_0 (0.5 GeV)	3.551 (+4.5%)	3.702 (+4.0%)	3.536 (+4.1%)
f_1 (0.8 GeV)	0.746 (-3.1%)	0.611 (-4.1%)	0.610 (-3.9%)
f_2 (1.4 GeV)	1.256 (+1.9%)	1.349 (+1.9%)	1.567 (+1.9%)
f_3 (2.6 GeV)	0.949 (-0.4%)	0.792 (+1.0%)	0.570 (-1.2%)
f_4 (4.0 GeV)	0.716 (-0.3%)	0.710 (-0.3%)	0.722 (-0.3%)

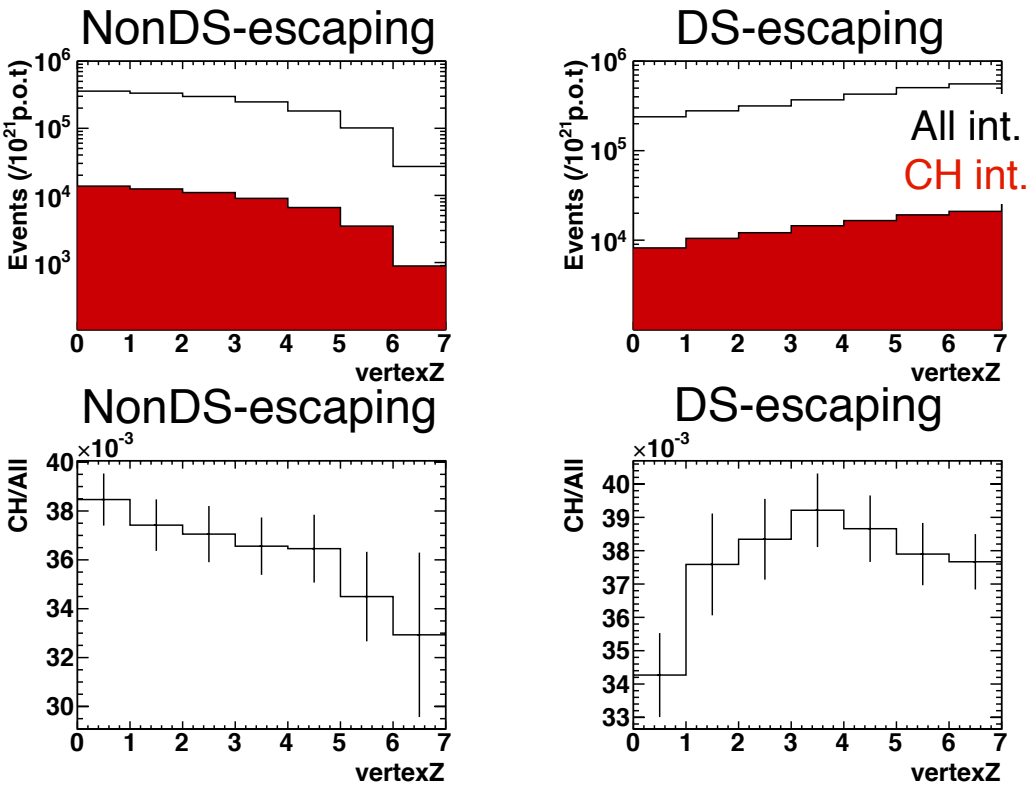

Figure G.1.: Contamination of CH interaction for each topology bin (tops) and the ratio of CH interaction to Fe+CH interaction (bottoms). Events are summed over all modules. This contamination is estimated by using QGSP_BERT.

Table G.2.: The normalization factor for the cross section at 1.1, 2.0, and 3.3 GeV after CH interaction is taken into account. The numbers in parentheses in the tables show fractional changes from the previous results.

	QGSP_BERT	FTFP_BERT	FTF_BIC
f(1.1 GeV)	1.001 (0.0%)	0.980 (0.0%)	1.089 (+0.3%)
f(2.0 GeV)	1.103 (+0.9%)	1.070 (+0.8%)	1.069 (+1.0%)
f(3.3 GeV)	0.833 (-0.4%)	0.751 (-0.7%)	0.646 (-0.8%)

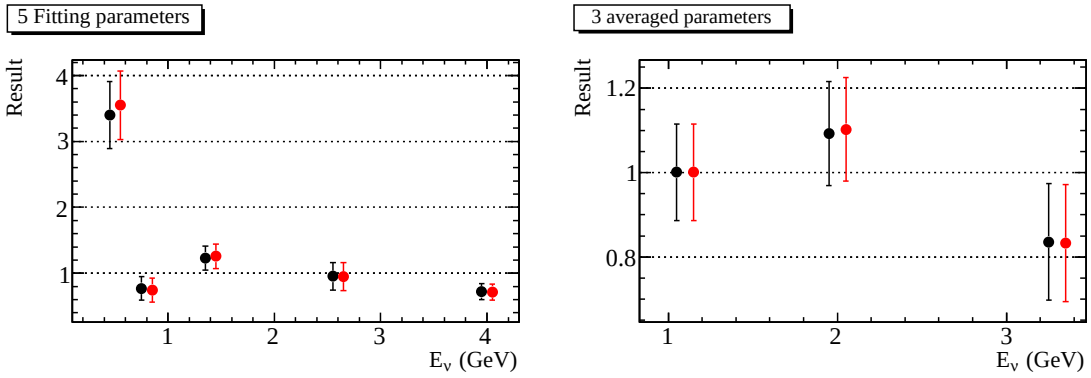

(a) QGSP_BERT

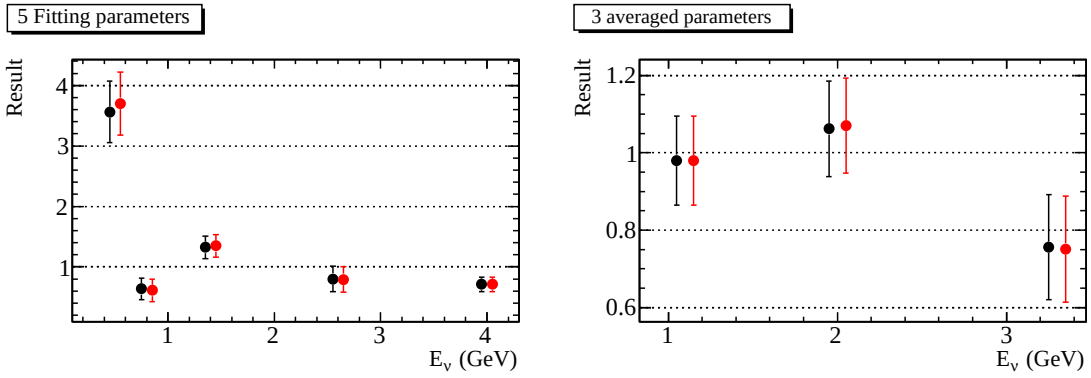

(b) FTFP_BERT

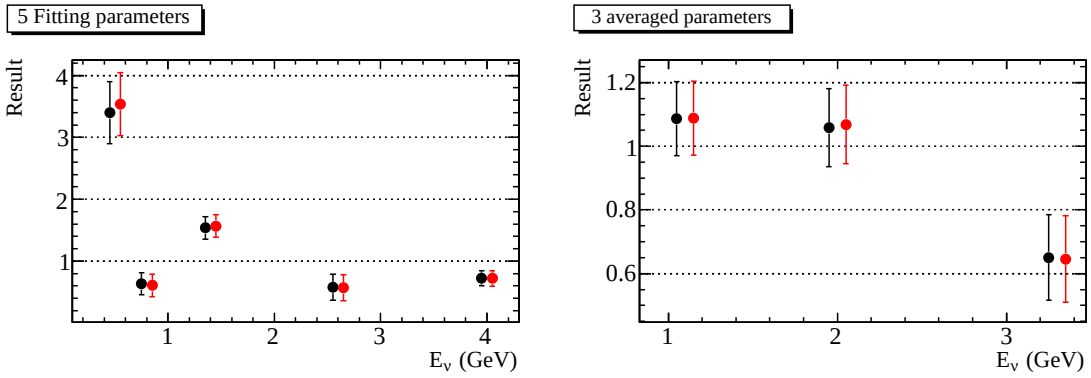

(c) FTF_BIC

Figure G.2.: Results for 5 fitting (left) and 3 averaged parameters (right) with the GEANT4 physics list of QGSP_BERT (a), FTFP_BERT (b), and FTF_BIC (c). Black and red points are respectively the results before and after CH interactions are taken into account.

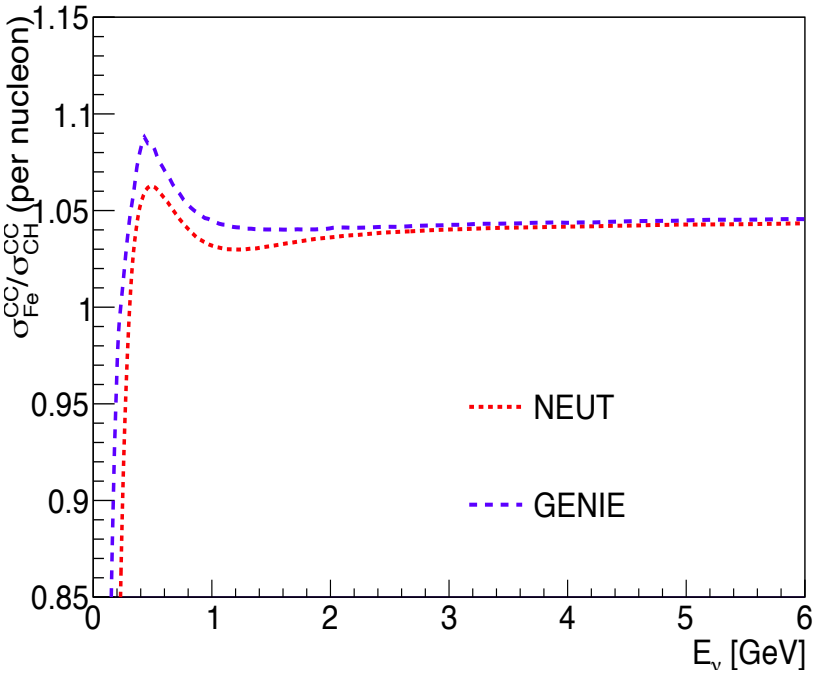

Figure G.3.: Ratio of the cross section of Fe to that of CH. The predictions of NEUT and GENIE are shown.

List of Figures

List of Tables

Bibliography

[1] A.D. Sakharov. Violation of CP Invariance, C Asymmetry, and Baryon Asymmentry of the Universe. *JEPT Lett.*, 5:24, 1967.

[2] J. Christenson et al. Evidence for the 2π Decay of the K_2^0 Meson. *Phys. Rev. Lett.*, 13:138–140, 1964.

[3] S. Fukuda et al. (The Super-Kamiokande Collaboration). The Super-Kamiokande detector. *Nucl. Instrum. Meth.*, A501:418–462, 2003.

[4] Y. Fukuda et al. (Super-Kamiokande Collaboration). Evidence for Oscillation of Atmospheric Neutrinos. *Phys. Rev. Lett.*, 81:1562–1567, 1998.

[5] C. L. Cowan Jr., F. Reines, F. B. Harrison, H. W. Kruse, and A. D. McGuire. Detection of the Free Neutrino: a Confirmation. *Science*, 124:103–104, 1956.

[6] C. S. Wu et al. Experimental test of parity conservation in beta decay. *Phys. Rev.*, 105:1413–1415, 1957.

[7] F.J. Hasert et al. Observation of neutrino-like interactions without muon or electron in the gargamelle neutrino experiment. *Phys. Lett.*, B46(1):138 – 140, 1973.

[8] G. Arnison et al. (UA1 Collaboration). Experimental observation of isolated large transverse energy electrons with associated missing energy at $s = 540$ GeV. *Phys. Lett.*, B122(1):103 – 116, 1983.

[9] P. Bagnaia et al. (UA2 Collaboratoin). Evidence for $Z_0 \to e^+e^-$ at the CERN pp collider. *Phys. Lett.*, B129(12):130 – 140, 1983.

[10] Z. Maki, M. Nakagawa, and S. Sakata. Remarks on the Unified Model of Elementary Particles. *Prog. Theor. Phys.*, 28:870–880, 1962.

[11] L. Wolfenstein. Neutrino oscillations in matter. *Phys. Rev. D*, 17:2369–2374, 1978.

[12] K. Abe et al. (T2K Collaboration). The T2K Experiment. *Nucl. Instrum. Meth.*, A659:106–135, 2011.

[13] D. S. Ayres et al. The NOνA Technical Design Report. 2007.

[14] K. Eguchi et al. (KamLAND Collaboration). First Results from KamLAND:

Evidence for Reactor Antineutrino Disappearance. *Phys. Rev. Lett.*, 90:021802, 2003.

[15] T. Araki et al. (KamLAND Collaboration). Measurement of Neutrino Oscillation with KamLAND: Evidence of Spectral Distortion. *Phys. Rev. Lett.*, 94:081801, 2005.

[16] K.A. Olive et al. Neutrino mixing. *Chin. Phys.*, C38:090001, 2014.

[17] K. Abe et al. (T2K Collaboration). Precise Measurement of the Neutrino Mixing Parameter θ_{23} from Muon Neutrino Disappearance in an Off-Axis Beam. *Phys. Rev. Lett.*, 112:181801, 2014.

[18] D.G. Michael et al. The magnetized steel and scintillator calorimeters of the MINOS experiment. *Nucl. Instrum. Meth.*, 596(2):190 – 228, 2008.

[19] P. Adamson et al. (MINOS Collaboration). Combined Analysis of ν_μ Disappearance and $\nu_\mu \to \nu_e$ Appearance in MINOS Using Accelerator and Atmospheric Neutrinos. *Phys. Rev. Lett.*, 112:191801, 2014.

[20] K. Abe et al. (T2K Collaboration). Indication of Electron Neutrino Appearance from an Accelerator-Produced Off-Axis Muon Neutrino Beam. *Phys. Rev. Lett.*, 107:041801, 2011.

[21] F.P. An et al. Observation of Electron-Antineutrino Disappearance at Daya Bay. *Phys. Rev. Lett.*, 108:171803, 2012.

[22] F.P. An et al. Independent measurement of the neutrino mixing angle θ_{13} via neutron capture on hydrogen at Daya Bay. *Phys. Rev.*, D90(7):071101, 2014.

[23] M.C. Gonzalez-Garcia, Michele Maltoni, and Thomas Schwetz. Updated fit to three neutrino mixing: status of leptonic CP violation. *JHEP*, 2014(11), 2014.

[24] K.A. Olive et al. The CKM quark-mixing matrix. *Chin. Phys.*, C38:090001, 2014.

[25] P.F. Harrison, D.H. Perkins, and W.G. Scott. Tri-bimaximal mixing and the neutrino oscillation data. *Phys. Lett.*, B530:167, 2002.

[26] Stephen F. King and Christoph Luhn. Neutrino Mass and Mixing with Discrete Symmetry. *Rept.Prog.Phys.*, 76:056201, 2013.

[27] Naoyuki Haba and Hitoshi Murayama. Anarchy and hierarchy. *Phys. Rev. D*, 63:053010, 2001.

[28] H. Minakata and Smirnov A.Y. Neutrino mixing and quark-lepton complementarity. *Phys. Rev. D*, 70:073009, 2004.

[29] D. S. Ayres et al. (LBNE Collaboration). The Long-Baseline Neutrino Experiment: Exploring Fundamental Symmetries of the Universe. http://arxiv.org/abs/1307.7335, 2013.

[30] K. Abe et al. Letter of Intent: The Hyper-Kamiokande Experiment – Detector Design and Physics Potential. http://arxiv.org/abs/1109.3262, 2011.

[31] G. Danby, J-M. Gaillard, K. Goulianos, L. Lederman, N. Mistry, M. Schwartz, and J. Steinberger. Observation of High-Energy Neutrino Reactions and the Existence of Two Kinds of Neutrinos. *Phys. Rev. Lett.*, 9:36–44, 1962.

[32] P. Zucchelli. A novel concept for a $\bar{\nu}_e/\nu_e$ neutrino factory: the beta-beam. *Phys. Lett. B*, B532(34):166 – 172, 2002.

[33] S. Geer. Erratum: Neutrino beams from muon storage rings: Characteristics and physics potential [Phys. Rev. D 57, 6989 (1998)]. *Phys. Rev. D*, 59:039903, 1999.

[34] S. van der Meer. A directive device for charged partilces and itss used in an enhanced neutrino beam. *CERN-61-07*, 1961.

[35] D.G. Baratov, A.P. Bugorsky, A.S. Vovenko, K.I. Gubrienko, E.V. Eremenko, et al. Ifve Neutrino Beam. 1. General Description and Main Characteristics. *Zh.Tekh.Fiz.*, 47:991–996, 1977.

[36] D.G. Baratov, N.Z. Bikbulatov, V.V. Vasilev, K.I. Gubrienko, S.A. Knyazev, et al. IHEP Neutrino Beam. 4. Focusing Device of Neutrino Channel. *Zh.Tekh.Fiz.*, 47:1014–1023, 1977.

[37] A. Asner and Ch. Iselin. A New Focusing System Considerably Increasing the Actual PS-Neutrino Beam Flux Intensity. *CERN-65-17*, 1965.

[38] A.G Abramov, N.A Galyaev, V.I Garkusha, J Hylen, F.N Novoskoltsev, A.D Ryabov, and V.G Zarucheisky. Beam optics and target conceptual designs for the NuMI project. *Nucl. Instrum. Meth.*, A485(3):209 – 227, 2002.

[39] A.K. Ichikawa. Design concept of the magnetic horn system for the T2K neutrino beam. *Nucl. Instrum. Meth.*, A690:27–33, 2012.

[40] Y. Hayato. Neut. *Nucl. Phys. (Proc. Suppl.)*, B112(13):171 – 176, 2002.

[41] Toshiba Electron Tubes and Devices Co., Ltd. http://www.toshiba-tetd.co.jp/eng/index.html.

[42] K. Abe et al. The T2K Neutrino Flux Prediction. *Phys. Rev. D*, 87:012001, 2013.

[43] M. Hartz et al. Optical Transition Radiation Monitor for the T2K Experiment. *Nucl. Instrum. Meth.*, A703:45–58, 2013.

[44] P.-A. Amaudruz et al. (T2K ND280 FGD Collaboration). The T2K fine-grained detectors. *Nucl. Instrum. Meth.*, A696:1–31, 2012.

[45] S. Assylbekov et al. (T2K ND280 P0D Collaboration). The T2K ND280 off-axis pi-zero detector. *Nucl. Instrum. Meth.*, A686:48–63, 2012.

[46] D. Allan et al. (T2K UK Collaboration). The electromagnetic calorimeter for the

T2K near detector ND280. *JINST*, 8:P10019, 2013.

[47] S. Aoki et al. The T2K Side Muon Range Detector (SMRD). *Nucl. Instrum. Meth.*, A698:135–146, 2013.

[48] K. Abe et al. (T2K Collaboration). Measurement of the inclusive ν_μ charged current cross section on iron and hydrocarbon in the T2K on-axis neutrino beam. *Phys. Rev. D*, 90:052010, 2014.

[49] K. Abe et al. (T2K Collaboration). Observation of Electron Neutrino Appearance in a Muon Neutrino Beam. *Phys. Rev. Lett.*, 112:061802, 2014.

[50] J. Beringer et al. Review of particle physics. *Phys. Rev. D*, 86:010001, 2012.

[51] K. Abe et al. Measurements of neutrino oscillation in appearance and disappearance channels by the T2K experiment with 6.6×10^{20} protons on target. *Phys. Rev.*, D91(7):072010, 2015.

[52] Alexander Himmel and Super-Kamiokande Collaboration. Recent results from Super-Kamiokande. *AIP Conference Proceedings*, 1604:345–352, 2014.

[53] K. Matsuoka et al. Design and performance of the muon monitor for the T2K neutrino oscillation experiment. *Nucl. Instrum. Meth.*, A624:591–600, 2010. doi:10.1016/j.nima.2010.09.074.

[54] Average energy required to produce an ion pair. ICRU Report 31, 1971.

[55] S.J. Harris and C.E. Doust. *Radiat. Res.*, 66:11, 1976.

[56] D.H. Wilkinson. IONIZATION CHAMBERS AND COUNTERS. Cambridge Univ. Press, 1950.

[57] T. Higuchi et al. Development of PCI based data acquisition platform for high intensity accelerator experiments. *eConf C* **0303241**, *TUGT004, hep-ex/0305088*, 2003.

[58] K. Abe et al. (T2K collaboration). Measurements of the T2K neutrino beam properties using the INGRID on-axis near detector. *Nucl. Instrum. Meth.*, A694:211–223, 2012.

[59] A. Pla-Dalman, A. Bross and V. Rykalin. FERMILAB-CONF-03-318-E.

[60] M. Yokoyama et al. Performance of multi-pixel photon counters for the T2K near detectors . *Nucl. Instrum. Meth.*, A622:567 – 573, 2010.

[61] A. Vacherete et al. The front end readout system for the T2K-ND280. *Nuclear Science Symposium Conference Record, 2007. NSS '07. IEEE*, 3:1984–1991, 2007.

[62] M.H. Ahn et al. Measurement of Neutrino Oscillation by the K2K Experiment. *Phys. Rev.*, D74:072003, 2006.

[63] S. Kopp, M. Bishai, M. Dierckxsens, M. Diwan, A.R. Erwin, et al. Secondary beam

monitors for the NuMI facility at FNAL. *Nucl. Instrum. Meth.*, A568:503–519, 2006.

[64] R. Acquafredda, T. Adam, N. Agafonova, P. Alvarez Sanchez, M. Ambrosio, et al. The OPERA experiment in the CERN to Gran Sasso neutrino beam. *JINST*, 4:P04018, 2009.

[65] A. Ferrari et al. FLUKA: A multi-particle transport code. *CERN-2005-010*, 2005.

[66] R. Brun, F. Carminati, and S. Giani. *CERN-W5013*, 1994.

[67] C. Zeitnitz and T. A. Gabriel. *In Proc. of International Conference on Calorimetry in High Energy Physics*, 1993.

[68] T. Nakamura et al. The OPERA film: New nuclear emulsion for large-scale, high-precision experiments. *Nucl. Instrum. Meth.*, A556:80–86, 2006.

[69] N. Armenise et al. High-speed particle tracking in nuclear emulsion by last-generation automatic microscopes. *Nucl. Instrum. Meth.*, A551:261–270, 2005.

[70] V. Tioukov et al. The FEDRA Framework for emulsion data reconstruction and analysis in the OPERA experiment. *Nucl. Instrum. Meth.*, A559:103–105, 2006.

[71] N. Abgrall et al. (NA61/SHINE Collaboration). CERN-PH-EP-2014-003. *JINST*, 9:P06005, 2014.

[72] N. Abgrall et al. (NA61/SHINE Collaboration). Measurements of Cross Sections and Charged Pion Spectra in Proton-Carbon Interactions at 31 GeV/c. *Phys. Rev. C*, 84:034604, 2011.

[73] N. Abgrall et al. (NA61/SHINE Collaboration). Measurement of production properties of positively charged kaons in proton-carbon interactions at 31 GeV/c. *Phys. Rev. C*, 85:035210, 2012.

[74] T. Eichten et al. Particle production in proton interactions in nuclei at 24 GeV/c. *Nucl. Phys. B*, 44:333, 1972.

[75] J. V. Allaby et al. High-energy particle spectra from proton interactions at 19.2 GeV/c. Technical Report 70-12, CERN, 1970.

[76] I. Chemakin et al. *Phys. Rev. C*, 77:015209, 2008.

[77] M. Bonesini et al. On particle production for high energy neutrino beams. *Eur. Phys. J. C*, 20:13, 2001.

[78] R.P. Feynman. Very high energy collisions of hadrons. *Phys. Rev. Lett.*, 23:1415, 1969.

[79] D. S. Barton et al. Experimental study of the A dependence of inclusive hadron fragmentation. *Phys. Rev. D*, 27:2580, 1983.

[80] P. Skubic et al. Neutral strange-particle production by 300 GeV protons. *Phys.*

Rev. D, 18:3115, 1978.

[81] K.A. Olive et al. Neutrino cross section measurements. *Chin. Phys.*, C38:090001, 2014.

[82] C.H. Llewellyn Smith. Neutrino reactions at accelerator energies. *Phys. Rept.*, 3(5):261 – 379, 1972.

[83] M. Gourdin. Weak and electromagnetic form factors of hadrons. *Phys. Rep.*, 11(2):29 – 98, 1974.

[84] T. Leitner et al. Electron- and neutrino-nucleus scattering from the quasielastic to the resonance region. *Phys. Rev. C*, 79:034601, 2009.

[85] D. Rein and L.M. Sehgal. Neutrino-excitation of baryon resonances and single pion production. *Ann. of Phys.*, 133(1):79 – 153, 1981.

[86] J.J. Aubert et al. The ratio of the nucleon structure functions $F2_n$ for iron and deuterium. *Phys. Lett.*, B123:275, 1983.

[87] Jorge G. Morfin, Juan Nieves, and Jan T. Sobczyk. Recent Developments in Neutrino/Antineutrino - Nucleus Interactions. *Adv.High Energy Phys.*, 2012:934597, 2012.

[88] B.G. Tice et al. Measurement of Ratios of ν_μ Charged-Current Cross Sections on C, Fe, and Pb to CH at Neutrino Energies 2-20 GeV. *Phys. Rev. Lett.*, 112(23):231801, 2014.

[89] D. Rein and L.M. Sehgal. Coherent π^0 production in neutrino reactions. *Nucl. Phys.*, B223(1):29 – 44, 1983.

[90] S Adler. Tests of the conserved vector current and partially conserved axial-vector current hypotheses in high-energy neutrino reactions. *Phys. Rev.*, 135:B963–B966, 1964.

[91] Alvarez-Ruso et al. Charged current neutrino-induced coherent pion production. *Phys. Rev. C*, 75:055501, 2007.

[92] Alvarez-Ruso et al. Neutral current coherent pion production. *Phys. Rev. C*, 76:068501, Dec 2007.

[93] R.A. Smith and E.J. Moniz. Neutrino reactions on nuclear targets. *Nucl. Phys.*, B43(0):605 – 622, 1972.

[94] M. Glck et al. Dynamical parton distributions revisited. *Eur. Phys. J*, C5(3):461–470, 1998.

[95] A. Bodek and U.K. Yang. Modeling Neutrino and Electron Scattering Inelastic Cross Sections. http://arxiv.org/abs/hep-ex/0308007, 2003.

[96] M. Derrick et al. Properties of the hadronic system resulting from $\bar{\nu}_\mu p$ interactions.

Phys. Rev. D, 17:1–15, 1978.

[97] Torbjrn Sjstrand. High-energy-physics event generation with PYTHIA 5.7 and JETSET 7.4. *Computer Physics Communications*, 82(1):74 – 89, 1994.

[98] L.L. Salcedo et al. Computer simulation of inclusive pion nuclear reactions. *Nucl. Phys.*, A484(34):557 – 592, 1988.

[99] A. Bodek et al. Vector and axial nucleon form factors: A duality constrained parameterization. *Eur. Phys. J*, C53(3):349–354, 2008.

[100] S.H. Ahn et al. Detection of accelerator-produced neutrinos at a distance of 250 km. *Phys. Lett. B*, 511(24):178 – 184, 2001.

[101] Measurement of the quasielastic axial vector mass in neutrino interactions on oxygen. *Phys. Rev. D*, 74:052002, 2006.

[102] M. Dorman et al. (MINOS Collaboration). Preliminary Results for CCQE Scattering with the MINOS Near Detector. *AIP Conference Proceedings*, 1189(1):133–138, 2009.

[103] A. Aguilar-Arevalo et al. (MiniBooNE Collaboration). First measurement of the muon neutrino charged current quasielastic double differential cross section. *Phys. Rev. D*, 81:092005, 2010.

[104] T. Katori et al. (MiniBooNE collaboration). First Measurement of Muon Neutrino Charged Current Quasielastic (CCQE) Double Differential Cross Section. *AIP Conference Proceedings*, 1222(1):471–474, 2010.

[105] V. Lyubushkin et al. A study of quasi-elastic muon neutrino and antineutrino scattering in the NOMAD experiment. *Eur. Phys. J*, C63(3):355–381, 2009.

[106] G. Fiorentini et al. (MINERνA Collaboration). Measurement of Muon Neutrino Quasielastic Scattering on a Hydrocarbon Target at E_ν $\sim$3.5 GeV. *Phys. Rev. Lett.*, 111:022502, 2013.

[107] J. Nieves et al. Inclusive charged-current neutrino-nucleus reactions. *Phys. Rev. C*, 83:045501, 2011.

[108] J. Nieves et al. Inclusive quasielastic charged-current neutrino-nucleus reactions. *Phys. Rev. C*, 70:055503, 2004.

[109] C. Andreopoulos et al. The GENIE neutrino Monte Carlo generator. *Nucl. Instrum. Meth.*, A614(1):87 – 104, 2010.

[110] D. Casper. The nuance neutrino physics simulation, and the future. *Nucl. Phys. (Proc. Suppl.)*, B112(13):161 – 170, 2002.

[111] Omar Benhar and Davide Meloni. Total neutrino and antineutrino nuclear cross-sections around 1-GeV. *Nucl. Phys.*, A789:379–402, 2007.

[112] O. Benhar, A. Fabrocini, S. Fantoni, and I. Sick. Spectral function of finite nuclei and scattering of GeV electrons. *Nucl. Phys.*, A579:493–517, 1994.

[113] A. Aguilar-Arevalo et al. (MiniBooNE Collaboration). Measurement of neutrino-induced charged-current charged pion production cross sections on mineral oil at $E_\nu \sim$1 GeV. *Phys. Rev. D*, 83:052007, 2011.

[114] A. Aguilar-Arevalo et al. (MiniBooNE Collaboration). Measurement of ν_μ-induced charged-current neutral pion production cross sections on mineral oil at $E_\nu \in 0.5 - 2.0$ GeV. *Phys. Rev. D*, 83:052009, 2011.

[115] C. Anderson et al. First Measurements of Inclusive Muon Neutrino Charged Current Differential Cross Sections on Argon. *Phys. Rev. Lett.*, 108:161802, 2012.

[116] P. Adamson et al. (MINOS Collaboration). Neutrino and antineutrino inclusive charged-current cross section measurements with the MINOS near detector. *Phys. Rev. D*, 81:072002, 2010.

[117] Q. Wu et al. A Precise measurement of the muon neutrino-nucleon inclusive charged current cross-section off an isoscalar target in the energy range $2.5 < E_\nu < 40$ GeV by NOMAD. *Phys. Lett.*, B660:19–25, 2008.

[118] Y. Nakajima et al. Measurement of inclusive charged current interactions on carbon in a few-GeV neutrino beam. *Phys. Rev.*, D83:012005, 2011.

[119] K. Abe et al. Measurement of the inclusive charged current cross section on carbon in the near detector of the T2K experiment. *Phys. Rev.*, D87(9):092003, 2013.

[120] K. Abe et al. (T2K Collaboration). Measurement of the inclusive ν_μ charged current cross section on iron and hydrocarbon in the T2K on-axis neutrino beam. *Phys. Rev. D*, 90:052010, 2014.

[121] K. Anderson, B. Bernstein, D. Boehnlein, Kenneth R. Bourkland, S. Childress, et al. The NuMI Facility Technical Design Report. 1998.

[122] S. Agostinelli et al. Geant4a simulation toolkit. *Nucl. Instrum. Meth.*, A506(3):250 – 303, 2003.

[123] Scitillations from Organic Crystals: Specific Fluorescence and Relative Response to Different Radiations. *Proc. Phys. Soc.*, A64:874, 1951.

[124] M. Otani, N. Nagai, D. Orme, A. Minamino, K. Nitta, et al. Design and construction of INGRID neutrino beam monitor for T2K neutrino experiment. *Nucl. Instrum. Meth.*, A623:368–370, 2010.

[125] H.C. Fesefeldt. Simulation of hadronic showers, physics and applictation. Technical report PITHA 85-02, 1985.

[126] A.B. Kaidalov. The quark-gluon structure of the pomeron and the rise of inclusive spectra at high energies. *Phys. Lett.*, B116(6):459 – 463, 1982.

[127] K.K. Gudima, S.G. Mashnik, and V.D. Toneev. Cascade-exciton model of nuclear reactions. *Nucl. Phys.*, A401(2):329 – 361, 1983.

[128] Yu.E. Titarenko et al. Experimental and Computer Simulation Study of Radionuclide Production in Heavy Materials Irradiated by Intermediate Energy Protons, 1999.

[129] R.G. Alsmiller Jr. M.P. Guthrie and H.W. Bertini. Calculation of the capture of negative pions in light elements and comparison with experiments pertaining to cancer radiotherapy. *Nucl. Instrum. and Meth.*, 66(1):29 – 36, 1968.

[130] Hugo W. Bertini and Miriam P. Guthrie. News item results from medium-energy intranuclear-cascade calculation. *Nucl. Phys.*, A169(3):670 – 672, 1971.

[131] B. Andersson, G. Gustafson, and B. Nilsson-Almqvist. A model for low-pT hadronic reactions with generalizations to hadron-nucleus and nucleus-nucleus collisions. *Nucl. Phys.*, B281(12):289 – 309, 1987.

[132] T. Kikawa. Ph.D. thesis. Kyoto University, 2014.

[133] K. Abe et al. Evidence of Electron Neutrino Appearance in a Muon Neutrino Beam. *Phys. Rev.*, D88(3):032002, 2013.

[134] K. Abe et al. Measurement of Neutrino Oscillation Parameters from Muon Neutrino Disappearance with an Off-axis Beam. *Phys. Rev. Lett.*, 111(21):211803, 2013.

[135] Alexis A. Aguilar-Arevalo et al. Measurement of ν_μ and $\bar{\nu}_\mu$ induced neutral current single π^0 production cross sections on mineral oil at E_ν $\sim$O(1 GeV). *Phys. Rev.*, D81:013005, 2010.

[136] A.A. Aguilar-Arevalo et al. Measurement of Neutrino-Induced Charged-Current Charged Pion Production Cross Sections on Mineral Oil at $E_\nu \sim 1$ GeV. *Phys. Rev.*, D83:052007, 2011.

[137] T. Yang, C. Andreopoulos, H. Gallagher, K. Hoffmann, and P. Kehayias. A Hadronization Model for Few-GeV Neutrino Interactions. *Eur.Phys.J.*, C63:1–10, 2009.

[138] Z. Koba, Holger Bech Nielsen, and P. Olesen. Scaling of multiplicity distributions in high-energy hadron collisions. *Nucl. Phys.*, B40:317–334, 1972.

[139] D. Zieminska et al. Charged-particle multiplicity distributions in νn and νp charged-current interactions. *Phys. Rev. D*, 27:47–57, 1983.

[140] P. Allen et al. Multiplicity distributions in neutrino-hydrogen interactions. *Nucl. Phys.*, B181(3):385 – 402, 1981.

[141] S. Bhadra et al. Letter of Intent to Construct a nuPRISM Detector in the J-PARC Neutrino Beamline. 2014.

[142] D. Ashery et al. True absorption and scattering of pions on nuclei. *Phys. Rev. C*,

23:2173–2185, 1981.

[143] K. Nakai et al. Measurements of cross sections for pion absorption by nuclei. *Phys. Rev. Lett.*, 44:1446–1449, 1980.

[144] M. K. Jones et al. Pion absorption above the $\Delta(1232)$ resonance. *Phys. Rev. C*, 48:2800–2817, 1993.

[145] C. J. Gelderloos et al. Reaction and total cross sections for 400 to 500 MeV π^- on nuclei. *Phys. Rev. C*, 62:024612, 2000.

[146] B.W. Allardyce et al. Pion reaction cross sections and nuclear sizes. *Nuclear Physics A*, 209(1):1 – 51, 1973.